Applications of Distributed Temperature Sensing in Subsurface Hydrology

A thesis submitted to the School of Environmental Sciences of the University of East Anglia in partial fulfilment of the requirements for the degree of Doctor of Philosophy

By Tom Oliver Trevett Read

June 2016

Abstract

In the study of dynamic subsurface processes there is a need to monitor temperature and groundwater fluxes efficiently in both time and space. Distributed Temperature Sensing has recently become more accessible to researchers in Earth Sciences, and allows temperatures to be measured simultaneously, at small intervals, and over large distances along fibre optic cables. The capability of DTS in conjunction with heat injection to detect groundwater fluxes, is assessed in this thesis using a combination of numerical modelling, laboratory tests, and field trials at the Ploemeur research site in Brittany, France. In particular, three methodological approaches are developed: thermal dilution tests, point heating, and the hybrid cable method. A numerical model was developed to assess the sensitivity range of thermal dilution tests to groundwater flow. Thermal dilution tests undertaken at Ploemeur showed lithological contrasts, and allowed the apparent thermal conductivity to be estimated in-situ, but failed to detect previously identified transmissive fractures. The use of DTS to monitor in-well vertical flow is then investigated. This is first using a simple experiment deploying point heating (T-POT), which tracks a parcel of heated water vertically through the borehole. The method allowed for the relatively quick estimation of velocities in the well. The use of heated fibre optics is then trialled, and through a field test was shown to be sensitive to in-well vertical flow. However, the data suffered from a number of artefacts related to the cable installation. To address this, a hybrid cable system was deployed in a flume to determine the sensitivity relationship with flow angle and electrical power input. Additionally, a numerical model was developed, which suggested a lower limit for velocity estimation due to thermal buoyancy. With the emergence of Distributed Acoustic Sensing, fibre optics may become an increasingly practicable and complete solution for monitoring subsurface processes.

Acknowledgements

I would first of all like to thank Victor Bense, for proposing the thesis on DTS, accepting me to take this on, and being my primary supervisor for over three years. I have thoroughly enjoyed the process of working together on various projects since 2009, and I hope we can continue to collaborate in the future. I would also like to thank Kevin Hiscock, who took on the primary supervisor role in the final six months of the PhD, for discussions during supervisory meetings and his on-going support. I also would like to thank NERC for funding the PhD studentship, conference trips to the IAH-2012 in Niagara, AGU-2013 and AGU-2014, and participation at a DTS workshop at Stanford.

I would like to send a big thanks to colleagues at Geosciences Rennes, of the University of Rennes 1, whose involvement greatly shaped the direction of my PhD thesis. They funded much of the fieldwork and allowed me to return to Rennes on several occasions. In particular I would like to thank Olivier Bour, for his generosity, spirit of collaboration, for commenting on manuscripts, and sharing his experience in the field. In the end, we never did get round to that fishing trip! I would also like to thank Tanguy Le Borgne for assistance in the field and contributions to analysing the field data. I also wish to thank Nicolas Lavenant, Rebecca Hochreutener, Maria Klepikova, Pascal Goderniaux, Vincent Boschero, and Hugo Le Lay, for their efforts during long days in the field and esprit de corps!

I must also thank John S. Selker, from Oregon State University, who contributed many of the original ideas in the thesis, commented on manuscripts, and was responsible for much of the novel bricolage at the field site. I also thank Stefan Krause (University of Birmingham), Athena Chalari, Michael Mondanos, and Thomas Coleman (Silixa Ltd), who have provided technical support with using DTS systems and sharing their knowledge of DTS deployments. Much of the work at UEA was made possible by the contributions of enthusiastic visiting students including Romain Aranda, Augustin Ollion, Antoine Guerin, Carolina Penalber, and Augusto Capum, who assisted with field, lab, and early COMSOL work. Good luck in your future endeavours! I would also like to thank all the ENV technical staff and the HPC support for making things happen smoothly. To friends made at UEA - thank you for the camaraderie during the mutual ups and downs experienced

while undertaking a PhD. Particular thanks go to those in office 3.16 including Alex, Katie, Mel P, Mel F, Jennie, Maria, Kostas, Chris, and Johanna.

Finally, the biggest thanks of all goes to Sarah for being incredibly rational, loving, and supportive.

Contents

List of tables

List of figures

Chapter 1

Introduction

1.1 Chapter summary

In this chapter, background information common to all chapters in the thesis is presented. The natural temperature distribution in the subsurface and characteristics of temperature-depth profiles obtained in aquifers are introduced. These are related to groundwater flow, specifically natural gradient flow, and in-well vertical flow. The measurement of these fluxes, using novel approaches using DTS which combine in-well heating and fibre optic temperature measurements, are the subject of the thesis. The principles of DTS are then outlined with emphasis given to key criteria affecting borehole DTS deployments. Options for cable configuration and calibration of the backscatter data are discussed, as well as key metrics for assessing the performance of DTS systems. Cable construction is shown to be a key part of the sensing system affecting the spatial and temporal resolution of DTS temperature data. Finally, the Ploemeur site, which is the location for field trials presented in Chapters 2, 3, and 4, is introduced, with background provided on the local geology, hydrogeology, and characteristics of the field site.

1.2 Aims and objectives of the thesis

Characterization of groundwater flow in the subsurface is necessary for an understanding and quantification of hydraulic properties, and in the wider context is key to understanding how fundamental processes such as solute and heat transport occur. There is a need for characterization methods that give more detail in often highly heterogeneous systems

(*Neuman*, 2005). The increasing performance capabilities of DTS instruments allow for highly resolved temperature measurements with distance and time. The aim of this thesis is to explore the potential uses of DTS in subsurface hydrology to monitor natural gradient groundwater flow and vertical flow in wells. Such approaches offer significant advances in that they can be made to be autonomous, and provide measurements over relatively large scales in much finer detail than can be feasibly achieved with point sensors.

Objective 1: Thermal response tests in the subsurface are means to identify thermal property variation. Analysis methods typically assume that heat conduction is the dominant mechanism of heat transfer, or that, if present, groundwater flow will act to enhance the decay of the thermal signal. A typical approach is to assign an apparent thermal property, which differs from the true thermal properties due to heat advection. The objective here is to identify how groundwater flow affects the response in such tests and the magnitude of the change in apparent thermal properties. We also seek to appraise DTS as a means to efficiently monitor such tests.

Objective 2: The measurement of vertical in-well flow presents a challenge, in that measurements are made with cumbersome flowmeters. The objective is to use DTS to provide efficient measurements of in well vertical flow by carrying out in-well thermal tracer tests.

Objective 3: A developing aspect of DTS is the use of the cable to simultaneously monitor temperature and be heated. In this sense, the cable behaves as a hot-wire anemometer. While the cable is heated, moving fluids transfer heat away and decrease the cable temperature, which can be measured with DTS. DTS therefore has the potential to be transformed into a distributed technology for fluid flow measurements. The objective here is to understand the heat transfer process, the key factors affecting the response of heated fibre optic cables to fluid flow, and how the method can be optimised to maximise the temperature response (i.e. the signal) to fluid flow. An additional objective is to trial this approach in a borehole.

1.2.1 Thesis structure

The content of the thesis is organised into self contained chapters, written in a manuscript style. To avoid repetition, background material common to all sections is provided in

Chapter 1, with more specific background provided at the start of each chapter.

- Chapter 2, 'Using DTS to measure apparent thermal conductivity profiles and estimate ambient groundwater fluxes' describes a field trial of a heat pulse test, monitored with DTS. The results are analysed for apparent thermal properties, and a model developed to investigate the significance of groundwater flow on cooling data from such tests.

- Chapter 3, 'Thermal-Plume fibre Optic Tracking (T-POT) test for flow velocity measurement in groundwater boreholes' outlines a field trial of an in-well test for vertical flow estimation.

- Chapter 4, 'Field trial of the hybrid cable method to measure in-well vertical flows' details an attempt to use heated fibre optics to measure vertical flow.

- Chapter 5, 'Optimisation of the hybrid cable method for measuring fluid flow', describes laboratory and numerical modelling work to identify the underlying physics and optimise the hybrid cable method.

- Chapter 6, 'Comparative discussion of borehole DTS methods' is a literature review of subsurface DTS deployments. It also seeks to clarify the expanding field of approaches involving DTS and active heating.

Appendices A, B, and C, are the full text papers containing content either directly incorporated or reworked for the thesis. Appendix D is a paper worked on during the PhD thesis using DTS in a meteorological context.

1.3 Background

Heat is widely recognised as a useful tracer for a range of hydrogeological processes (e.g., *Saar*, 2011). The advantage of using heat over other tracers such as geochemical tracers, is that temperature is ubiquitous, and easily and economically measured in-situ with a variety of probes and loggers. Where temperature changes are small (typically less than 0.1 °C), high precision temperature loggers are available with resolutions of 0.001°C (*Pehme et al.*, 2013). A disadvantage of using point temperature loggers is the incomplete space-time coverage when trolling a probe, or incomplete depth coverage with a few fixed data

loggers. The emergence of DTS allows some of these monitoring issues to be overcome. DTS allows temperatures to be measured rapidly and in detail along fibre optic cables (e.g., *Selker et al.*, 2006). DTS is enhancing our understanding of dynamic subsurface processes through high resolution temperature monitoring, and pushing forward new investigation methods. However, the unique limitations on DTS need to be well understood in the design of subsurface applications.

1.3.1 Natural gradient groundwater flow and temperature

Near surface temperature measurements can be used to identify contributions to surface water of relatively deep groundwater (e.g., *Schuetz and Weiler*, 2011). In the relatively shallow subsurface, the temperature depth profile is subject to seasonal and diurnal forcing. Rates of groundwater upwelling or downwelling affect the propagation of the seasonal temperature wave into the subsurface which can be observed in shallow boreholes through temperature-depth profiles and analysed for seepage or infiltration rates (*Taniguchi*, 1993; *Bense and Kooi*, 2004). Exploiting the same effect, measurements of temperature at a fixed depth in streambeds taken at different moments in a season allow the variability of groundwater flux to be estimated in great detail (e.g. *Bense and Kooi*, 2004; *Conant*, 2004). These and other approaches have been critically reviewed by *Anderson* (2005), and there are many examples where DTS has been appraised for the investigative studies of this kind (e.g., *Briggs et al.*, 2012a; *Hare et al.*, 2015). Here, we specifically focus on the application of DTS to infer hydrogeological conditions at depths below where diurnal an seasonal temperature fluctuations can be exploited for this purpose. In this setting, DTS is increasingly deployed to measure temperature variation with depth and through time in piezometers, boreholes, or direct push approaches.

At depths from $\sim$20 metres, the geothermal gradient usually dominates temperature-depth profiles and is a function of both the local geothermal heat flux and thermal conductivity of the formation, primarily governed by Fourier's Law of heat conduction. Where a temperature depth profile departs from this expected behaviour, it is often taken as indicative of groundwater flow which causes the advection of heat in addition to conduction (Figure 1.1). Over a depth scale of metres to kilometres, temperature depth profiles can become convex or concave for upward or downward groundwater flow respectively (e.g.,

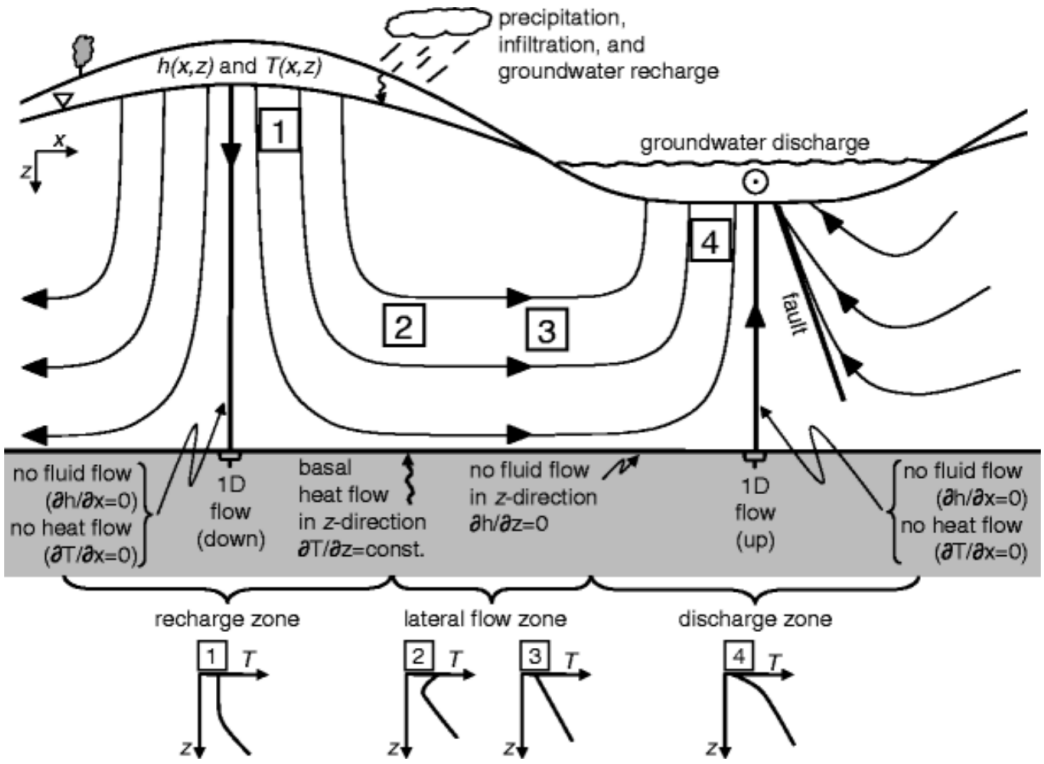

Figure 1.1: Schematic of the expected temperature depth profiles in different locations within a topographically driven groundwater flow regime. (1) shows cold water recharge, (2) low temperature horizontal flow, (3) thermally equilibrated lateral flow, (4) elevated temperature near the surface in the recharge zone. From (*Saar*, 2011)

Bredehoeft and Papaopulos, 1965). Localised horizontal flow of groundwater through fractures or faults often results in localised abrupt temperature changes that depart from the geothermal gradient (*Ge*, 1998; *Bense et al.*, 2008).

Ambient groundwater flow also affects the response observed in thermal tests carried out in the subsurface. Thermal tests typically seek to quantify the thermal properties of the subsurface. Flowing groundwater typically reduces any warm thermal signal introduced into the subsurface, as advection adds to the conductive temperature dissipation. Where this is considered, the thermal properties are often termed 'apparent', as they do not necessarily correspond to the true thermal properties. In studies of aquifer properties, Active Line Source (ALS) tests seek to quantify apparent thermal property variation with depth through prolonged heating (*Pehme et al.*, 2007), and application of analytical solutions to the heating and cooling data. Additionally, Thermal Response Tests (TRTs) are a relatively standard test carried out in the context of ground source heated pumps (*Liebel et al.*, 2012). Fluid is circulated through a closed loop installed in a borehole. As the fluid

circulates, a constant amount of heat is applied, and the evolution of temperature measured in the circulating fluid is a function of the mean thermal properties of the formation and groundwater specific discharge.

1.3.2 In-well flow

The monitoring of the aforementioned processes is typically carried out in piezometers or continually cased boreholes, where it can be assumed that the temperature measured in the fluid at a given depth is the same as the temperature in the formation. In open or long screened boreholes, this is often not the case. The borehole itself behaves as a high permeability vertical conduit for fluid flow, which can connect otherwise hydraulically isolated aquifers or fractures. In this case, small differences in hydraulic head in the vertical can drive fluid flow through the borehole, transporting water with a potentially different temperature. Despite the overprinting of the background temperature-depth profile by this borehole induced effect, temperature data collected under these conditions are still useful. The inflow of water with different temperature to the resident water causes small inflections in the temperature-depth profile and is useful to identify hydraulically active fractures (*Drury et al.*, 1984). For large inflows of distinctly different temperature, the temperature signal may be advected vertically through the well. This temperature signal may allow the flow to be estimated using analytical (*Drury et al.*, 1984), or numerical modelling approaches (*Klepikova et al.*, 2011).

When conducted under ambient conditions, the flow in the well is a function of the transmissivity weighted heads of the fractures or aquifer units intersecting the well. Vertical flow measured in a single well under ambient conditions allows the direction of the hydraulic gradient as well as transmissive zones to be identified. When obtained under pumping conditions, the transmissivity of individual fractures is assigned using a flow proportional weight of the transmissivity of the well. When measured under cross-pumping conditions, flow data can be used to obtain transmissivity, head, and storage coefficients of the geological unit or fractures between boreholes (*Paillet*, 1998; *Paillet et al.*, 2011). In-well vertical flow is typically measured with a heat-pulse, electromagnetic, or impeller flowmeter (Figure 1.2). Measuring flow variation over depth in a well takes time by raising and lowering the probe. There is therefore an opening for new methods that allow

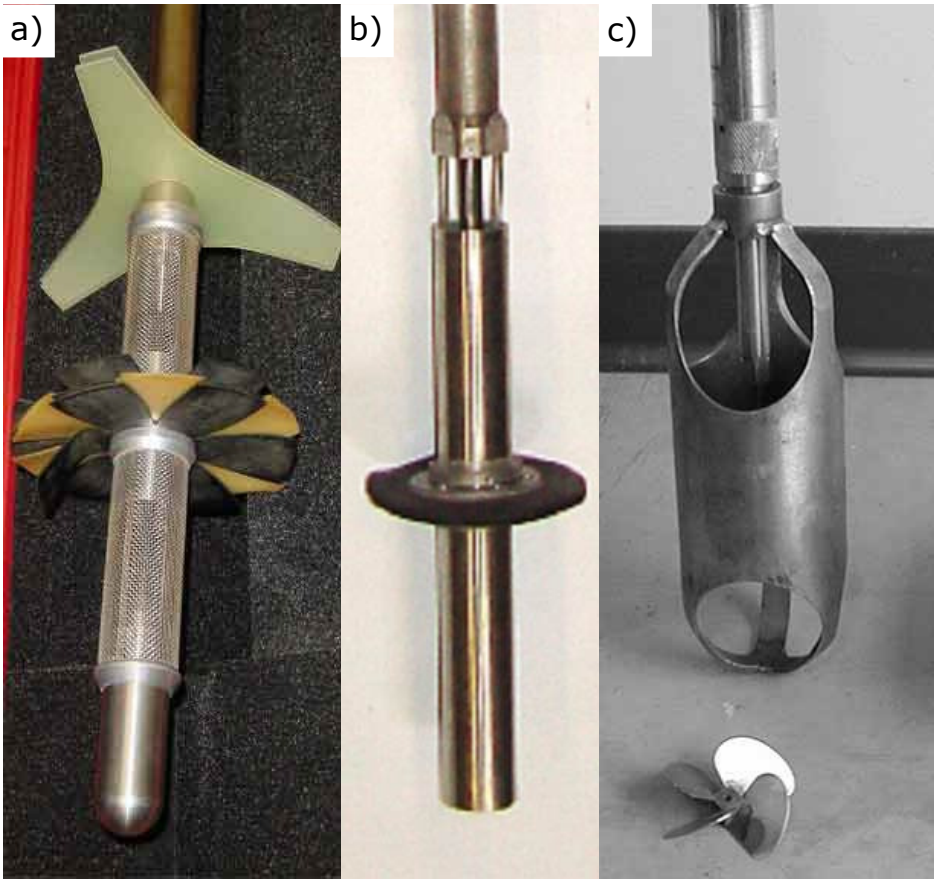

Figure 1.2: Examples of downhole flow meters including a) heat-pulse, b) electromagnetic, and c) impeller (*USGS*, 2013)

flow to be quickly measured over large depth intervals, especially with methods such as hydraulic tomography that require flow measurements in multiple wells under different pumping conditions (e.g., *Klepikova et al.*, 2013). This thesis aims to develop DTS based methods that use temperature measurements to derive hydrological conditions, to overcome these monitoring issues.

1.4 Principles of Distributed Temperature Sensing

DTS is the measurement of temperature along a fibre optic cable, potentially exceeding 10 km in length, using light. The temperature along the fibre optic cable is determined by a base unit that emits laser pulses and detects distance via the transit time of light and temperature dependent Raman backscatter signal. The Raman backscatter is generated by the inelastic interaction of the incident light with the glass crystal lattice structure (*Rogers*,

1999) (Figure 1.3). The ratio of the intensity of photons returning at specific higher (anti-Stokes, I_{aS}) and specific lower frequency (Stokes, I_S) allows the temperature T [K], as a function of distance along the fibre z [m], to be computed according to (*Farahani and Gogolla*, 1999; *Hausner et al.*, 2011)

$$T(z) = \frac{\gamma}{\ln \frac{I_S(z)}{I_{aS}(z)} + \epsilon - \Delta\alpha z} \tag{1.1}$$

where $\Delta\alpha$ [m^{-1}] is the differential attenuation of the Stokes and anti-Stokes signals (a property of the fibre optic cable), C [-] is specific to the instrument laser source and detector, and γ [K] is related to the energy shifts between incident and scattered Raman photons. The differential attenuation may be a function of distance if there are point defects or strains, and C (strongly) and γ (weakly) are a function of instrument operating temperature. The distance to the location of scattering is calculated from the two-way travel time for light using the refractive index of the optical fibre. After sending out many repeated short laser pulses, the DTS analyses the Stokes and anti-Stokes intensities integrated over user specified time and spatial intervals along the cable. To translate the backscatter to temperature data the three calibration parameters need to be determined.

1.4.1 Temperature calibration and monitoring modes

DTS systems typically report the distance, Raman Stokes and anti-Stokes intensities, and computed temperature for each increment of length along a fibre optic cable. To generate these temperature values the unit typically makes use of an internal reference coil of fibre and temperature probe, but since light loss at any location along the path can result in offsets in apparent temperature, these values often exceed $\pm$ 1 K. Much more accurate temperatures can be obtained through use of external reference temperature baths (*Tyler et al.*, 2009), and post-processing of the observed Stokes and anti-Stokes data to calculate temperature values based on equation 1.1 (*Hausner et al.*, 2011; *van de Giesen et al.*, 2012). These reference baths must create homogeneous temperature conditions, in which a length of fibre optic cable at least 10-times the sampling interval, and reference temperature logger are installed (*Hausner et al.*, 2011; *van de Giesen et al.*, 2012).

Establishment of conditions required to obtain accurate temperature calibration is a critical element of the DTS set-up in the field, and must be designed in the context of

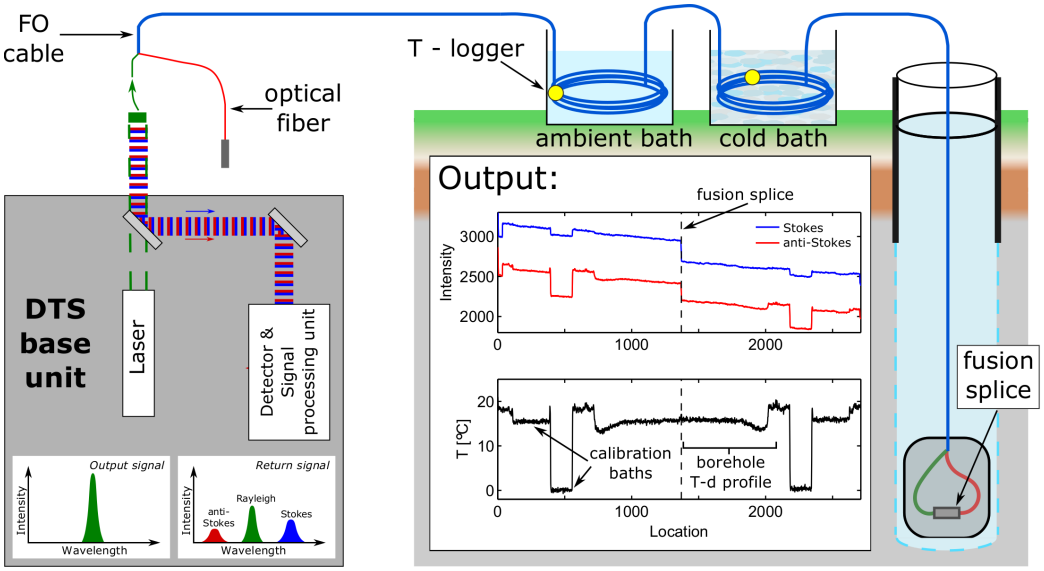

Figure 1.3: Schematic of DTS principles, with the cable connected to the base unit, and sequentially passing through an ambient temperature bath, cold bath, and then deployed down a borehole. The short pulse emitted by the instrument (green) propagates along the fibre. Backscattered anti-Stokes (red) and Stokes light (blue) return to the instrument, and their intensities recorded for each spatial measurement interval. Two of the optical fibres contained in the cable are joined at the far end with a fusion splice, such that by pulsing light down one of the fibres and monitoring the back scatter, two measurements of backscatter are provided at each position on the cable (a duplexed single-ended measurement). The resulting backscatter data and interpreted temperatures along the cable are shown for a 30 s averaging time. The temperature data show the relatively homogeneous temperatures of the ambient and cold reference baths, followed by the borehole temperature depth profile. This is then seen in reverse order, after the emitted light traverses the fusion splice. A double-ended measurement would be possible by additionally connecting the red fibre to the instrument, and alternately taking measurements on this and the green fibre

the objectives and geometry of the installation. Foremost, the location and number of splices or defects in the cable must be considered, with logistical considerations including access to a power supply and protection against rapid changes in temperature. In a general sense, calibration requires that along each distinct length of fibre (i.e., between locations of splices or connectors) there be at least three externally measured temperatures, two of which must be separated in space.

The two general configuration options for the optical path of the fibre are known as single-ended and double-ended configurations. In borehole deployments both may be appropriate and are outlined briefly here. In a conventional single-ended set up, a single fibre is coupled to the base unit and terminated at the other end. If the cable passes through three reference baths, then equation (1.1) can be rewritten for each of the reference baths at known values of z, measured values of Ia_S, I_S, and independently measured T, and solved for the three calibration parameters. With a corresponding value of $z*$ for the mean

distance to the reference section, equation (1.1) becomes (*Hausner et al.*, 2011):

$$\gamma + T_i z_i^* \Delta\alpha - T_i C = T_i \ln \frac{I_S\left(z_i^*\right)}{I_{aS}\left(z_i^*\right)} \tag{1.2}$$

where subscript i denotes the reference bath. Equation (1.2) can be written three times for i=1,2,3 and explicitly solved for the calibration parameters. The most robust approach is to do this for every measurement in time to give a dynamic calibration, and to use spatially averaged values from well within the reference sections of Ia_S and I_S, rather than from a single location, to minimise the effect of calibration parameter uncertainty on the subsequent calculated temperature uncertainty (*Suárez et al.*, 2011). The main assumption implicit in equations (1.1) and (1.2) is that the differential attenuation is constant with distance. For accurate solution, the three calibration sections must be of at least two different temperatures (ideally bracketing the expected observed temperature range), and to accurately estimate $\Delta\alpha$, one should be located far from the others (ideally with one at the start and one at the end of the cable). Effort in the field and the amount of equipment needed can be reduced by having a duplexed set-up (a single cable that has two parallel fibres), with a fusion splice at the far end of the cable connecting the fibres into a single optical path, such that only two baths need to be set up (Figure 1.3). In this case the data after the splice need to be adjusted for potential differential loss of the return signals at the fusion splice (*Hausner et al.*, 2011). Additionally, such splices can generate spatially distributed defects in temperature measurement seen in wound and non-wound cables (e.g., *J.S. Selker*, personal communication, 2015; *Arnon et al.*, 2014a), which can be challenging to detect and correct.

An alternative is to use a double-ended calibration, which allows correction for non-uniform differential attenuation along the cable commonly seen at bends, connectors, splices, and where there has been fibre degradation (e.g., hydrogen ingress). Here, two connections must be made to two separate channels of the base unit, such that light can travel from one connection to the other via the installed cable. Measurements are taken alternately from each instrument channel, which are referred to as the forward and reverse directions. Assuming that the temperature remains constant between the two measurements, the differential attenuation is calculated for short intervals Δz (typically the

sampling interval) according to (*van de Giesen et al.*, 2012):

$$\int_{z}^{z+\Delta z} \Delta\alpha\left(z'\right) dz' = \ln\left(\frac{I_S\left(z+\Delta z\right)}{I_{aS}\left(z+\Delta z\right)}\right)_{\Rightarrow} - \ln\left(\frac{I_S\left(z\right)}{I_{aS}\left(z\right)}\right)_{\Rightarrow} + \ln\left(\frac{I_S\left(z\right)}{I_{aS}\left(z\right)}\right)_{\Leftarrow} - \ln\left(\frac{I_S\left(z+\Delta z\right)}{I_{aS}\left(z+\Delta z\right)}\right)_{\Leftarrow} \quad (1.3)$$

where directional arrows denote the forward and reverse directions. The differential attenuation of signal coming from a certain location is then found by summing all of the differential attenuation from the location of scatter to the instrument. The other calibration parameters may then be found explicitly using two reference baths or from a single bath if γ is assumed to be a known, constant value in time.

1.4.2 DTS performance metrics

The key metrics of DTS system performance are the accuracy and precision of reported temperature, at the specified spatial resolution. The uncertainty in temperature is typically characterised by the standard deviation or Root Mean Square Error (RMSE) of the reported temperature in comparison to the true temperature. The RMSE in temperature normally scales with the inverse of the square root of the product of the integration time and the length of cable over which the temperature is being reported. This reflects the central limit theorem applied to the number of photons employed in the intensity estimates. The RMSE is also a function of distance along the cable due to Beer's Law attenuation of light with travel distance from the base unit, with data further from the instrument having poorer resolution. The relationship between RMSE and distance is more complicated in the case of double ended measurements, wherein reported temperatures are computed using light travelling in both directions along the cable. This generally results in the lowest RMSE at the midpoint of the cable equidistant from the base unit along each channel.

While units report back temperatures at a given minimum sampling interval, the spatial resolution is always larger than this value (*Selker et al.*, 2014). For a step change in temperature along a cable, this is usually defined as the distance between the points at 10% and 90% of the true temperature change (*Tyler et al.*, 2009; *Selker et al.*, 2014). Each reported Stokes and anti-Stokes backscatter intensity at a specific distance is in fact from

a unit Gaussian distribution times the true temperature conditions along the cable (Figure 1.4). Temporal resolution is the ability to resolve temperature changes in time, which can be limited by the DTS instrument or properties of the cable. Contemporary DTS systems typically can read temperatures every few seconds, so cable construction is often the most significant factor in thermal responsiveness, with larger diameter more massive cables of high thermal inertia responding less rapidly to temperature changes in time. As long as data storage is not a limiting factor, it is usually advisable to set the spatial and temporal averaging to the highest possible frequency the instrument supports, since internal averaging applied by the instrument cannot be subsequently undone, while post-processing averaging provides all the advantages which would be obtained from longer collection intervals.

1.4.3 Cable selection and installation

Cable design is critical to success, and includes decisions regarding fibre selection and protection against tension, bending, and compression of the fibre. Bend tolerant multimode fibres (which for DTS are typically 50 μm core diameter, 125 μm cladding diameter) are preferable for borehole DTS applications, since single-mode fibres have lower backscatter intensity, and bends in the cable can be unavoidable from the instrument housing to the borehole. However, it is often useful to include single-mode fibres in addition to allow for the possibility of acoustic detection (using Distributed Acoustic Sensing (DAS)), to complement thermal data (*Noni et al.*, 2011). Cable design that includes multiple fibres are advisable for environmental applications as these provide redundancy in case of damage occurring to one but not all fibres, and allows duplexed single-ended or double ended measurements to be obtained by fusion splicing two fibres together at the far end of the cable. Every fusion splice, if it is to be submerged or exposed to humidity or moisture, needs physical protection either in pressure rated enclosures or as an alternative by setting it in resin. The optical fibres need to be protected from depth varying pressure changes that can cause non-uniform differential attenuation. Typically, loose tube cable constructions, wherein the fibres are placed helically in an over-sized capillary tube, are preferred as pressure changes are not transmitted to the fibres and the fibres do not experience stress if the cable is slightly stretched or compressed. For high-pressure settings such a cable

design includes the fibres housed inside a hydrogen-scavenging gel-filled stainless steel capillary tube to prevent hydrogen migration and alteration of the attenuative properties of the fibre (*Reinsch et al.*, 2013). There may also be additional armoring and typically an external plastic jacket.

In borehole installations it is generally advantageous to seek the highest spatial resolution possible, to detect, for instance, if there are closely spaced fractures with groundwater flow. As stated above, should lower spatial resolution be desired, the data may be averaged in post-processing with no loss in performance relative to having obtained the data at lower spatial resolution at the outset (though this should be confirmed for each base unit, at least one manufacturer employs methods which violate this assumption). One may achieve a desired spatial resolution either by selecting an instrument with the desired spatial resolution, or, a wrapped cable can be deployed. In such a cable, the optical fibre is wrapped around a central strength member, such that for every unit length of cable there is a greater length of optical fibre, so the effective spatial resolution is increased. Custom made solutions have been used to measure shallow temperatures with depth in glaciers and lakes (*Selker et al.*, 2006), and stream bed sediments (*Briggs et al.*, 2012b; *Vogt et al.*, 2010), while pre-wrapped cables can also be purchased and have been deployed in lakes (*Arnon et al.*, 2014a), and boreholes (*Banks et al.*, 2014). Data from wrapped cables need careful processing. In the case of tightly wrapped fibres, there have been documented entrance effects in approximately the first 100 m of fibre after the transition from a straight cable to wrapped cable that if not corrected for, will result in erroneous data (*Arnon et al.*, 2014a). Because of the distance and time varying nature of the correction, *Arnon et al.* (2014b) developed an empirically based method for the processing of wrapped cable data.

To illustrate the various spatial averaging options, it is useful to look in detail at a 3 m section of a borehole at the Ploemeur research site, France, using different combinations of instruments and cables (Figure 1.4). Data were collected by instruments with manufacturer specified spatial resolutions of 2.0 and 0.3 m (sampling at 1.01 and 0.12 m respectively) on standard (Figure 1.4 panels b and c), and wrapped cables (Brugg High Resolution cable, Brugg, Switzerland, Fig 1.4 panels d and e). An open fracture was encountered at a depth of 24 m, providing an outflow for groundwater which flowed up the borehole. Data from the 2 m spatial resolution instrument and straight cable would give

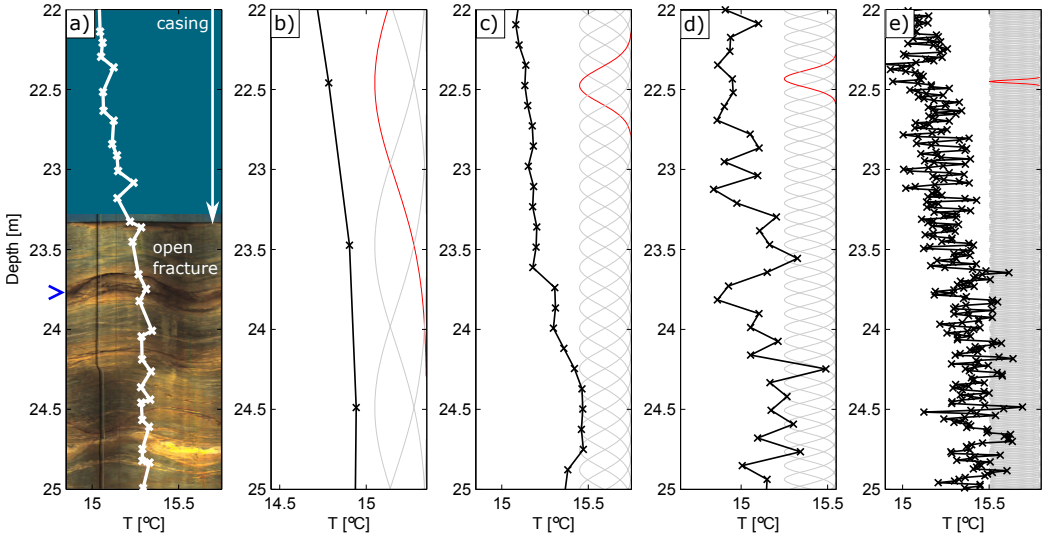

Figure 1.4: Different options for enhancing the spatial resolution of DTS temperature data, with data shown from four instrument and cable combinations deployed to measure borehole temperature-depth profiles in Ploemeur, France. a) shows a 3 m section of the temperature-depth profile measured using a conventional downhole logging approach. An optical televiewer image in this interval is shown to give the location and spatial extent of a fracture (out of which ambient flow in the borehole discharges), and the location of the end of the borehole casing. At the depth of the fracture, there is a change in the gradient of the temperature depth profile. Figures b), c), d), and e) show corresponding DTS temperature-depth data, collected using b) a 2 m spatial resolution instrument with a standard cable, c) 0.3 m spatial resolution instrument with a standard cable, d) 2 m spatial resolution instrument and wrapped cable, and e) 0.3 m spatial resolution instrument and wrapped cable. Each DTS temperature-depth profile is a 5 minute time average. Gaussian distribution curves, shown in the right of each figure, indicate the spatial weighting of each temperature measurement, calculated using the approach described in *Selker et al.* (2014). The red Gaussian distribution in each plot indicates the spatial weighting of the DTS temperature measurement at a depth of approximately 22.45 m

the impression of a relatively smooth temperature depth profile. The 2 m Gaussian spatial weighting of each temperature measurement spans the cased, fractured, and fractured intervals, rendering these features indistinguishable. In contrast, the 0.3 m spatial resolution instrument with the straight cable allows identification of the location and quantification of the step temperature change at the fissure. The wrapped cable data suffers greater noise due to the Beer's law light loss along the additional optical path length. The effective spatial averaging in Figure 1.4d) is similar to Figure 1.4c), but for this reason, the temperature resolution is lower. Pairing the 0.3 m spatial resolution instrument with the wrapped cable gives an effective spatial resolution of 0.03 m, which is now comparable to the spatial extent of the fractures. While the data have higher RMSE, the change in temperature gradient is visible. Additionally, the systematic structure of the variability, apparent only with this instrument-cable configuration, appears to be indicative of thermal convection in the borehole.

1.5 Passive DTS temperature monitoring in boreholes

DTS has been used in various settings to monitor downhole temperatures. The cable can be installed easily by spooling off cable to the desired maximum depth in the well and left to monitor temperature over a period of time. In borehole deployments, DTS measurements are termed 'passive' if there is no active heating of the cable itself or in the DTS monitored well. In such installations DTS is typically used for temperature logging, process monitoring in engineering applications, and thermal tracer tests.

1.5.1 Passive temperature logging

DTS has been used to measure the temperature-depth profile in the subsurface in a variety of settings. *Grosswig et al.* (1996) monitored seasonal temperature changes in the subsurface at a waste disposal site. They detected a warm temperature signal just beneath the zone of seasonal fluctuation, and attributed this to exothermic reactions in surrounding waste material. DTS has also been used to assess lithological changes from passive temperature data using the temperature gradient approach (*Foerster et al.*, 1997; *Wisian et al.*, 1998). *Wisian et al.* (1998) found that, with their set-up, there was a temperature offset of up to 0.4 °C between the DTS and probe measured temperature, but that this was not critical for the temperature gradient method. *Foerster et al.* (1997) concluded that DTS was suitable for studies of terrestrial heat flow, but had a temperature resolution 5 to 10 times less than their conventional logging approach. *Henninges et al.* (2005) used a similar approach in an area of permafrost, and quantified thermal properties with depth by assuming a constant vertical heat flow rate. The distinct advantage of using DTS in cold regions is that the cable can be installed immediately after drilling or incorporated into the well construction (*Henninges et al.*, 2003), after which re-freezing of the hole prevents access to logging devices (*Hurtig et al.*, 1996). Again in a permafrost setting, *Stotler et al.* (2011) make use of DTS to monitor permafrost and sub permafrost temperature conditions.

1.5.2 Engineering process monitoring

The reliability of DTS temperature monitoring, and availability of cables resistant to high temperature, pressure, and corrosive conditions, has lead to DTS deployments in a number of industrial applications. DTS has been used for temperature monitoring in ground

source heating and cooling operations (*Siska et al.*, 2016). Rather than obtaining a single thermal conductivity for the system, DTS allows the thermal conductivity to be estimated at a number of depths during thermal response tests with fibre optic cables installed directly in the u-tube of a heat exchanger (*Acuña and Tockner*, 2009). Fibre optic cables have also been deployed inside geothermal production wells (*Benoit and Thompson*, 1998). *Yamano and Goto* (2001) show temperature data monitored in a well to a depth of 1.5 km collected over a 2.5 year period, and found that the temperature-depth profile was highly stable over time despite fracture and fault related temperature anomalies. DTS has also been used to monitor and assess stimulation activities in Enhanced Geothermal Systems (EGS) in near real-time. *Petty et al.* (2013) show DTS temperature data collected from the Newberry Volcano EGS Demonstration site, which allowed the main outflow zones to be identified during the injection of stimulation fluids. In this application, the main advantage is that DTS, particularly if deployed behind the casing, can provide near real-time temperature measurements during cementing, drilling, and production without interrupting the processes (*Asmundsson et al.*, 2014). In a pilot project on CO_2 sequestration, fibre optic cables were installed behind the casing of an injection well and two monitoring wells (to depths of 750 m) (*Giese et al.*, 2009). This allowed the zones most readily accepting CO_2 to be identified, as well as the spreading of the CO_2 plume.

1.5.3 Thermal tracer tests

There has also been renewed interest in carrying out thermal tracer tests, with passive temperature monitoring in a number of observation wells (*Wagner et al.*, 2014). The objective of thermal tracer tests may be to directly study heat transport in the subsurface, or to use temperature as an easily monitored tracer for groundwater flow. The advantage of using DTS here is that multiple observation wells can be monitored simultaneously using the same instrument, meaning that there is no need to adjust for temperature or time offsets between multiple probes. Thermal tracer tests monitored using DTS have been carried out in a variety of settings including: a sedimentary aquifer (*Macfarlane et al.*, 2002); a fractured sandstone (*Hawkins and Becker*, 2012); a fractured granite (*Read et al.*, 2013); and a shallow sedimentary aquifer (*Hermans et al.*, 2015). Recently, *Bakker et al.* (2015) carried out a thermal tracer test monitored with DTS without monitoring wells using fibre

optic cable in the subsurface installed by direct push. In unconsolidated sediments, this approach allows thermal tracer tests to be monitored economically, in detail, and with minimal disturbance to the aquifer.

1.6 DTS temperature monitoring in active mode

In Active-DTS, the cable, borehole fluid, or surrounding rock formation is heated. There are two ways of obtaining an Active-DTS measurement in the subsurface. The first is to physically inject a fluid into the borehole. This may be carried out at a single location and for a short period of time to create a discrete plume in the borehole (*Leaf et al.*, 2012). Or, the injection may be carried out over a longer time scale to replace the fluid in a longer section of the borehole with fluid warmer or colder than the surrounding rock (*Yamano and Goto*, 2005; *Read et al.*, 2013).

Alternatively, electrical heating is possible and offers several advantages over injecting a fluid. Critically, the head in the borehole is not altered, as is likely even under the most controlled fluid injection. This means that if the borehole is open, the ambient vertical flows are not disturbed. It is also easier to quantify the amount of heat injected by integrating the input power over time. Heating at a point can be achieved using a small heating element (*Sellwood et al.*, 2015a; *Read et al.*, 2015). Uniform heating over a much greater length can be achieved with Joule heating along an electrical conductor (*Kurth et al.*, 2013). It is possible to heat the same cable used for DTS temperature monitoring by driving electrical current through coaxial metallic armouring (e.g., *Sayde et al.*, 2015; *Read et al.*, 2014), or by utilising a composite cable design that incorporates parallel electrical conductors and optical fibres (*Coleman et al.*, 2015). Speciality cables are typically required since standard cable jackets may not be designed to be safe at elevated voltage. Electrically insulated heating elements inside the same cable construction can be more economical, however, the geometry is not radially symmetric, and small differences in the separation between the heating element and optical fibres may cause temperature anomalies observable during heating (*Cao et al.*, 2015). For heated cable methods, the power output can be calculated according to $P = V^2/R$, where P is power output per unit length [W m^{-1}], V is the voltage drop per unit length [V m^{-1}], and R is the electrical resistance of the cable per unit length [Ω m^{-1}]. If constant power output through time is

required, an active power controller is needed to supply constant total power.

Three active mode DTS approaches seeking to detect and quantify groundwater fluxes are developed in this thesis and trialled at the Ploemeur research site in Brittany, France.

1.7 Characteristics of the Ploemeur research site, Brittany

The Ploemeur research site was used to test methods presented in the thesis in Chapters 2, 3, 4 and 6, and is introduced here. The site was chosen as transmissive fractures are sparsely located with depth, allowing natural gradient flow through the fractures to be assessed in comparison to large depth intervals where there are no transmissive fractures. In terms of in-well vertical flow, this also means that there are long intervals of constant flow with depth, allowing the proposed DTS methods for measuring vertical flow to be assessed over large depth intervals of known, constant flow. The Ploemeur site is also already very well characterised, belonging to the H+ network of hydrogeological research sites, and therefore the expected flow responses to pumping are have been previously observed and documented.

The site is located a few kilometres west of Lorient in the Morhiban department, north west France. The area is underlain by mica schist and granite, the contact of which is approximately 40 m bgl and dips 30° to the north (Figure 1.5). The granite is a laccolith, and extends down to approximately 1 km depth (*Vigneresse et al.*, 1987). Although such rocks are generally considered to be poorly transmissive, the contact zone at the interface between the mica schist and granite is locally highly transmissive, due to significant fracturing in a band of alternating granitic sheets, schists, pegmatite and aplite dykes, and quartz veins. This subhorizontal contact zone, is known as the Ploemeur aquifer, with the mica schist behaving as a confining unit. A pumping site was established and since 1991 has supplied around 10^6 m^3 a^{-1} of water to the town of Ploemeur (*Touchard*, 1999). The recharge providing the high and seemingly sustainable yield from the Ploemeur aquifer, is thought to be provided through the many subvertical fractures in the area (*Ruelleu et al.*, 2010).

The site consists of four boreholes. B1 (83 m deep), B2 (100 m deep) and B3 (100 m deep) are located within 10 m of each other, while F22 (70 m deep) is located around 30 m away. The boreholes are cased and cemented to the base of the weathered zone at

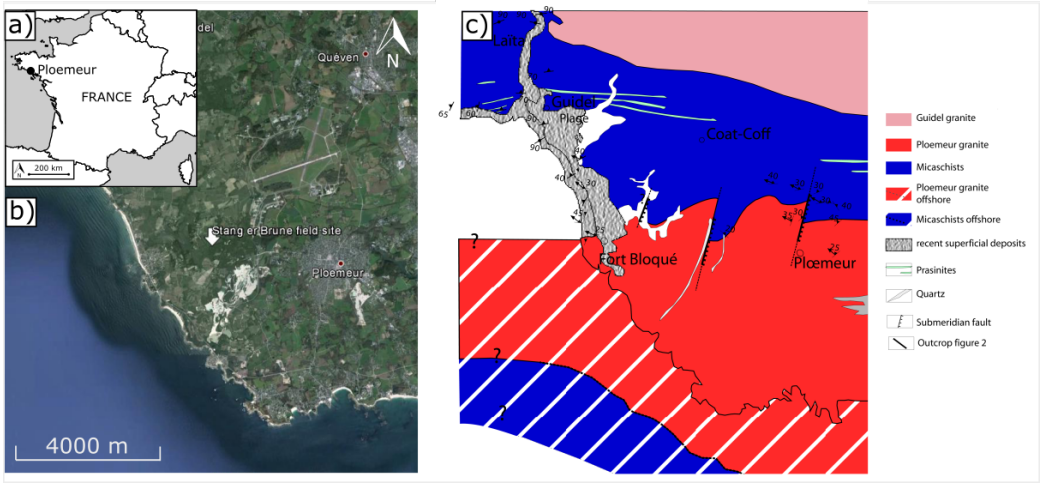

Figure 1.5: a) Location of Ploemeur, b) aerial view of the Stang er Brune (Ploemeur) research site, c) geology of the Ploemeur commune from *Ruelleu et al.* (2010)

around 25 m in B1, B2, and B3, and around 12 m in F22. The open section of each well encounters mica schist and then comprises granite (Figure 1.6). Each borehole intersects many closed fractures, with relatively few open and transmissive fractures (those identified by *Le Borgne et al.* (2007) are shown in Figure 1.6). Fracture traces, from the optical televiewer logs, indicate that many of these are steeply dipping and intersect the boreholes over depth intervals of up to 1 m. The optical televiewer logs also provide evidence of groundwater flow from the orange iron oxide staining of the fractures, attributed to the flow of oxygenated water (*Belghoul*, 2007).

Under ambient conditions, there is generally an upwards flow of water in all of the wells of up to 5 L min^{-1} (Figure 1.6). This reflects the local trend for increasing hydraulic head with depth, with each borehole connecting deep fractures with shallow fractures. The temperature depth profiles collected under ambient conditions show a rapid change in the temperature gradient at the shallowest fracture (B1-1, B2-1, B3-1). This is caused by warm water, from depth, flowing up the well and then out of these shallow fractures. When pumped, the flow in each well originates from the few transmissive fractures present, with individual fracture transmissivities of up to $1x10^{-3}$ m^2 s^{-1} (*Klepikova*, 2013). Under pumped conditions, the temperature depth profile in each borehole changes considerably. Warmer water, from depth, is advected up the borehole and loses less heat to the surrounding formations during transit relative to ambient conditions. In B1, the temperature-depth profile between B1-4 and B1-3 is near isothermal under pumped conditions. There are then three, slight reductions in temperature as the groundwater flows

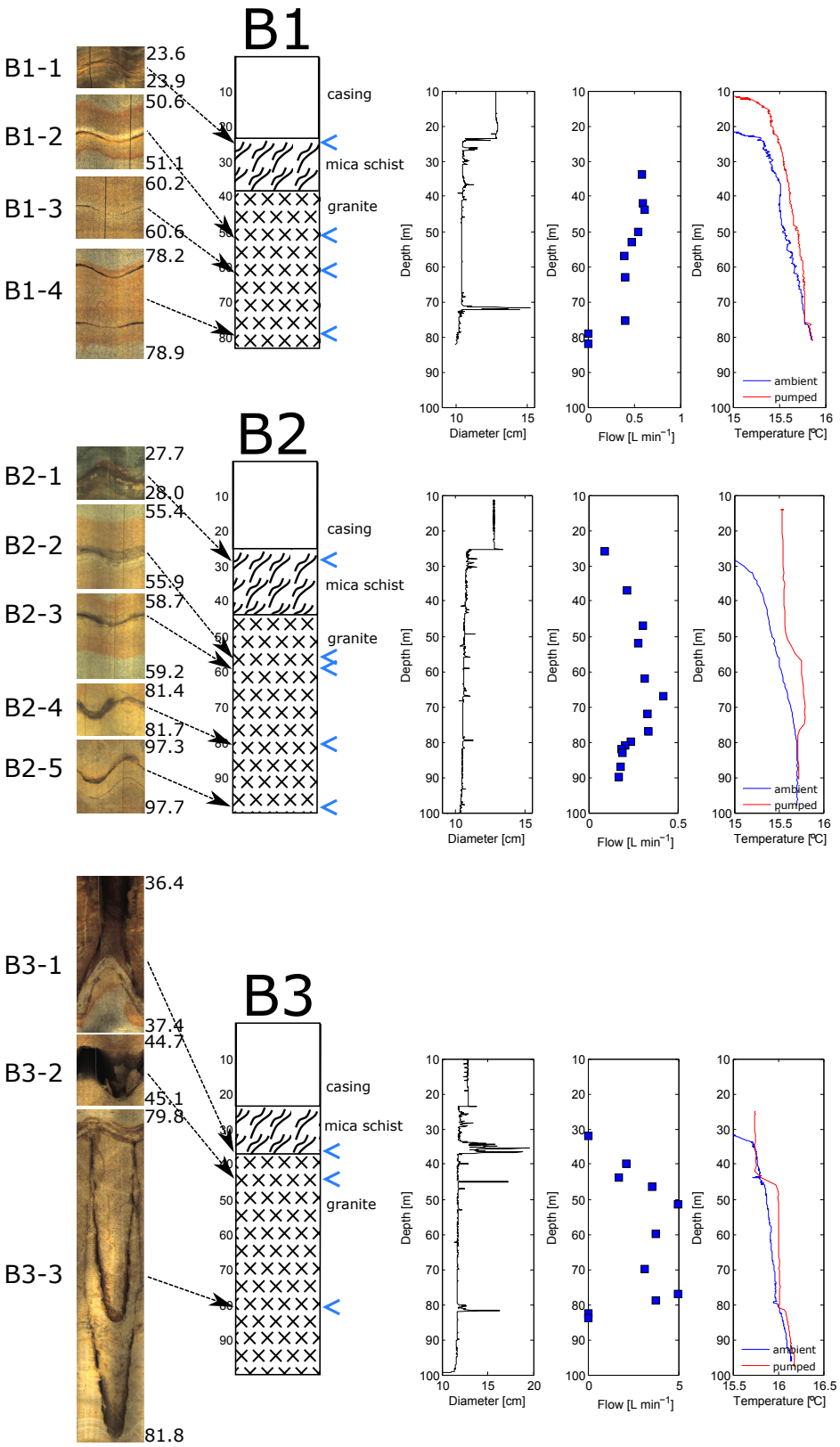

Figure 1.6: Optical televiewer, generalised geological log, and corresponding flow, calliper, and temperature logs from boreholes B1, B2 and B3. The optical televiewer images are sections of the full log taken at the depths of hydraulically significant fractures as identified in *Le Borgne et al.* (2007). The locations of these fractures are shown as '¡' on the interpreted geological logs. The flow logs were taken with a heat pulse flowmeter under ambient conditions. The temperature-depth profiles were obtained under both ambient (blue) and pumped conditions (red), and were made using a conventional logging tool. The data were obtained from the H+ Observatory (http://www.ore.fr/en/)

up past B1-3, B1-2, and B1-1, as these appear to be contributing cooler water. In B2, the temperature-depth profiles are similar in both ambient and pumped conditions between B2-5 and B2-4, suggesting that either there is a relatively small difference in flow between these states. When pumped, B2-4 contributes relatively warmer water, which is then advected upwards. This is then cooled by inflows from B2-3 and B2-2. B2-1 then either does not significantly contribute to flow, or is contributing water that is close in temperature to the water already present. In B3, pumping generates near isothermal conditions between B3-3 and B3-2, indicating that groundwater entering the well is rapidly advected upwards, with no other observable inflows over this interval. B3-2 then contributes cooler water, with the impact of B3-1 less visible under pumped conditions than ambient conditions. The calliper log is able to provide some information on the extent of the fracturing, but is unable to distinguish between fractures that are hydraulically active and inactive. The flow log collected in ambient conditions, is a direct measurement of the in-well flow. Due to the time taken to obtain each individual flow measurement, the number of data points is somewhat limited. So while the temperature logs cannot provide a complete description of the flow conditions, they provide useful complementary information that can be used in tandem with other available logs.

The Ploemeur research site has been subject to many previous hydraulic tests (*Le Borgne*, 2004; *Le Borgne et al.*, 2007), solute tracer tests (*Dorn et al.*, 2011, 2012), and temperature based approaches (*Klepikova et al.*, 2011). The latter was on the use of temperature-depth profiles to calculate in-well vertical flow. It was shown that the curvature of the temperature-depth profile between fractures in pumped conditions can be used to calculate vertical flow rates. If the inflowing groundwater from the fracture delivers water of sufficiently different temperature, the resulting temperature depth profile will vary according to the extent to which the altered temperature inside the wellbore equilibrates with the formation as the water moves vertically through the well. In part, this is governed by the flow velocity, which *Klepikova et al.* (2011) show can be derived using an inverse model. Part of the work presented here seeks to extend this by using approaches that could be used when the temperature of the groundwater of the inflowing fracture is insufficiently different to the resident water in the well, and by utilising DTS could continuously monitor flows over time as well as depth.

Chapter 2

Using DTS to measure apparent thermal conductivity profiles and estimate ambient groundwater fluxes*

2.1 Chapter summary

The use of thermal dilution tests to measure apparent thermal conductivity profiles and produce estimates of ambient groundwater fluxes is assessed. In-situ measurement of apparent thermal conductivity has hydrological significance, in that in addition to being dependent on the true thermal conductivity, it is also a function of groundwater specific discharge. To test the sensitivity range of thermal dilution tests to groundwater flow, a numerical model was created to simulate groundwater and heat flow through an aquifer and borehole. The test sensitivity was then assessed, considering that the cooling should be controlled by a combination of advection and conduction. For the typical aquifer thermal properties used, at specific discharges less than 5x10^{-6} m s^{-1}, the response was found to be conduction dominated and insensitive to groundwater flow. At specific discharges greater than 2.2x10^{-4} m s^{-1}, the response was found to almost entirely be advection

*Parts of the Chapter (experiment set up and results from borehole B3) were published in: Read, T., O. Bour, V. Bense, T. Le Borgne, P. Goderniaux, M. Klepikova, R. Hochreutener, N. Lavenant, and V. Boschero, Characterizing groundwater flow and heat transport in fractured rock using fiber-optic distributed temperature sensing, *Geophysical Research Letters*, *40*, 2055–2059, 2013

dominated and can be approximated by an analytical solution ignoring conductive effects. In situations where the cooling response is a combination of advection and conduction, an assigned apparent thermal conductivity value is likely to poorly replicate the observed response. A thermal dilution test was then carried out at the Ploemeur field site in four boreholes under natural gradient conditions, and repeated in one with cross pumping in another borehole. In each test, fluid in the borehole was replaced with heated water, and the subsequent cooling monitored with DTS. The DTS temperature data showed differences in the rate of cooling in the cased section, mica schist, and granite. Evidence for active groundwater flow was strongest in F22, with significantly enhanced cooling at a depth with known open fractures. However, groundwater flow in open fractures was less clear in the other boreholes. An in-house numerical model was used to determine profiles of apparent thermal conductivity for each of the boreholes. Estimated apparent thermal conductivities were granite $>$ mica schist $>$ casing (as would be expected), and these were elevated at the depth of enhanced cooling in F22. Using DTS to monitor thermal tests has significant practical advantages over traditional point sensors, and allows the in-situ estimation of thermal properties and potentially groundwater flow when the instrument spatial resolution is not limiting.

2.2 Background

In open or screened wells, single borehole solute dilution tests allow permeable zones to be identified (e.g., *Brouyère et al.*, 2008; *Doughty et al.*, 2005; *Maurice et al.*, 2011; *Novakowski et al.*, 2006). The water in the borehole is replaced or spiked with a tracer, typically NaCl or a fluorescent dye (others may be appropriate provided that it is conservative, readily measurable, and buoyant effects can be ignored). The aim of the approach is to create an initial, uniform concentration of tracer with depth in the borehole. The concentration of tracer is then monitored in the time - depth domain.

In the absence of any vertical flow in the borehole, the decay in solute concentration is dominated by horizontal groundwater flow through the aquifer. If the background tracer concentration is negligible, and ignoring decay of the solute by diffusion from the

borehole, the horizontal specific discharge is calculated according to (*Lewis et al.*, 1966):

$$\frac{\zeta(t)}{\zeta_0} = \exp\left(-\frac{4qt}{\pi r_{\text{bh}}}\right) \tag{2.1}$$

where $\zeta(t)/\zeta_0$ [-] is the relative tracer concentration, q [m s^{-1}] is the specific discharge in the formation, and r_{bh} [m] is the borehole radius. An open or screened borehole without vertical flow, as required for application of this analytical solution, is rarely encountered however. The borehole itself acts as a high permeability vertical conduit for flow by connecting permeable layers or fractures at different depths (with potentially different hydraulic heads) (*Elci et al.*, 2001). In such case the loss of solutes from the borehole following emplacement is no longer a one dimensional problem. The rate of change in solute concentration is due to the same diluting effect if there is an inflow, but this then propagates up or down the borehole due to the vertical flow (*Maurice et al.*, 2011). Because there are often many, closely spaced permeable features intersected by a borehole, the response in a dilution test over depth and time may be complex and require a more involved numerical inversion to obtain a velocity-depth profile (e.g. *Moir et al.*, 2014).

A dilution test may be carried out using heat, rather than solutes, as the tracer. This allows the monitoring problem of having to obtain measurements at multiple depths through time to be overcome with DTS. Experiments similar to solute dilution tests have been carried out with temperature, albeit without DTS, for example using the Active Line Source (ALS) technique (*Pehme et al.*, 2007). ALS uses an electrical strip heater or cable to heat the borehole fluid and surrounding rock over a long depth interval. The heat source is both uniform over depth and, with adequate power control, constant through time. The temperature during the heating and cooling phases is measured by slowly moving a probe up and down the borehole. Given the highly controlled test conditions that can be achieved, analytical solutions can be applied to both the late-time heating and cooling data, relating the rate of temperature change to the 'apparent' thermal conductivity of the formation (*Beck et al.*, 1971). The term 'apparent' is used for the estimated thermal conductivity since it is potentially affected by groundwater flow. In such case, the 'apparent' thermal conductivity of the formation found during the field test will be higher than the 'true' formation thermal conductivity as advection enhances heat flow.

If, rather than using an electrical heater to provide a continuous heat source, fluid is

injected to replace the water in the borehole with heated water, an alternative analytical solution can potentially be used. Ignoring any fluid flow or vertical heat conduction, the thermal dilution test could be approximated as a 1D radial flow problem. *Carslaw and Jaeger* (1959) derive an analytical solution for the cooling of an instantaneously heated cylinder in an infinite medium. Applying the generic solution in *Carslaw and Jaeger* (1959) for heat conduction from a cylinder, for a borehole initially with a temperature T_0, the subsequent cooling of the borehole is given by:

$$T(t) = T_{\text{amb}} + \frac{4\Gamma\left(T_0 - T_{\text{amb}}\right)}{\pi^2} \int_0^\infty \mathrm{e}^{-D_{\text{eq}} t u^2 / r_{\text{bh}}^2} \frac{du}{\Delta\left(u\right)} \tag{2.2}$$

where T_{amb} is the ambient (undisturbed) temperature in the rock at a large distance away, and the other parameters are defined below. The effective thermal diffusivity of the porous medium, D_{eq}, is given by:

$$D_{\text{eq}} = \frac{k_{\text{eq}}}{\left(\rho C_p\right)_{\text{eq}}} \tag{2.3}$$

where $\left(\rho C_p\right)_{\text{eq}}$ [J K^{-1} m^{-3}] is the equivalent volumetric heat capacity of the solid-water system at constant pressure, given by:

$$\left(\rho C_p\right)_{\text{eq}} = \left(1-\theta\right)\rho_{\text{s}} C_{p,\text{s}} + \theta \rho_{\text{w}} C_{p,\text{w}} \tag{2.4}$$

where θ [-] is the porosity of the formation, ρ [kg m^{-3}] is density, C_p [J K^{-1} kg^{-1}], is the heat capacity at constant pressure, and subscripts $_{\text{s}}$ and $_{\text{w}}$ denote the solid and liquid (water) phases of the formation respectively. k_{eq} [W m^{-1} $^{\circ}$C^{-1}] is the equivalent thermal conductivity and is a volume average given by:

$$k_{\text{eq}} = \left(1-\theta\right) k_{\text{s}} + \theta k_{\text{w}} \tag{2.5}$$

The parameter Γ in Equation 2.2 is twice the ratio of the heat capacities of the porous medium and that of the borehole:

$$\Gamma = 2\frac{\left(\rho C_p\right)_{\text{eq}}}{\rho_{\text{w}} C_{p,\text{w}}} \tag{2.6}$$

The function $\Delta(u)$ in Equation 2.2 is given by:

$$\Delta(u) = [uJ_0(u) - \Gamma J_1(u)]^2 + [uY_0(u) - \Gamma Y_1(u)]^2 \tag{2.7}$$

where $J_0(u)$ and $J_1(u)$ are Bessel functions of the first kind, and $Y_0(u)$ and $Y_1(u)$ are Bessel functions of the second kind. The water in the borehole is considered to be a perfect conductor, equivalent to being well mixed. Applying Equation 2.2 to thermal dilution test data therefore assumes that the cooling at each measurement depth is independent of the cooling above and below in the same manner as the ALS method. This analytical solution was used by *Silliman and Neuzil* (1990) to estimate formation thermal conductivities in-situ following the addition of fluid to a borehole in a shale, where the hydraulic conductivity was low enough to give a conduction dominated cooling response.

In the following, we firstly develop and apply a numerical model to investigate the typical thermal dilution test response to groundwater flow, and compare the response to analytical solutions that have different governing assumptions. We then perform a series of thermal dilution tests, with the objective of identifying locations of discrete groundwater flow in boreholes at the Ploemeur site, and assess its ability in conjunction with DTS temperature monitoring as a method for identifying lithological and hydrogeologically significant contrasts.

2.3 Forward modelling of thermal dilution test responses

2.3.1 Model set-up

To determine how 'apparent' thermal conductivity relates to groundwater flow, an idealised groundwater-heat flow model was set up in COMSOL Multiphysics (*COMSOL*, 2013). COMSOL is a general purpose finite element software, with in-built solvers for finding solutions to the governing partial differential equations of physical problems. The model created simulates the temperature decay in thermal dilution tests due to the combined effects of conduction and advection by groundwater flow. The model domain consists of a cross section in the *x*-*y* plane through a borehole and aquifer. The model combines the continuity equation and Darcy's Law to solve for the velocity field according

to:

$$\nabla \cdot (\rho_{\mathrm{w}} \mathbf{u}) = 0 \tag{2.8}$$

$$\mathbf{u} = -\frac{\kappa}{\mu_{\mathrm{w}}} \nabla p \tag{2.9}$$

where $\mathbf{u}$ [m s^{-1}] is the velocity vector, ρ_{w} [kg m^{-3}] is water density, κ [m^2] is intrinsic permeability, μ_{w} is the dynamic viscosity of water [kg m^{-1} s^{-1}], and p [kg m^{-1} s^{-2}] is pressure. In this formulation, $\mathbf{u}$ is also the specific discharge, rather than the true linear velocity.

A flow inlet and outlet are specified on the left and right boundaries respectively along which the specific discharge is specified. The rock permeability is set at 10^{-9} m^2, equivalent to a well sorted gravel. For simplicity in the model, the borehole itself is treated as a porous medium, with porosity of 1 and the 'permeability' of the water in the borehole at 10^{10} m^2. In reality the modelled groundwater flow distribution is not sensitive to these parameters as long as the 'permeability' of the water in the borehole is much greater than the permeability of the rock. In this case, the flow through the borehole (validated by integrating the component of the velocity vector normal to the left half of the borehole perimeter), is equal to twice the flow through width $2r_{\mathrm{bh}}$ of aquifer, as is usually assumed in solute dilution tests (*Hiscock and Bense*, 2014). For each input specific discharge, the code solves for the pressure and velocity distribution in the domain. Figure 2.1 shows simulated groundwater flow lines and hydraulic head, h [m] (converted from pressure by dividing by $\rho_{\mathrm{w}} g$). Groundwater flow is predominantly parallel, except in the vicinity of the borehole where due to the contrast in hydraulic properties, flow converges. Since the pressure and velocity distribution is not time dependent, this is solved for first and the solution used during the time dependent stage when heat flow is considered.

The second step is to simulate the time dependent temperature decay in the model domain according to:

$$\left(\rho C_{\mathrm{p}}\right)_{\mathrm{eq}} \frac{\partial T}{\partial t} + \rho_{\mathrm{w}} C_{p\mathrm{w}} \mathbf{u} \cdot \nabla T = \nabla \cdot \left(k_{\mathrm{eq}} \nabla T\right) \tag{2.10}$$

The equivalent volumetric heat capacity, $\left(\rho C_{\mathrm{p}}\right)_{\mathrm{eq}}$, is defined based on the solid and water physical properties and Equation 2.4. The equivalent thermal conductivity is specified in the model, rather than a calculated value based on water and solid properties. Table 2.1

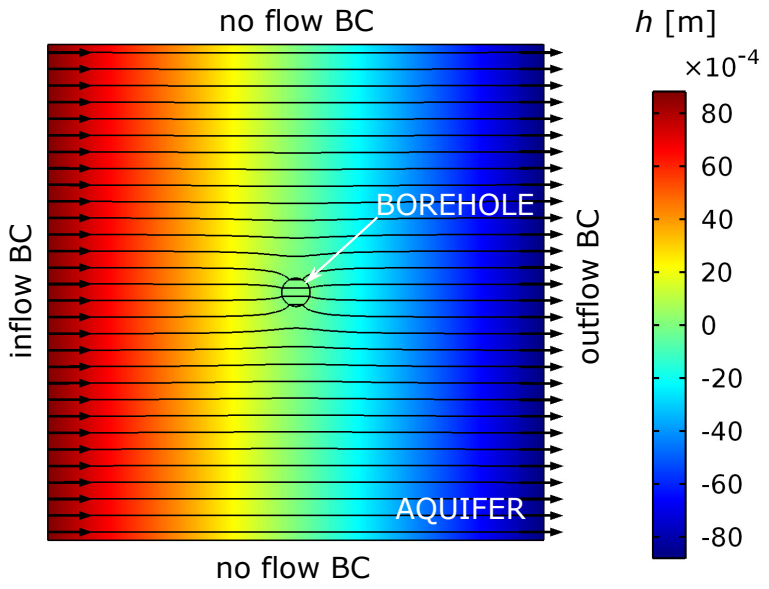

Figure 2.1: Simulated hydraulic head and groundwater flow lines in the thermal dilution test simulations. In this instance, the specific discharge is specified as 4.84x10^{-5} m s^{-1}.

Table 2.1: Parameters used in the COMSOL thermal dilution test forward model

Parameter		Value	Units
Borehole radius	r_{bh}	0.0575	m
Heat capacity of water	$C_{p,\text{w}}$	4200	J kg^{-1} °C^{-1}
Heat capacity of solid	$C_{p,\text{s}}$	775	J kg^{-1} °C^{-1}
Density of water	ρ_{w}	1000	kg m^{-3}
Density of solid	ρ_{s}	2700	kg m^{-3}
Equivalent thermal conductivity	k_{eq}	2	W m^{-1} °C^{-1}
Porosity	θ	0.2	-
Ambient temperature	T_{amb}	20	°C
Initial borehole temperature	T_0	21	°C

lists the parameter values used. Outflow boundary conditions for temperature are specified on the edges of the domain. The ambient temperature in the aquifer is initially specified as 20 °C, and initial temperature in the borehole is 21 °C. Temperatures presented in the results section have the background temperature subtracted and therefore range from 0 to 1 °C. There is no heating phase, so this process is effectively instantaneous. The cooling phase is simulated for a total of 6 hours.

A parametric sweep of specific discharge was undertaken, with specific discharges ranging from 5x10^{-6} to 1.0x10^{-3} in seven logarithmically spaced increments. For each specific discharge, the temperature distribution in the domain was stored at specified times and output along with the temperature in the centre of the borehole.

2.3.2 Results

Figure 2.2a shows the temperature response for the different specific discharges in the parametric sweep. For high specific discharge, the shape of the temperature decay is similar, albeit shifted in the time domain. As the specific discharge decreases, the temperature decay curves increasingly appear to overlap. The temperature decay as calculated using the *Carslaw and Jaeger* (1959) analytical solution for radial conduction is also plotted in Figure 2.2c. At a specific discharge of 5.0x10^{-6} m s^{-1}, the temperature decay is the same as the radial conduction analytical solution. In this case, cooling is conduction dominated and solely a function of the thermal properties of the aquifer. This represents the lower limit to which the thermal dilution tests are sensitive to flow.

Thermal dilution tests could potentially be analysed using analytical solutions that either assume heat loss by conduction is negligible (the solution presented by *Lewis et al.* (1966)), or, that advection can be ignored (e.g. the cooling of a heated cylinder according to Equation 2.2). Figure 2.2b shows the modelled response in Figure 2.2a along with the analytical solution of Equation 2.1 applied using the same specific discharges in the parametric sweep. The solution provides a good fit, down to specific discharge of 2.2x10^{-4} m s^{-1}. Below, this, the solution becomes progressively less accurate, particularly at early times. Figure 2.2c compares the model result with the analytical solution of Equation 2.2 which assumes that groundwater flow is negligible. When the equivalent thermal conductivity is 2 W m^{-1} °C^{-1}, the solution is in close agreement with the modelled decay for specific discharges $<$ 5.0x10^{-6} m s^{-1}. Increasing the equivalent thermal conductivity, as in the 'apparent' thermal conductivity method, clearly increases the rate of temperature decay. However, the shape of the decay is intrinsically different and poorly replicates the cooling at high specific discharges, where the cooling is advection dominated. In between the advection and conduction dominated cooling regimes, there is an intermediate range of flows from 2.2x10^{-4} down to 5.0x10^{-6} m s^{-1}, where cooling is significantly affected by the combined effects of both advection and conduction. Groundwater flow enhanced cooling should be readily identifiable from field data, since the temperature decay is more rapid than expected from conduction alone, and is poorly replicated by analytical solutions or numerical models considering only heat conduction.

Applying a typical naturally occurring hydraulic gradient of 0.001, flows capable of

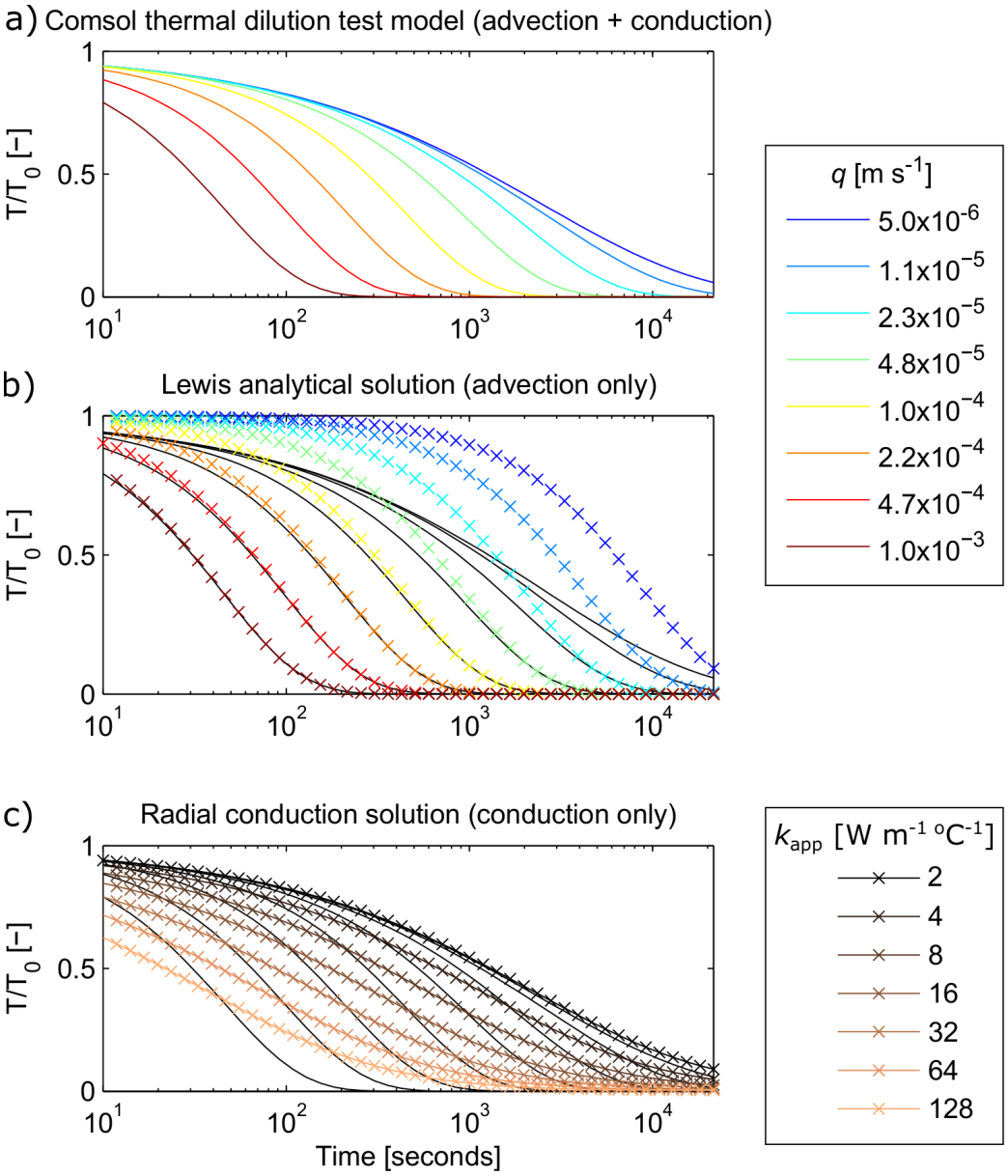

Figure 2.2: Comparison of modelled thermal dilution test response under varying flow conditions, showing a) temperature decay as a function of flow, b) comparison of temperature decay with analytical solution for flow, c) comparison of temperature decay with analytical solution of radial conductive cooling

enhancing the cooling response are only likely to occur in the most permeable of porous media. The schematic of Figure 2.3 shows calculated specific discharges over a range of hydraulic gradients and permeabilities, with typical permeability ranges for various geologic materials. With a hydraulic gradient of $<10^{-5}$, there is unlikely to be any response to groundwater flow regardless of the strata. With a hydraulic gradient between 10^{-5} and 10^{-3}, clean gravels, well sorted sands, transmissive basalts, and karst limestone likely exhibit a response which is mixed advection-conduction. Increasing the hydraulic gradient

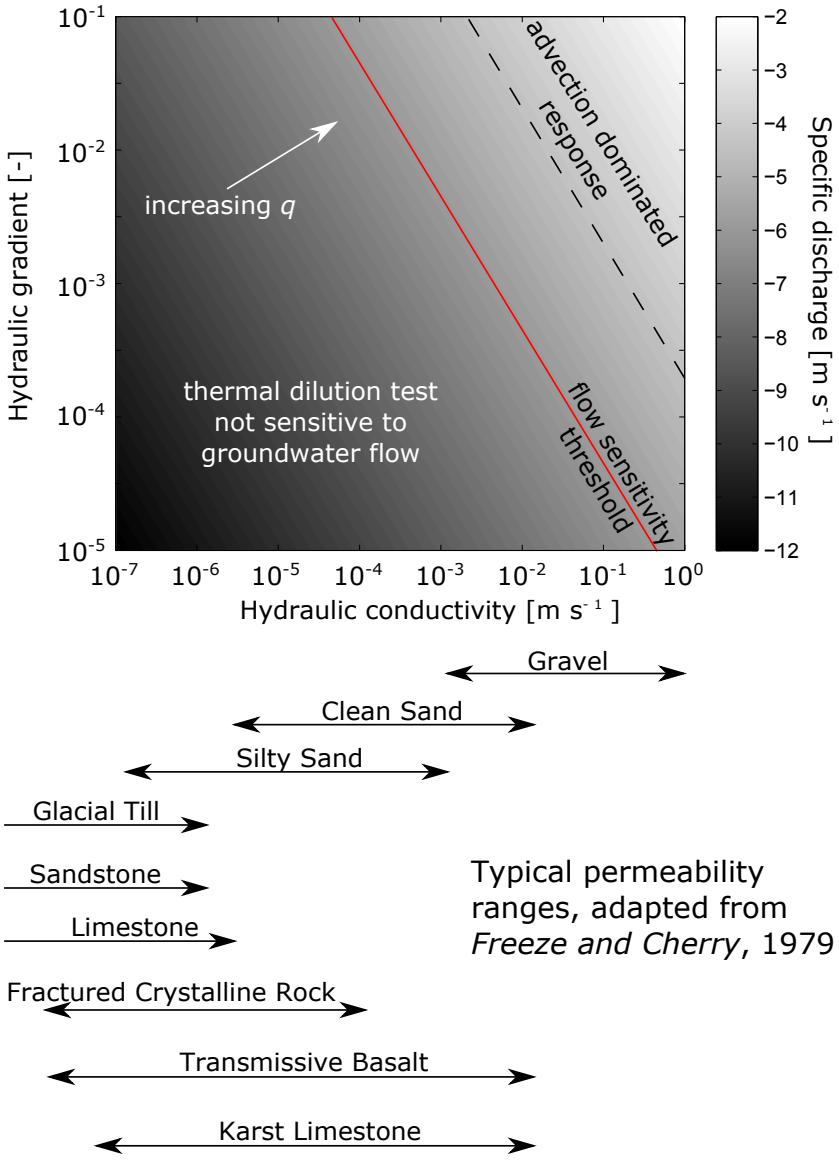

Figure 2.3: Expected thermal dilution test response as a function of hydraulic gradient and hydraulic conductivity. The hydraulic conductivities of various geologic materials, adapted from *Freeze and Cherry* (1979) are shown below.

further, as may be encountered for instance in the vicinity of a pumped borehole, extends the sensitivity range to silty sands and fractured crystalline rocks. A further implication is that in clays, shales, and unfractured igneous and metamorphic rocks (with hydraulic conductivities typically $<10^{-9}$ m s^{-1} and beyond the axis limit in Figure 2.3), the thermal dilution test will be insensitive to groundwater flow regardless of the hydraulic gradient. The cooling in thermal dilution tests carried out in these formations will be purely conduction dominated, and the estimated apparent thermal conductivity equal to the true formation thermal conductivity.

The expected sensitivity in fractured media in Figure 2.3 is potentially misleading

however. Even though when measured at the aquifer scale, a fractured rock aquifer may have the same hydraulic properties as a granular aquifer, the flow distribution, solute transport, and heat transport are completely different due to the restriction of groundwater flow to the fracture network. Where transmissive fractures with groundwater flow intersect a borehole, it would be anticipated that there would be much more significant cooling localised to this small interval, with cooling by conduction in the unfractured intervals . Thermal dilution tests in fractured media are therefore likely to be sensitive to groundwater flow driven by smaller hydraulic gradients than show in Figure 2.3.

2.4 Field trial of thermal dilution tests

2.4.1 Field set-up

Thermal dilution tests were carried out at the Ploemeur research site, north west France, in February and March 2012. The thermal dilution tests were designed so that cooling at a known transmissive interval in each borehole, where cooling would potentially be enhanced by advection, could be assessed against cooling in the remainder of each borehole that would be expected to be by conduction only. The tests were carried out in four boreholes (B1, B2, B3 and F22), separated by a distance of 6 to 30 m and ranging in depth from 70 to 100 m deep (Figure 2.4). For the DTS experiments discussed here, a single BRUsteel (Brugg Cables, Switzerland) steel armoured fibre optic cable of 1 km in length was installed in all four boreholes for the continuous monitoring of temperature (Figure 2.5). Additionally, two coiled sections of cable were placed in a calibration bath consisting of water wetted ice and monitored with a submersible temperature logger. We deployed the widely used Oryx-DTS unit (Sensornet Ltd., UK, Herts) (e.g. *Becker et al.*, 2012; *Lauer et al.*, 2013; *Sebok et al.*, 2013), configured to take single-ended temperature measurements with a spatial sampling interval of 1.01 m along the cable and an integration time of 2 minutes. Manual calibration of the data was not possible for these experiments due to excessive ice melt in the cold calibration bath, with a resulting non homogeneous temperature, so in this instance we used the inbuilt static calibration of the device.

To test the sensitivity of the thermal dilution test to cross flowing fractures, an inflatable packer was installed in each borehole to prevent vertical flow (with the exception

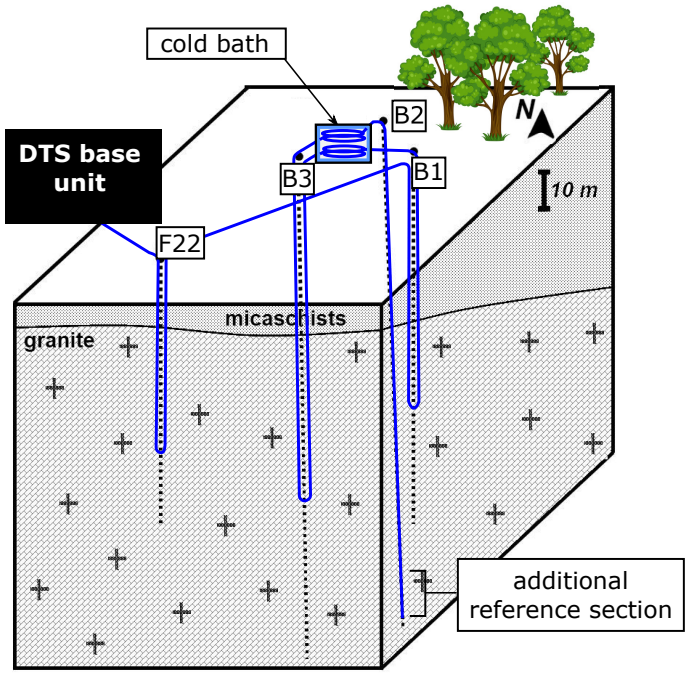

Figure 2.4: Configuration of the fibre optic cable during the 2012 field campaign at the Ploemeur field site

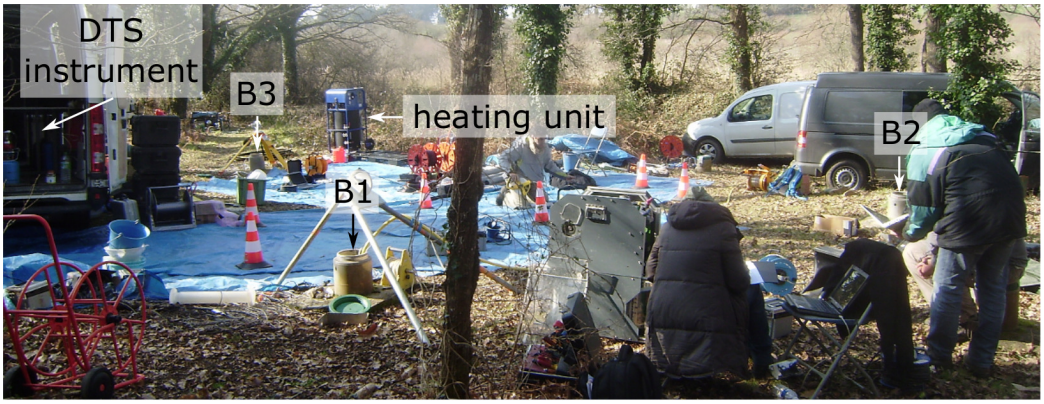

Figure 2.5: Ploemeur field site, with the three main boreholes (B1, B2, B3), heating unit used to provide heated water for the thermal dilution tests, and location of DTS instrument (F22 not in view)

of F22, where no ambient vertical flow has ever been detected). In B1, B2, and B3, the packer was positioned between 5 and 10 m below the contact of the mica schist and granite, such that in these upper test sections there was only a single transmissive fracture (fractures B1-1, B2-1, and B3-1). To perform the thermal dilution test, water was heated to 50 °C using a mobile heating system and injected just above the top of the packer. Each borehole was pumped at the same rate at shallow depth in order to draw the warm injected water upwards. During the experiments, the hydraulic head in each borehole was monitored to verify that the injection rates and abstraction rates were equal. The injection

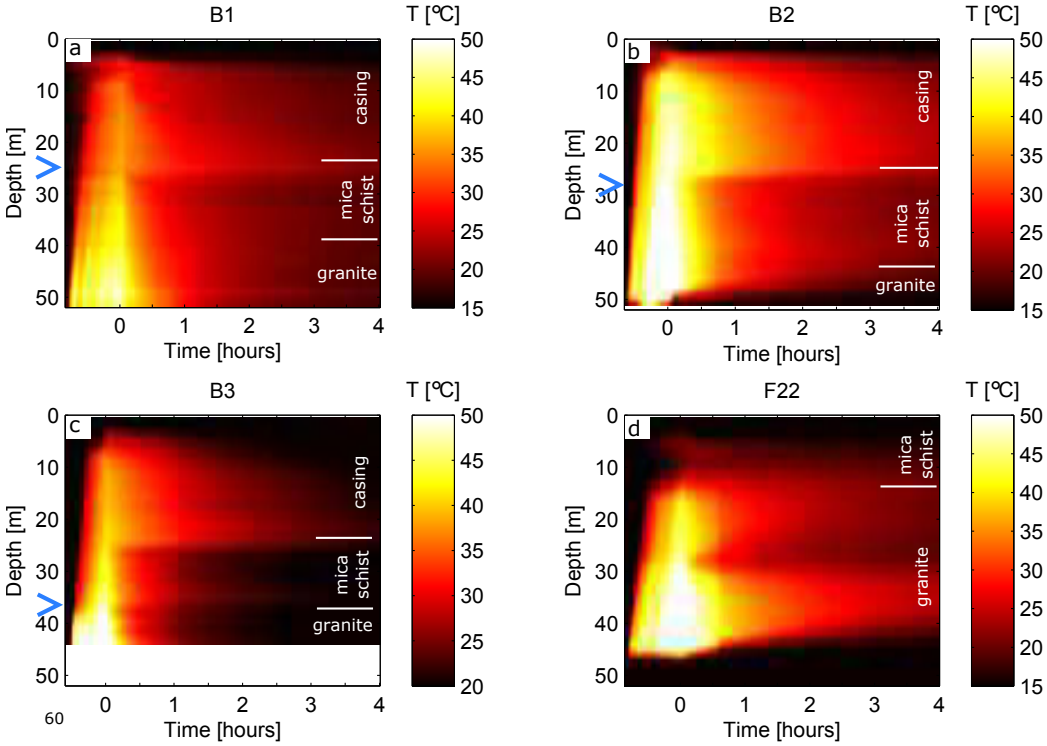

Figure 2.6: Temperatures during the thermal dilution tests in a) B1, b) B2, c) B3, and d) F22 under ambient conditions. In each plot, the injection of heated fluid stopped at $t = 0$. Previously identified transmissive fracture zones are shown with arrows.

process was stopped once the temperature-depth profile began to stabilise, typically after between 30 minutes and 1 hour. DTS temperature logging continued during the cooling phase for 4 hours after the end of injection. The thermal dilution tests were carried out in all boreholes under ambient conditions, and then repeated in B3 while pumping B2 at 140 L min^{-1} (referred to as cross pumping).

2.4.2 Results

DTS data during the injection and cooling phases of the thermal injection tests in B1, B2, B3, and F22 are shown in Figure 2.6. By the time the injection ceases, the fluid between the point of injection and abstraction is replaced with water approximately 25 to 40 °C warmer than ambient temperatures. During the cooling phase ($t > 0$ hours), the transitions between the cased to open sections in B1, B2, and B3 are clearly defined (there is no casing in F22). The remaining sections in the mica schist and granite exhibit some spatial variability in temperature during the cooling phase. However, it is difficult to determine if this variability is due to differences in groundwater flow, or is an artefact of the variable initial temperature conditions at t=0.

To compensate the data for the influence of the initial non-isothermal temperature profile in the borehole on the depth-variant cooling rates observed later, the Relative Temperature Anomaly (RTA [-]) was calculated according to:

$$\mathrm{RTA}(z,t) = \frac{T(z,t) - T_{\mathrm{amb}}(z)}{T_0(z) - T_{\mathrm{amb}}(z)} \tag{2.11}$$

where $T_{\mathrm{ambient}}(z)$ is the temperature prior to the start of the injection and $T_0(z)$ is the temperature when the injection ceased. This scales the initial temperature anomaly to unity at all depths, with a value of zero representing a full return to pre-testing ambient temperature conditions. Figure 2.7 shows the RTA in B1, B2, B3 and F22. Where present, the cased section cools more slowly than the open section below, clearly locating where the transition from casing to mica schist. In B1, B2, and B3, the rate of cooling in the mica schist is relatively uniform. This is despite the presence of fractures just below the casing in B1 and B2, that therefore do not appear to have any significant effect on the cooling. In B1, the transition to granite does not abruptly change the cooling trend. In B2, the cooling in the granite is more rapid than in the mica schist, but it appears to be affected by vertical heat transfer to the unheated section below. In B3, the cooling in the granite is also more rapid than in the mica schist. Although it would again be difficult to rule out vertical heat loss, this finding corroborates with the location of fracture B3-1, and the flow observed during the injection phase. In F22, the abstraction of the heated water occurred near the contact between mica schist and granite, making the RTA calculated in the mica schist unreliable (*cf.* Figure 2.6d). In the granite however, cooling of much of the test interval is uniform. At around 28 m, there is a zone of more enhanced cooling that then widens with time. This zone corresponds to a zone of fracturing and moderate transmissivity previously identified by *Druillennec et al.* (2010). Cooling in the lower part of the section of F22 also appears to be affected by vertical heat loss.

2.5 Inversion of field data for apparent thermal conductivity

The RTA calculation using equation 2.11 normalises the cooling data, but does not account for the variable heat transfer into the rock during the heating phase. It also does not determine whether the cooling observed may be explained by conduction, or is so rapid

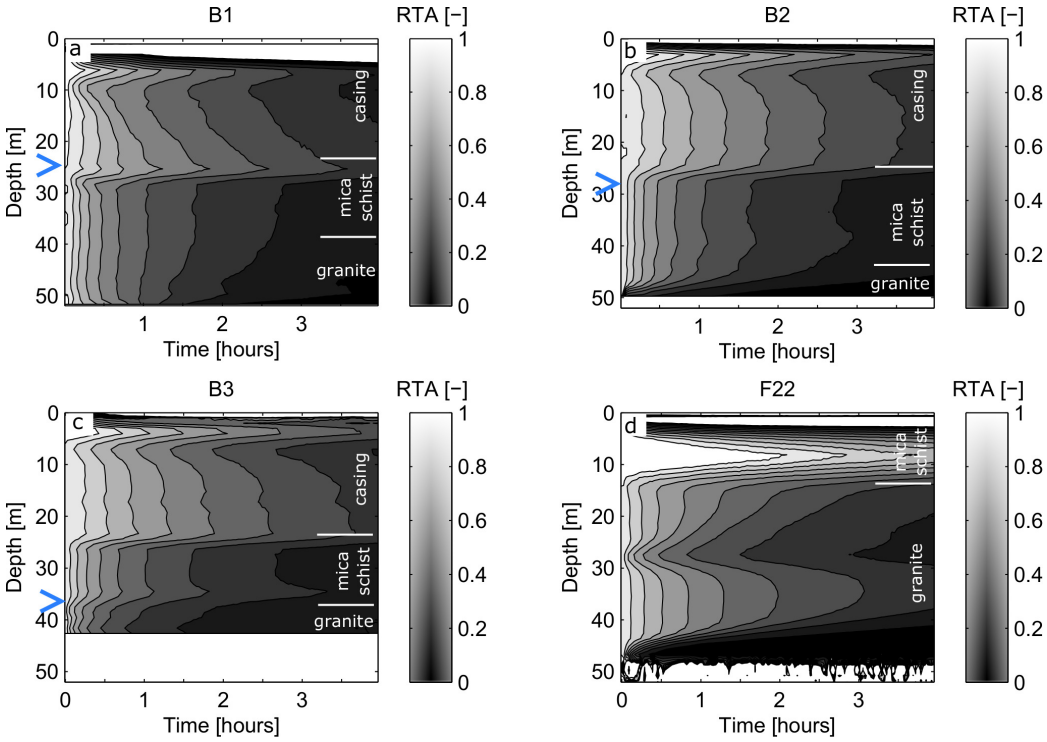

Figure 2.7: RTA during the cooling phase of the thermal dilution tests in a) B1, b) B2, c) B3, and d) F22 under ambient conditions. Previously identified transmissive fracture zones are shown with arrows.

that advective heat transfer by flowing groundwater also contributes. For this reason, a simple 1D conduction only finite difference numerical model was developed to simulate heat conduction into the rock during the heating phase, and the subsequent cooling after heating ceased. The finite difference model gives equivalent results to the COMSOL model when there is no groundwater flow, but is more flexible in that the time and depth dependent heating in the borehole can be more easily incorporated while also varying the thermal properties. Heat conduction in cylindrical coordinates is given by:

$$\frac{\partial T}{\partial t} = \frac{k_{\text{eq}}}{C_{\text{eq}}} \frac{1}{r} \left[\frac{\partial}{\partial r} \left(r \frac{\partial T}{\partial r} \right) \right] \tag{2.12}$$

The forward in time, centred in space explicit approximation for this is given by:

$$\frac{T_i^{n+1} - T_i^n}{\Delta t} \approx \frac{k_{\text{eq}}}{C_{\text{eq}}} \left[\frac{r_{i+\frac{1}{2}} \frac{T_{i+1}^n - T_i^n}{\Delta r} - r_{i-\frac{1}{2}} \frac{T_i^n - T_{i-1}^n}{\Delta r}}{r_i \Delta r} \right] \tag{2.13}$$

where Δt and Δr are the time and spatial steps respectively, and i denotes the node position ranging from 1 to $R/\Delta r$ (R is the distance to the outer limit of the model domain).

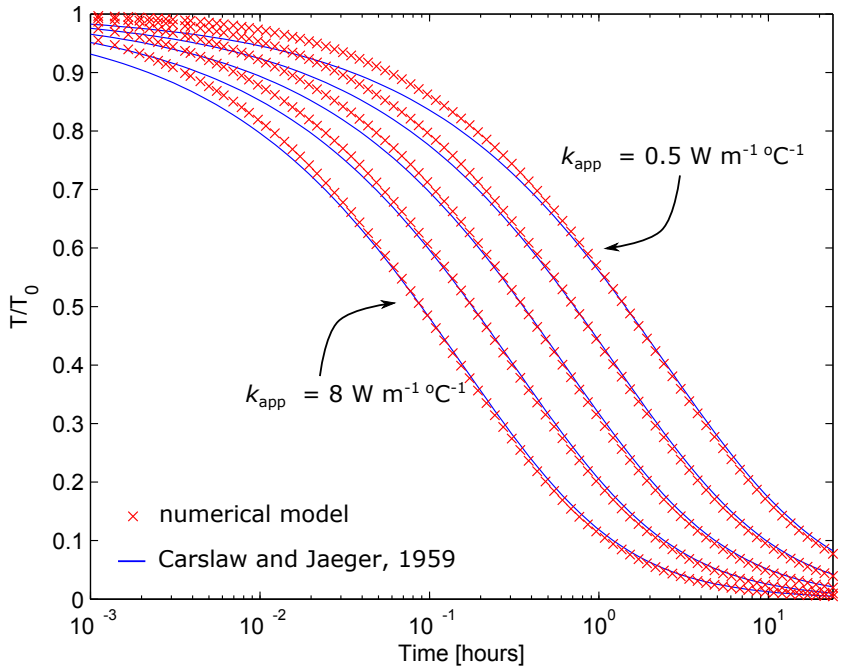

Figure 2.8: Comparison of the finite difference numerical model and *Carslaw and Jaeger* (1959) analytical solution for the same input parameters, and thermal conductivities of 8, 4, 2, 1, and 0.5 W m^{-1} $°C^{-1}$ from left to right

Table 2.2: Parameters used in the thermal dilution test finite difference cooling model for the estimation of apparent thermal conductivity

Parameter		Value	Units
Model domain	R	2	m
Time step	Δt	1	s
Spatial step	Δr	0.005	m
Thermal conductivity of rock	k_r	0.1:0.1:20	W m^{-1} $°C^{-1}$

Values of parameters used in the model, in addition to those used in Table 2.1, are given in Table 2.2. The value of the heat capacity used is the mean of lab measured values on the core from B1 (*Klepikova et al.*, 2013), with the value for mica schist and granite having no significant difference. The heat capacity is therefore assumed not to vary with depth. Figure 2.8 compares the temperature decay obtained with the finite difference model and analytical solution result using Equation 2.2, for a range of thermal conductivities, and temperature initially 1 in the borehole and 0 in the rock.

The inversion procedure to determine the thermal conductivity consists of two principle steps. Firstly, heat conduction into the rock during the heating phase is simulated by prescribing the time varying DTS measured temperature as the boundary condition at the borehole-rock interface. Secondly, the cooling phase is simulated using the temperature distribution in the rock from the heating phase as the initial condition. The borehole fluid

is assumed to be laterally well mixed, with the temperatures in the borehole averaged after each time step. These two steps are repeated for a range of values of thermal conductivity, and the modelled temperature in the borehole during the cooling phase output at the DTS measurement times to allow direct comparison between the numerical model and field data. Figure 2.9a shows DTS observed temperature with modelled response in B2 at 30 m depth for a range of thermal conductivities. In the inversion procedure, the thermal conductivity is increased in increments of 0.1 W m^{-1} $°C^{-1}$. The apparent thermal conductivity of the rock is found by finding the thermal conductivity which gives the lowest RMSE between modelled and observed temperature during the cooling phase. The RMSE as a function of thermal conductivity is shown in Figure 2.9b, showing minimum RMSE at around 3 W m^{-1} $°C^{-1}$. This procedure is repeated at all depths to obtain a thermal conductivity profile for each borehole.

Figure 2.10 shows the thermal conductivity profiles obtained through the optimisation procedure, along with the RMSE of the optimum model data. The thermal conductivity of the cased section (plastic) is universally lower than the open section in B1, B2, and B3 (F22 lacks casing). The apparent thermal conductivity of the mica schist ranges from 3-4 W m^{-1} $°C^{-1}$ in B1, B2 and B3. The shallower depth of the mica schist in F22 means that values are not available here. The lab measured thermal conductivity of cored samples available from B1 range from 1.7 - 3.4 W m^{-1} $°C^{-1}$ (3 samples, mean of 2.6 W m^{-1} $°C^{-1}$). The thermal conductivity of the granite appears to be higher. This corroborates with values of 2.9 - 4.1 (7 samples, mean 3.3 W m^{-1} $°C^{-1}$). However, the relatively short section of granite tested in each borehole and the non radial heat condition at the bottom of the heated section, with the effect of increasing the apparent thermal conductivity, overprints much of the data. The known transmissive fractures B1-1, B2-1, and B3-1, are not visible in the profiles of apparent thermal conductivity. The fracture zone in F22 at around 28 m, also readily identifiable in Figure 2.6 and identified by *Druillennec et al.* (2010), has a slightly elevated apparent thermal conductivity relative to the surrounding rock at 3.9 W m^{-1} $°C^{-1}$.

Figure 2.11 shows cooling data at depths of 30, 35, and 40 m in B3 under ambient and cross pumping conditions. Despite having a higher RMSE relative to depths of 30 and 35 m, the response at 40 m still appears to give a conduction like cooling response. The radial

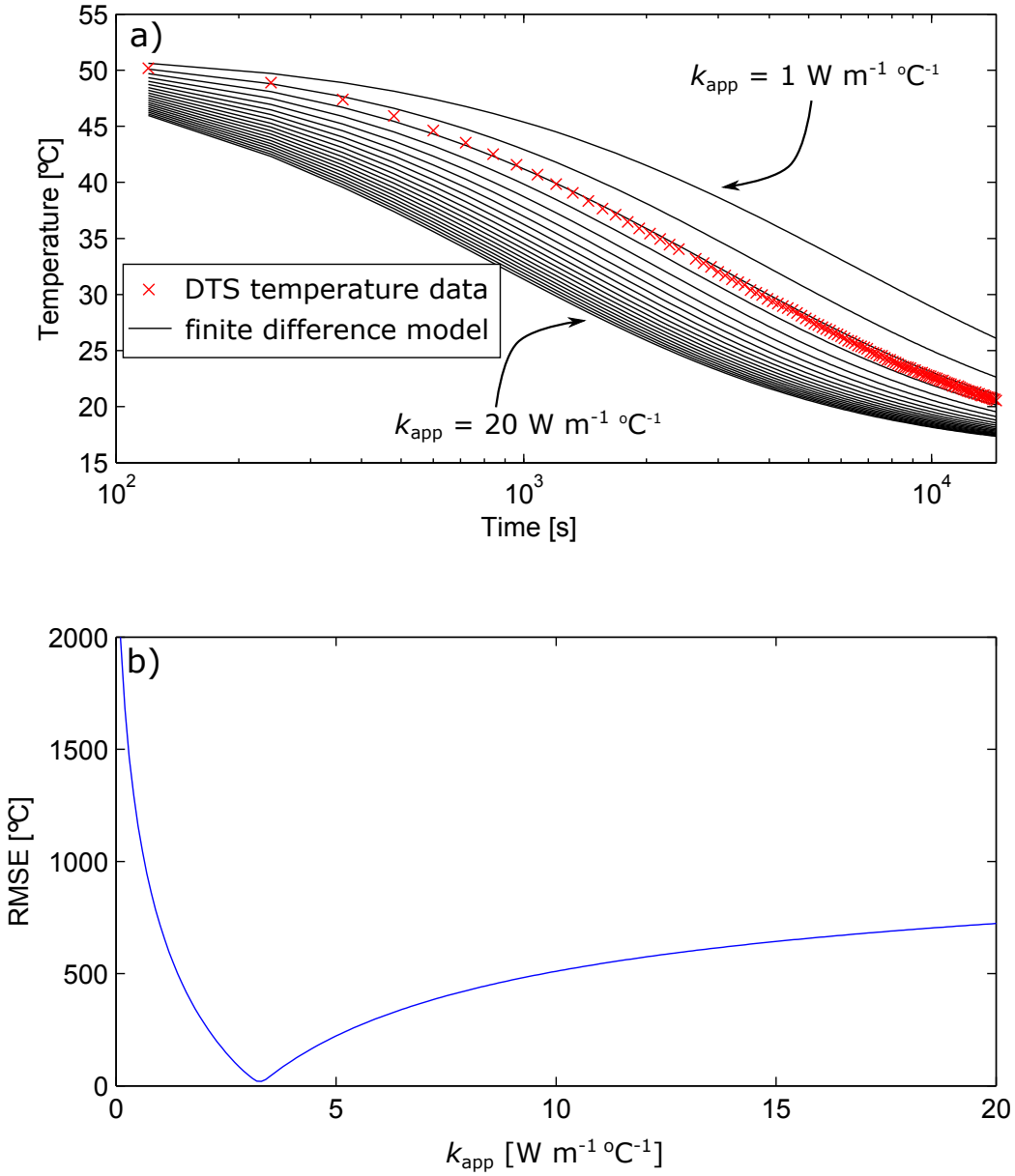

Figure 2.9: a) Cooling in B2 at a depth of 30 m, with radial conduction numerical model solutions shown. b) RMSE as a function of apparent thermal conductivity at a depth of 30 m in B2

conduction model gives a good approximation for the cooling with a slightly elevated apparent thermal conductivity relative to the shallower depths. The response appears to be similarly conductive under cross pumping conditions. There is a good agreement with the thermal dilution test conducted under ambient flow conditions at 30 and 35 m depth where there are known to be no transmissive fractures. At 40 m, the responses show similarly elevated apparent thermal conductivities. The effect of cross pumping does not significantly increase the apparent thermal conductivity or give a cooling response that indicates an advective effect.

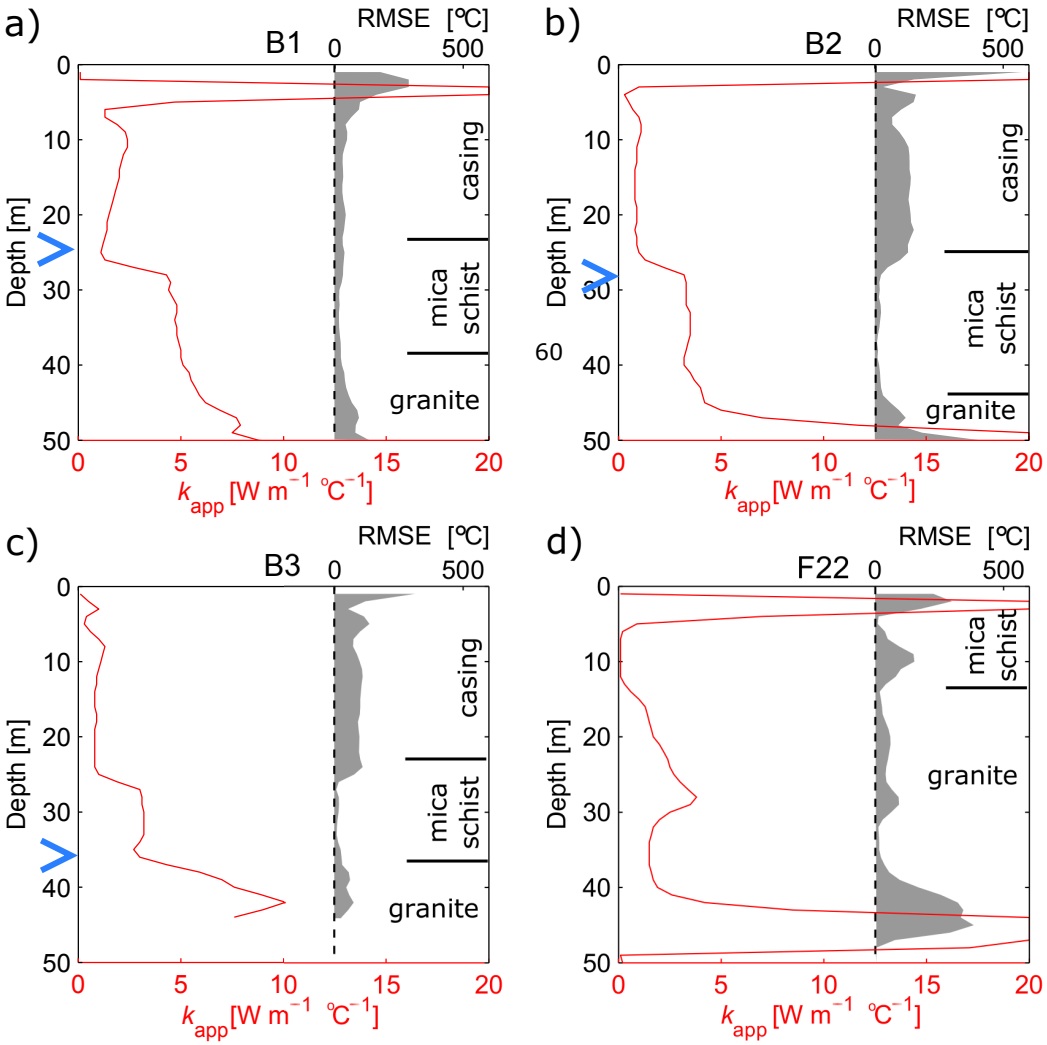

Figure 2.10: Optimal apparent thermal conductivity profiles in a) B1, b) B2, c) B3, and d) F22, with RMSE between the optimum model and DTS cooling data. Previously identified transmissive fracture zones are shown with arrows.

2.6 Discussion and conclusions

Since analytical solutions can only consider either conduction or advection, a numerical model of groundwater flow and heat transport was devised to investigate the sensitivity of thermal dilution tests to groundwater flow. The simulations indicate that, for specific discharges of $< 5.0\text{x}10^{-6}$ m s^{-1}, the thermal dilution test would be insensitive to groundwater flow as the cooling is conduction dominated. At specific discharges $> 5.0\text{x}10^{-6}$ m s^{-1}, the cooling is increasingly more strongly influenced by groundwater flow, and the temperature decay curve departs from a 'heat conduction' response. Therefore, both the rate of cooling, and shape of the decay curve, are indicators of groundwater flow.

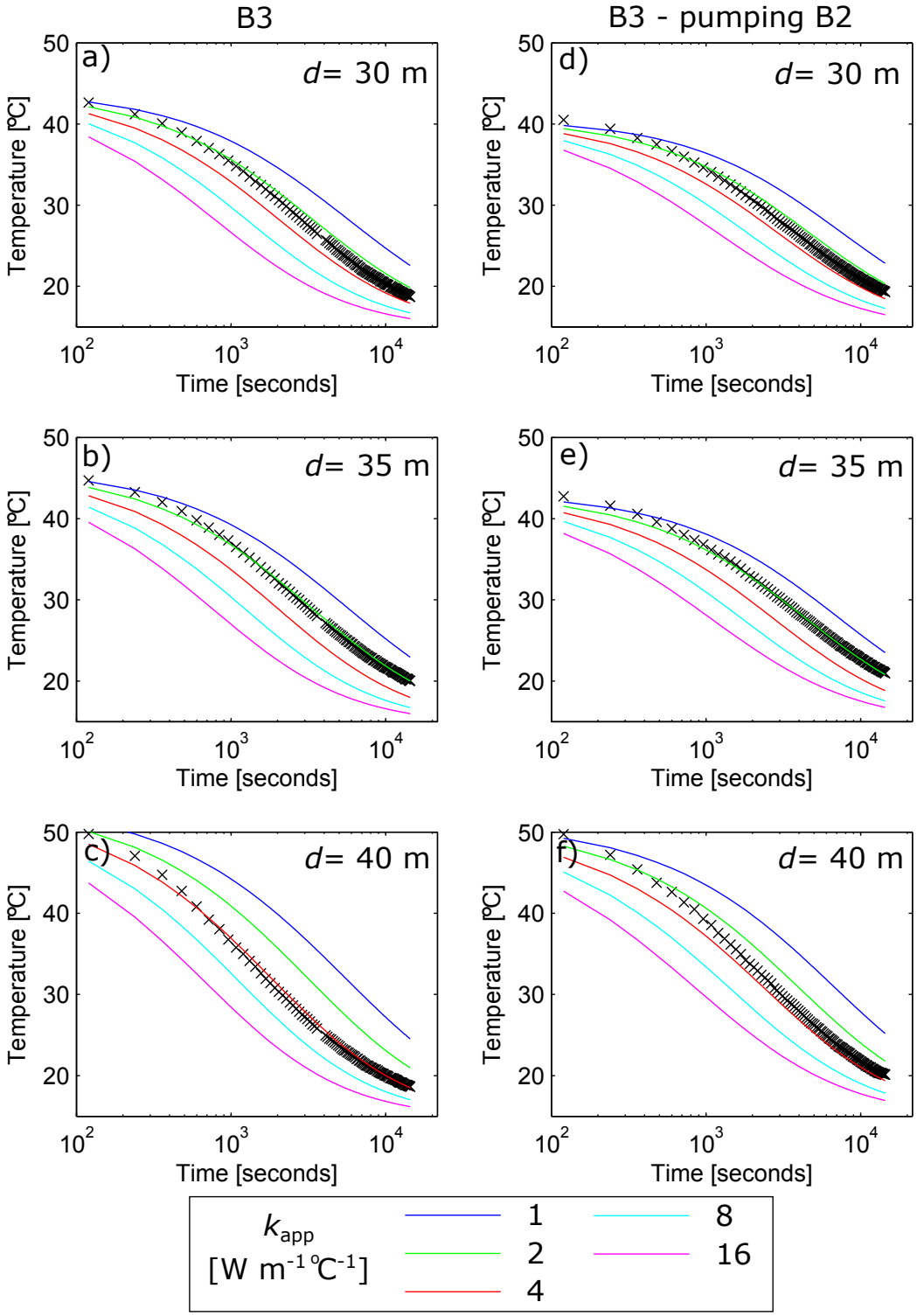

Figure 2.11: Time series of temperature in B3 during the cooling phase under ambient (a-c) and cross pumping conditions (d-f). The radial conduction numerical model results for apparent thermal conductivities of 1, 2, 4, 8, and 16 W m^{-1} °C^{-1} are shown for each depth

Data were analysed from thermal dilution tests carried out in 4 boreholes at the Ploemeur research site. The cooling phase highlighted differences in the thermal properties of the casing, mica schist and granite. Thermal data did not elucidate transmissive fractures in B1, B2, and B3, but a transmissive zone, identified from previous logging in F22 at 28 m, was clearly identifiable from the cooling data. A finite difference cooling model was developed and used to estimate apparent thermal conductivity profiles in each borehole. These profiles showed that the apparent thermal conductivity of the granite is higher than the mica schist, corroborating with lab analysed samples. However, there was no evidence of an elevated apparent thermal conductivity at the depth of the known fractures in B1, B2 and B3. F22 exhibits a slightly elevated apparent thermal conductivity at 28 m, with the cooling appearing to still be conduction dominated however.

The inability of the thermal dilution tests carried out in the field to identify the fractures can be explained by two factors. Firstly, the cooling data and apparent thermal conductivity estimation suffers from non-radial conduction effects that towards the base of the borehole enhance the cooling, most notable in B2 and F22. This effect, according to the DTS temperature data, occurs over approximately 5 m, hence care must be taken to ensure that this is not a critical zone of interest. Secondly, the DTS instrument used had a relatively poor spatial resolution compared to instruments available now, or that could be achieved with this instrument and a wrapped cable. The manufacturer stated spatial resolution of the instrument used was 2 m (although in the field we estimated this to be closer to 5 m). This means that any fracture enhanced cooling, limited to the interval of the borehole intersected by the fracture, is therefore averaged with a much wider zone of conduction only cooling. The much improved spatial resolutions given by the latest instruments, when combined with a wrapped cable, can give spatial resolutions of a few cm. This is much closer to the spatial scale of the fractures encountered. However, the problem still exists in that where the spatial extent of the temperature signal is less than the spatial resolution, the true temperature signal due to the cooling will remain unknown. In this case, any quantitative attempt to derive flow from the cooling data will be erroneous. At present, the utility of DTS monitored thermal dilution tests therefore seems most appropriate in layered, unconsolidated aquifers. Here, as long as the heterogeneity occurs over wider depths than the spatial resolution, the thermal dilution test would be sensitive

to hydraulic conductivity and flow variability in the coarsest intervals, while most likely exhibiting a conduction dominated signal in the relative low permeability layers.

Chapter 3

Thermal-Plume fibre Optic Tracking (T-POT) test for flow velocity measurement in groundwater boreholes *

3.1 Chapter summary

An approach is developed for measuring in-well vertical flow using point electrical heating combined with spatially and temporally continuous temperature monitoring using DTS. The method uses a submersible electric heater to warm a discrete volume of water. The rate of advection of this plume, once the heating is stopped, equates to the cross sectionally averaged flow velocity in the well. We conducted Thermal-Plume fibre Optic Tracking (T-POT) tests in B3 at the Ploemeur site, with the heater at a fixed depth and multiple pumping rates. Tracking of the thermal plume peak allowed the spatially varying velocity to be estimated up to 50 m downstream from the heating point, depending on the pumping rate. The T-POT technique can be used to estimate the velocity throughout long intervals provided that thermal dilution due to inflows, dispersion, or cooling by conduction do not render the thermal pulse unresolvable with DTS. A complete flow log may be

*This chapter was published as: Read, T., V. Bense, O. Bour, T. Le Borgne, N. Lavenant, R. Hochreutener, and J.S. Selker, Thermal-Plume fiber Optic Tracking (T-POT) test for flow velocity measurement in groundwater boreholes, *Geoscientific Instrumentation, Methods and Data Systems Discussions*, *5*, 161–175, 2015

obtained by deploying the heater at multiple depths, or with multiple point heaters.

3.2 Introduction

The measurement of the vertical flow in wells can improve our conceptual understanding of subsurface fluid movement, which can aid in, for example, groundwater resources management or geothermal resource assessments. In open or long-screened wells penetrating multiple permeable units or fractures, vertical flow typically occurs in hydraulically unstressed conditions due to the natural occurrence of a vertical head gradient. Flow logs obtained in unstressed conditions gives a qualitative guide to fracture inflow and outflow zones (*Hess*, 1986). Alternatively, flow logs obtained in a pumping well at multiple different pumping rates allow the depth variability of transmissivity to be estimated (*Paillet et al.*, 1987). Flow logs in observation wells affected by nearby pumping enables the connectivity of fractures to be determined (*Paillet*, 1998; *Klepikova et al.*, 2013). In all cases, the in-well flow is not directly indicative of flow in the formation itself since the presence of the well as a high permeability vertical conduit allows the short circuiting of flow. In addition, flow logs have inherent value for geochemical sampling campaigns. Ambient vertical flow through the well may redistribute contaminants and mean that passive sampling approaches do not reproduce the same depth variability as present in the aquifer itself (*Elci et al.*, 2003). Typical flow logging techniques involve lowering an impeller or electromagnetic flowmeter down a well and either measuring continuously (trolling) or at multiple points with the probe held stationary. At low flows a heat pulse flowmeter may be used at fixed depths (*Paillet*, 1998).

Alternatively, tracer based approaches may be used. Most commonly, a tracer is emplaced over the entire length of the borehole and the change in concentration monitored over time. Typically, slightly saline (*Maurice et al.*, 2011), or distilled water (*Doughty et al.*, 2005) is added since fluid electrical conductivity (EC) can be easily logged with an EC meter. The EC is then monitored over depth and time by making repeated logs. The dilution of the saline profile at inflow locations or increase in EC if using distilled water can be used to estimate horizontal flow through the aquifer using simple analytical solutions (*Pitrak et al.*, 2007). If there is vertical flow in the well, a salinity front

then migrates up or down the well. In the case of multiple inflows with multiple salinity fronts, the response over depth and time may become complex and require numerical modelling (*Maurice et al.*, 2011), or inversion methods to extract the vertical flow profile (*Moir et al.*, 2014). A limitation of this method is that when the vertical velocity or losses from the borehole to the aquifer are high, the EC signal rapidly dissipates and monitoring this process over a large depth interval with a single EC logger yields an incomplete dataset. Additionally, density induced flow effects in well bores are significant even for small gradients of fluid density (*Berthold*, 2010).

Instead of a hydrochemical signal that can be difficult to monitor over space and time, *Leaf et al.* (2012) introduced a slug of warm water to a target depth. By using temperature as the tracer, it is possible to monitor the response continuously over depth and time along a fibre optic cable installed in the well with the Distributed Temperature Sensing (DTS) technique (see *Selker et al.* (2006) for a description of the DTS method). *Leaf et al.* (2012) heated water at the surface and injected it at multiple depths to identify the flow direction and velocity. However, the process of heating water is cumbersome and, its injection is likely to result in head changes in the well resulting in an altered flow regime particularly if ambient or low pumping rate conditions are of interest. *Sellwood et al.* (2015a) adapted this method by using an electrical heater to generate the thermal disturbance and carried out tests under non-hydraulically stressed conditions in a dual permeability sandstone aquifer. In this study we deploy a single electrical heater to warm a discrete interval of water at depth in a pumping well in a fractured rock aquifer, monitored with DTS. We apply post-collection averaging to the DTS temperature data and track the peak of the plume over time to estimate the mean vertical velocity. We call this method Thermal-Plume fibre Optic Tracking (T-POT).

3.3 T-POT field application

We deployed T-POT at the H+ network research site (hplus.ore.fr/en), Ploemeur France (Figure 3.1a). The site has multiple boreholes up to 100 m deep, penetrating mica schist and granitic rock. Open fractures, although sparse ($<$ 5 hydrogeologically significant fractures per borehole), are reasonably transmissive (up to 4x10^{-3} m^{-2} d^{-1}). We show T-POT results from borehole B3 (11.8 cm diameter), which is intersected by three previously

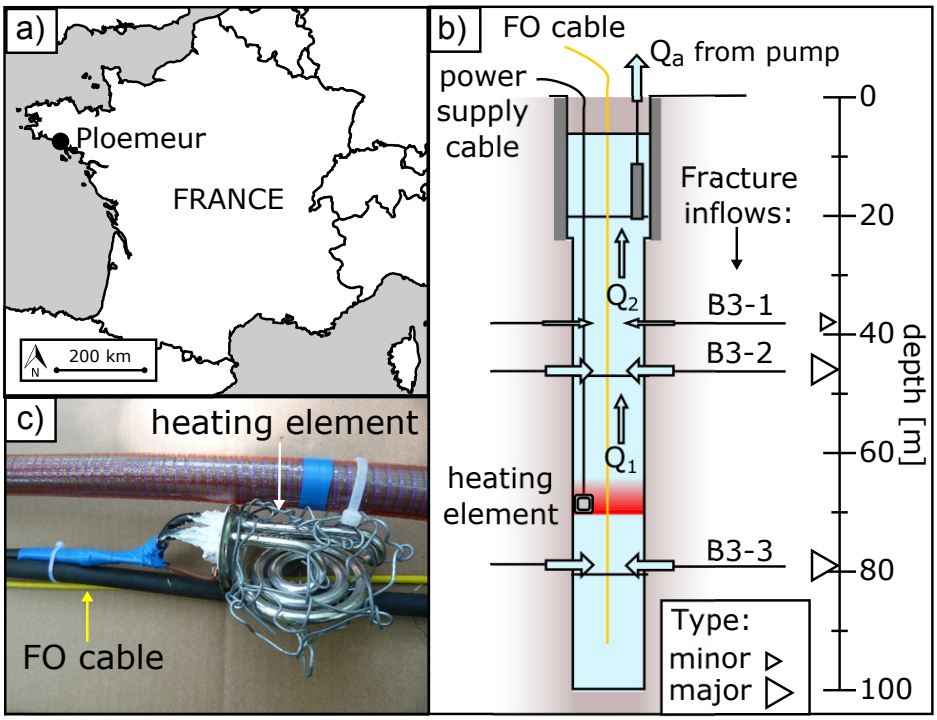

Figure 3.1: a) Location of the Ploemeur research site, b) heating element and fibre optic cable along which temperature is measured, c) schematic of the set-up in borehole B3 at the site

identified transmissive fractures (Figure 3.1b). Fractures B3-2 and B3-3 have similar transmissivities ($\sim$ 2x10^{-3} m^{-2} d^{-1}), while B3-1 is approximately an order of magnitude less transmissive *Klepikova* (2013).

We used a 2 kW rated heating element as the heat source (Figure 3.1c), lowered down to 68 m depth for the duration of the experiment. Additionally, an armoured fibre optic cable was installed in the well down to a depth of approximately 80 m. This allowed temperature measurements to be made over a time average of 5 seconds and sampling interval of 0.12 m with DTS by connecting it to a Silixa ULTIMA base unit. The cable was configured for a duplexed single ended measurement. The DTS data were calibrated using 3 reference sections from a cold and ambient bath, according to the method described by *Hausner et al.* (2011). The standard deviation of temperature in the cold and ambient baths for the 5 second integration time averaged 0.38 and 0.33 °C respectively over the duration of the T-POT tests.

We ran a series of tests at different pumping rates to determine the fracture inflow for each pumping rate, in order to evaluate the T-POT method. For each pumping rate, a similar procedure was followed: heat for $\sim$ 10 minutes, then switch off the heating and simultaneously turn on the pump at the selected rate. We repeated this procedure

for pumping rates of 7.3, 40.0, 86.6, 104.0, 136.2 L min^{-1}. During each experiment we measured the pumping rate manually and with an in-line flowmeter, drawdown, electrical power supplied to the heating element, and temperature along the length of the borehole with DTS.

3.4 T-POT results and interpretation

Figure 3.2 shows successive DTS temperature depth profiles from the 5 T-POT experiments. During the heating phase ($t < 0$ min), it appears that the plume develops asymmetrically, with the base of the plume at 68 m at the approximate depth of the heater. The heater is switched off at $t = 0$ and at this moment pumping is initiated. The plume is then advected upwards at higher velocity. In all cases, the linear path of the plume in the temperature-depth-time plot suggests a uniform velocity from 68 m to around 45 m, as would be expected given the lack of transmissive fractures and uniform borehole diameter in this interval. At 45 m, the temperature signal is significantly reduced and the plume then continues to move upwards at higher velocity (steeper gradient in Figure 3.2c,d,e). This coincides with a transmissive fracture identifiable in previous flowmeter tests and optical borehole logs (*Le Borgne et al.*, 2007).

To aid the identification of the plume peak, the 5 second time averaged and 0.12 m spatially sampled DTS temperature data were then subsequently further averaged to give the equivalent of 15 second time averaged DTS temperature data. Each point was then spatially smoothed with a 9 point moving average window. These are plotted as temperature-depth profiles in Figure 3.3. Below 45 m, the plume is clearly defined. Above the inflow from B3-2 at 45 m, the plume becomes much less discernible (Figure 3.3c,d,e).

The depth location of the maximum temperature was then extracted and plotted over time (Figure 3.4). While the peak of the plume remains below fracture B3-2, the plume is readily resolvable in the temperature data. Linear least-squares regression of the plume depth with time yields an $r^2 \geq 0.98$ for all of the pumping rates. The average flow velocities v_1 and v_2 were calculated from the gradient of the best fit line through plume peak location data. The corresponding volumetric flow rates Q_{B3-3} and $Q_{B3-1,2,3}$ were calculated from v_1 and v_2 respectively using the known borehole diameter over this interval.

Above 45 m, the peak of the plume was not detected for 1 - 2 minutes after the arrival

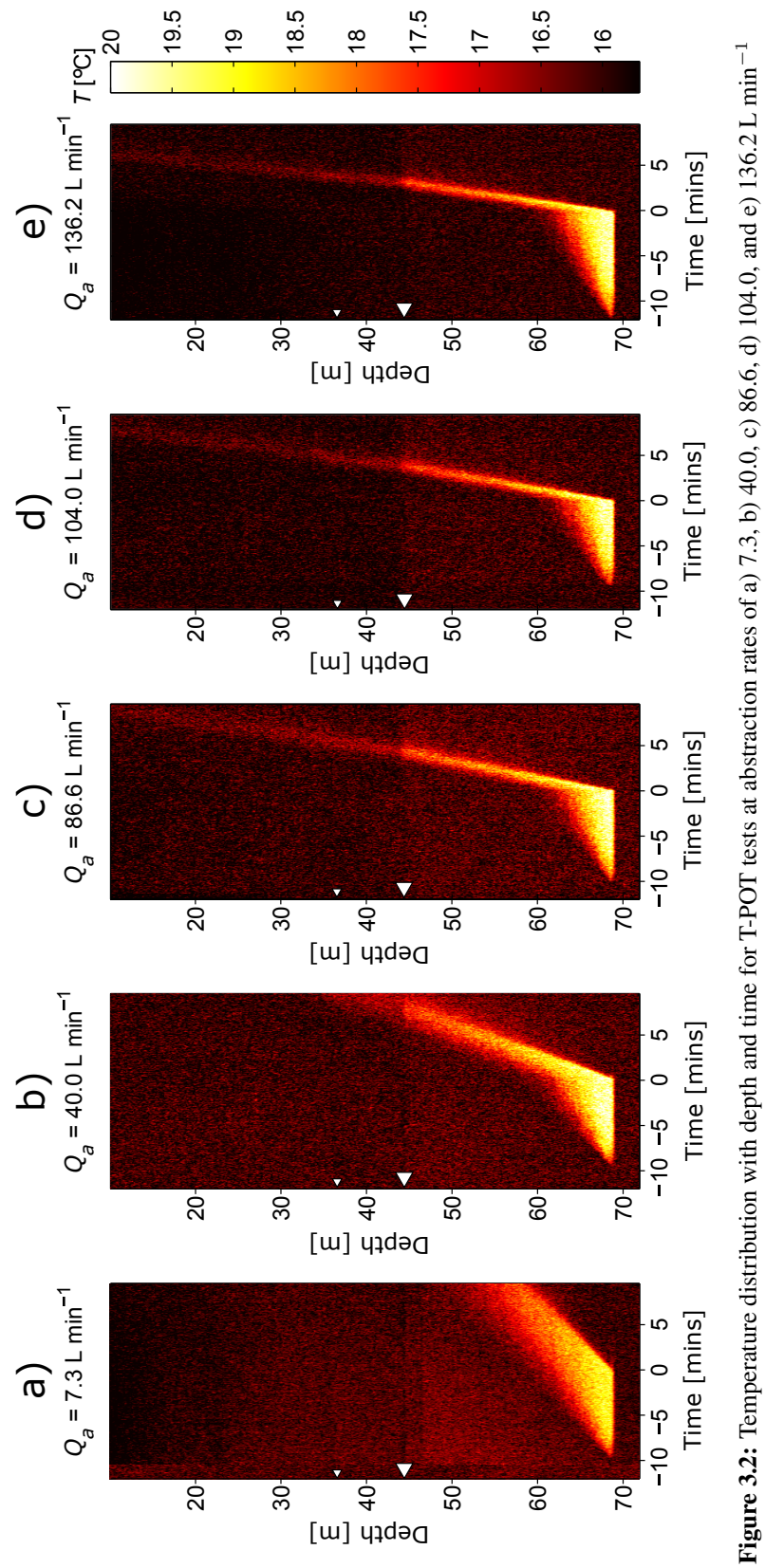

Figure 3.2: Temperature distribution with depth and time for T-POT tests at abstraction rates of a) 7.3, b) 40.0, c) 86.6, d) 104.0, and e) 136.2 L min^{-1}

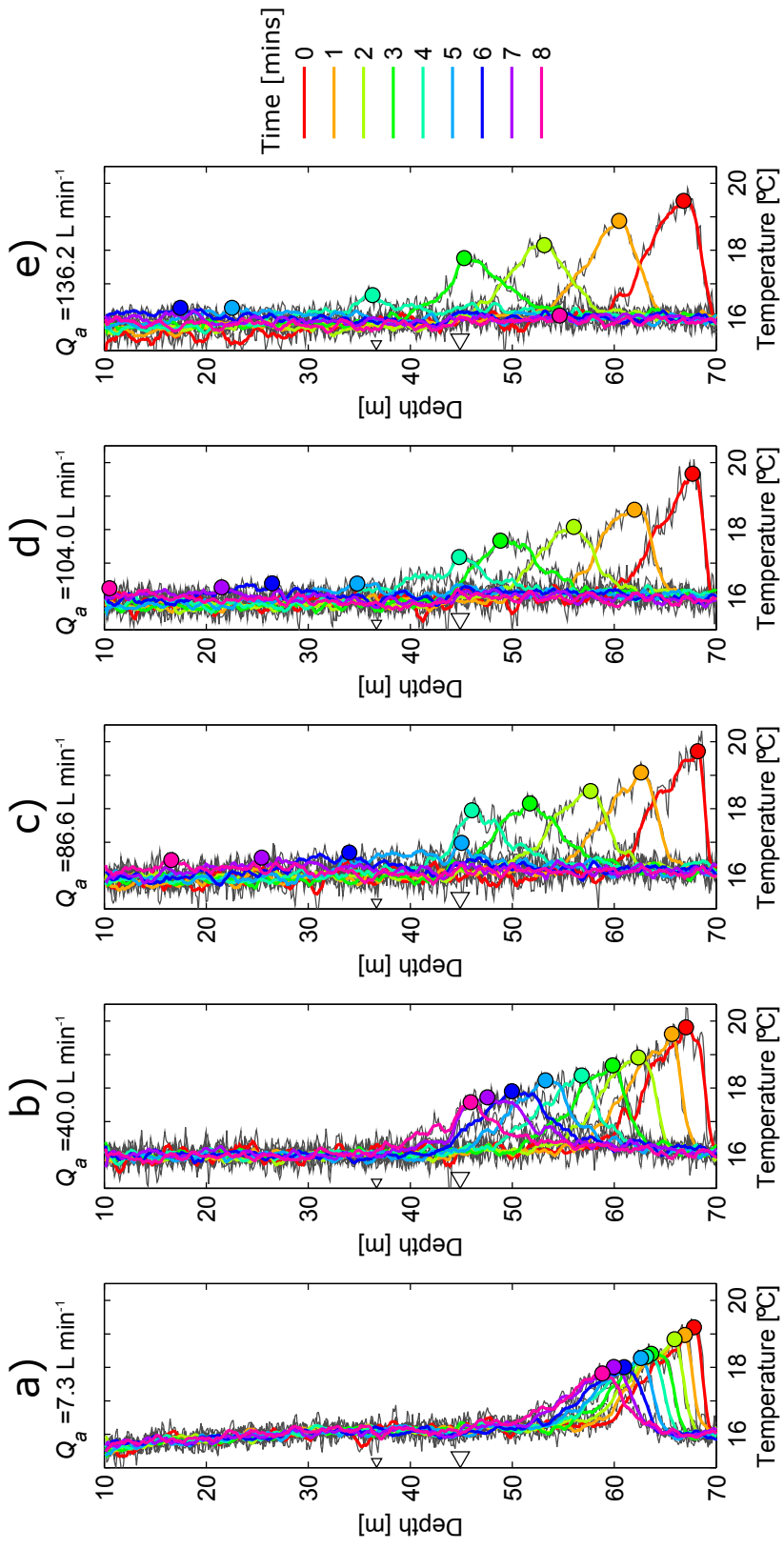

Figure 3.3: Temperature-depth profiles after pumping begins for the T-POT tests at abstraction rates of a) 7.3, b) 40.0, c) 86.6, d) 104.0, and e) 136.2 L min^{-1}. Grey lines indicate the DTS data without the spatial smoothing applied

a)

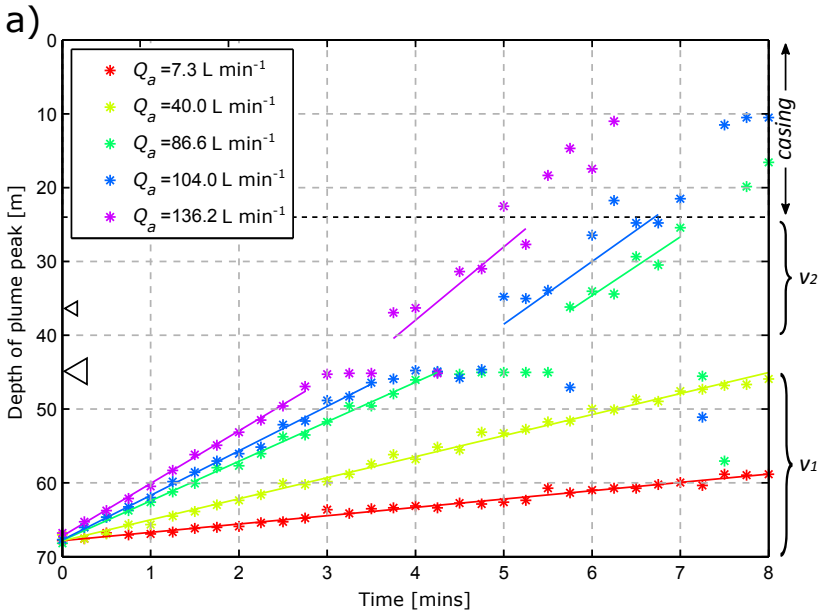

b)

v_1 [cm s^{-1}]	v_2 [cm s^{-1}]	r^2 (v_1)	r^2 (v_2)	$Q_{B3\text{-}3}$ [L min^{-1}]	$Q_{B3\text{-}1,2,3}$ [L min^{-1}]	Q_a [L min^{-1}]
1.88	-	0.98	-	10.73	-	7.3
4.75	-	0.99	-	27.09	-	40
8.92	13.23	0.99	0.87	50.88	75.42	86.6
10.05	14.15	0.99	0.39	57.30	80.66	104
11.87	16.53	1.00	0.54	67.69	94.27	136.2

Figure 3.4: Temperature peak depth over time for each of the pumping rates, with linear least-squares regression best fit lines used to estimate the in-well vertical flow velocity

of the plume peak at B3-2. This is because in this situation, the inflow from B3-2 greatly dilutes the thermal signal, such that until most of the plume has moved above the fracture, the highest temperature (and plume peak, as identified with this method), remains at the depth of the fracture. Once identified again, now at approximately the depth of B3-1, the peak location data show that the plume is now travelling at higher velocity. Here it is much less detectable, with an r^2 for the three cases where the plume passes this point of 0.76, 0.65, and 0.91. However, it is not possible to assess separately the flow contributions of B3-2 and B3-1, since two separate contributions are not apparent in Figures 3.2-3.4. Therefore we are only able to estimate Q_{B3-3} (the flow below 45 m) and $Q_{B3-1,2,3}$ representing the cumulative flow contribution from all transmissive fractures intersecting the well.

3.5 Discussion

The upwards expansion of the plume during the heating phase is driven by upward ambient fluid flow in the borehole. The rate of the ambient flow component between B3-3 and B3-2 has been measured at approximately 5 L min^{-1} in previous studies (*Klepikova*, 2013). When pumping at 7.3 L min^{-1}, the calculated flow between B3-3 and B3-2, Q_{B3-3}, is almost double the abstraction rate. At this low pumping rate, the hydraulic head in the borehole remains higher than the hydraulic head in B3-1, so that B3-1 remains an outflow. The flow from B3-3 is proportional to the pumping rate (r^2 =0.99), as would be expected from linear scaling behaviour, giving us confidence in these flow estimates. The discrepancy between $Q_{B3-1,2,3}$ and Q_a is at most 20%. Much of this error may arise from the error determining the plume location above B3-1. Further additional sources of error that may contribute to the discrepancy in flow estimates are the high sensitivity of the volumetric flow estimate to borehole diameter used for the calculation, and error in independently measuring the flow at the surface. The inability of the method to reliably track the velocity immediately downstream of fracture B3-2 in the present study is due to the strong dilution effect by inflow from the fracture of a similar magnitude to the vertical flow in the borehole. The relatively low r^2 for the peak depth-time data beyond this fracture and discrepancy from Q_a is because the resulting plume is much more dispersed with a poorly defined peak. The T-POT method as used here, would more likely perform better in cases where there are multiple outflows (e.g. under ambient flow conditions), rather than inflows. This is because inflows affect both the size and shape of the signal.

Free convection due to T-POT heating induced buoyancy, as occurs naturally in groundwater wells even for small temperature gradients (*Sammel*, 1968), may disturb the in-well flow. The potential for heat transfer by natural convection in a fluid is expressed by the Rayleigh number, given by:

$$Ra = \frac{\beta g \Delta T/\Delta z}{D\nu} r^4 \tag{3.1}$$

where β is the thermal expansion coefficient, g is acceleration due to Earth's gravity, $\Delta T/\Delta z$ the temperature gradient, D the thermal diffusivity, ν kinematic viscosity, and r the characteristic length, which in this case is the borehole radius. For the T-POT experiments here in a borehole with radius 0.059 m, with $\Delta T/\Delta z$ at most 0.5 °C m^{-1} during the

heating phase, and substituting values of 2x10^{-4} °C^{-1}, 9.81 m s^{-2}, 0.14x10^{-6} m^2 s^{-1}, and 1x10^{-6} m^2 s^{-1} for β, g, κ and ν respectively gives a Ra of 85,000. Scaling the results of *Berthold and Resagk* (2012), who imaged flow velocities due to free convection in a vertical cylinder, using this Rayleigh number, suggests that in the absence of any forced convection, free convection due to T-POT heating would give rise to flow velocities of the order of 2 cm s^{-1}. This is similar to the velocity that would be expected under ambient flow conditions. However, this velocity is the velocity magnitude in a diametrically anti-symmetric convection cell. Therefore even though the velocity due to natural convection is of a similar magnitude to the ambient flow, if the convection cells are relatively small then the warming front would not propagate up the well at this rate. A further in-depth analysis is beyond the scope of this paper, but we note that if present, the development of large convection cells would place a lower limit on the velocity estimate that can be obtained with the T-POT method.

The upper limit of velocity estimation is reached when the plume travels the length of the monitoring interval in less than the integration time of the DTS temperature measurement (i.e. $v_{max} = Z/t_i$, where Z is the length of flow path away from the heater in the direction of flow, and t_i is the integration time of the DTS temperature measurement). The depth resolution of the velocity estimate using the T-POT method are flow velocity dependent. At high velocities, the depth spacing between velocity estimates is $t_i v$. At low flow velocities, the spatial sampling of the DTS instrument determines the number of velocity estimates with depth that the T-POT method can provide.

The basic method, using DTS with a fibre optic cable and point source electrical heating in the well, can be easily adapted to include the use of multiple heaters or more prolonged heating in a constant source type experiment. While the method at present assumes a constant velocity profile in time, time varying velocities could be monitored by cycling through heating and non-heating phases. The method is completely complementary to and can be easily used alongside other fibre-optic down hole tests and to validate vertical velocity estimates made by other Active-DTS methods such as *Read et al.* (2014).

3.6 Conclusions

We deployed the T-POT method in a groundwater well in fractured rock. By heating a discrete volume of the resident water in the borehole, estimates of vertical in-well velocity were obtained by tracking its subsequent migration with DTS. The advantage of this method is that it is quick and simple, especially if the well is already instrumented for fibre optic temperature monitoring. The plume was however significantly reduced beyond a major inflowing fracture, but was still detectable, albeit with much increased uncertainty. This highlighted that using this downhole method, where inflows are large, the signal is potentially completely lost. There is therefore scope for the further development of DTS methods for measuring vertical flow, that have a greater range of settings in which they can be successfully deployed.

Chapter 4

Field trial of the hybrid cable method to measure in-well vertical flows*

4.1 Chapter summary

A field trial is conducted of a distributed borehole flowmeter created from a hybrid cable (containing both optical fibres and a heatable element), and using DTS in active mode (A-DTS). Rather than just sensing the temperature of the surrounding fluid, the cable itself is heated by current flowing along the inner steel capillary tube. The principle is that in a flowing fluid, the increase in temperature due to the electrical heating is a function of the fluid velocity. The physical basis of the methodology is outlined and results presented from the deployment of a prototype A-DTS flowmeter in borehole B2 at the Ploemeur site. On heating the submerged fibre optic cable, the temperature plateaued within 60 s. This value of this temperature plateau was determined at different pumping rates in a series of heating tests. It was found that an increase in flow velocity from 0.01 m s^{-1} to 0.3 m s^{-1} elicited a 2.5°C cooling effect. It is envisaged that with further development this method will have applications where point measurements of borehole vertical flow do not fully capture combined spatio-temporal dynamics.

*This chapter was published as: Read, T., O. Bour, J. S. Selker, V. F. Bense, T. L. Borgne, R. Hochreutener, and N. Lavenant, Active-distributed temperature sensing to continuously quantify vertical flow in boreholes, *Water Resources Research*, *50*(5), 3706–3713, 2014.

4.2 Introduction

Fluid flow logs in boreholes provide direct insight into the hydrogeological conditions encountered with depth in the sub-surface. Such information provides not only a qualitative addition to other geophysical logs, but can classically be used to derive hydraulic property variations with depth during pumping tests (*Molz et al.*, 1994; *Paillet*, 1998). Various designs of flowmeter currently exist: impeller flowmeters (*Molz et al.*, 1989); heat pulse flowmeters which rely on the time taken for a packet of heated water to reach a thermistor (*Hess*, 1982); and electromagnetic flowmeters which output the voltage generated as water moves through a magnetic field (*Molz et al.*, 1994).

With the above mentioned methods, a flow log is obtained by continuously trolling a flowmeter down a borehole or by making stationary measurements at multiple depths. The use of traditional flowmeters can be time consuming where inversion methods used for aquifer characterization require many measurements in space, for example in multiple boreholes for flow tomography (*Klepikova et al.*, 2013), or space and time, for example for fracture zone storage coefficient estimation (*Paillet*, 1998). Furthermore, the physical presence of a flowmeter causes a resistance to flow in the borehole, potentially disturbing the fluid flow (*Ruud et al.*, 1999). We develop a new flow logging method based on DTS along fibre optic cables, a technology which gives spatially and temporally distributed measurements of temperature (*Selker et al.*, 2006; *Tyler et al.*, 2009). With DTS, temperature measurements along a fibre optic cable are derived from the return Stokes and anti-Stokes intensities; light at two predictable frequencies, backscattered from an initial laser pulse.

DTS can be deployed in an active mode, which we call Active-DTS (A-DTS). Here we define A-DTS as the distributed measurement of temperature along a fibre optic cable with a distributed heat source incorporated into or in contact with the same cable, where the temperature data collected whilst actively heating are of primary interest. These temperature data reflect the combined efficiency of heat dissipation from the cable and the surrounding medium, so that spatially distributed estimates of the surrounding physical properties or fluid fluxes are possible. Temperature sensing fibre optic cables are often ruggedised with steel armouring, allowing commonly available cables to be utilised for

A-DTS by passing an electrical current through the metal cable materials. Example applications already exist in soil moisture studies. In an unsaturated porous medium, heat conduction from the heated cable depends on the moisture dependent structure of soil water bridges between grains (*Sayde et al.*, 2010; *Striegl and Loheide*, 2012), such that with A-DTS a distributed soil moisture sensor can be created.

A-DTS methods potentially can provide measurements of fluid fluxes in boreholes. *Liu et al.* (2013) showed that the temperature of a fibre optic cable wrapped with a heating cable and deployed down hole is sensitive to horizontal groundwater flux through the surrounding porous medium. Here, we propose a method based on A-DTS for the monitoring of vertical fluid velocity in boreholes. The general principle is that in steady state heat flow conditions, the temperature difference between a heated fibre optic cable and adjacent unheated cable deployed down hole will be a function of the velocity of the fluid flowing parallel to the borehole axis. In this study we first present an analytical relationship between fluid flow velocity and this quantity, ΔT. Here we make the assumption that using a differential temperature accounts for any warming of the fluid due to the electrical heating or background fluid temperature differences caused by inflows to the borehole. We then present temperature data from a prototype A-DTS flowmeter deployed in a fractured rock aquifer, which we invert for the fluid velocity using the analytical result, conditioned in part from field data.

4.3 A simple analytical model of heat transfer through an A-DTS cable exposed to a flowing fluid

Prediction of the temperature measured on a heated fibre optic cable requires consideration of both the cable construction and environmental setting. For example, *Neilson et al.* (2010), quantified the undesirable temperature increase on the surface of fibre optic cables submerged in flowing rivers and heated by solar radiation. This analytic approach accounted for the fluid velocity dependent heat transfer coefficient at the cable-fluid interface. In the borehole setting considered here, we adopt a similar approach, except that the heat input occurs in the cable centre. We therefore also need to consider heat conduction through the cable materials if we are to reasonably predict the DTS measured temperature.

In our A-DTS flowmeter, we use a BRUsens cable (Brugg cables, Switzerland), which

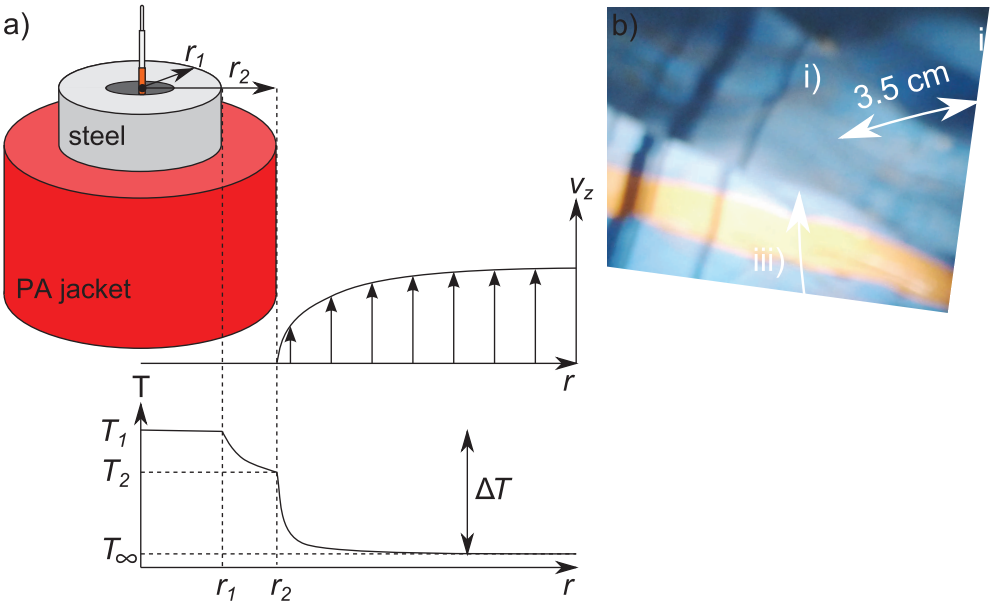

Figure 4.1: a) Schematic of the heated fibre optic cable with idealised fluid velocity and temperature profiles radially from the centre of the cable when the cable is electrically heated. b) Section of the A-DTS tool with i) centrally held heated fibre optic cable, ii) reference fibre optic cable, iii) power supply cable, and iv) steel rope

consists of a stainless steel capillary tube, surrounded by braided stainless steel, held in a polyamide (PA) cladding (Figure 4.1a). The cable itself is kept centralised in the borehole using a series of 2 m spaced cable ties. The optical fibres, along which the temperature is measured, are located centrally in the capillary tube of the cable. This general construction is typical of many armoured fibre optic cables manufactured for temperature sensing applications (*Tyler et al.*, 2009). Connecting the steel armouring to a power supply generates a constant amount of heat per unit length. In steady state heat flow conditions, this amount of heat is transferred from the steel to the cladding, and then across the interface between the cladding and fluid.

In the heat transfer model, we consider steady state heat conduction through the cylindrical shell prescribed by the electrically insulating cladding of thickness $r_2 - r_1$. We assume that the temperature gradient inside the steel is negligible, such that the temperature at the centre of the cable is equivalent to the temperature at the steel-PA interface, r_1. If the heat transfer across the PA-fluid interface obeys Newton's Law of Cooling, then the diffusion equation in the cylinder can be solved to give:

$$T_1 - T_\infty = \Delta T = \frac{Q}{2\pi}\left(\frac{1}{hr_2} + \frac{1}{k_c}\ln\frac{r_2}{r_1}\right) \tag{4.1}$$

where T_1 is the temperature at r_1, T_∞ is the temperature of the fluid beyond the thermal boundary layer, Q [W m^{-1}], is the heat input to the cable, h [W m^{-2} °C^{-1}], is the heat transfer coefficient, and k_c [W m^{-1} °C^{-1}], is the thermal conductivity of the material between r_1 and r_2. From inspection of equation (4.1), it can be seen that the value of ΔT can be increased by increasing Q, decreasing k_c, and decreasing r_1. The effect of increasing r_2 has two opposing effects; a greater surface area for heat exchange decreases ΔT, whilst the resulting higher thermal resistance thus increases ΔT.

The heat transfer coefficient is a function of the thermal conductivity of the fluid, the Nusselt number, and the characteristic length:

$$h = \frac{k_f}{L} Nu \tag{4.2}$$

where k_f is the thermal conductivity of the fluid, L [m], is the characteristic length (here, we use 0.11 m, the diameter of the borehole). At low flow velocities, heat transfer by free convection, driven by buoyant forces, becomes significant. Therefore, in the present case Nu is the Nusselt number for combined forced (Nu_F) and free (natural) convection (Nu_N). This combined Nusselt number is given by (*Incropera et al.*, 2007):

$$Nu = (Nu_F^n \pm Nu_N^n)^{\frac{1}{n}} \tag{4.3}$$

where n typically ranges from 3 to 4. For a vertically orientated surface, n is usually taken as 3. The plus or minus sign in equation (4.3) depends on whether the buoyant fluid motion assists or opposes the fluid flow, thus either enhancing or reducing the efficiency of heat transfer. In the following interpretation of the field trial we assume that all of the flow is upwards (as would be expected to be the case while pumping from the top of the borehole), allowing the addition form of this equation to be used. The Nusselt number approximation for forced convection due to fluid flow is based on laminar flow over a flat isothermal plate, and is given by (*Incropera et al.*, 2007):

$$Nu_F = 0.664 Re^{\frac{1}{2}} Pr^{\frac{1}{3}} \tag{4.4}$$

where Pr is the Prandtl number, and Re, the Reynolds number, is calculated for the characteristic length L. Many relationships exist for free convection Nusselt number

approximations over a range of geometries (e.g. *Churchill and Chu*, 1975). Due to the sensitivity of ΔT to the value of Nu_N, in the following, Nu_N is treated as an unknown and used to fit the model to observed ΔT values.

4.4 Field calibration of the A-DTS method

The field site at Stang-er-Brune, Brittany, France, was chosen to test the A-DTS method as a large amount of hydrogeophysical data for the site already exist (*De Dreuzy et al.*, 2006; *Bour et al.*, 2013). Four boreholes up to 100 m deep and shallower piezometers in close proximity are accessible in a fractured granite and mica schist. Previous field campaigns have identified the most transmissive fractures intersecting the boreholes and inter-borehole connectivity (*Le Borgne et al.*, 2007), and flow routes through the fracture network (*Dorn et al.*, 2012). Hydraulic heads at the site generally increase with depth and drive a mainly upwards vertical flow in the boreholes in ambient conditions. To test the prototype system, borehole B2 was used. This borehole is cased from the surface to 24.8 m and then open to a depth of 100 m. The cased section has a larger diameter (12.8 cm) than the open hole (10.4-10.9 cm). When pumped, flow to the borehole originates from fractures at depths of 27.9, 55.6, 58.9, 79.9, and 98.0 m (*Le Borgne et al.*, 2007).

4.4.1 Method

We constructed the prototype A-DTS flowmeter from a single 295 m length of BRUsens fibre optic cable. Of this, 78 m could be heated by connecting this electrically isolated section to a power supply. During the experiments, the heated cable was powered by 220 and 233 ACV, giving power intensities along the cable of 18.8 and 21.8 W m^{-1} respectively. An equal length of unheated cable, obtained by bending the cable back on itself after the latter electrical connection, was held at a uniform distance away of 3.5 cm using cable ties every 2 m (Figure 4.1b). From DTS temperature measurements along these two parallel lengths of heated and unheated cable, the heating effect ΔT can be obtained. A power supply cable and a steel cable to support the weight of the system were also fixed relative to the central heated cable using cable ties. These cable tie centralisers also helped to ensure that the heated cable remained away from the borehole wall. The flowmeter was then installed in B2 to monitor the borehole vertical flow at all depths

simultaneously.

For the DTS calibration, additional lengths of unheated cable at the surface were placed in ambient (water kept mixed with an air pump) and a cold calibration bath (water wetted ice in an insulated box). Because the tool was constructed from a single length of cable containing two fibres, spliced together at the far end, the resulting duplexed DTS data set contained four reference sections. In each bath a Tinytag logger (Gemini Data Loggers, UK), independently recorded the temperature. The Stokes and anti-Stokes backscatter intensities were obtained every 12.5 cm along the cable using a Silixa ULTIMA instrument with 5 km range. The instrument integrated the backscatter over times ranging from 1 to 10 s. The data were subsequently post-processed to derive the temperature using the Stokes and anti-Stokes intensities from three of the reference sections and the single-ended algorithm outlined in *Hausner et al.* (2011).

To test the response of the A-DTS system to a range of flow velocities, we pumped the borehole from a depth of around 10 m at rates ranging from 5.2 to 181 L min^{-1}, generating upflow throughout the borehole. The ΔT response and relationship to flow, as reported in the following, corresponds to a 2 m spatially averaged value between depths of 25.4 and 27.4 m. This section is in the open borehole above all known inflow zones and is referred to as the test section.

4.4.2 Results and discussion

To give an indication of the responsiveness of the A-DTS system, Figure 4.2 shows a spatially averaged time series of the heated cable and reference cable temperature over the test section. Upon heating, the A-DTS system responded very rapidly, with the heated cable increasing in temperature by almost 10°C. Within 15 s 90% of this temperature plateau was achieved. Over the time frame shown, the reference cable does not experience any warming, suggesting that it is located far enough away to be out of the thermal boundary layer.

The relationship between ΔT and the fluid velocity in the test section is shown in Figure 4.3. The ΔT values shown here are after further spatial filtering for reasons outlined in the following. Over a velocity range from 0.01 to 0.33 m s^{-1}, a 2.5°C range in ΔT is obtained. The analytical solution, optimised to Nu_N = 80 and 86 for the heating

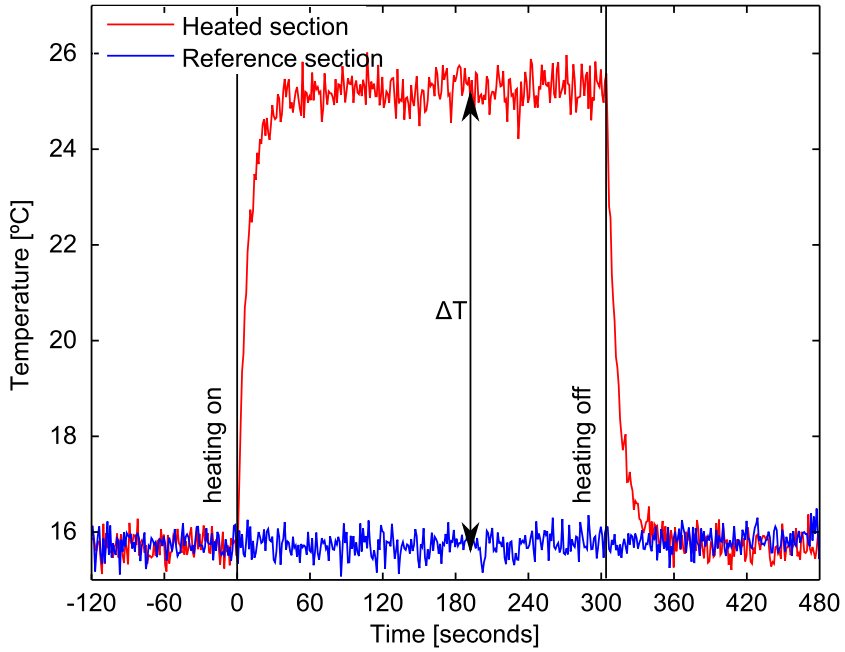

Figure 4.2: Spatially averaged temperature on the heated and reference cable over the test section (25.4 to 27.4 m), while pumping at 14.7 L min^{-1}

rates of 18.8 and 21.8 W m^{-1} respectively, suggests a diminishing sensitivity to fluid velocity towards low and high flow extremes. The lower limit to the sensitivity occurs as heat transfer to the fluid by free convection begins to dominate over forced convection. The upper limit to the flow sensitivity is the result of the thermal boundary layer reducing to a minimum. The A-DTS system as deployed here in this configuration, seems to be most suited to measuring mid-range velocities that typically would be measured with an electromagnetic or impeller flowmeter.

A 5 min average of the entire heated section and reference section temperature while pumping at 180 L min^{-1} are shown in Figure 4.4a. The temperature profile measured on the reference section is the result of previous heating tests, so does not reflect the undisturbed temperature-depth profile of the borehole. On the heated cable, the effect of the 2 m spaced centralisers is to locally reduce the temperature. We hypothesise that this is due to the development of more energetic turbulent flow as the water moves through the centraliser structure, enhancing the heat exchange between fluid and cable. For the borehole geometry and velocities we have here, the Reynolds number is up to 6x10^3, thus turbulence may be readily stimulated downstream of any obstructions. We do not account for this in the analytical model, and a full analysis of this would need a simulation of the applicable equations for turbulent flow within the flow geometry here. For the ΔT-flow

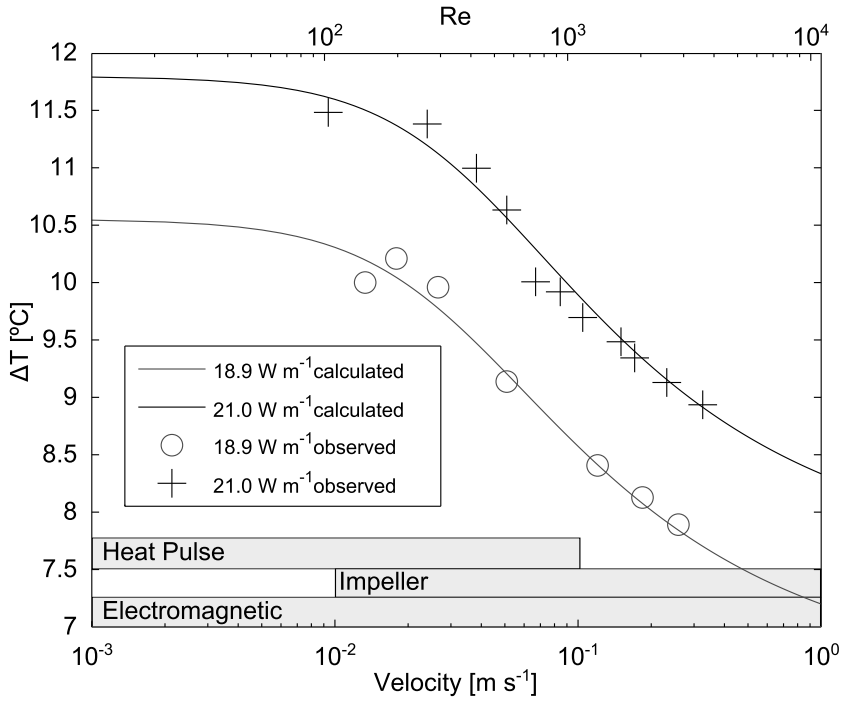

Figure 4.3: Observed ΔT based on the filtered data and computed ΔT relationship with fluid velocity for power inputs of 18.9 and 21.0 W m^{-1}, with typical sensitivity ranges of heat pulse, impeller, and electromagnetic flowmeters

Table 4.1: Physical and thermal properties of water and the BRUsens fibre optic cable used in the analytical solution

	BRUsens Cable	Water	Units
Diameter of Steel Core	0.00226		m
Cable Diameter	0.00385		m
Thermal Conductivity	0.245	0.598	W m^{-1} $°C^{-1}$
Density	2.41	1.00	g cm^{-3}
Dynamic Viscosity		1.00E-03	N s m^{-2}
Kinematic Viscosity		1.00E-06	m^2 s^{-1}

calibration, the temperature data from the heated cable were first filtered to remove these artefacts introduced by the centralisers so that the analytical solution could be used with realistic parameters (bold line in Figure 4.4a). The cold spots in the heated cable profile were removed by applying a moving median filter to select the upper 25% of temperature data within a 2 m window. We assume that this results in heated cable temperatures that are unaffected by the centralisers, therefore the ΔT-flow calibration can only be expected to provide reasonable velocity estimates either for the filtered data, or the unfiltered data away from the centralisers. It should however be noted that the removal of these artefacts is not essential as the flowmeter could be entirely empirically calibrated. The reference cable data were also processed but with a simple 2 m moving average.

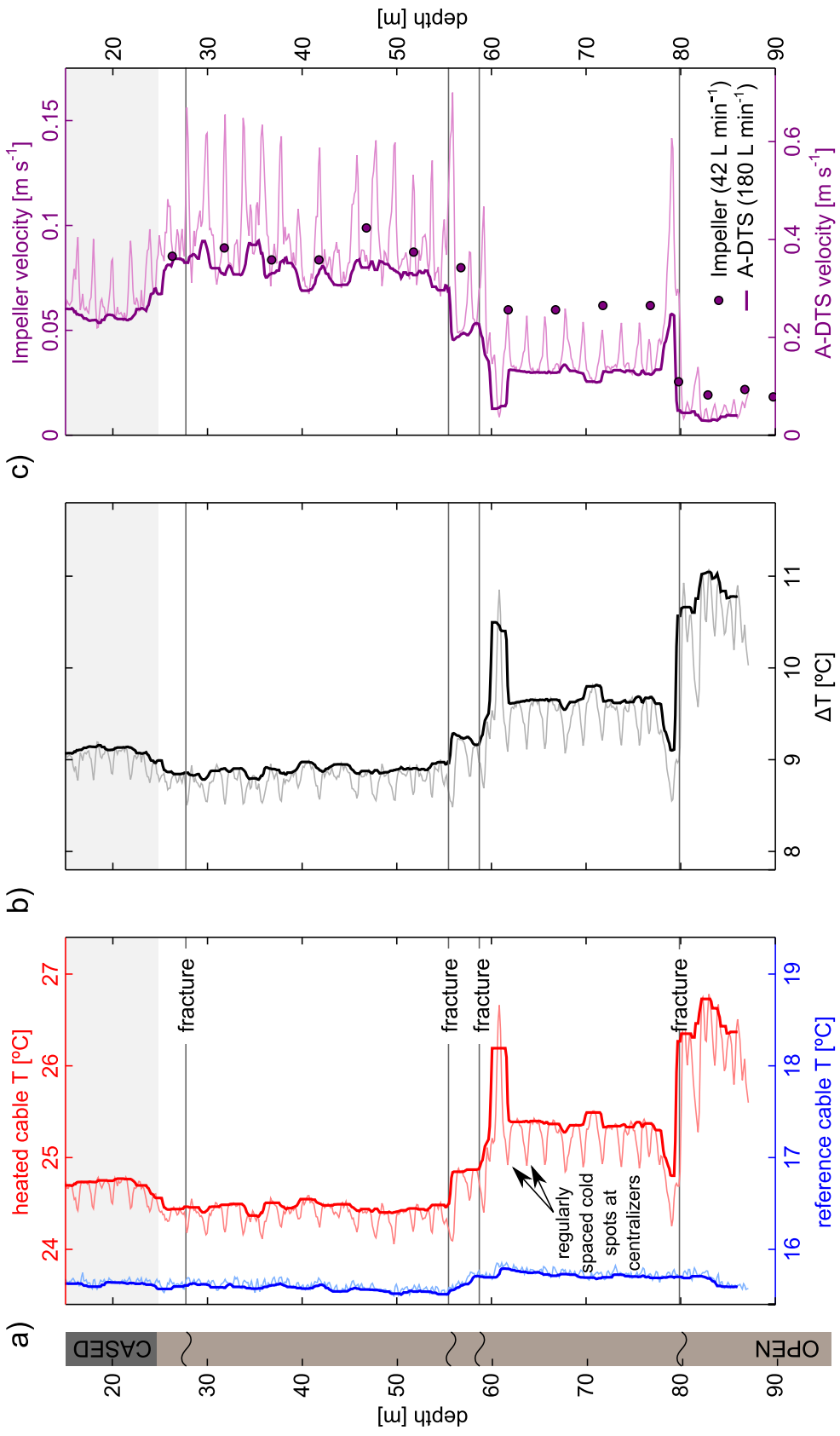

Figure 4.4: a) Reference cable and heated cable temperatures while pumping from 7 m depth at 180 L min^{-1} (pale lines are temporally averaged, bold lines temporally averaged with additional spatial filtering). b) Corresponding ΔT profile (the light line is the difference between the purely temporally averaged data, and the bold line is the difference between the combined time averaged and spatially filtered profiles). c) Calculated velocity profile from ΔT and equations (4.1)-(4.4), with measurements of the flow velocity made using an impeller flowmeter while pumping at 42 L min^{-1} in July 2012 for comparison

The velocity profile for a pumping rate of 180 L min^{-1}, calculated from ΔT (Figure 4.4b), using equations (4.1)-(4.4) and the parameters in Table 4.1 is shown in Figure 4.4c. In addition, flow velocities measured with an impeller flowmeter [H+ Network, www.hplus.ore.fr], are also plotted. These data were obtained at a lower pumping rate of 42 L min^{-1} in July 2012. Despite this, the velocity profile should at least provide a qualitative comparison, since due to variations in the hydraulic conditions of each fracture, it cannot be expected to be entirely constant through time or scale exactly with the pumping rate (*Paillet*, 1998). The profile of ΔT measured with the A-DTS flowmeter is clearly anti-correlated with the impeller measured fluid velocity, with the resulting flow log showing similar step changes in velocity arising from discrete fracture zone inflows.

Additionally, there are both some anomalously high and low values of ΔT that translate into anomalously low and high velocities respectively, that cannot easily be explained just by considering vertical flow up the borehole. The high value of ΔT centred at around 60 m was present at all pumping rates and is thought to be due to the heated cable touching the borehole wall. This is likely to be an issue in most deployments of the system where there is any deviation in the borehole but is something we envisage can be minimised with alternative designs. The low value of ΔT at around 79 m appears to correspond to the fracture at this depth. Inflowing fractures generate non axial velocity components and even turbulence, that could locally increase heat dissipation from the heated cable. However, it may be difficult to quantitatively relate this ΔT value to fracture zone inflows due to the complexity of such regions and limited spatial resolution of standard DTS installations. Similar problems at discrete inflow zones are nevertheless also encountered with other flow logging methods.

A key issue in the future design of A-DTS flowmeters is the centralizing mechanism. Where the cable touches the borehole wall, as would commonly happen in boreholes with any deviation, we have seen that this causes major temperature artefacts. The centralisers used in this study were designed to minimise this but they too give temperature artefacts of their own, which in this set up were readily identified due to their regular spacing. This effectively limited the spatial resolution of the flowmeter to detect changes in the fluid velocity to around 2 m, which is significantly poorer than the spatial resolution possible with the DTS deployed (0.29m). A further unexpected outcome was that at the centraliser

locations, ΔT had an enhanced sensitivity to flow at low velocities (see Supporting Material). This raises the possibility that future designs could include a denser centralizing system that uniformly disturbs the flow, and is optimised to provide maximum sensitivity over a given velocity range. This would give a spatial resolution for fluid flow logging similar to the spatial resolution of the DTS instrument. Whilst it would be more difficult to forward model the temperature response of the A-DTS flowmeter, one could readily build up an empirical calibration between ΔT and flow velocity in the field as we also did here.

Additional work needs to be carried out to assess the significance of the flow direction on the ΔT response. Equation (4.3) suggests that at least at low flow velocities, two different ΔT responses may result depending on whether the fluid flow is acting in the same direction or opposing buoyancy driven flow. This need not be a prohibitive issue as the flow direction can be found from the gradient of the change in reference cable temperature relative to pre-heating. While Figure 4.2 shows that over a short time scale the warming of the fluid is negligible, after carrying out multiple simultaneous heating experiments, we observed that the reference cable temperature had increased. A similar effect can be seen in the recent work of *Banks et al.* (2014), where in the example from the Willunga field site the sign of the gradient of the fluid temperature profiles indicates that the flow direction is upwards to the pump. This effect is apparent because the water just before it reaches the pump has a longer mean residence time and has therefore experienced more heating than water which has only just entered the borehole. So using the method proposed here, if in fact two ΔT-flow calibrations exist, then the appropriate calibration for flow can be chosen. This is something that we did not fully explore in this set of field experiments, but could be tested on a smaller scale with a laboratory set-up.

4.5 Conclusions

We have shown that the hybrid cable method, deploying DTS in active mode, is a feasible approach for monitoring spatially and temporally changing borehole vertical flows. The difference in temperature between an electrically heated fibre optic cable and a passive, non-heated reference cable can be related to vertical fluid velocities. With fibre optic cables of small thermal inertia, as used here, the thermal time constant of the cable is likely

to be much smaller than the time constant of the borehole when hydraulically stressed. Therefore, the hybrid cable method is likely to find applications where it is necessary to monitor temporal changes in fluid flow. The general advantages of using DTS that have been found in other disciplines similarly apply here for fluid flow measurements with A-DTS. With an A-DTS flowmeter constructed from a single fibre optic cable, full spatio-temporal coverage of flow measurements could be achieved simultaneously in multiple boreholes at a site. While we have shown here that in general the method shows great promise for fluid flow logging, future work is needed to address the issues related to field deployment, and to determine how to optimise the sensitivity for the desired application.

Chapter 5

Optimisation of the hybrid cable method for measuring fluid flow

5.1 Chapter summary

The hybrid cable method, where a cable is heated while DTS temperature measurements are made along an optical fibre in the same cable, has been shown in Chapter 4 to be sensitive to fluid flow. The objectives of this chapter are to further understand the heat-transfer physics of this process and how the response can be improved. The chapter describes a laboratory set-up and cable scale numerical model. In the laboratory set-up, a short section of heated cable was installed in a recirculating flume to test the hybrid cable method sensitivity to flow with varying electrical power input and flow-cable contact angle. Results showed that the ΔT value and sensitivity approximately scale linearly with electrical power input. The ΔT value was to a lesser extent also sensitive to flow angle, with greater contact angles reducing the value of ΔT and also reducing the sensitivity to flow. A cross section model of the cable, incorporating fluid flow and heat transfer in the cable and fluid, was then developed. The model allowed the impact of more parameters, including cable design, to be evaluated. Model results corroborated with the laboratory data in that electrical power input was found to be the most crucial parameter for enhancing flow sensitivity. Cable design, including material layer thickness and thermal properties affected the value of ΔT but did not significantly change the sensitivity to flow. A ridged cable design was then simulated which suggested that further enhancements to the sensitivity

may be possible if the cable is more readily able to retain a flow and thermal boundary layer.

5.2 Introduction

The hybrid cable method has been shown by *Read et al.* (2014) to be sensitive to vertical flow velocity in wells. The method combines DTS temperature measurements along an optical fibre and electrical heating of conductive elements in the same cable construction. The principle is that electrical heating generates a thermal boundary layer around the cable. The extent of this thermal boundary layer and therefore the DTS measured temperature inside the cable depends on the velocity of the fluid that removes the thermal boundary layer by forced convection. While the method was in this case deployed in a borehole, it could potentially be used to measure water flows in other settings such as rivers or lakes. This basic principle has already been exploited for the estimation of wind speeds (*Sayde et al.*, 2013, 2015), and seepage monitoring through saturated porous media in the context of earth embankments (*Aufleger et al.*, 2007).

In the field deployment of *Read et al.* (2014), the hybrid cable response was assessed for one cable design and a narrow range of electrical power inputs (19 and 21 W m^{-1}). The objective of this chapter is to address this by determining the hybrid cable method sensitivity to electrical power, angle of attack, and cable design, through a laboratory experiment and numerical model, to gain process understanding and investigate means of enhancing the flow sensitivity.

5.3 Laboratory study of the hybrid cable method in a flowing fluid

5.3.1 Method

The 10 m long, 1 m wide, Armfield recirculating flume at the University of East Anglia was used for the laboratory experiments. The flume was chosen as it provides a sufficiently long channel for flow, and the volumetric flow rate can be controlled through two variable rate pumps. Although the system is essentially rotated 90° relative to vertical flow in a well, it is considered to be suitable to test fundamental aspects of the hybrid

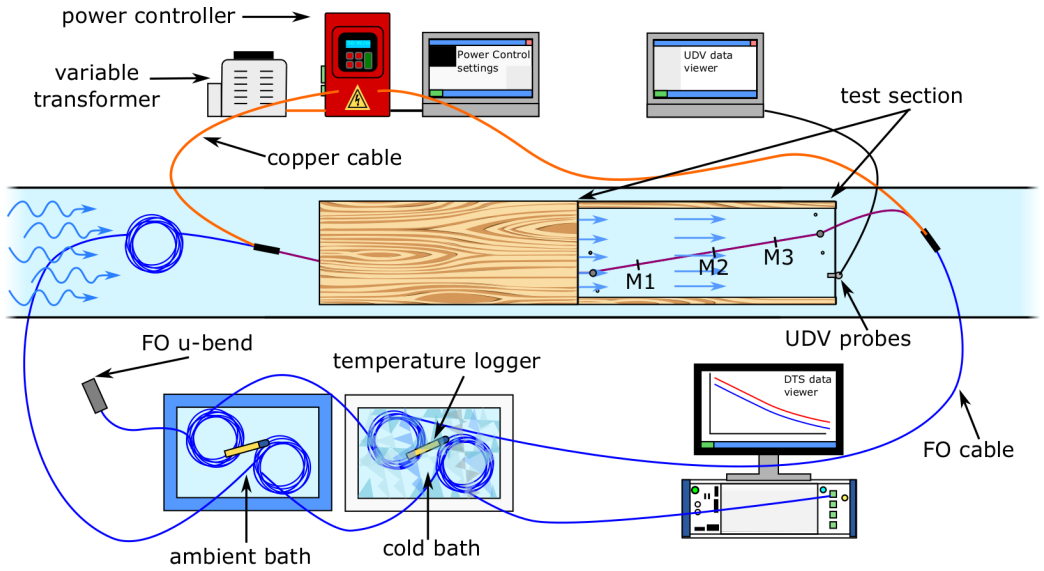

Figure 5.1: Schematic plan view of the laboratory set-up showing heating system, location of UDV probes, and path of the fibre optic cable. M1, M2, and M3 are specific locations on the fibre optic cable referred to in the chapter

cable method in a controlled way. The effect of buoyancy induced free convection and related heat transfer, which may be an issue when considering deployments in different orientations, is assessed in section 5.4.2 and is found to be insignificant over the velocity range tested in the lab.

To create as idealised measurement conditions as possible, a system was designed to hold the cable under tension and independently monitor fluid velocities while causing minimal disturbance to the flow. Two boxes were constructed in the flume (Figure 5.1). These were open at each end and could be joined together, so that a proportion of the flow in the flume would be channelled through. The first box, constructed of wood, was included to provide a long enough entrance section so as to minimise flow entrance effects in the second section. The second box was constructed with a perspex top so that the cable could be seen inside. The perspex top had fixing points drilled in two arcs to allow the cable angle relative to the flow to be varied, without changing the length of cable between the fixing rods.

A BRUsteel fibre optic cable was passed through the two sections and the anchoring locations on the cable fixed for all experiments. The fixing system, using two rods, is shown in Figure 5.2. The fixing rods were required to hold the cable under tension. While designed to minimise disturbance to the flow, later results show they had an observable effect. This length of cable between the fixing rods is referred to as the test section. A

coiled section of cable was made upstream of the boxes to allow the background water temperature to be monitored, and was used for the calculation of ΔT along the test section. Additional coils of cable were placed in ambient water and ice-water slush baths for the temperature calibration. Coils were placed in each bath for cable before and after the flume to provide 4 potential reference sections. Temperature in the ambient and cold baths was independently logged every 10 s with a precision $> \pm 0.002$ °C using RBR Solo loggers (RBR Ltd, Ontario, Canada). Temperature measurements along the cable were made with a Silixa ULTIMA (Silixa Ltd, Elstree, UK) instrument every 0.12 m, with a time average of either 1 or 30 seconds (with corresponding temperature standard deviations of 0.5 and 0.1 °C respectively. The cable and instrument were configured for duplexed single ended monitoring, with the data post-processed using the 3-section calibration method (Equation 1.2). In the following, results are shown from all 16 DTS measurement points within the test section, as well as at three specific locations (M1, M2, and M3), shown in Figure 5.1.

Sealed electrical connections, separated by 10 m, were made to the steel core of the BRUsteel cable to heat this section. These were connected to a Control Concepts Compact FUSION Single Phase Power Controller (Control Concepts, Minnesota, USA). This allowed the total electrical power supplied to the cable to be set and regulated during the experiments. This was found to vary no more than $\pm$ 0.3%.

At the outflow end of the test section, an array of Ultrasonic Doppler Velocimeters (UDVs) was positioned. The array consisted of 8 probes spaced vertically by 20 mm that allowed profiles, cross sections, and temporal monitoring of velocity to be made during hybrid cable experiments. Each probe measured the velocity within the region 27.4 to 90.3 mm in front of the tip of the probe. During the monitoring of the hybrid cable experiments when a single probe was used, velocity measurements were made at 100 Hz, with measurements from 80 channels within the measurement interval averaged to give a single value of velocity. In order to assess the velocity distribution through the test section, the UDV probes were sequentially moved across the outlet (Figure 5.3). At a flume recirculation rate of 55 L s^{-1}, the velocity through the centre of the box is around 22 cm s^{-1}. Towards the base of the flume there is a frictional edge effect, which is also present but thinner on the upper acrylic. A flow boundary layer is also observed at the sides of

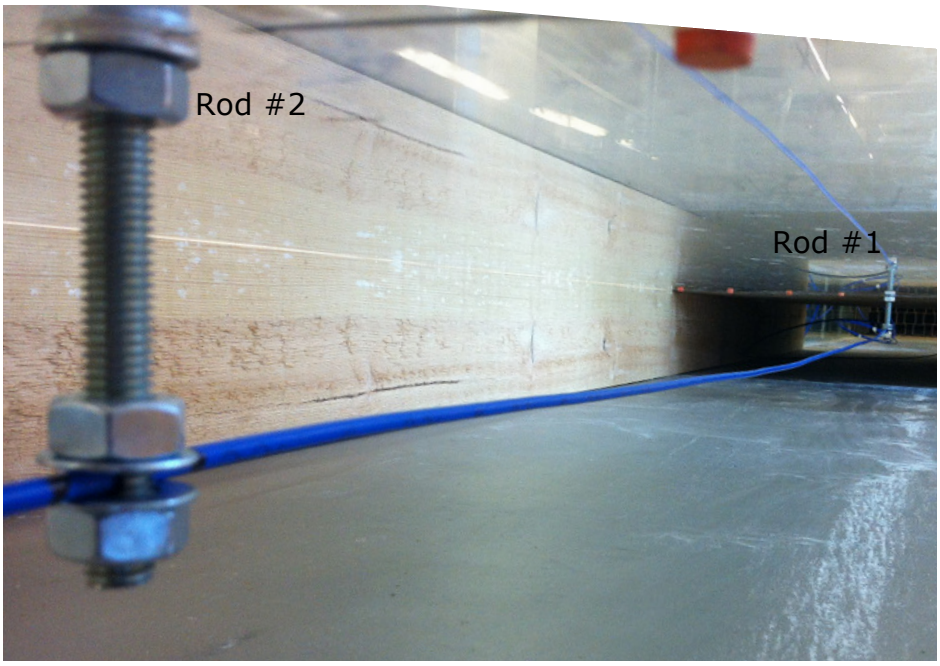

Figure 5.2: Fixing rods through which the fibre optic cable was held at fixed height and under tension

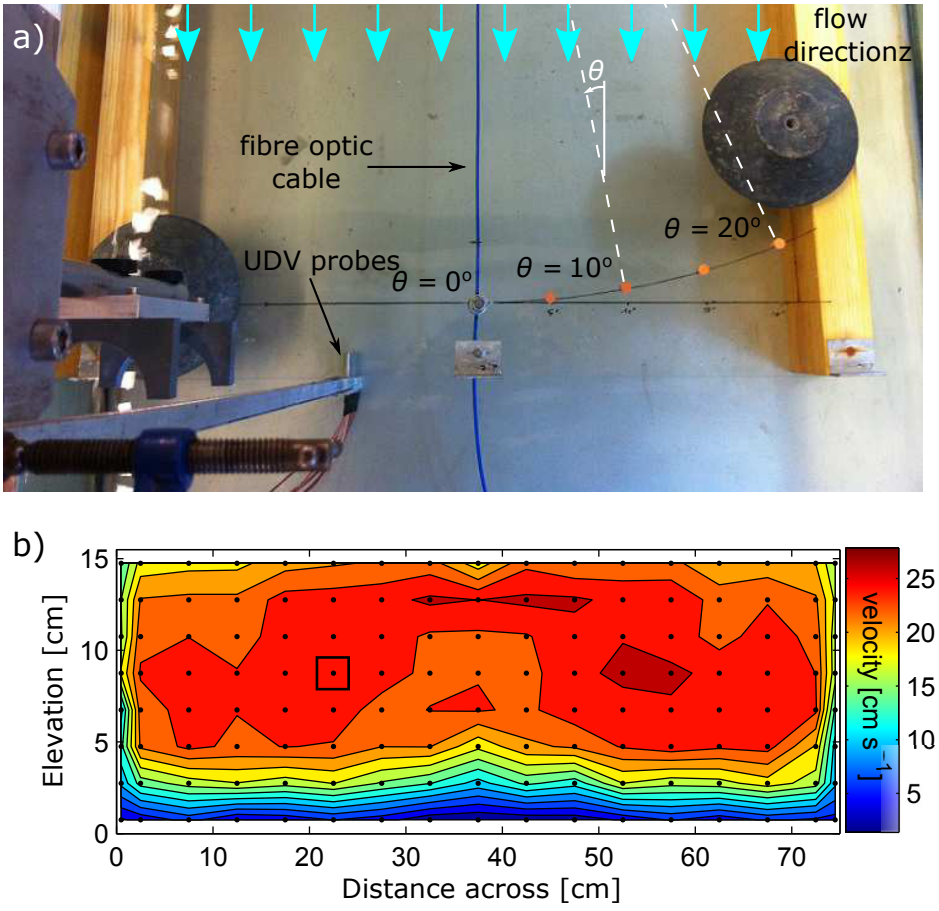

Figure 5.3: a) Plan view of the test section in the flume. b) Velocity distribution at the end of the test section measured with the array of UDV probes during a recirculation rate of 55.5 L s^{-1}. Black dots indicate UDV measurement locations, and the black dot surrounded by a square showing the UDV probe position used for comparison with the DTS response.

the box, and this is again limited to a < 5 cm zone. The central region therefore is used to test the hybrid cable method, where errors due to slight changes in deployment heights between different experiments are least likely to impact on the velocity, and, particularly when the cable is deployed at an angle, lateral variations in velocity are minimal.

To test the hybrid cable response, the cable was tested under different flow velocities, power inputs (P), and cable angles (θ). The angle was set using the cable fixings on the box and the electrical power set using the power controller. The cable was fixed at a height 8.5 cm above the base of the flume to allow direct comparison with the UDV probe at the same elevation. The velocity was then incrementally changed by adjusting the recirculation rate of the flume over the course of around 30 minutes. This allowed velocities in the range of approximately 8 - 60 cm s^{-1} to be tested. During this time, DTS measurements were obtained along the cable every 30 s. This was then repeated for cable angles of 0, 10, and 20° , and electrical power inputs of 10, 20, and 50 W m^{-1}. Following this, tests were carried out where the velocity was more rapidly varied over time to test the temporal response of the hybrid cable method.

5.3.2 Results

To test the experiment set-up, an experiment was initially run at a constant pumping rate (θ = 0° , P = 50 W m^{-1}). Figure 5.4 shows the UDV measured velocity, electrical power input, and temperature during this experiment. The UDV measured velocity, despite a constant pumping rate, is not constant and includes some time variability ($\bar{v}$ = 2.56 cm s^{-1}, σ_v = 0.13 cm s^{-1}). This is likely related to variable discharge from the recirculating pump. The electrical power input, set at 50 W m^{-1}, remains constant throughout the test ($\bar{P}$ = 50.0 W m^{-1}) with a standard deviation of 0.019 W m^{-1}. The time series of DTS measured temperature (shown as ΔT, the difference between the temperature at a given location on the heated section of cable and the background water temperature), shows that ΔT also remains constant over time (e.g. at M1, $\bar{\Delta T}$ = 22.56 °C, $\sigma_{\Delta T}$ = 0.12 °C). Plotting ΔT at the three locations M1, M2, and M3 shows that ΔT varies with distance along the test section. ΔT at M2 is consistently higher than at M1, while ΔT at M3 is consistently higher than at M2. This pattern of behaviour, with an increasing ΔT in the downstream direction of flow obstructions, is consistent with *Read et al.* (2014), where

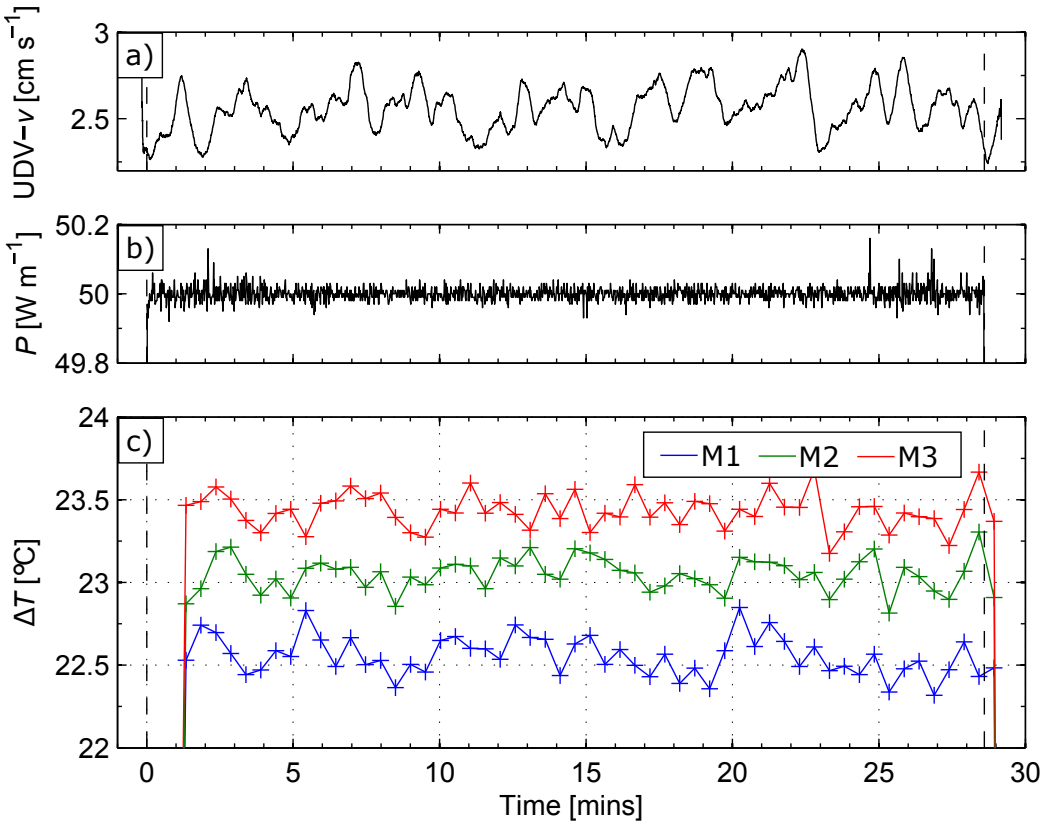

Figure 5.4: Constant flow test with the hybrid cable, showing a) UDV measured velocity, b) electrical power input, and c) DTS measured ΔT at locations M1, M2 and M3

cable centralisers appeared as cold anomalies in ΔT. There is also the potential, in the parallel flow case, for heat accumulation in the thermal boundary layer flow along the cable, increasing the observed ΔT with travel distance.

The extent to which ΔT varies along the test interval is shown in Figure 5.5, with ΔT shown for all cable angles and power inputs tested. These profiles are the average of the first four 30 second measurements in time (equivalent to a 2 minute DTS time averaged measurement) during the cable calibration experiments. In each case, the pumping rate was left at the minimum and velocity therefore approximately constant during this time. Downstream of Rod 1, ΔT gradually increases. This is most clearly visible in Figure 5.5c, and is most pronounced for flow parallel to the cable. This increasing trend in ΔT appears to occur in two stages; an initial more rapid rise over the first 0.5 m, followed by a linear increase until Rod 2. The relatively low ΔTat the location of the anchoring point and initial rapid increase may be due to flow around the rod, causing small vortices and components of flow normal to the cable that enhance heat transfer. The then more gradual increase in ΔT along the remainder of the test section may be due to the accumulation of

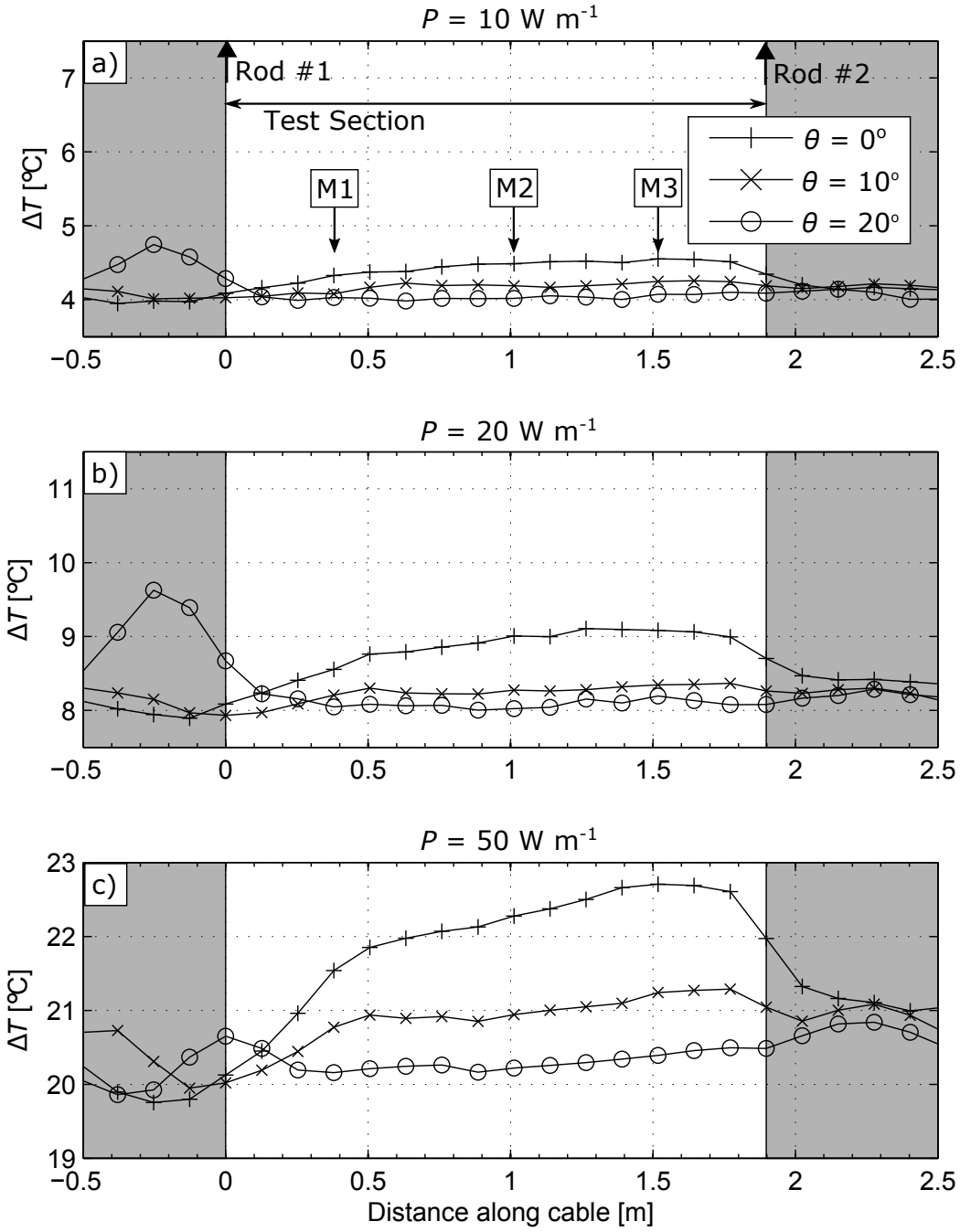

Figure 5.5: DTS measured ΔT along the cable passing through the test section at a) 10 W m^{-1}, b) 20 W m^{-1}, and c) 50 W m^{-1}. Profiles within each sub-plot are for different cable angles (0, 10, and 20°).

heat in the thermal boundary layer along the cable.

The temporal cable response was investigated during a step change in velocity for parallel flow, and flow at 10° and 20° (5.6). The exact velocity change was not the same between experiments but allows the timings of the cable response to be compared. In all three experiments, the pumping rate was rapidly lowered to bring about an abrupt velocity

change. The ΔT response at the three cable locations is shown in Figures 5.6d, e, and f. In all cases, the UDV response time t_{r-UDV} to the step decrease in pumping rate is between 35 and 48 s. With flow parallel to the cable, it takes between 111 and 170 s for ΔT to plateau, with the temperature equilibration occurring earlier at M1 than M3. For the 10 and 20° angle experiment, the ΔT response times are more rapid than with parallel flow, with t_{r-M3} of 77 and 54 seconds for flow at 10 and 20° respectively. This time for equilibration is similar to the 60 second equilibration time that was observed by *Read et al.* (2014). The increased response time for flow parallel to the cable, coupled with the increase in response time from M1 to M3, suggests that the increase in ΔT with distance along the test section can at least be partly explained by longitudinal warming of the water in the vicinity of the cable.

Nine experiment runs were then carried out to test three different electrical power inputs (P = 10, 20, and 50 W m^{-1}) and three different cable angles (θ = 0, 10, and 20°) (Figure 5.7). During these empirical calibration runs, the flume recirculation rate was manually changed, initially from the minimum, up to around 130 L s^{-1}, producing a range of velocities typically between 8 and 60 cm^{-1}. In general, the pumping rate increased monotonically, giving a decrease in ΔT over time. With this gradual increase in pumping rate and fluid velocity, it is assumed that the cable is approximately in thermal equilibrium at all times.

The UDV measured velocities were interpolated at the DTS measurement time, and ΔT plotted against this in Figure 5.8 for each of the angle-power input combinations tested. An empirical relationship was established by fitting a second order polynomial through the data points for locations M1, M2, and M3 on the cable. Firstly, the maximum and minimum observed temperatures appear to scale according to input electrical power. Table 5.1 shows these values extracted from the data. For instance, at 0°, the maximum ΔT is 4.60, 9.20, and 22.83 °C at 10, 20 and 50 W m^{-1}. The maximum ΔT at 20 W m^{-1} and 50 W m^{-1} is therefore 2.00 and 4.96 times the maximum ΔT at 10 W m^{-1} respectively. This scaling behaviour holds for the minimum ΔT and for the cable angles of 10° and 20°. With an increasing angle between the cable and flow, the maximum value of ΔT decreases. For instance, for a power input of 10 W m^{-1}, the maximum value of ΔT decreases from 4.60, to 4.35, to 4.18 °C for angles of 00, 10, and 20° respectively.

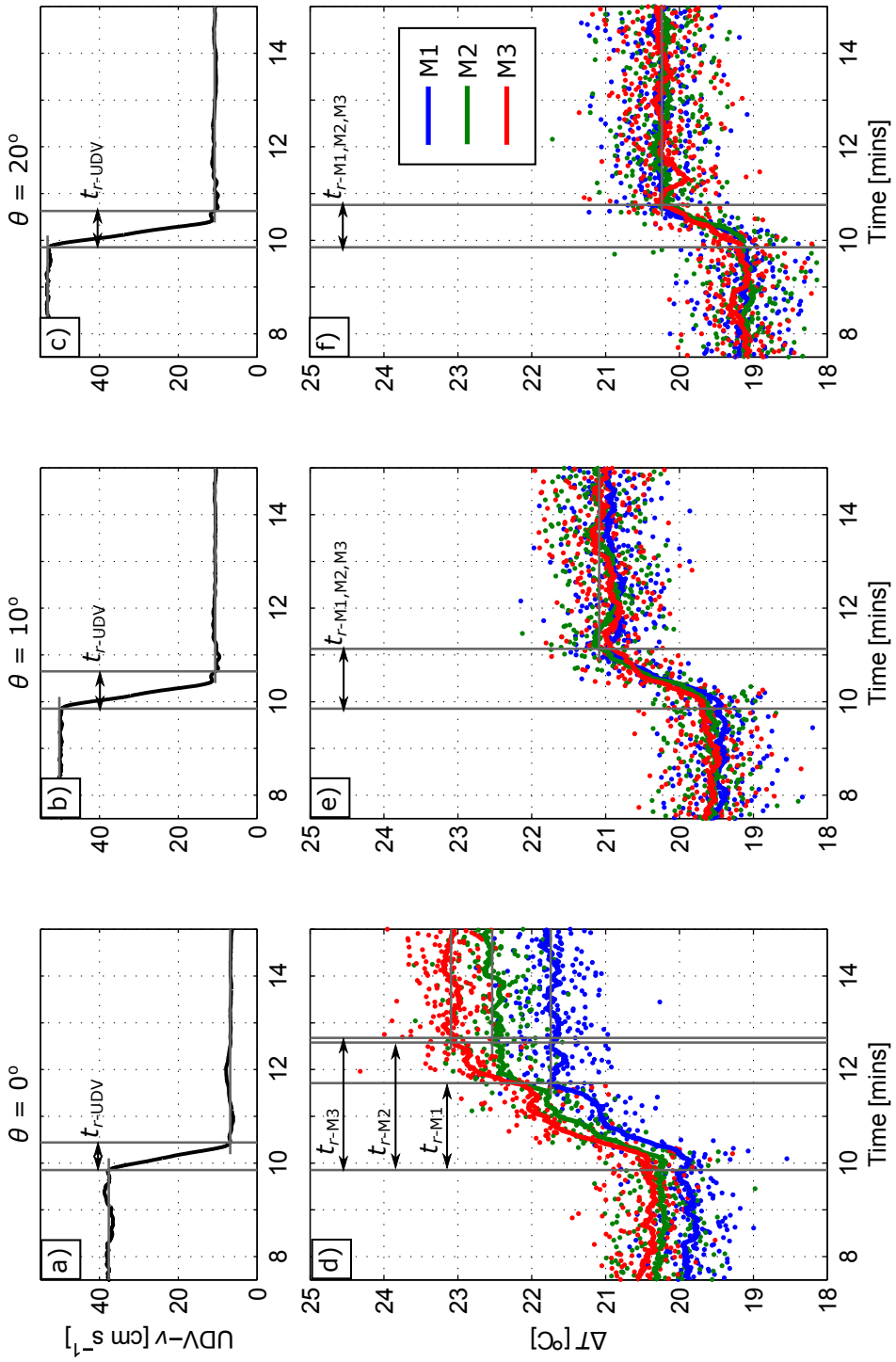

Figure 5.6: Experiment runs with a step change in velocity showing UDV velocity (a, b, c), and ΔT (d, e, f) at M1, M2, and M3 for θ of 0 , 10, and 20° .

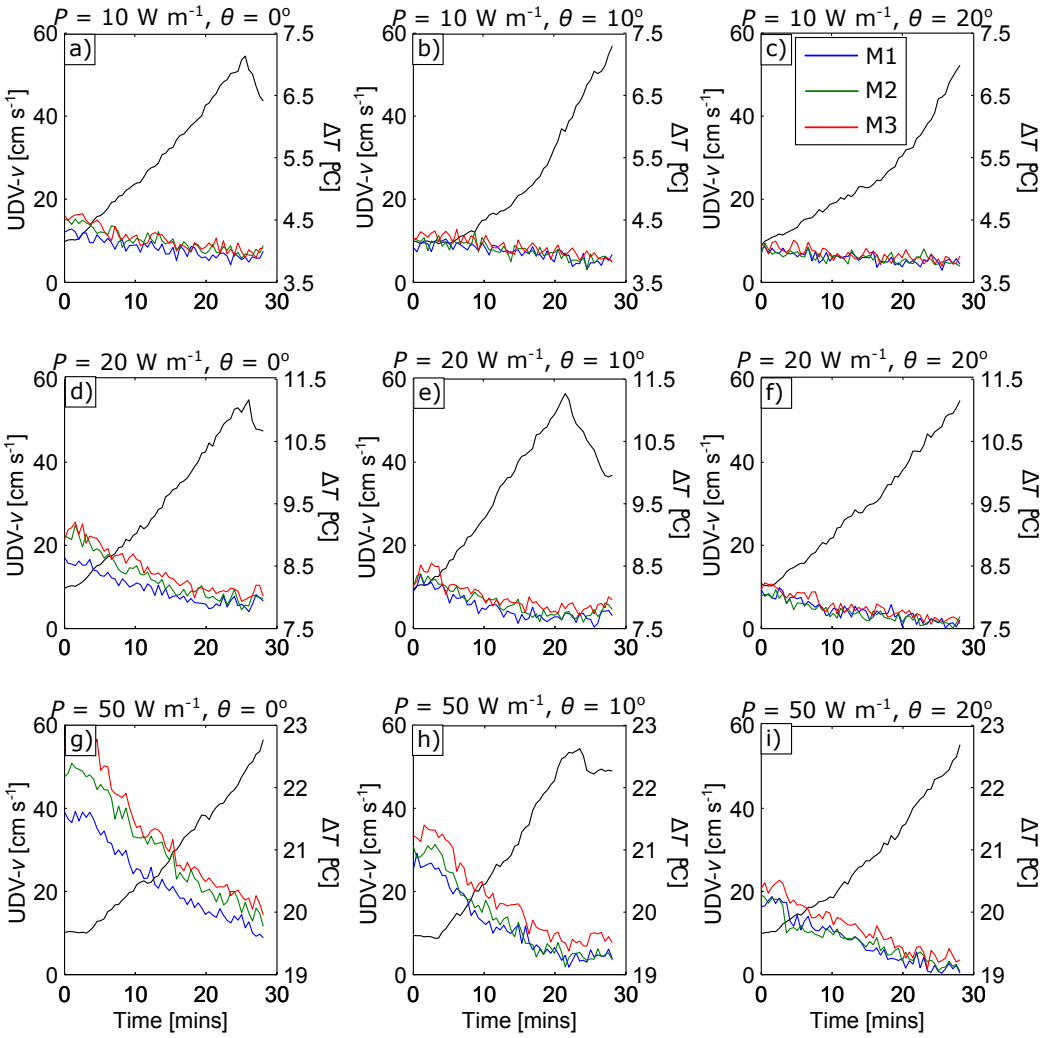

Figure 5.7: UDV measured velocity and ΔT during empirical calibration of the cable response for varying cable angles (0, 10, and 20° from left to right), and electrical power inputs (10, 20 and 30 W m^{-1} from top to bottom). ΔT values are shown for locations M1, M2, and M3.

This decline is also present and is scaled accordingly for higher power inputs. The decline in minimum value of ΔT with increasing cable angle is less severe, decreasing from 3.78 to 3.71 and 3.69 for angles of 0, 10, and 20° respectively. The range in ΔT, and therefore sensitivity to flow, is greatest for parallel flow, and decreases with increasing cable angle. Plotting the ΔT-v relationship at three positions on the cable highlights that it is location dependant. This is most pronounced when flow is parallel to the cable (Figure 5.8a, d, and g). The ΔT-v relationship becomes increasingly independent of position as the cable angle increases (Figure 5.8c, f, and i). This is likely to be for the reasons discussed previously, that the parallel flow data are subject to longitudinal heat transport, and the flow is likely to be impacted by the wake of the anchoring system giving non-uniform velocity along the cable length.

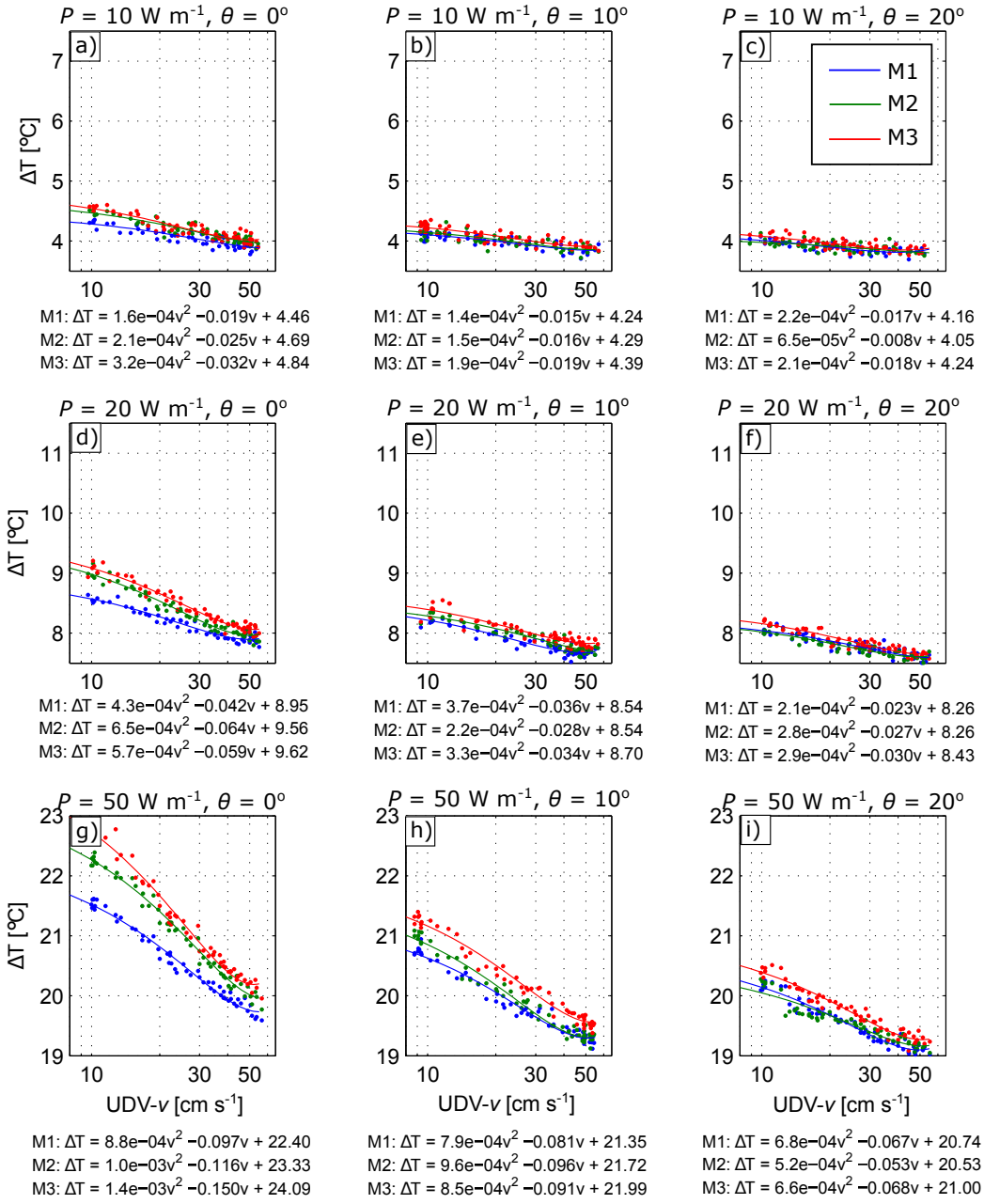

Figure 5.8: ΔT relationship with velocity for varying cable angles (0, 10, and 20° from left to right), and electrical power inputs (10, 20 and 50 W m^{-1} from top to bottom), given for each position M1, M2, and M3. The equation of the 2nd order polynomial best fit is given for each of M1, M2, and M3

Table 5.1: Maximum, minimum, and range of ΔT values observed in each of the angle and power input combinations tested

		θ = 0°	θ = 10°	θ = 20°
P = 10 W m^{-1}	max(ΔT) [°C]	4.6	4.35	4.18
	min(ΔT) [°C]	3.78	3.71	3.69
	range(ΔT) [°C]	0.82	0.64	0.49
P = 20 W m^{-1}	max(ΔT) [°C]	9.2	8.55	8.23
	min(ΔT) [°C]	7.77	7.52	7.51
	range(ΔT) [°C]	1.43	1.03	0.72
P = 50 W m^{-1}	max(ΔT) [°C]	22.83	21.4	20.51
	min(ΔT) [°C]	19.59	19.12	19.02
	range(ΔT) [°C]	3.24	2.28	1.49

To test the empirical calibration and the ability of the hybrid cable method to track a time varying velocity, an experiment was conducted where the pumping rate was varied, often abruptly, over a period of 50 minutes to give a time varying response, parts of which might be observed when deploying the hybrid cable to monitor flows in abstraction or observation boreholes during hydraulic tests. Figure 5.9 shows the hybrid cable estimated velocity when heating at 50 W m^{-1} and an angle of 20°, with the UDV measured velocity for comparison. These are given for time averages of 1, 10, and 30 s, which correspond to DTS temperature precisions of 0.43, 0.12, and 0.05 °C respectively. When time averaging for 1 s, the hybrid cable velocity measurement suffers high noise (r^2 = 0.28). Increasing the time averaging to 10 s significantly reduces the measurement noise and the hybrid cable estimated velocity closely reproduces the UDV velocity (r^2 = 0.78). Increasing the time averaging further, to 30 seconds, improves the hybrid cable velocity estimates during periods of relatively constant flow (r^2 = 0.87). However, the time averaging of the DTS temperature measurement begins to smooth the data such that relatively fast changing velocities are either underestimated when transitioning to a high velocity, or overestimated when changing to a low velocity. Also apparent, particularly in Figures 5.9b, d, and f, is an increasing range in hybrid cable estimated velocities at high UDV measured velocities.

The precision of hybrid cable estimate velocities is highly dependent on DTS temperature measurement precision, that for a given instrument, increases with the square root of spatial and time averaging intervals (*Tyler et al.*, 2009). Using the empirically derived relations between ΔT and velocity, the impact of DTS temperature uncertainty on hybrid cable estimated velocities can be assessed. For the relationship $v = f(\Delta T)$,

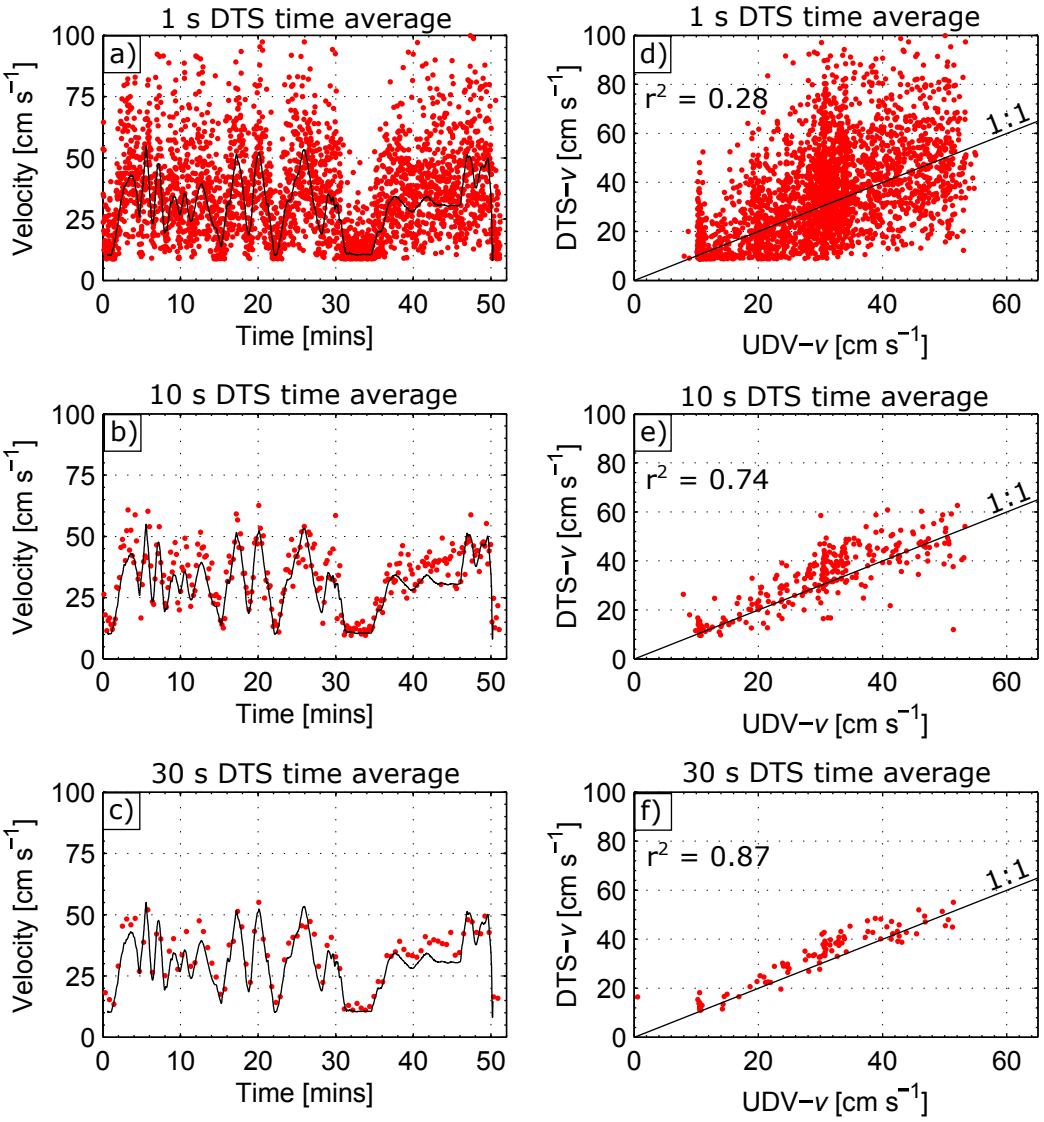

Figure 5.9: Time series of UDV measured velocity and hybrid cable estimated velocity for DTS time averaging of 1, 10, and 30 s (a, b, c respectively), with a comparison of the response (d, e, f). The experiment was run with an electrical power input of 50 W m^{-1} and angle of 20° .

the uncertainty in estimated velocity is given by:

$$\sigma_v^2 = \left(\frac{\mathrm{d}v}{\mathrm{d}\Delta T}\right)\sigma_{\Delta T}^2 \tag{5.1}$$

where σ is the error associated with the measured ΔT and velocity estimate v. The function $v = f(\Delta T)$ is obtained from the curve fitting in Figure 5.8.

Figure 5.10 shows the calculated hybrid cable estimated uncertainty based on Equation 5.1 as a function of true velocity, and a range of DTS temperature measurement uncertainties. This range in temperature uncertainties, from 0.5 to 0.01 °C, approximately correspond to time averages of 1 s and 30 min respectively at the minimum sampling

interval of the instrument used here. Firstly, the uncertainty in the estimated velocity increases with velocity. This is evident from the empirical calibration curves in Figure 5.8, with the most rapid reduction in ΔT occurring at low velocities. Secondly, estimated velocity uncertainty decreases with increasing DTS temperature measurement integration time. Measurements with DTS temperature uncertainties of 0.5 °C (approximately a 1 s time average) have a velocity uncertainty ranging from 4.6 to 30.2 cm s^{-1} at velocities of 10 and 60 cm s^{-1} respectively. For a DTS temperature precision of 0.01 °C (approximately equivalent to a 30 s time average), the estimated velocity uncertainty reduces to between 0.1 and 0.6 cm s^{-1}.

This reduction in uncertainty is most clearly shown in Figure 5.9 between 31 and 35 minutes (a period of constant velocity). During this time, the standard deviation of the estimated velocity is 7.43, 2.11, and 0.80 cm s^{-1} for the integration times of 1, 10, and 30 s respectively. Inputting the values for the standard deviation of the temperature measurements (i.e. instrument noise using calibration bath data), and mean ΔT between times of 31 and 35 minutes into Equation 5.1 gives the estimated error for each of the averaging times. These are 6.75, 1.91, and 0.81 cm s^{-1} for the integration times of 1, 10, and 30 s respectively. These values are in good agreement with the velocity uncertainty of the estimated ΔT values and suggests that application of Equation 5.1 is robust means of predicting quality of hybrid cable velocity estimate data.

5.4 Cable scale numerical model of the hybrid cable method

A numerical model of combined heat and fluid flow was set up to investigate how cable design influences the sensitivity to flow. There already exist several cable options for DTS temperature monitoring that can also be electrically heated. Cables can also be custom made, and 3D printing could potentially allow the addition of extra components to fibre jackets. Therefore, an understanding of how cable construction impacts on the sensitivity of the method may allow for more informed selection or even design of future installations applicable to both air and water deployments.

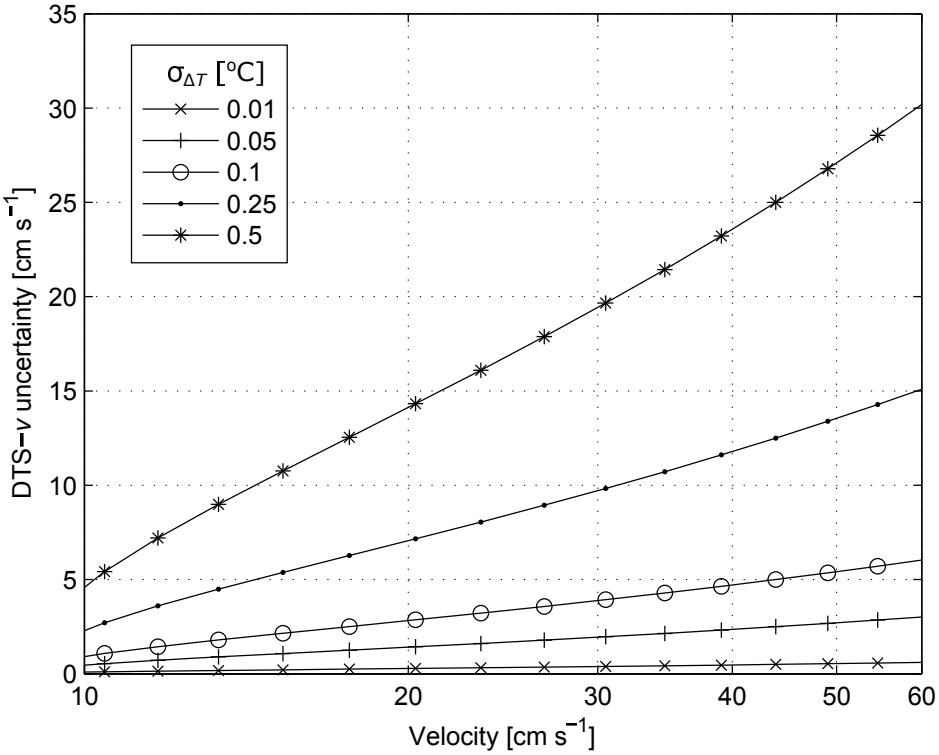

Figure 5.10: Uncertainty (standard deviation) in hybrid cable velocity estimates as a function of velocity and DTS temperature measurement uncertainty (standard deviation) in ΔT

5.4.1 Model set-up

A 2D cross section model of a FO-DTS cable surrounded by water, was initially set up in COMSOL Multiphysics. COMSOL Multiphysics is a general purpose finite element modelling software for simulating physics based problems. The 2D model set up was chosen for its simplicity, as the cable design (rather than position or flow angle) is the principle determinant of the cable temperature for any given flow. The 2D model set-up does not allow the same conditions in the flume to be tested, since with any component of flow velocity parallel to the cable, a 3D model would be required. This 2D cross section model, with flow at 90° to the cable, represents the far end-member of the laboratory experiments where flow angle was varied from 0 to 20°.

Figure 5.11 shows the geometry of the model and naming conventions. The cable consists of a steel core, with radius r_1, and plastic jacket with radius r_2. The detailed cable construction, including steel strands, capillary tube, optical fibres, and hydrophobic gel, is not considered. However, given that the majority of the volume is occupied by steel, and the high thermal conductivity of the steel relative to the plastic jacket, the steady state temperature distribution in the cable centre should be relatively uniform. In the following

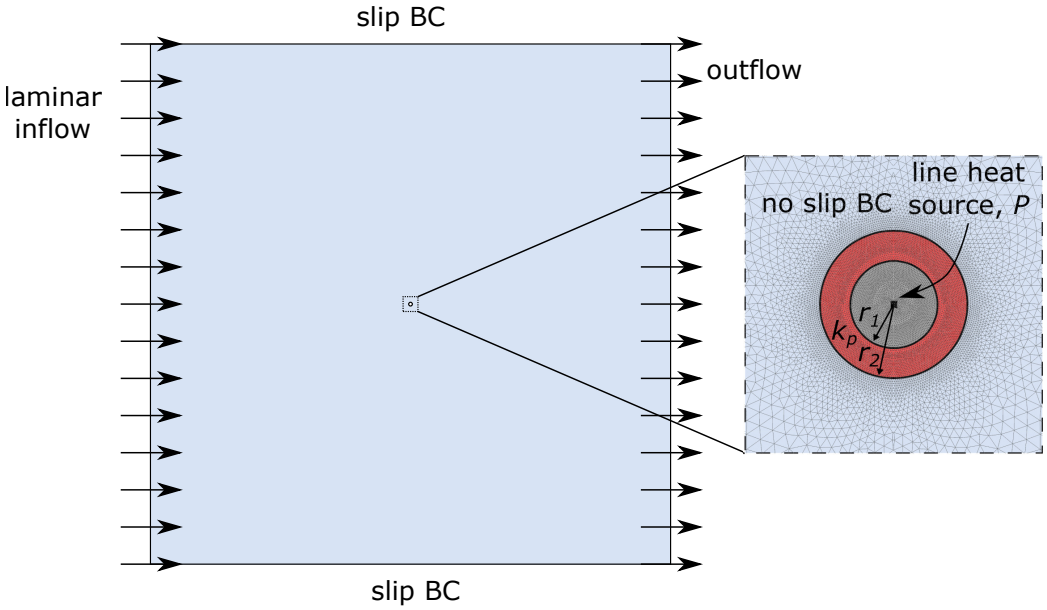

Figure 5.11: Schematic of the numerical model geometry and boundary conditions used in the sensitivity analysis

simulations, laminar inflow with a uniform velocity and constant temperature are specified on the left boundary. The right outflow boundary is specified to total the sum of the inflows and is an outflow temperature boundary. The upper and lower boundaries are specified as slip boundaries for flow, such that the cable is in effect simulated to be in an infinite body of water.

Steady state fluid flow and heat transfer are simulated using the Conjugate Heat Transfer module of COMSOL Multiphysics. Laminar flow is simulated in the fluid according to the Navier Stokes equation for a compressible fluid and continuity equation, given by:

$$\rho_{\mathrm{w}} \left(\mathbf{u} \cdot \nabla \mathbf{u} \right) = -\nabla p + \nabla \cdot \left(\mu_{\mathrm{w}} \left(\nabla \mathbf{u} + \left(\nabla \mathbf{u} \right)^T \right) - \frac{2}{3} \mu_{\mathrm{w}} \left(\nabla \cdot \mathbf{u} \right) \mathbf{I} \right) + \mathbf{F}. \tag{5.2}$$

$$\nabla \cdot \left(\rho_{\mathrm{w}} \mathbf{u} \right) = 0 \tag{5.3}$$

where $\mathbf{F}$ is a vector representing body forces on the fluid, and $\mathbf{I}$ is the identity matrix.

In general, temperature induced changes to fluid density and buoyancy are ignored in the simulations. In some simulations, where the sensitivity of the DTS measured temperature to this is assessed, the buoyant effect included as a body force in equation 5.2 according to:

$$F_z = g \rho_{\mathrm{w}} \beta \left(T - T_0 \right) \tag{5.4}$$

Table 5.2: Parameter values used in the finite element model of the hybrid cable (* denotes the parameter was varied during the sensitivity analysis)

	Value	Units
*Electrical power input	30	W m^{-1}
Density of water	f(T)	kg m^{-1}
*Radius of steel core	1.13	mm
*Radius of cable	1.925	mm
*Thermal conductivity of plastic	0.245	W m^{-1} $°C^{-1}$
Thermal conductivity of steel	13.4	W m^{-1} $°C^{-1}$
Thermal conductivity of water	f(T)	W m^{-1} $°C^{-1}$
Mesh elements (triangular)	233 860	
Model size	0.5 x 0.5	m

where β [$°C^{-1}$] is the linear coefficient of thermal expansion for water, taken to be 6.9x10^{-5} $°C^{-1}$, and $T - T_0$ is the temperature above the background temperature. Heat transfer in the cable is by conduction, given by:

$$\nabla \cdot (k \nabla T) + Q = 0 \tag{5.5}$$

where Q [W m^{-3}] is a heat source term. The hybrid cable method is simulated by applying this heat source term in the steel core, according to:

$$Q = \frac{P}{\pi {r_1}^2} \tag{5.6}$$

In the fluid, heat transfer is by both conduction and advection and is given by:

$$\rho C_p \mathbf{u} \cdot \nabla T = \nabla \cdot (k \nabla T) \tag{5.7}$$

Default parameter values used in the simulations are listed in Table 5.2. The default parameter values relating to the cable construction are for a typical BRUsteel cable as used in *Read et al.* (2014) and Section 5.3. The diameter of the steel core and outer jacket were measured with a digital callipers. The thermal conductivity of the plastic is the same as used by *Read et al.* (2014), and both this and the thermal conductivity of the steel are within the typical ranges specified for these materials (*Incropera et al.*, 2007). The governing equations were solved using the inbuilt MUMPS solver. After several trial simulation runs, a triangular mesh with a maximum separation of 5x10^{-5} m was specified in the cable. A parameter sweep over a velocity range of 1 cm s^{-1} to 50 cm

Table 5.3: Parameter values used in the sensitivity analysis of the hybrid cable response to fluid flow

	Value (min : step size : max)	Units
Electrical power input	10 : 10 : 50	W m^{-1}
Radius of steel core	0.63 : 0.25 : 1.63	mm
Radius of cable	1.425 : 0.25 : 2.425	mm
Thermal conductivity of plastic	0.145 : 0.5 : 0.345	W m^{-1} °C^{-1}

s^{-1} was then carried out. The steady state temperature distribution throughout the domain and temperature in the cable centre were output for each input velocity. The temperature at the cable centre is assumed to be equivalent to the temperature that would be measured using DTS. To test the sensitivity of the hybrid cable method to input power, cable thermal properties and thickness, the ΔT-v response was computed for each of these parameters, with the ranges listed in Table 5.3.

5.4.2 Model results

The modelled velocity and temperature distribution in the fluid for a flow of 1 cm s^{-1} and default parameter values is shown in Figure 5.12a. Flow is uniform across the domain, as specified by the left hand boundary condition, except downstream of the cable which obstructs the flow. The effect of heating, in this case at 30 W m^{-1}, is to create a thermal boundary layer around the cable that is then advected downstream. In the fluid, the temperature is increased by no more than 4 °C. The temperature profile through the water and centre of the cable is plotted in Figure 5.12b for a range of flow velocities. The thermal boundary layer around the cable is asymmetric, and extended downstream due to the advection of heat. Increasing the flow velocity reduces the size of the thermal boundary layer, such that at 50 cm s^{-1}, the temperature of the water on the downstream side of the cable is < 0.5 °C above the ambient water temperature. The temperature in the core, for a given steady state simulation, is highest in the centre, but shows little lateral variability ($<$ 0.1 °C). The temperature in the core is much higher than even close by in the fluid. The high temperature in the core is maintained by the plastic jacket, with a steep temperature gradient occurring across it.

Figure 5.13 shows the value of ΔT at the cable centre, which we assume is equivalent to that which would be measured along the cable with DTS, as a function of water velocity for the default model parameters. ΔT decreases as velocity increases, from 11.8 °C

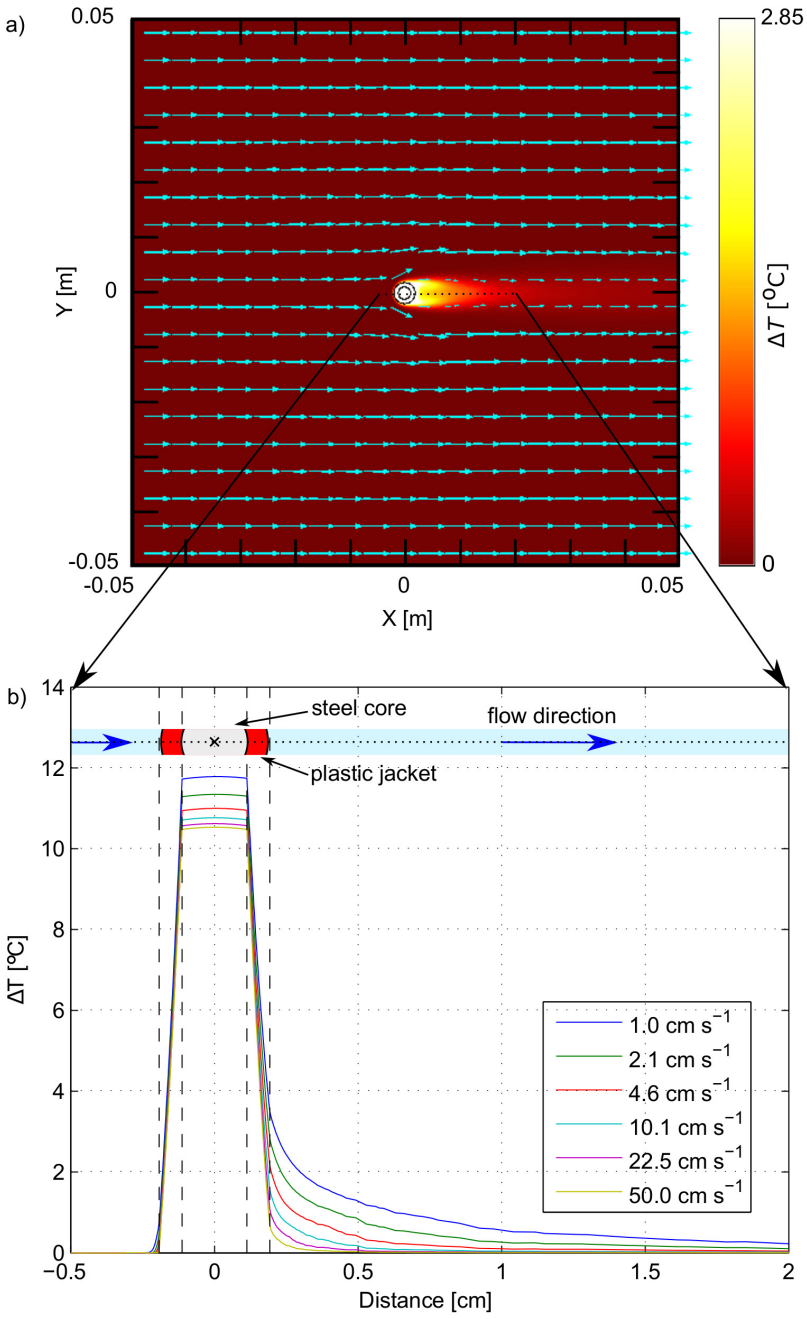

Figure 5.12: a) Flow and temperature distribution in the fluid for default model parameters and a flow of 1 cm s^{-1}. b) Cross section of temperature through the fluid and centre of the cable for a range of velocities

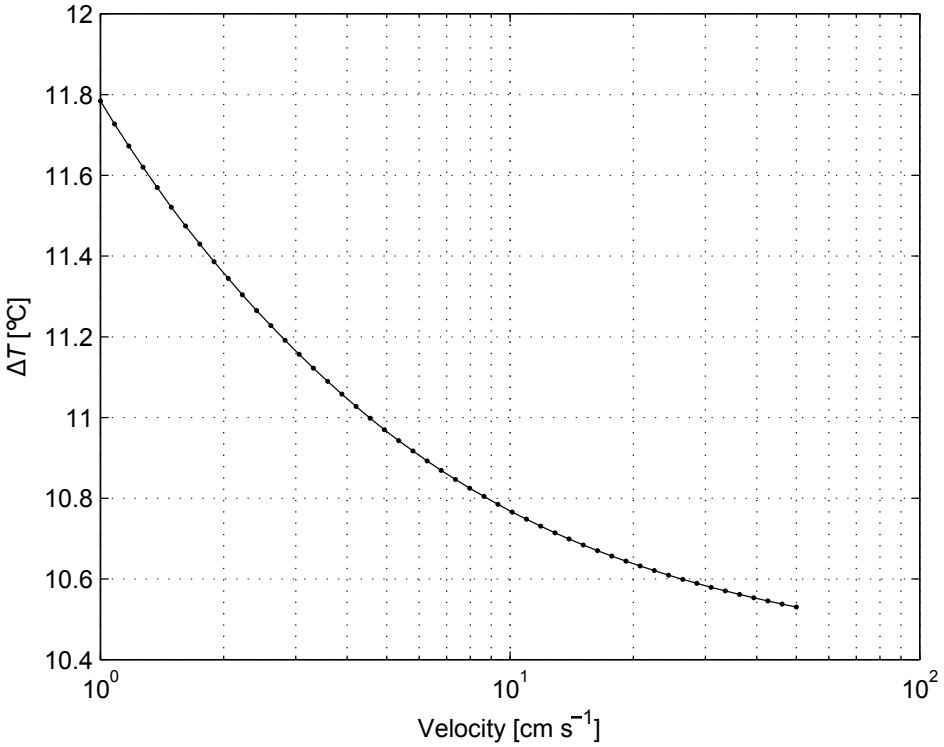

Figure 5.13: Steady state ΔT response to fluid flow with the default model parameters listed in Table 5.2

at 0.01 m s^{-1} to 10.5 °C at 0.5 m s^{-1}. Similar model runs were then carried out to determine ΔT response to flow for electrical power input, thermal conductivity of the jacket material, cable outer radius (r_2), and radius of the steel core (r_1). The simulations used the default parameters listed in Table 5.2, with the parameters of interest varied according to Table 5.3.

5.4.2.1 Parametric sweeps of cable construction parameters

Figure 5.14a-d shows the ΔT-v response for all of the parameter sweeps instructed. The sensitivity is also plotted below (e-h), and is defined as the change in ΔT per unit increase in flow velocity (i.e. the first derivative of the ΔT-v curve). This is the key metric for identifying changes in the method sensitivity, since ideally, a small change in velocity elicits a large ΔT response that is readily measurable above the instrument noise with DTS. The value of ΔT at a particular flow velocity linearly scales with the electrical power input. This in turn results in a linear scaling of the sensitivity to flow (i.e. increasing the electrical power input by a factor of two doubles the sensitivity to flow). Increasing the thermal conductivity of the plastic jacket leads to lower ΔT values, since the heat

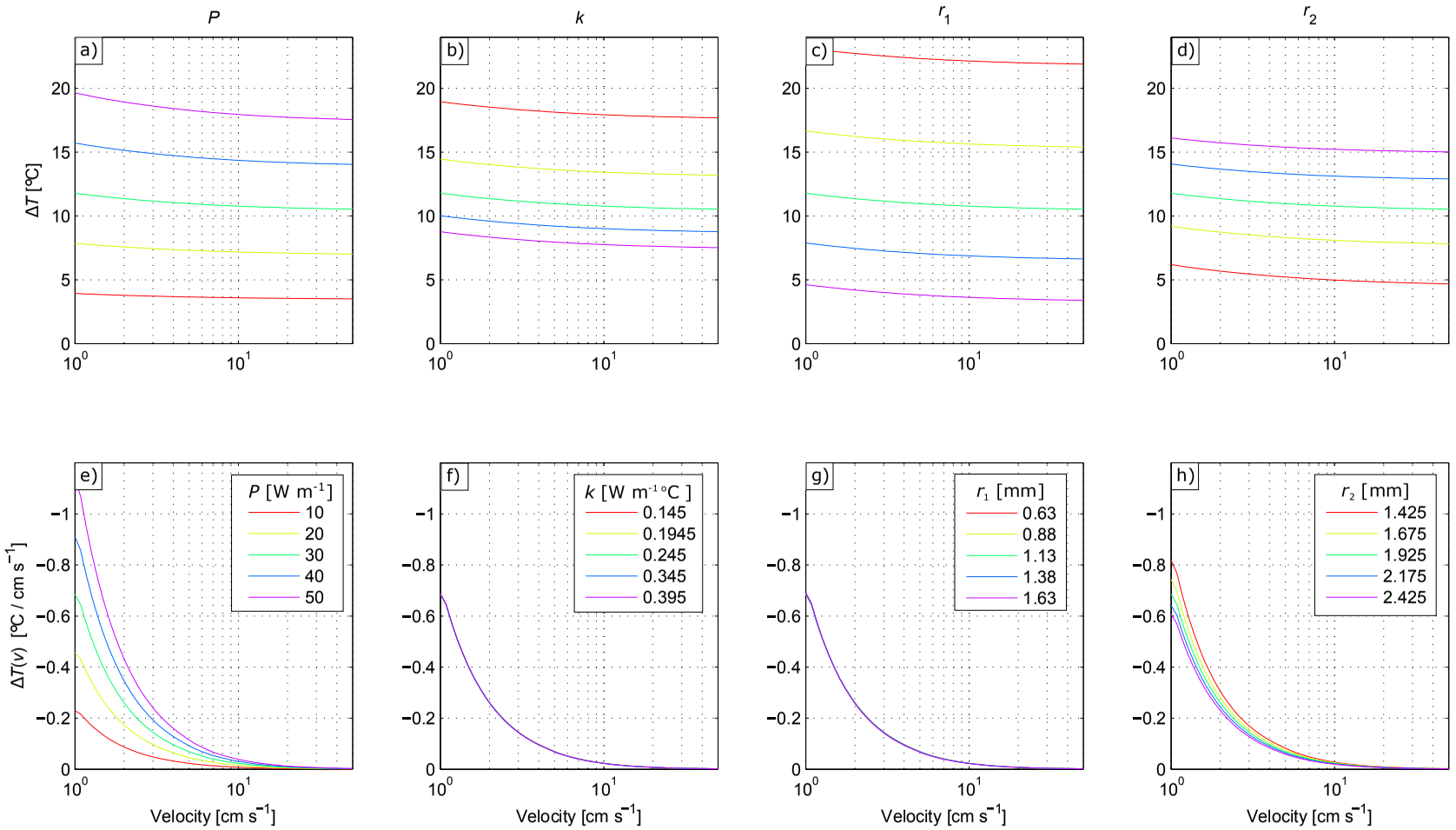

Figure 5.14: Steady state ΔT response to velocity for different electrical power inputs (a), thermal conductivity of plastic jacket (b), steel core radius (c), and cable outer radius (d) defined according to Table 5.3. Figures e-h are the first derivative of figures a-d, respectively, to illustrate the method sensitivity to velocity

applied in the centre is lost more readily through the jacket. However, the sensitivity to the flow remains unchanged. Increasing the radius of the steel core r_1 reduces ΔT. This is because the outer radius remains fixed, so increasing the steel radius effectively reduces the thickness of the plastic jacket, therefore providing less thermal insulation. Despite this, the sensitivity to flow remains unchanged. On the other hand, reducing the thickness of the cable through r_2 leads to a reduction in ΔT, as the low thermal conductivity plastic jacket becomes thinner. In this case, the sensitivity to the flow is slightly increased. The reason for this is that the heat flux from the cable is distributed over a smaller surface area, generating a larger thermal boundary layer.

5.4.2.2 Impact of free convection on the method response

The previous simulations neglected the effect of buoyancy induced free convection in the surrounding fluid as a mechanism for mass and therefore heat flux. A further set of parametric sweeps was then instructed using the default parameters in Table 5.2 but also including buoyancy. These simulations were carried out for forced convection acting in the same direction, opposing, and perpendicular to the direction of the buoyant force. In these simulations, the direction of the buoyant force is always upwards and the direction of the flow through the domain is changed.

Figures 5.15 and 5.16 show the temperature of the water surrounding the cable and flow velocity vectors, for simulations where buoyancy is incorporated using Equation 5.4. These are shown for velocities of 0.28, 0.49, 0.86, and 1.01 cm s^{-1}. With flow in the same direction as buoyancy (Figure 5.15e-h), the effect on the flow and temperature distribution in the fluid appears to be relatively small, relative to ignoring the buoyant force (Figure 5.15a-d). However, for low velocities, the buoyant force acts in an positive way to remove fluid and heat, reducing the thickness of the thermal boundary layer (Figure 5.15a and b). When forced convection opposes the buoyant force, the flow at low velocities is very different (Figure 5.16a and b). Warm, buoyant fluid heated by the cable attempts to migrate upwards but is then forced down by the flow. This creates a large shadow zone downstream of the cable with relatively warm water and allows a large thermal boundary layer to develop. Increasing the flow eventually overwhelms the buoyant force such that with an inflow of 1 cm s^{-1}, the flow regime and temperature distribution is the same as

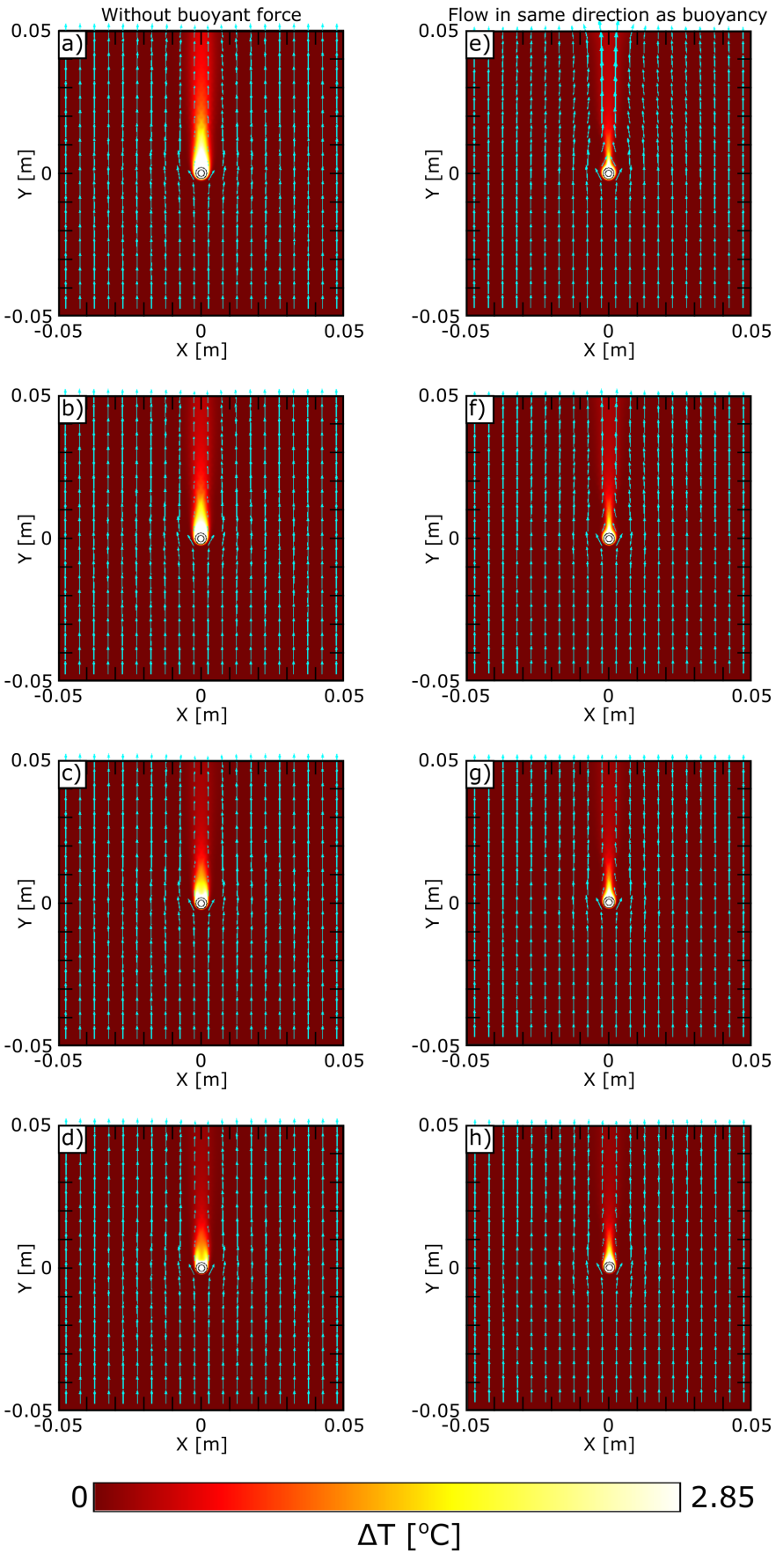

Figure 5.15: Temperature distribution for flow ignoring the buoyant force (a-d), and flow acting in the same direction as the buoyant force (e-h), for velocities of 0.28, 0.49, 0.86, and 1.01 cm s^{-1} (top to bottom).

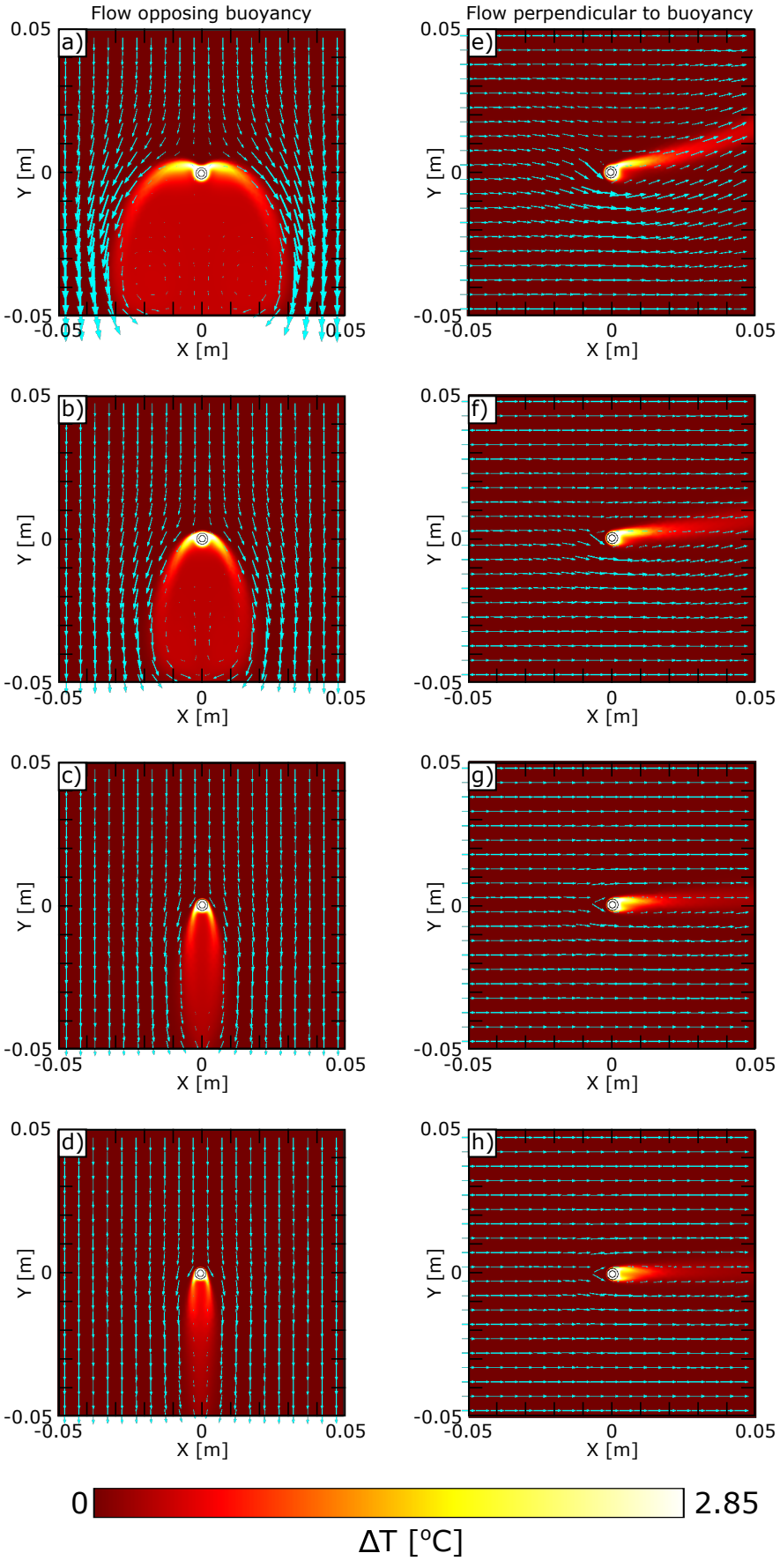

Figure 5.16: Temperature distribution for flow in the opposite direction to the buoyant force (a-d), and perpendicular direction to the buoyant force (e-h), for velocities of 0.28, 0.49, 0.86, and 1.01 cm s^{-1} (top to bottom).

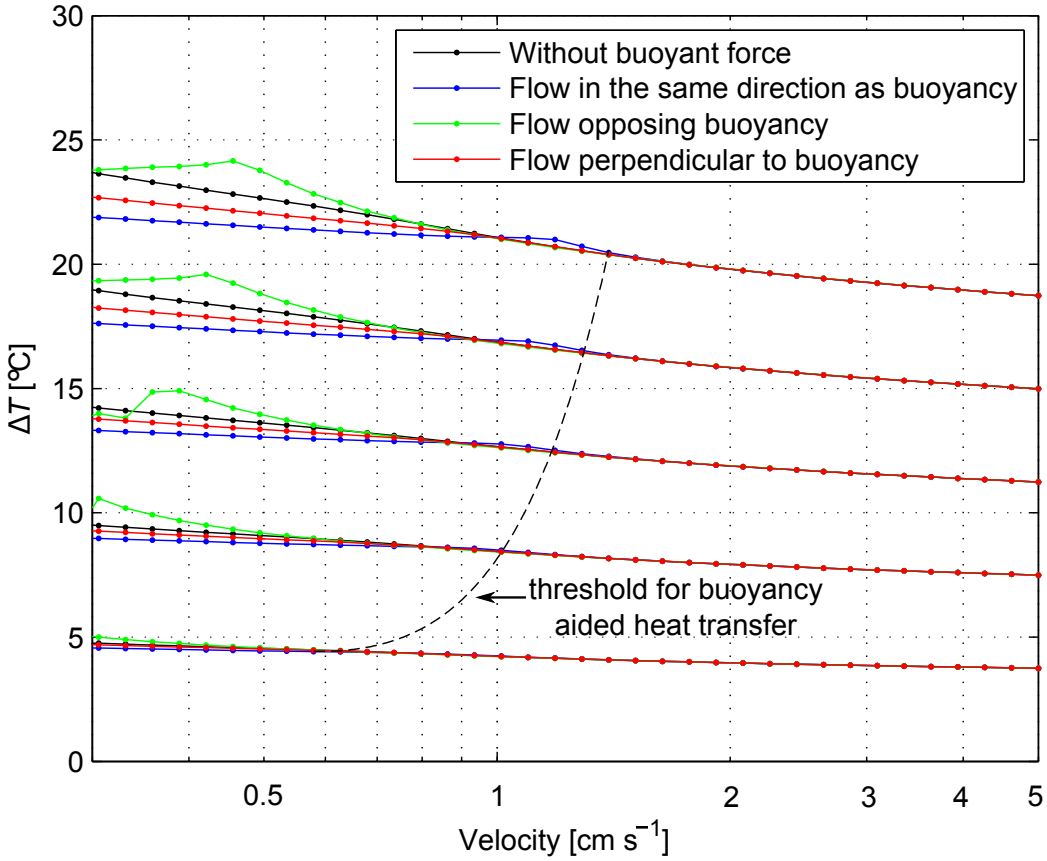

Figure 5.17: Effect of buoyancy on the ΔT relationship with fluid velocity at low flows

the previous cases (Figure 5.16d). When the flow is perpendicular to the buoyant force, at low velocities, both forced and free convection contribute to heat and mass transfer (Figure 5.16e and f). By 0.0086 m s^{-1}, the path of the warm plume is almost parallel to the flow (Figure 5.16d).

The effect that this has on the overall ΔT response to flow is shown in Figure 5.17. At low velocities, when flow is either in the same or perpendicular direction to buoyancy, the heat transfer process is enhanced and ΔT is lowered. When flow oppose the buoyant force, ΔT is initially lower, but as the buoyancy related flow is of comparable magnitude to forced convection, ΔT increases. These effects are significant until a certain threshold velocity, when the buoyant free convection effect can then be ignored as it overwhelmed by forced convection. This threshold velocity is a function of electrical power input, since the greater the energy input, the more heat is available to warm the surrounding water, and higher velocities are required to overcome the buoyant effect. However, even at an electrical power input of 50 W m^{-1}, free convection driven by fluid density gradients becomes insignificant at around 1 cm s^{-1}, and the ΔT response is then therefore independent of

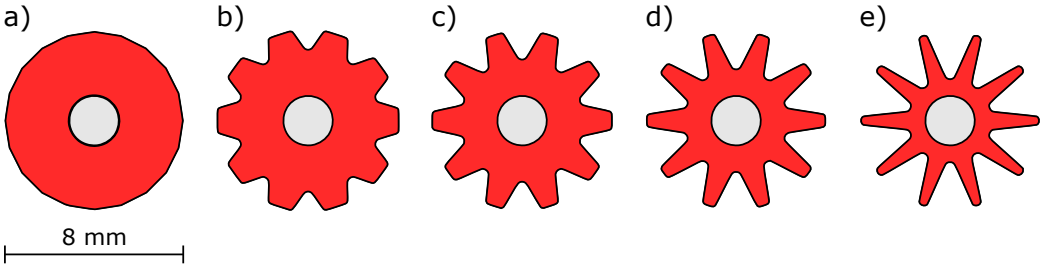

Figure 5.18: Cable jacket geometry incorporating increasingly deeper grooves from Design 1 (smooth jacket), to Design 5

the flow direction.

5.4.2.3 Enhancing the flow sensitivity through modified designs

The modelling results of section 5.4.2 show that with a standard circular cable, increasing the electrical power input is the only way to significantly enhance the hybrid cable method sensitivity to flow. The hybrid cable method becomes insensitive to fluid flow once the thermal boundary layer in the fluid is removed. To enhance the sensitivity and to potentially extend the sensitivity range to flow, one alternative approach could be to deploy a cable with a jacket or additional wrapping, such that the boundary layer is not so readily removed by fluid flow. To test this idea, the numerical model outlined in section 5.4.1 was modified to include a cable with an outer surface defined by a circle with radius 4 mm, with increasingly deeper recesses (increasing in 0.5 mm increments) (Figure 5.18). Design 2 resembles a ribbed cable jacket, and in the extreme case, the cable jacket in Design 5 resembles a 10-point star.

Figure 5.20 compares flow and temperatures in a smooth jacketed cable (Design 1) with that of the textured jacket (Design 5). For both designs, the general velocity distribution is similar. As the flow velocity is increased, the thermal boundary layer for the smooth cable is almost reduced to a minimum by around 10 cm s^{-1}. In contrast, for Design 5, the recesses in the cable trap warmer water such that it retains heat. Even at 50 cm s^{-1}, there still exist significant warmed regions of fluid in the cable recesses in comparison to Design 1, where the temperature distribution in the vicinity of the cable is largely unchanged. Figure 5.19a shows the ΔT response to flow for the cable designs tested. The ΔT values for Design 2-5 are shifted vertically so that the ΔT values at a velocity of 10^0 cm s^{-1} are all equal to the ΔT of Design 1. Without this vertical shift, the ΔT values

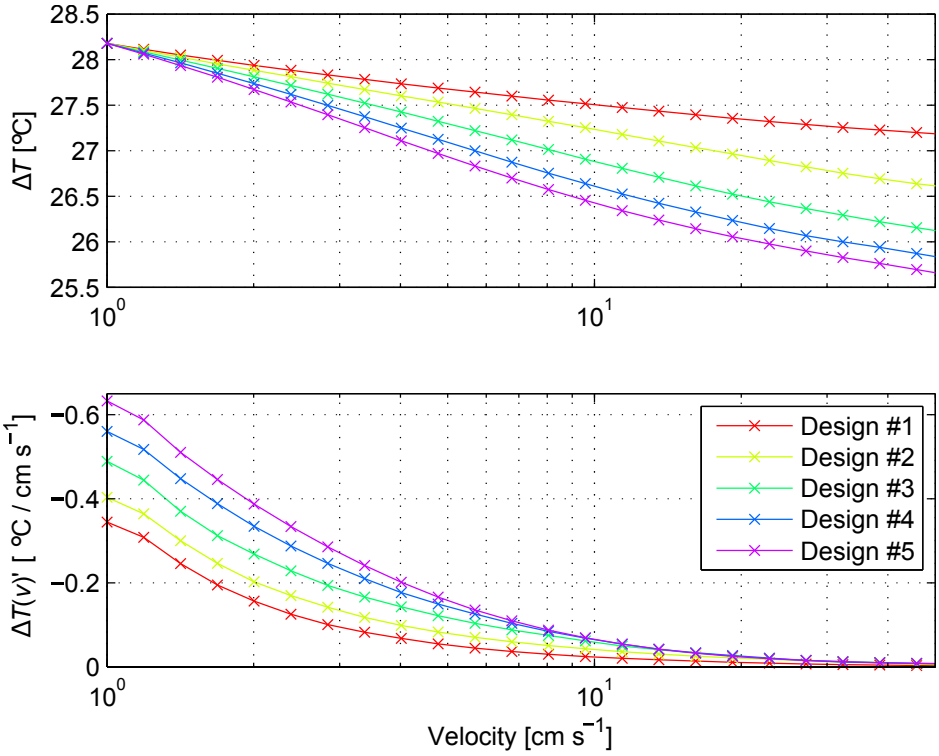

Figure 5.19: a) ΔT response to fluid flow for the modified cable designs (note that the temperatures have been shifted vertically so that ΔT at a velocity of 10^0 cm s^{-1} are all equal) and b) corresponding sensitivity plot

are in general higher for Design 1, and decrease with the increased size of the recesses, as there is less thermal mass to provide an insulating effect. The effect of having a textured cable is to more rapidly reduce the ΔT value. Between velocities of 1 cm s^{-1} and 50 cm s^{-1}, there is a decrease in ΔT of 0.97 °C for Design 1. This is in contrast to 2.68 °C in the case of Design 5. This difference in ΔT over the given velocity range increases as the depth of the recesses increases. Figure 5.19b shows that the method sensitivity is always greater when the cable surface includes recesses, over the velocity range tested here.

5.5 Discussion and conclusions

The laboratory calibration experiments highlighted the scaling significance of electrical power input on the sensitivity of the hybrid cable method. The numerical model tested a further range of parameters and showed that out of electrical power input, jacket thermal properties, and material layer thickness, it is only the electrical power input that affects the sensitivity of the method over realistic parameter ranges. The default parameter values

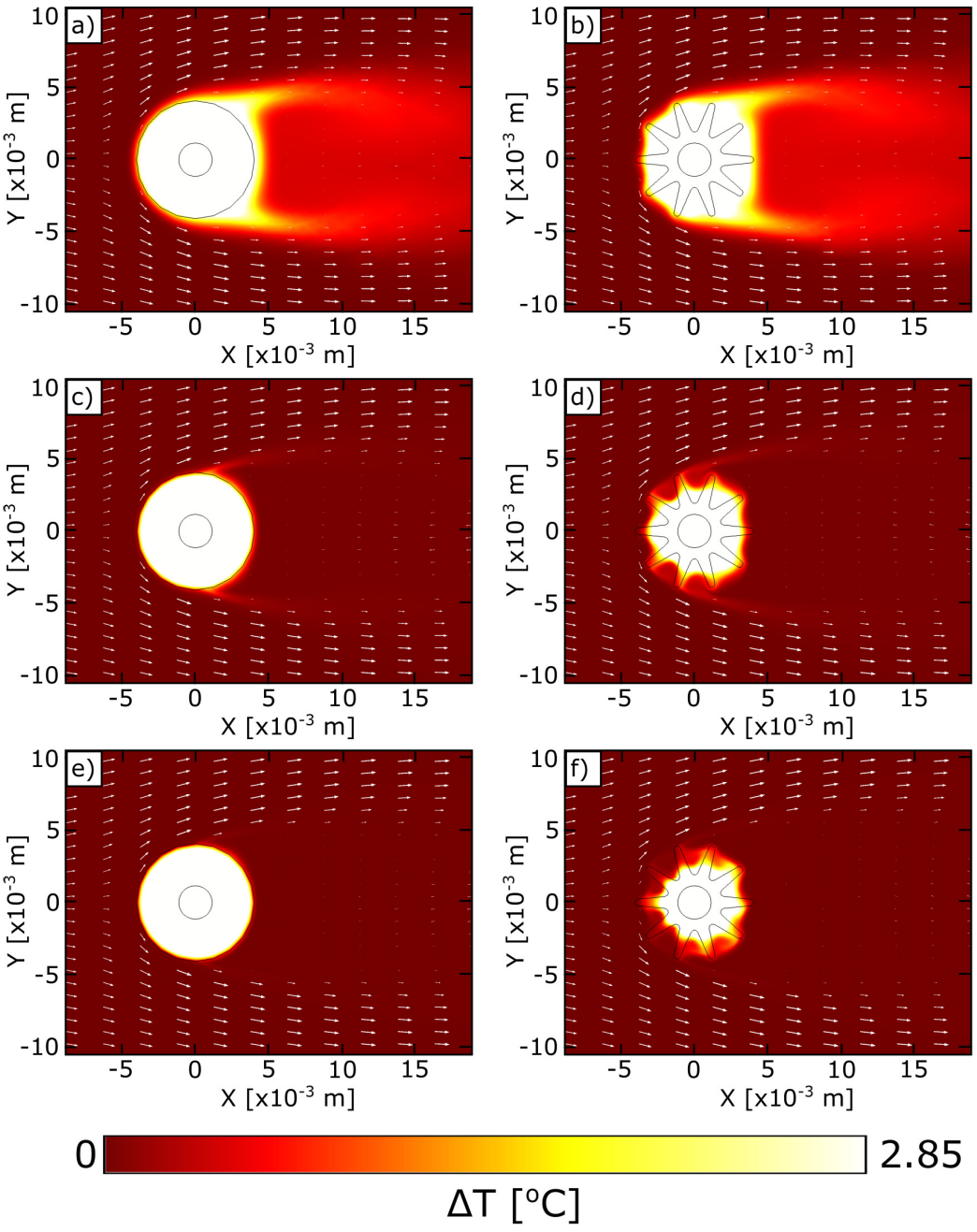

Figure 5.20: Temperature and flow around a smooth cable (Design 1, a, c, and e), and ridged cable (Design 5, b, d, and f) for velocities of 1, 10, and 50 cm s^{-1} from top to bottom

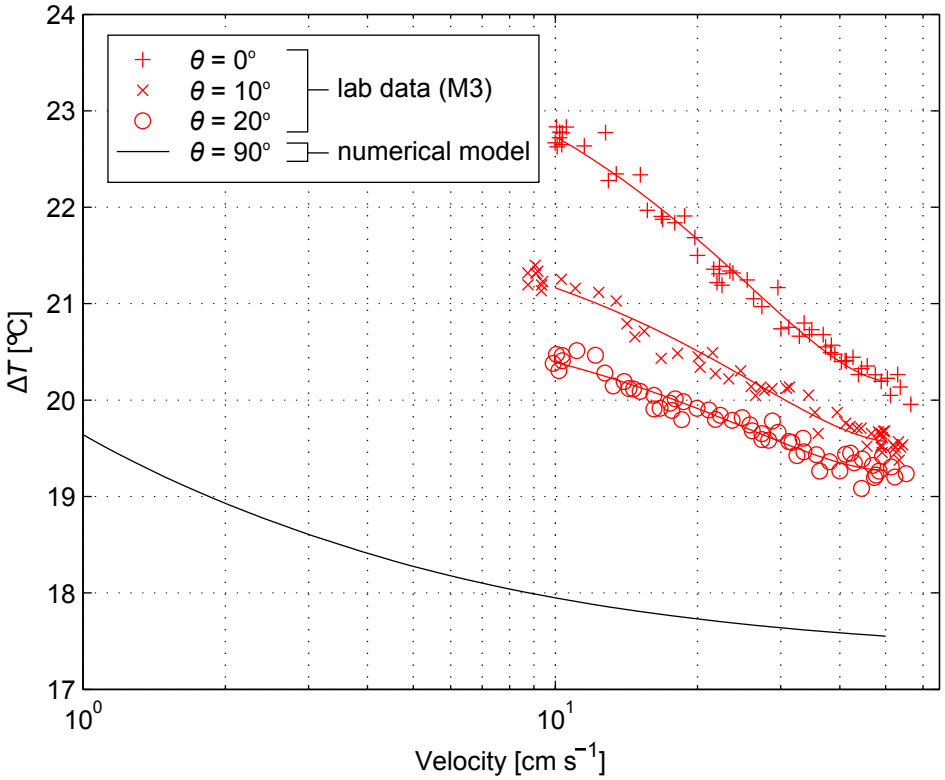

Figure 5.21: Comparison of laboratory and numerically modelled ΔT response to flow (P = 50 W m^{-1}, the laboratory data are from position M3)

used in the model are for a BRUsteel cable, hence, these results should be directly comparable to the laboratory results. Figure 5.21 shows the laboratory measured ΔT with an electrical power input of 50 W m^{-1} at position M3, with the numerical model results using the default input parameters and an electrical power input of 50 W m^{-1}. The general trend is for a decrease in ΔT with increasing contact angle θ. The numerical model essential gives the extreme end-member scenario, with θ = 90°. In comparison the laboratory results, the gradient of the ΔT-v curve is shallower, although this is a trend which also appears with increasing cable angle.

Figure 5.22 shows values of ΔT extracted from the best fit curves in Figure 5.21 plotted against the sine of the cable angle. The sine of the angle θ gives the fraction of the velocity vector that is normal to the cable (i.e., when flow is parallel to the cable sin(θ) is 0, and sin(θ) is 1 when flow is perpendicular to the cable). The plot consists of 5 curves, which correspond to 5 velocities. Each curve comprises 4 points; 3 from the laboratory data and 1 from the numerical model. The final 3 points, corresponding to cable angles of 10, 20, and 90° lie approximately on a straight line. Thus, for a given velocity, the value of ΔT depends linearly on the sine of the cable angle relative to the flow. This also

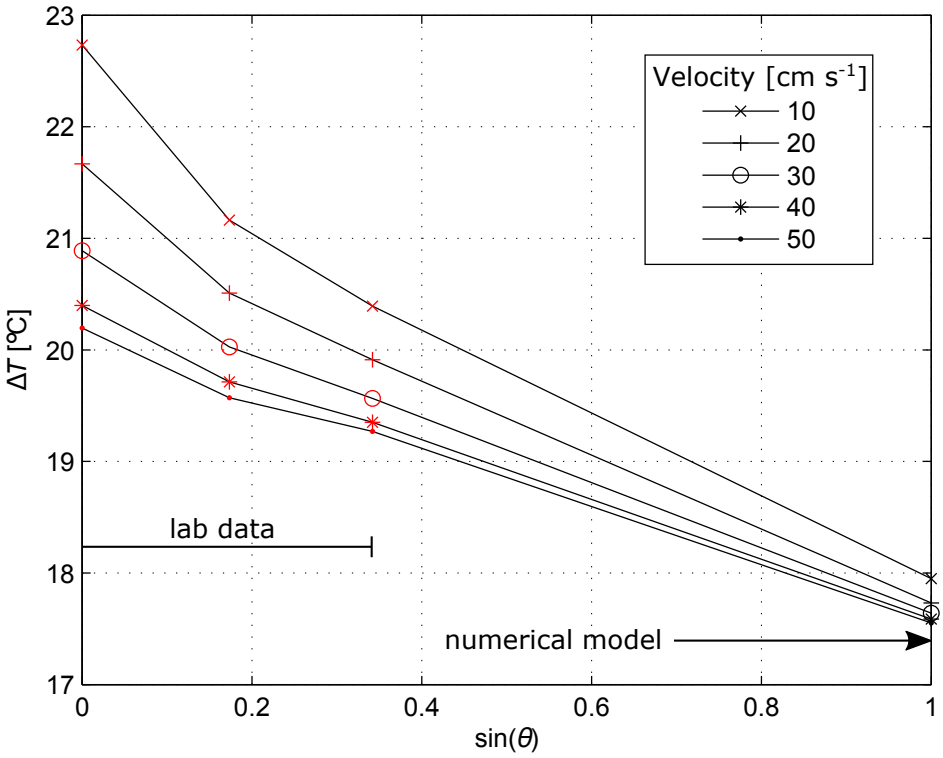

Figure 5.22: ΔT as a function of the sine of the cable angle θ for five velocities (P = 50 W m^{-1}, the laboratory data are from position M3)

highlights that the flow sensitivity decreases with increasing θ since the ΔT values shown decrease in range as θ increases. This also provides a good validation of the numerical model. Even though the numerical model did not exactly replicate the laboratory set up, the results are consistent with what would be expected from the laboratory results, projecting them forwards. The data from where $\sin(\theta) = 0$ do not fit the linear trend, with the ΔT values appearing higher than the linear trend would suggest. This departure could be explained by longitudinal warming, which, from the early laboratory results, was shown to be significant when flow is parallel to the cable.

Both the laboratory measurements and numerical model show that electrically heating standard armoured fibre optic cable and measuring the temperature response with DTS is a viable means of monitoring fluid flow. Such standard cable designs, including centrally located fibre optic cables, steel armouring, and an outer plastic jacket, are readily available. The results of the numerical model suggest that in terms of measurement sensitivity and within realistic parameter bounds, it does not matter what the thickness of each of these layers is, or the thermal properties. These will however affect the time response of the cable to changes in flow, with thicker and less thermally conductive cables responding

more slowly. While cables which do not have radial symmetry in their construction are also likely to be sensitive to fluid flow, these were not tested in the laboratory and unless there is a highly uniform separation distance between the heating element and the optical fibres, this non-uniform separation is likely to overprint hybrid cable DTS temperature data.

The simplest way to enhance the sensitivity to flow is through increasing the electrical power input. Care needs to be taken, since if free convection is the dominant mechanism of heat transfer in the fluid, then the hybrid cable method will be insensitive to forced convection through the borehole. The numerical model suggests that for power inputs up to 50 W m^{-1}, free convection is significant up to flow velocities of 1 cm s^{-1}. There are some conceivable deployments, for instance, measuring ambient vertical flow or lateral groundwater flow through an open or screened borehole, where velocities would potentially be lower than this. For field deployments, the available electrical power may be limiting. For instance, a 3 kW generator would be capable of heating at most 60 m of cable at 50 W m^{-1}. Depending on the system being investigating, a compromise may have to be made over the total heated length of cable, and electrical power input per unit length. Systems exist for heating sections of the same cable at different times using a relay board, and this system has been utilised in soil moisture studies (*Sayde et al.*, 2014). Such a system could be used in borehole DTS deployments but care would need to be taken to ensure that the presence of extra cables within the well bore do not disturb the hybrid cable measurement.

The laboratory tests highlighted that longitudinal heat accumulation is significant. There was also the potential in the laboratory tests for variability in the velocity along the cable which was not detectable with the single probe used to provide a reference velocity measurement, which may have additionally contributed to the spatial variation in ΔT. While a parallel unheated reference cable may partially counter the longitudinal heating effect, the thermal boundary layer is extremely close to the cable making this a challenge. In field deployments, this could be overcome by heating for only a short duration, with repeated cycling of heating and non-heating phases if temporal variations in velocity are of interest. Alternatively, it could be possible to add a continuous structure to the cable to uniformly disturb the flow. This way, with a relatively well mixed temperature distribution laterally through the well, a reference cable providing adjacent temperature measurements

may be able to correct for the longitudinal warming.

Cable designs that retain a thermal boundary layer may increase the measurement sensitivity and extend the sensitivity range to higher velocities. The numerical model, of a cross section through a cable with perpendicular flow, tested the effect of recesses parallel to the cable axis. If flow was closer to parallel to the cable, as may be the case in a borehole deployment, enhanced sensitivity could possibly achieved with a corrugated jacket. Wrapped cables, such as the ones used by *Arnon et al.* (2014a) and *Banks et al.* (2014) already have a slightly corrugated surface due to the wound cables beneath.

Borehole deployments require extra considerations. Electrical power needs to be supplied to the cable at the bottom of the borehole, and this cable is an extra object present in the well. It is also necessary to ensure that the cable is located centrally in the well rather than touching the borehole walls, as this is likely to produce erroneous ΔT values. Perhaps the optimal system would be a mesh, through which the fibre optic cable, reference cable, and power supply cable are threaded. This could be at a slight angle to minimise the longitudinal heating effect. The mesh would provide a means of centralising the cable, whilst also uniformly altering the flow (unlike point centralisers used in *Read et al.* (2014)).

Chapter 6

Comparative discussion of borehole DTS methods

6.1 Chapter summary

In recent years there have been an increasing number of borehole DTS deployments and methodological developments for measuring groundwater fluxes. Within these deployments there have been a variety of approaches, for instance, using either electrical heating or fluid injections, located at a point in space or fully distributed, carried out continuously in time or as a pulse, and undertaken in open, cased, or temporarily lined boreholes. This chapter aims to review the methods developed in the previous chapters alongside the most current DTS deployments. Three distinct approaches are identified in the literature, with the methods developed in the thesis falling into each of these. Heat pulse tests are carried out in boreholes in the absence of vertical flow (e.g. cased, lined, or packered boreholes), in order to estimate thermal properties and natural gradient groundwater flow in the formation. Thermal advection tests, which utilise a thermal anomaly either at a point or distributed along the borehole, are a means of estimating vertical flow in the borehole. Lastly, hybrid cable methods combine electrical heating and DTS temperature measurements along the same cable to estimate in-well vertical flows. The combination of the deployment method and borehole construction control whether the method used is sensitive to in-well vertical flow or natural gradient groundwater flow in the formation. Potential future areas for DTS developments and the emergence of Distributed Acoustic

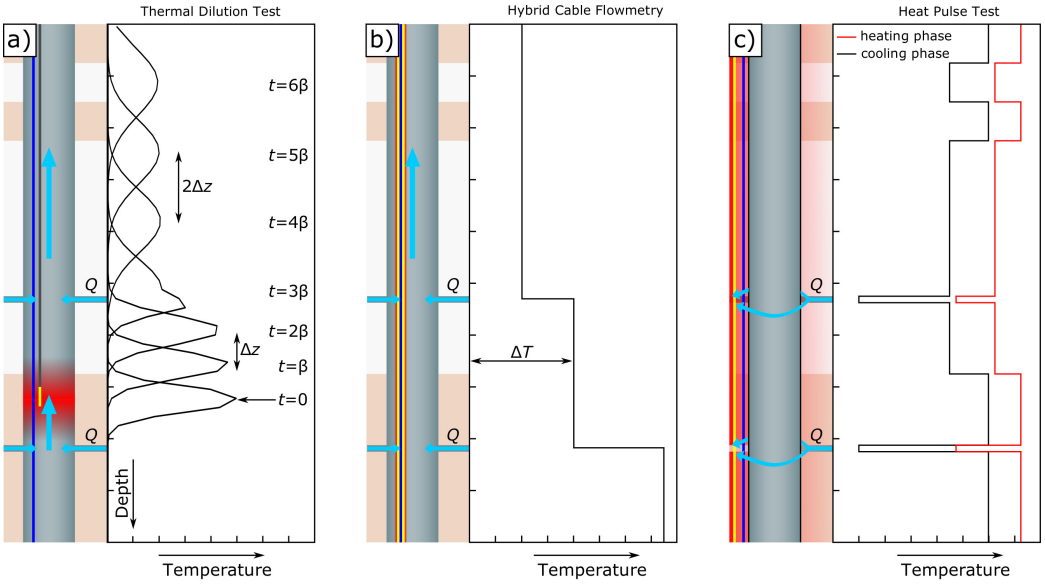

Figure 6.1: Schematic of possible Active-DTS methods in a borehole intersected by two transmissive fractures, showing a) thermal advection test with example temperature depth profiles as may be obtained from a point injection or point heating (both fracture inflows are of equal magnitude). DTS temperature measurements are obtained in time increments of β. b) Hybrid cable method with a profile of ΔT, and c) heat pulse test with temperature data from the heating and cooling phases

Sensing as a complementary fibre optic monitoring tool are then discussed.

6.2 Introduction

Borehole DTS deployments for measuring groundwater fluxes have to date been 'active' in their approach, in that heat has been added to the subsurface. With Active-DTS methods, the temperature response at some or all points during or after the heating process is then indicative of either the lithology, ambient groundwater flow, or in well flow, and depends closely on how the cable is deployed in the borehole and the nature of the thermal disturbance. These issues are the subject of this section. Three Active-DTS methods are summarised in Figure 6.1. These are heat pulse tests, thermal advection tests, and hybrid cable flow. Figure For each test, Figure 6.1 shows typical cable set-ups, heating locations, and data, for a well intersecting two fractures with additional layered heterogeneity. The three DTS methods developed in the thesis approximately fall within these categories and are reviewed in turn in the following sections.

6.3 Heat pulse tests

Apparent thermal properties measured in-situ are sensitive to groundwater flow. Therefore measurement of these vertically through a well will potentially yield information on the hydraulic conditions with depth. In Chapter 2, a type of heat pulse test was used to identify apparent thermal property variation in boreholes at the Ploemeur site. Apparent thermal conductivity at 1 m intervals was derived from cooling data by optimising a radial conduction numerical model. The method presented Chapter 2, was sensitive to lithological changes but failed to identify transmissive fractures. However, an instrument with a low spatial resolution was used here.

An alternative approach is to heat the subsurface using an electrical heating cable (*Coleman et al.*, 2015; *Freifeld et al.*, 2008). Such heat pulse tests can be conducted using either separate heating and fibre optic cables or with a composite cable that incorporates both resistance heating wires and optical fibres. In heat pulse tests, heating or cooling data may be used. An analytical solution exists for constant heat injection in a homogeneous, radially symmetric porous medium. This is given by (*Shen and Beck*, 1986):

$$k = \frac{Q}{4\pi} \cdot \frac{\ln\left(t_2/t_1\right)}{T_2 - T_1} \tag{6.1}$$

where T_1 and T_2 are the measured temperatures at times t_1 and t_2 respectively. This is the key advantage of electrical heating over fluid injections - in that the heating per unit length is closely controlled, and a simple analytical solution can be applied.

There are limitations to this approach however. Care must be taken when applying equation 6.1, in that only temperature data after a sufficiently long period of heating may be used to give an accurate measure of the rock apparent thermal properties. To determine the appropriate heating time scale, a 1D conduction only numerical model was run including a BRUsteel cable located centrally in a well, borehole with diameter 11.5 cm, and electrical power input of 10 W m^{-1}. Figure 6.2 shows the simulated heat pulse test response for varying rock thermal conductivities. The temperature response, as would be measured with DTS, is the same regardless of the thermal properties of the formation until around 17 min. Following this, there is some variation in the rate of temperature increase based on rock thermal properties. But it is not until around 500 min that the temperature

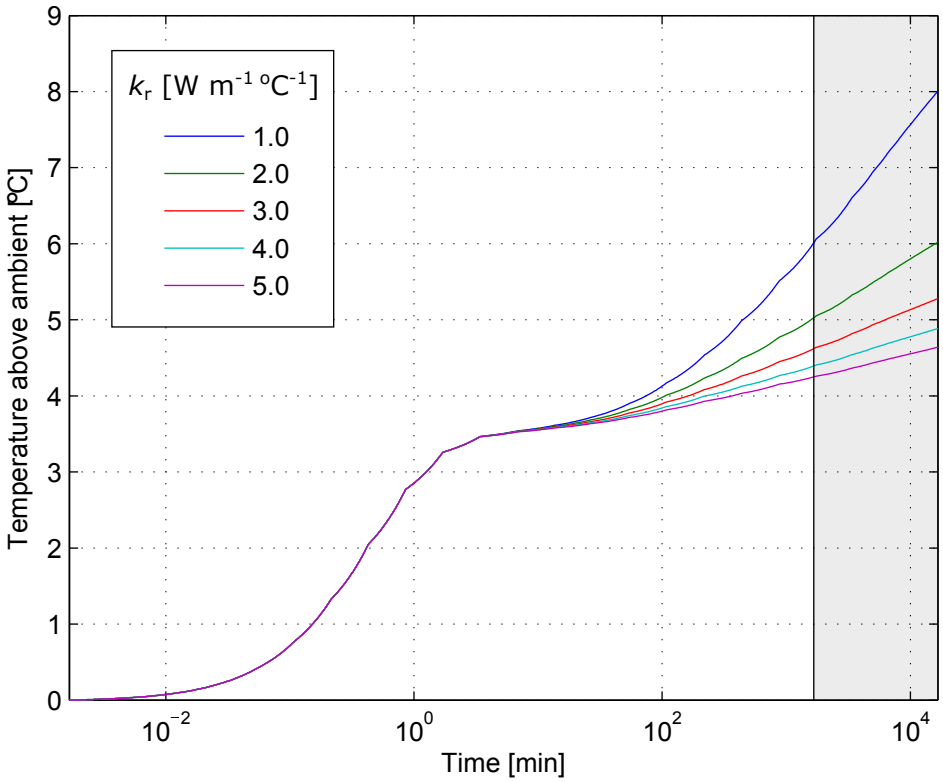

Figure 6.2: Modelled DTS temperature response of a heated BRUsteel cable in a borehole surrounded by rock with formation thermal conductivities of 1, 2, 3, 4, and 5 W m^{-1} K^{-1}. Grey area denotes the time range used for the calculation of thermal conductivity from the model output

increase becomes log linear and equation 6.1 is applicable. Equation 6.1 applied to the numerical model output, with t_1 = 10^5 s and t_2 = 10^6 s gives thermal conductivities of 0.92, 1.85, 2.79, 3.72, and 4.71 W m^{-1} K^{-1} for the modelled scenarios of 1, 2, 3, 4, and 5 W m^{-1} K^{-1} respectively.

Additional care needs to be made with the cable selection and how it is installed downhole. The installation of *Freifeld et al.* (2008), utilised separate cables for electrical heating and DTS temperature measurements. They observed that temperature measurements during heating are highly dependent on the distance between the heating wires and optical fibres; thus, cooling data were exclusively used for data analysis where distance variations had much less of an effect. *Coleman et al.* (2015) used a composite cable, containing both optical fibre and electrically conductive elements.They found that in this case, both heating and cooling data could be analysed.

Since heat pulse tests measure apparent thermal properties, specific information regarding the field installation is required if isolating the conductive and advective components of heat transfer is desired. *Freifeld et al.* (2008) deployed cable inside a 535 m

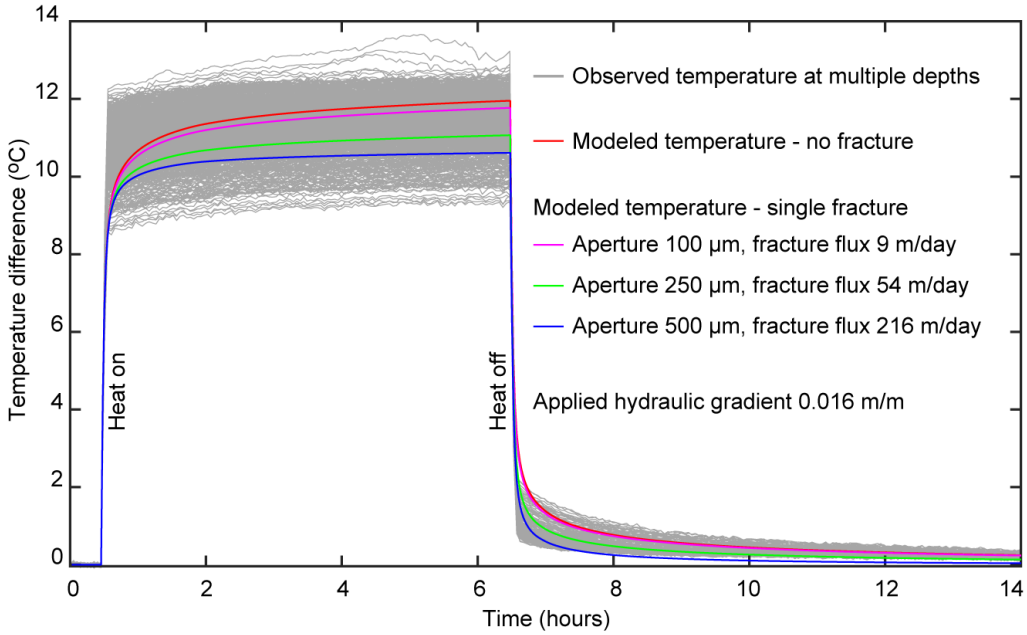

Figure 6.3: Comparison of modelled heat pulse test temperature responses including varying groundwater fluxes with observed field data from (*Coleman et al.*, 2015)

borehole through volcanic strata and used a 1-D radial model to invert cooling data from a heat pulse test to determine a thermal conductivity profile. In this case both natural gradient flow and vertical well bore flow variations were assumed to be negligible in order to calculate thermal conductivity profiles of the rock strata. If the thermal properties of the rock strata are known there is significant potential for using apparent thermal data to quantify flow (*Coleman et al.*, 2015). Figure 6.3 from *Coleman et al.* (2015) shows the modelled effect of flow on heat pulse temperature data in comparison with field data collected in a dolostone aquifer, for a composite cable deployed between a flexible borehole liner and the borehole wall. Increasing groundwater flow through the fracture decreases the observed temperature during heating, and enhances the return to pre-testing temperatures during the cooling phase.

One of the key issues affecting heat pulse tests carried out as in Chapter 2, and those of *Freifeld et al.* (2008) and *Coleman et al.* (2015), is the separation of lithology (which affects heat conduction), and groundwater flow (which affects heat advection). If the former is to be quantified, then groundwater flow needs to be assumed to be negligible. While groundwater flow is to be quantified, then the rock thermal properties must be known. A particular strength of the method is the ability to monitor changes in apparent thermal properties such as for characterising a CO_2 injection (*Freifeld et al.*, 2009). The

requirement for only a single downhole cable that can be installed through a variety of means provides a great deal of flexibility allowing the method to be used in installations ranging from shallow groundwater applications to deep CO_2 sequestration or geothermal wells.

6.4 Thermal advection tests

The general principle a thermal advection test is shown in Figure 6.1a. In general, the principle is that the introduction of water with an anomalous temperature is tracked as it moves vertically in the well. Assuming that dispersion can be assumed to be symmetrical, then the movement of the temperature peak (or minimum) will be representative of the cross-sectionally averaged velocity. Qualitative inspection of the DTS data obtained allow the local flow characteristics to be inferred, for example, the identification of vertical flow, flow direction, and locations of inflows or outflows. Quantitative analysis involves calculation of vertical flow velocities from the displacement of plume peaks between successive DTS temperature profiles, and volumetric flow rates through additional consideration of the borehole diameter. Example temperature-depth profiles are shown in Figure 6.1a, calculated using a 1D advection-dispersion model. The plume peak, as it moves up and past the inflowing fracture, decreases in height and spreads vertically. At a given mid-point between peaks, the velocity is obtained from $\Delta z/\beta$.

The thermal advection tests carried out in Chapter 3, used DTS to track vertically a packet of heated water through a well to quantify vertical flow rates at the Ploemeur research site (Figure 6.4). Here a point heater, installed at a depth of 68 m, was used to generate a localised region of warmer water. The heating was switched off, and pumping at shallow depth simultaneously began, advecting the plume upwards. Tracking the plume peak allowed the velocity to be estimated to be 8.86 and 11.45 cm s^{-1} below and above a major inflow zone, respectively.

A similar set of tests was carried out by *Leaf et al.* (2012). Here, *Leaf et al.* (2012) used a thermally insulated hose, lowered down to the depth of interest, to add a small volume of heated fluid to the well bore. The movement of the heated fluid was then tracked with DTS. If attempting to measure very low velocities, then fluid injections are likely to disturb the hydraulic head in the well and therefore the velocity itself. In such

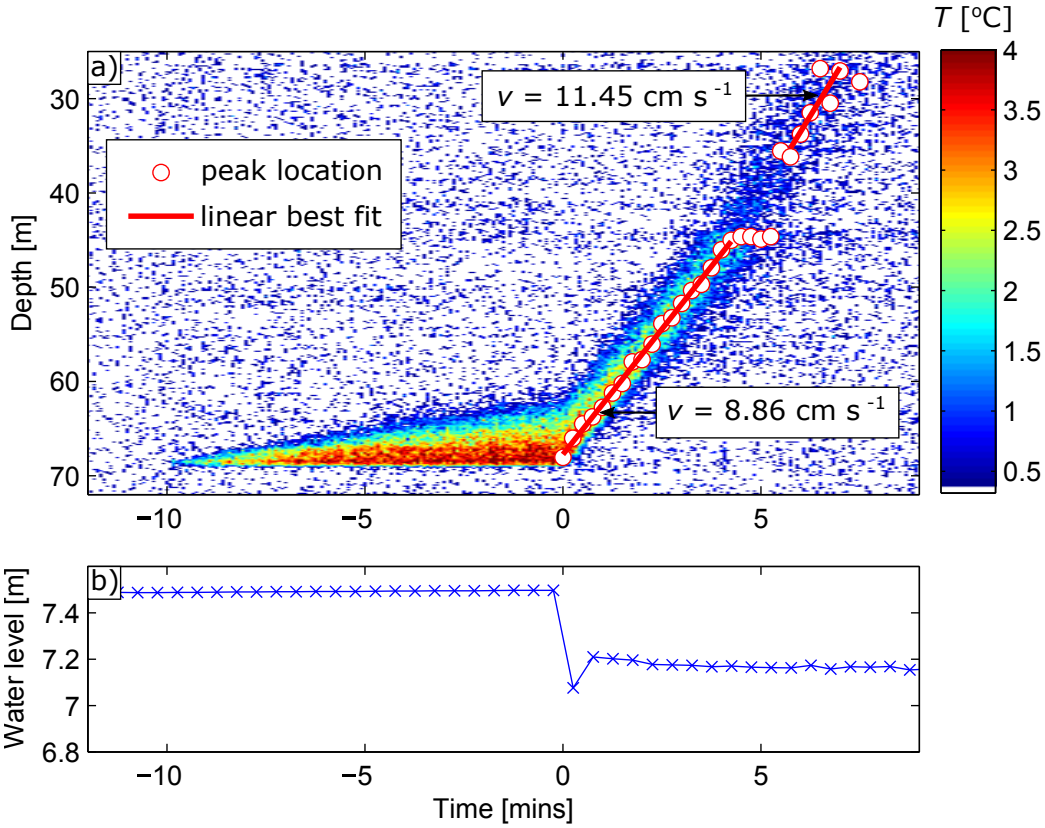

Figure 6.4: Thermal advection test carried out in borehole B2 at the Ploemeur research site (data from Chapter 3), showing a) DTS measured temperature increase (red circles indicate plume peak depth, red line indicates linear best fit), b) water level

conditions, point electrical heating is therefore preferable. Electrical point heating experiments with subsequent DTS temperature monitoring have also been carried by *Sellwood et al.* (2015a,b). Through a series of controlled tests, *Sellwood et al.* (2015b) showed that thermal advection tests were able to measure velocities in the range 10^{-1} to 10^{-1} m min^{1}.

As discussed in Chapter 3, one particular issue with this method is that large inflows have the potential to dilute the temperature signal such that it is not resolvable above the DTS instrument noise. An alternative method that may not suffer to the same extent is heating or injecting at a point continuously with time. With this a approach, the result is a front of warm or cold water that propagates vertically through the well. This has been applied mainly in deep wells (*Yamano and Goto*, 2005), and geothermal wells (*Ikeda et al.*, 2000; *Sakaguchi and Matsushima*, 2000). In such tests, the spacing of the front as it vertically propagates can be used to locate inflows and outflows. Additionally, the analytical solution presented by *Yamano and Goto* (2005) allows the temperature depth profile, following prolonged injection of water at the surface, to be inverted for flow.

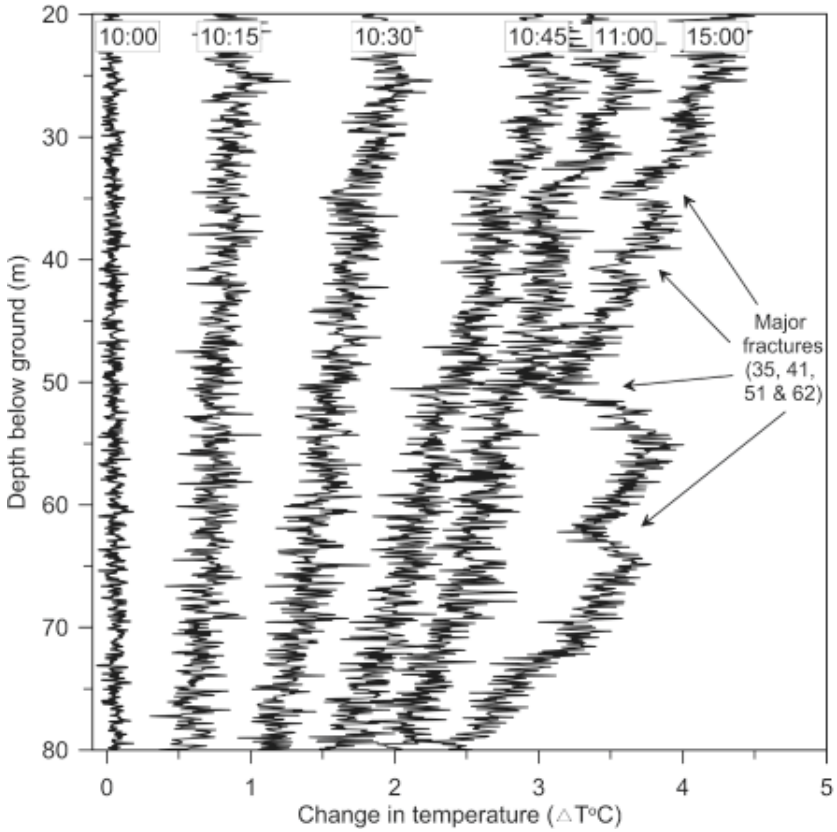

Figure 6.5: Schematic response after heating an open borehole with separate heating cable in both ambient conditions (10:15-11:00) and then during pumping (15:00), taken from *Banks et al.* (2014)

A further alternative that would not suffer from temperature signal loss, would be to use a heat source that is distributed over depth, rather than a point heat source. This was carried out by *Banks et al.* (2014) using a separate heating cable and a wrapped high resolution fibre optic cable separated by a fixed distance. Figure 6.5 shows DTS temperature data obtained prior to heating (10:00), during heating (10:15-11:00), and then after pumping is initiated at the top of the borehole (15:00). Once pumping starts, the inflowing fractures cause step-like reductions in fluid temperature. As suggested by *Banks et al.* (2014), it may be possible to derive a flow log based on the gradients of the temperature depth profile between fractures, and the size of the temperature reductions. While this method is not as simple as the point method for velocity estimation, it has the advantage that the entire borehole can be evaluated simultaneously.

6.5 Hybrid cable flow logging

In Chapter 4 it was shown that in-well vertical flow may also be monitored with hybrid cable flow logging. In this method, heating occurs within the same cable as the optical fibres, and the cable is deployed in a well in contact with flowing groundwater (Figure 6.1b). The principle is that when the cable is heated with a constant power input over time, the temperature inside the cable at steady state is a function of the velocity of the surrounding water. Higher velocities reduce the cable temperature by more effectively removing the thermal boundary layer in the fluid around the cable. In Figure 6.1b, moving up the well, the temperature decreases at the location of inflows, and remains constant along sections where the velocity remains constant.

This method has also been used to estimate wind speeds (*Sayde et al.*, 2015), and a modified approach adopted to estimate fluid fluxes in saturated porous media (*Aufleger et al.*, 2007). In Chapter 4 it was shown that for a typical armoured cable with radial symmetry, the temperature difference between the cable centre and water temperature ΔT is given by:

$$\Delta T = \frac{Q}{2\pi}\left(\frac{1}{hr_2} + \frac{1}{k_c}\ln\frac{r_2}{r_1}\right) \tag{6.2}$$

where Q [W m^{-1}], is the heat input to the cable, h [W m^{-2} K^{-1}], is the heat transfer coefficient (a function of fluid velocity), r_1 is the radius of the armouring, r_2 is the total cable radius, and k_c [W m^{-1} K^{-1}], is the thermal conductivity of the insulating material between $r1$ and $r2$. In practice, it is difficult to calculate h from first principles, so the ΔT-v relationship can be found empirically by taking measurements at a number of known flow velocities.

Figure 6.6a shows values of ΔT collected in an abstraction well at two different pumping rates and also under ambient conditions, from the field campaign reported in Chapter 4. A velocity profile obtained with an impeller flowmeter under pumped conditions is shown in Figure 6.6b for comparison. The hybrid cable method identifies step changes in flow from inflowing fractures that appear as step reductions in the ΔT. The hybrid cable log also however, suffers from some artefacts due to cable deployment. Where the cable touched the borehole wall, at around 60 m depth, the ΔT value is elevated. The presence of other objects inside the well, in this case 2 m spaced centralisers to keep the

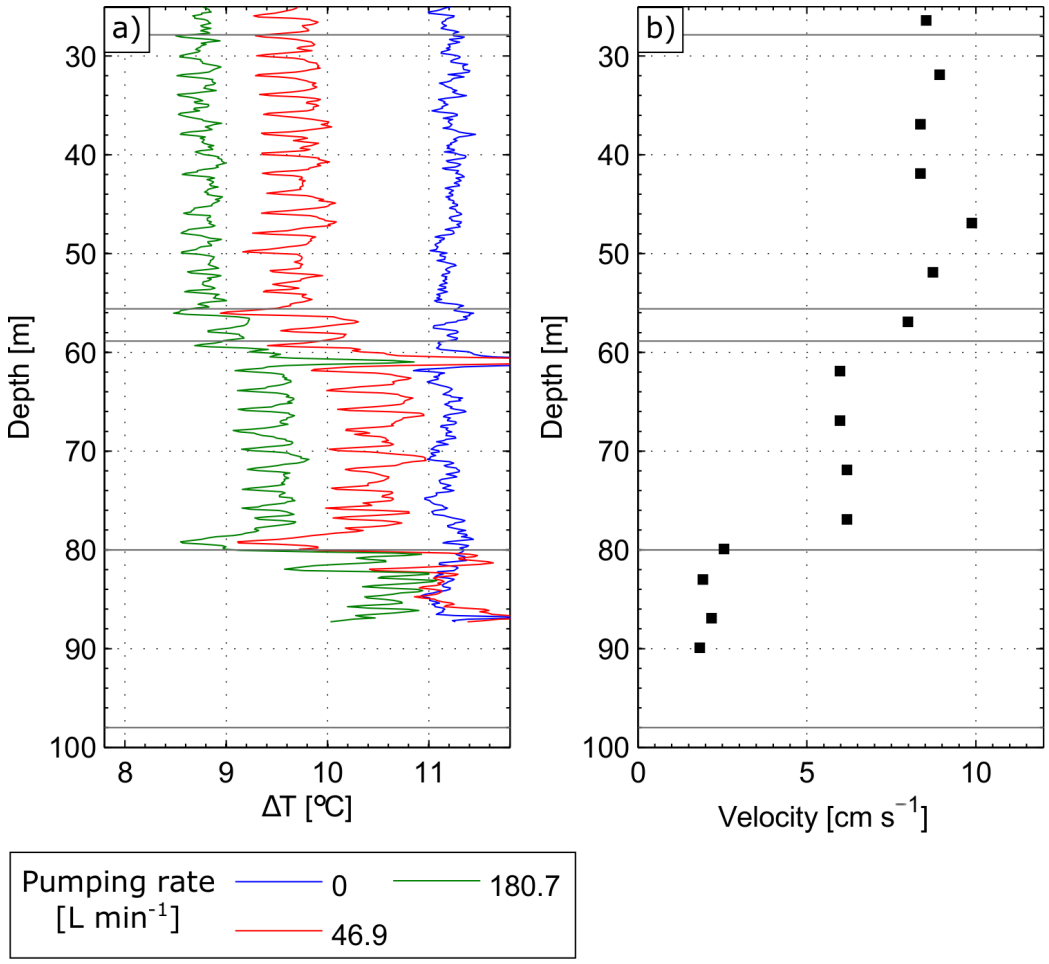

Figure 6.6: Comparison of a) ΔT profile obtained under ambient conditions (pumping rate of 0 L min^{-1}) and pumped (rates of 46.9 and 180.7 L min^{-1}), with b) velocity profile measured with an impeller flowmeter during a pumping test. Depths of transmissive fractures are shown as grey lines

heated cable in the center of the borehole, caused localised cooling thought to be due to the stimulation of vortices enhancing the heat transfer.

Figure 6.7 compares ΔT measured in the field with laboratory data and numerical model results presented in Chapter 6. The field data, obtained with an electrical power input of 21.0 W m^{-1}, have been scaled by multiplying by 2.38 to allow direct comparison with the other data sets obtained with a power input of 50 W m^{-1}. The data collected in the field show sensitivity in the range from 1 to around 30 cm s^{-1}. Despite the presence of artefacts in the original data set related to the deployment, which were removed as best as possible by applying a filter to the data, the field data show good agreement with the data obtained in the lab with flow parallel to the cable. The greatest sensitivity to flow occurs at low velocities, before the relationship between ΔT and v begins to plateau. This plateau occurs when the thermal boundary layer around the cable is completely removed.

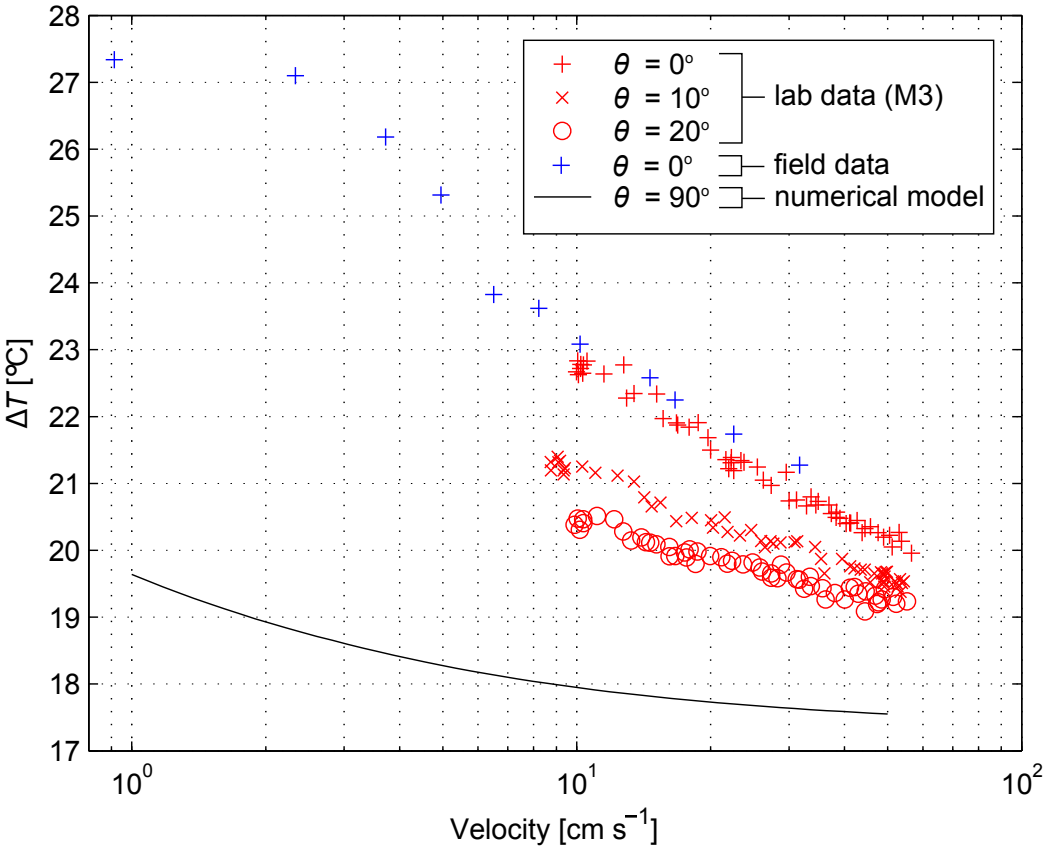

Figure 6.7: ΔT as a function of fluid velocity in laboratory experiments for cable angles θ of 0, 10, and 20°, the borehole deployment of Chapter 4, and numerical model of Chapter 6, for electrical power inputs of 50 W m^{-1}

The hybrid cable approach has the advantage that it is possible to monitor time varying velocity and flow changes more readily than with point thermal advection tests. However, since the response is sensitive to anything altering the efficiency of heat transfer from the cable, effects due to varying cable centralization or other instrumentation in the well disturbing the flow may be apparent. It is also likely to require empirical calibration in the field and each well prior to use.

6.6 Future developments

Both the hybrid cable and heat pulse methods are at a relatively early stage of development and there remain technical challenges that need to be addressed. With the hybrid cable method, data collected in field trials to date have always been affected by temperature anomalies located around centralisers located on the cable. This could be investigated through numerical modelling of different deployment options. In trials of the heat pulse

method, variable coupling between the cable and borehole wall has been shown to produce anomalies in heating phase data. Work is still also needed, in the case of heat pulse tests, to translate the DTS observed response to a quantitative estimate of groundwater flux. However, where the scale of the flow is below the spatial resolution of the instrument (e.g. within fractures), the response is likely to be ambiguous.

The use of DTS in the subsurface is not affected by some of the issues affecting surface water applications, such as vegetation growth, shading, and the potential for exposure or burial. Where steep temperature gradients exist, for instance in Active-DTS methods, the location of the cable within the well bore is critical and the degree to which this is controlled is critical. There are similarities here with DTS methods for soil moisture estimation, where DTS promises to give spatially distributed measurements of this parameter, but also requires that when it is deployed, the cable is uniformly positioned. This can be a challenge in the field.

DTS is just one of a number of distributed fibre optic sensing approaches. Distributed measurements along fibre optic cables are also possible for pressure, strain, and acoustics. Recently, Distributed Acoustic Sensing (DAS), based on Rayleigh scattering, has been explored. DAS in effect gives a fully distributed array of geophones along a fibre optic cable. Depending on the phase shift of backscatter signal from closely located intervals, the base unit can determine the strain on the cable which is then converted into an acoustic signal (*Parker et al.*, 2014). DAS has seen much trial use in the oil and gas sectors and has been applied to determine vertical seismic profiles, micro-seismic events during well stimulation, hydraulic fracturing, and flow monitoring during production. Early trials suffered from low signal to noise ratio, however, this has been improved through better coupling of the fibre to the subsurface through installation behind casing (*Daley et al.*, 2013). DAS has also been applied in CO_2 sequestration (*Freifeld et al.*, 2014). It is possible to have multiple fibres for different purposes in the same cable construction, so, as DAS becomes more commonplace, DAS data may be increasingly presented alongside either passive or active DTS data. By combining different distributed fibre optic approaches, it may be possible to reduce the uncertainty in subsurface interpretations.

6.7 Conclusion

DTS has been used in studies of aquifer heterogeneity, groundwater flow, subsurface heat transport, geothermal energy, and CO_2 sequestration. Such deployments are typically either passive or active. In passive mode, DTS can provide near real time temperature monitoring, simultaneously, potentially in multiple deep wells at high spatial resolution. This allows dynamic processes to be monitored in detail, and long data sets through time to be efficiently collected. DTS deployed in active mode also benefits from these generic advantages, while additionally creating a thermal signal in the subsurface. These methods primarily aim to measure in-well flow (thermal advection tests and hybrid cable flow measurements), and thermal properties and natural gradient groundwater flow (heat pulse tests). While there are some similarities between the active methods, it is important to note the differences in the sensitivities of each method and the underlying physics. Despite this, when considering undertaking such experiments some may easily be combined to efficiently obtain different but complementary data. For instance, after heating a cable for a long duration, it may be possible after hybrid cable flow logging to monitor the return of the slightly warmed borehole to background temperature. The first measurements would give flow in the well, while the second may yield information on aquifer heterogeneity and thermal properties.

When to use DTS in a borehole setting requires careful consideration. If there is a passive process to be monitored with either little time or depth variability, then a log obtained with a high resolution temperature probe, or time series from a data logger at a particular depth might yield equivalent or better datasets with less effort. DTS is proving invaluable in applications where there is significant time and depth variability. Here, the required effort in terms of providing power supply, calibration baths, and the post-processing of the data should far be outweighed by the increased information with the complete space-time coverage. Furthermore, some of the emerging Active-DTS methods, such as thermal recovery tests with combined fibre optic and heating cables, and hybrid cable flow logging, are methods specific to the DTS approach where fibre optic sensing is an integral component.

While there are many literature examples of subsurface DTS, there is scope for future work as instrument and cable performance improves and develops. Further work is also

needed to assess the sensitivity of active methods under different conditions to both in well vertical flow and natural gradient flow, and turn them into readily deployable monitoring solutions. Ongoing developments in the field of hydrogeophysics, and recent advances with DAS, mean that there is great potential to provide complementary data sets to supplement DTS temperature data. DTS is an extremely adaptable monitoring solution that is allowing complex environmental problems to be addressed.

Chapter 7

Thesis conclusions and further research

7.1 Chapter summary

Three different approaches using DTS have been investigated using a combination of numerical modelling, laboratory experiments, and field trials. In the following, the main research conclusions are summarised and areas for future work discussed.

7.2 Main research developments

7.2.1 Thermal dilution tests

Chapter 2 focussed on understanding the response of thermal dilution tests - a form of test not unique to using DTS but that is facilitated by the high depth-time coverage. A numerical model was used to test the sensitivity range of thermal dilution tests to groundwater flow. Unlike typically conservative solute dilution tests, where tracer decay is due solely to groundwater advection in all but the lowest permeability settings, the thermal dilution test response may be governed by both advection and conduction. The numerical model indicated that there exists a lower limit to groundwater flow detection, at around 5x10^{-6} m s^{-1}. Below this, any advective cooling effect is overprinted by conductive cooling, which dominates. Above this limit, the temperature decay becomes increasingly dominated by groundwater advection. This threshold represents a relatively high flow in porous media

that would be typically expected in sands and gravels, and may also be present in lower permeability materials when the hydraulic gradient is elevated (e.g. in the vicinity of an abstraction well).

A thermal dilution test was then carried out at the Ploemeur research site in four boreholes. The temperature response showed the lithological contrasts between the granite and mica schist. A numerical model was deployed to extract the apparent thermal conductivity profiles from the cooling data. These profiles suffered from non-radial cooling at the base of the test section that was not incorporated in the numerical model. Transmissive fractures at shallower depths were not however visible. It could be that under the test conditions, ambient flow through the fracture was too small. Furthermore, the relatively poor spatial resolution of the instrument deployed (at around 4 m), is likely to have averaged out any cooling effect localised to the fracture.

7.2.2 T-POT point heating tests

In Chapter 3, point heating tests were carried out in a borehole at the Ploemeur research site. This involved heating a small interval in the borehole, and then monitoring the vertical migration of this warmed fluid. Tracking the peak of the plume showed that this moved with a constant velocity along the travel path from the heating location, up to the next fracture. An additional inflowing fracture diluted the thermal signal, but, was still detectable above this but with increased uncertainty. The method, using electrical heating, is improved over previous approaches which have used injected warm water to produce a thermal anomaly, which has the potential to disturb the hydraulic head and flow in the well. The T-POT method is therefore a quick method that can be used in the field to measure vertical flows.

7.2.3 Hybrid cable flow measurements

In Chapter 4, a prototype hybrid cable set-up was constructed and deployed at the Ploemeur research site. The cable set-up was subjected to a number of pumping rates to develop a relationship between the measured ΔT and flow velocity. The results showed that from 1 cm s^{-1} to 30 cm s^{-1}, there was an approximately 2.5 °C reduction in ΔT, which was readily detectable with DTS. Applying this relationship, found empirically over a

small interval where the velocity was known, allowed the complete profile of velocity to be estimated in the borehole. It was found however, that the profile of temperature during heating, and therefore ΔT and estimated velocity, included artefacts due to the installation. This included regularly spaced 'cold' spots, associated with the cable centralisers, and an anomalously warm region thought to coincide with a depth of deviation in the borehole where the cable touched the borehole wall.

In Chapter 5, a similar heated cable was tested in a recirculating flume and the relationship between ΔT and fluid velocity established for different electrical power inputs and cable angles. The data from a series of calibration experiments showed that at a given velocity, the value of ΔT scales with electrical power input, as does the measurement sensitivity. The value of ΔT is also dependent on the cable angle and appears to decrease linearly with the sine of the contact angle (from a maximum at 0°, to a minimum at 90°). This also impacts on the measurement sensitivity, with greater sensitivities achieved for flow closer to parallel. The deployment of a single straight cable does however present the problem of heat accumulation, which causes the value of ΔT to increase along the path length.

A numerical model was then used to determine whether the sensitivity of the hybrid cable could be enhanced through the cable construction. The model results indicated that only the electrical power input was significant in altering the measurement sensitivity. Simulations run with low velocities indicated that buoyancy and free convection are significant drivers of the ΔT response at velocities below around 1 cm s^{-1}, with this threshold being dependent on electrical power input. Simulations were also run using a modified cable design, incorporating recesses in the cable jacket. This had a positive effect on the hybrid cable response, and is therefore a potential way to improve the measurement sensitivity.

7.3 Areas for future work

The temperature response in thermal dilution tests to fracture flow was not tested in the thesis. This would require 3D numerical modelling, and while this may be an interesting exercise, it may be of limited practical utility. In field deployments there are likely to be too many unknowns, such as fracture aperture, inclination, and the exact position of the

Gaussian weighted DTS averaging window relative to the fracture. The most promising aspect of this appears to be in sedimentary aquifers, as has been recently reported *Hausner et al.* (2015).

The T-POT approach does not place high accuracy demands on the DTS and can therefore be used with almost any DTS instrument. Calibration of the temperatures is also not strictly necessary if all that is required is an estimate of the flow, removing the need for calibration baths that are time consuming to set-up in the field. It should therefore be possible to produce a safe, portable, and easy to use system for field deployment.

While the hybrid cable method offers the potential to measure flows simultaneously through an entire borehole, and continuously in time, further work is needed to produce a system, using knowledge gained from the numerical modelling and laboratory work, that does not suffer from the deployment artefacts seen in Chapter 4. Field deployments need to ensure that the heated cable, reference cable, and power supply cable are located in a uniform way throughout the borehole using a system of fixings or centralisers. Here there are potentially two options. The first would be to design centralisers that impact negligibly on the flow. This seems unlikely, as the centralisers used in the field deployment of *Read et al.* (2013) were already relatively thin. Alternatively, the centralising system could be comprised of components spaced more frequently than the spatial resolution of the instrument so that they would appear 'invisible' in the ΔT response. Such a system could, for instance, be a continuous mesh through which the heated, reference, and power supply cables are all woven, similar to the cable deployment of *Banks et al.* (2011). It would also be worth pursuing the use of composite cable constructions that include two separate heatable elements, rather than an armoured cable, to determine whether or not this has an impact on ΔT. The deployment of such cables in the hybrid cable approach would mean that a separate power supply cable would not be necessary, simplifying the field set-up, but it has not yet been determined whether the potential variable separation between the heating element and optical fibres is significant.

Appendix A

Paper 1

Read, T., O. Bour, V. Bense, T. Le Borgne, P. Goderniaux, M. Klepikova, R. Hochreutener, N. Lavenant, and V. Boschero, Characterizing groundwater flow and heat transport in fractured rock using fiber-optic distributed temperature sensing, *Geophysical Research Letters*, *40*, 2055–2059, 2013

GEOPHYSICAL RESEARCH LETTERS, VOL. 40, 1–5, doi:10.1002/grl.50397, 2013

Characterizing groundwater flow and heat transport in fractured rock using fiber-optic distributed temperature sensing

T. Read,[1] O. Bour,[2] V. Bense,[1] T. Le Borgne,[2] P. Goderniaux,[2,3] M.V. Klepikova,[2] R. Hochreutener,[2] N. Lavenant,[2] and V. Boschero[2]

Received 11 February 2013; revised 19 March 2013; accepted 20 March 2013.

[1] We show how fully distributed space-time measurements with Fiber-Optic Distributed Temperature Sensing (FO-DTS) can be used to investigate groundwater flow and heat transport in fractured media. Heat injection experiments are combined with temperature measurements along fiber-optic cables installed in boreholes. Thermal dilution tests are shown to enable detection of cross-flowing fractures and quantification of the cross flow rate. A cross borehole thermal tracer test is then analyzed to identify fracture zones that are in hydraulic connection between boreholes and to estimate spatially distributed temperature breakthrough in each fracture zone. This provides a significant improvement compared to classical tracer tests, for which concentration data are usually integrated over the whole abstraction borehole. However, despite providing some complementary results, we find that the main contributive fracture for heat transport is different to that for a solute tracer. **Citation:** Read, T., O. Bour, V. Bense, T. Le Borgne, P. Goderniaux, M.V. Klepikova, R. Hochreutener, N. Lavenant, and V. Boschero (2013), Characterizing groundwater flow and heat transport in fractured rock using Fiber-Optic Distributed Temperature Sensing, *Geophys. Res. Lett.*, *40*, doi:10.1002/grl.50397.

1. Introduction

[2] Heterogeneous aquifers, such as fractured rocks, often require detailed characterization for water resources assessment and for the prediction of potential contaminant pathways [*Neuman*, 2005]. Such characterization may consist of simply identifying the most transmissive fractures to the formulation of a statistical model of the solute transport properties of the fracture network such as permeability and dispersivity. This is usually carried out in situ through cross-flowmeter tests or hydraulic response tests [*Paillet*, 1998; *Illman et al.*, 2009], or with tracer experiments using solutes. In between two or more boreholes, tracer tests allow the advective velocity and dispersion of solutes to be quantified [e.g., *Becker and Shapiro*, 2003]. While these well-established aquifer characterization techniques successfully yield results in terms of flow through the fracture network, the requirement for frequent sampling and subsequent analysis may be time consuming and expensive. Only with sophisticated multi-depth sampling, multi packer systems, or repetitive continuous logging, can a more continuous log along the borehole be obtained. This, as opposed to a time series recorded at a single depth that incorporates the response of all transmissive features intersecting the borehole, is required for the analysis of the transport properties through individual fracture zones or permeable units. There is, therefore, a great need for new sensors capable of providing continuous measurements in space and time.

[3] The availability of fully distributed fiber-optic temperature sensors (FO-DTS) allows such continuous measurements for temperature [*Selker et al.*, 2006; *Tyler et al.*, 2009]. It is long-established that heat can be used as a tracer to estimate groundwater flow in a range of hydrogeological settings [*Anderson*, 2005]. Heat is more diffuse than solutes by several orders of magnitude, but in some cases, has been shown to be a reasonable proxy for solute tracers and hence can be used to calibrate models of hydraulic conductivity distribution [*Ma et al.*, 2012]. In fractured media, heat may be expected to bring different and complementary information compared to solute tracers, since it is much more sensitive to matrix diffusion processes [*Geiger and Emmanuel*, 2010].

[4] The application of FO-DTS has been demonstrated in boreholes for thermal conductivity estimation and surface temperature reconstruction [*Freifeld et al.*, 2008]. FO-DTS was also used to infer fluid flow rates inside boreholes as an alternative for a directly measured flow log [*Leaf et al.*, 2012]. In the application of aquifer characterization as described above, FO-DTS deployments have been limited to only a few case studies [*Hurtig et al.*, 1994; *Macfarlane et al.*, 2002], and there have been significant advances in the measurement precision of FO-DTS systems in the intervening time. Here, we demonstrate the potential for FO-DTS monitoring of heat dilution and tracer tests in heterogeneous systems such as fractured rock aquifers. We show how cross flow rates from fracture zones and temperature breakthrough curves for individual fractures can be calculated and find that FO-DTS offers some significant advantages over point temperature loggers for monitoring such tests and for characterizing flow and heat transport in fractured rocks.

2. Methodology

[5] Thermal test data were collected at Ploemeur, Brittany, northwest France, in four boreholes (B1, B2, B3, and F22), separated by a distance of 6 to 30 m and ranging from 70 to 100 m deep (Figure 1). The geology of the site

[1]School of Environmental Sciences, University of East Anglia, Norwich, UK.
[2]Géosciences Rennes (UMR 6118), University of Rennes 1, Rennes, France.
[3]Department of Geology and Applied Geology, University of Mons, Mons, Belgium.

Corresponding author: T. Read, School of Environmental Sciences, University of East Anglia, Norwich, UK. (Tom.read@uea.ac.uk)

0094-8276/13/10.1002/grl.50397

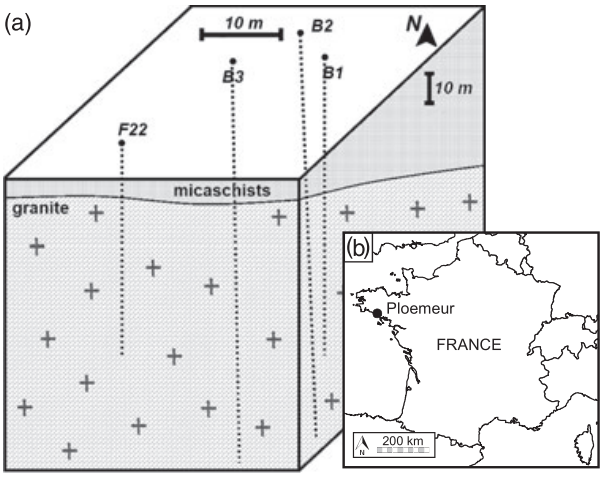

Figure 1. (a) Borehole array configuration and (b) location of the site.

consists of mica-schist, underlain by an intrusive granite, the contact of which provides a locally significant groundwater resource [*Le Borgne et al.*, 2004; *Ruelleu et al.*, 2010]. The site is considered a typical fractured crystalline basement aquifer and has been subject to numerous hydraulic [*Le Borgne et al.*, 2004, 2007], and geophysical tests [e.g., *Dorn et al.*, 2012]. Interference tests have suggested that fluid flow and associated tracer transport between boreholes are concentrated in only a few transmissive fracture zones [*Le Borgne et al.*, 2007]. Solute dispersion is dominated by fracture network connectivity showing that few interconnecting fractures contribute to solute transport at the scale of several meters by which the boreholes are separated [*Dorn et al.*, 2012].

[6] For the FO-DTS experiments discussed here, a single BruSteel (Brugg Cables, Switzerland) steel armored fiber-optic cable of 1 km in length was installed in all four boreholes for the continuous monitoring of temperature. Additionally, two coiled sections of cable were placed in a calibration bath consisting of water wetted ice and monitored with a submersible temperature logger. We deploy the widely used Oryx-DTS unit (Sensornet Ltd., UK, Herts), configured to take single-ended temperature measurements with a spatial sampling interval of 1.01 m along the cable and an integration time of 2 min. To convert the laser backscatter detected by the instrument to a temperature, we post-processed the raw backscatter data to further improve the instrument accuracy using the dynamic calibration procedure outlined by *Hausner et al.* [2011]. However, this was not possible for the thermal dilution tests due to warming of the ice baths; so here, we rely on the inbuilt calibration software of the device.

2.1. Thermal Dilution Test Set-Up

[7] Thermal dilution tests were conducted in borehole B3. The method we employ is similar to a borehole dilution test using solutes [e.g., *Novakowski et al.*, 2006; *Brouyère et al.*, 2008], but here using heat instead. A similar method has been applied in lined boreholes using the Active Line Source technique [*Pehme et al.*, 2007]. Since we are interested in cross flowing fractures, an inflatable packer was installed at a depth of 44 m to prevent ambient vertical flow in between fractures tapping into the borehole which otherwise occurs in most boreholes at the site. We injected water, heated to 50°C using a mobile heating system, just above the packer at 43 m. The borehole was pumped at the same rate at shallow depth in order to draw the warm injected water upwards. During the experiment, the hydraulic head in the borehole was monitored to verify that any changes were small enough to ensure no net flow in or out of the borehole, taking into account effects of temperature on fluid density. The thermal dilution test was carried out under ambient conditions and then under cross pumping conditions, with B2 at a distance of 10 m pumped at 140 L min^{-1}.

2.2. Thermal Tracer Test Set-Up

[8] For the thermal tracer test, we concentrate on B1, the injection well, and B2, the abstraction well, separated by approximately 6 m. Two inflatable packers were used to hydraulically isolate a known fracture at a depth of 78.7 m in B1 (B1-79). Water was injected into a 1-m interval across this fracture at a constant rate and temperature of 35 L min^{-1} and 50°C. Simultaneously, B2 was pumped at a constant rate of 140 L min^{-1}. The injection of heated water in B1 continued for approximately 11 h and was followed by a "push" of water at ambient groundwater temperature for 5 h to test the heat recovery under similar hydraulic conditions. Subsequently, the injection at B1 ceased but pumping in the abstraction well, B2, continued. In addition to monitoring by FO-DTS, temperature in the abstraction well was recorded continuously using three temperature loggers located at set depths of 40, 60, and 72 m.

3. Results

3.1. Thermal Dilution Tests

[9] FO-DTS data for the thermal dilution tests carried out in B3, including both the injection and cooling phases, are shown in Figures 2a and 2c for ambient and cross pumping conditions, respectively. In both cases, $t = 0$ h corresponds to when the injection stopped. By the time the injection ceases, the fluid between the point of injection and abstraction is replaced with water approximately 25 to 40°C warmer than ambient temperatures. During the cooling phase, the absolute temperature values are clearly influenced by the initial conditions at 0 h which were not entirely isothermal. To correct for the influence of the initial non-isothermal distribution of heat in the borehole on the depth-variant cooling rates observed later, the Relative Temperature Anomaly (*RTA*) was calculated according to

$$RTA(z,t) = \frac{T(z,t) - T_{ambient}(z)}{T_{initial}(z) - T_{ambient}(z)} \quad (1)$$

where $T_{ambient}$ is the temperature prior to the start of the injection and $T_{initial}$ is the temperature when the injection ceased. This scales the initial temperature anomaly to unity at all depths, with a value of zero representing a full return to pretesting ambient temperature conditions. The cased section cools more slowly than the open section below, which can be explained by the larger borehole diameter and low thermal conductivity casing material. From the end of the casing to 36 m, the cooling is relatively uniform, which corresponds well with core data and flow logs that suggest there are no significant transmissive fractures intersecting the borehole along this depth interval (Figures 2b and 2d). A zone of enhanced cooling beneath 36 m can be readily distinguished

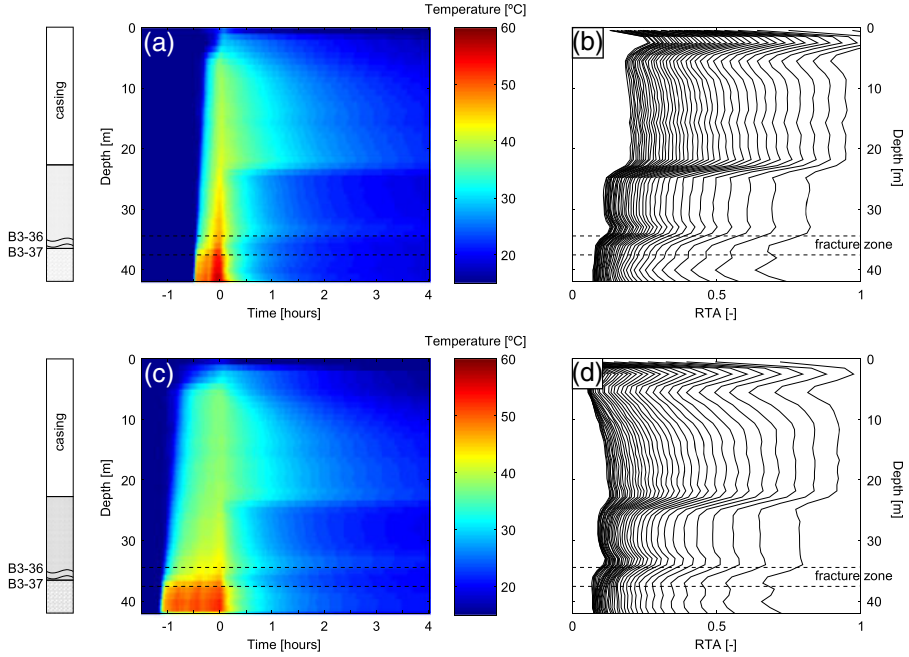

Figure 2. Temperature in B3 during the thermal dilution test under (a) ambient conditions and (c) while pumping B2, and (b) corresponding Relative Temperature Anomaly and (d) at normalized times of 0.2 to 8 [-] (right to left). The time was normalized to account for the different injection durations, with 1 h taken as the standard injection length.

in ambient and cross pumping conditions. The top of this zone coincides with two transmissive fractures located just above the transition from mica-schist to granite identified by *Le Borgne et al.* [2007] and continues to 42 m.

[10] The fast cooling below 36 m is potentially due to both advective flow in the fracture zone, and also partly to the higher thermal diffusivity of granite compared to mica-schist (1.8×10^{-6} and 1.4×10^{-6} $m^2 s^{-1}$, respectively). Nevertheless, during the injection phase, in particular during cross-pumping (Figure 2c), the injected water is cooled significantly as it passes the fracture zone. During this time, the contrast in temperature across the fracture zone would not be explained by the contrast in thermal diffusivity between granite and mica-schist. In the following, we assume that during the injection phase, this step-like change in temperature across the fracture zone is due solely to an advective effect.

[11] To estimate the cross-flow rate Q_f [L min^{-1}] through the fracture zone, we use a mixing equation applicable during the injection phase:

$$Q_f = \left(\frac{T_{below} - T_{above}}{T_{above} - T_f} \right) Q_{inject} \qquad (2)$$

in which Q_{inject} [L min^{-1}] is the rate of injection, and T_{above} and T_{below} are the temperatures above and below the fracture zone of interest, respectively, and T_f is the temperature of groundwater flowing through the fracture zone, which is assumed to be constant with time. This mixing equation assumes that water from the cross flowing fracture enters the borehole and becomes fully mixed before being advected upwards or leaving the borehole. Application of equation (2) using the FO-DTS data for B3 and a T_f of 15°C results in a calculated cross flow of 3.4 L min^{-1} for the fracture zone at 36 m. When the thermal dilution test was repeated, but under cross pumping conditions, the calculated flow through this zone increases to 3.9 L min^{-1}, a slight but measurable change. Hence, using FO-DTS to monitor thermal dilution tests allowed us to measure significant ambient flow through the identified fracture. The ambient flow measured through the fracture is quantitatively comparable with the vertical ambient flows measured by precise borehole flowmeters [*Le Borgne et al.*, 2007]. Such ambient flows are explained by the location of the site in a discharge area of the catchment. The effect of pumping in an adjacent well, although small, apparently produces a temperature effect strong enough to be detected.

3.2. Thermal Tracer Tests

[12] Time series of temperature data from the temperature loggers and corresponding post-processed FO-DTS measurements at these depths during the thermal tracer test are shown in Figure 3a. The data show good agreement with the FO-DTS data having high temporal repeatability characterized by a standard deviation of 0.03°C. Thus, the FO-DTS appears to be an excellent tool for detecting and monitoring temperature change during thermal tracer tests.

[13] FO-DTS data for all depths in the abstraction well are shown in Figure 3b in terms of a temperature breakthrough, calculated as the difference between the measured temperature and the mean of the 10 temperature-depth profiles obtained prior to the injection of heated water. Based on visual inspection of the temperature data alone, there are three readily identifiable fractures contributing to the upflow in the borehole to the pump. At approximately 79 and then 67 m, there are sources of warmer water that must therefore be fracture zones that are in connection with the fracture zone B1-79 in the injection well. Between 57 and 59 m, there appears to be a wider zone of fracture inflows that results in the cooling of the upflowing borehole water and therefore appear to be disconnected from B1-79. From this point upwards, there appear to be no thermal breakthroughs.

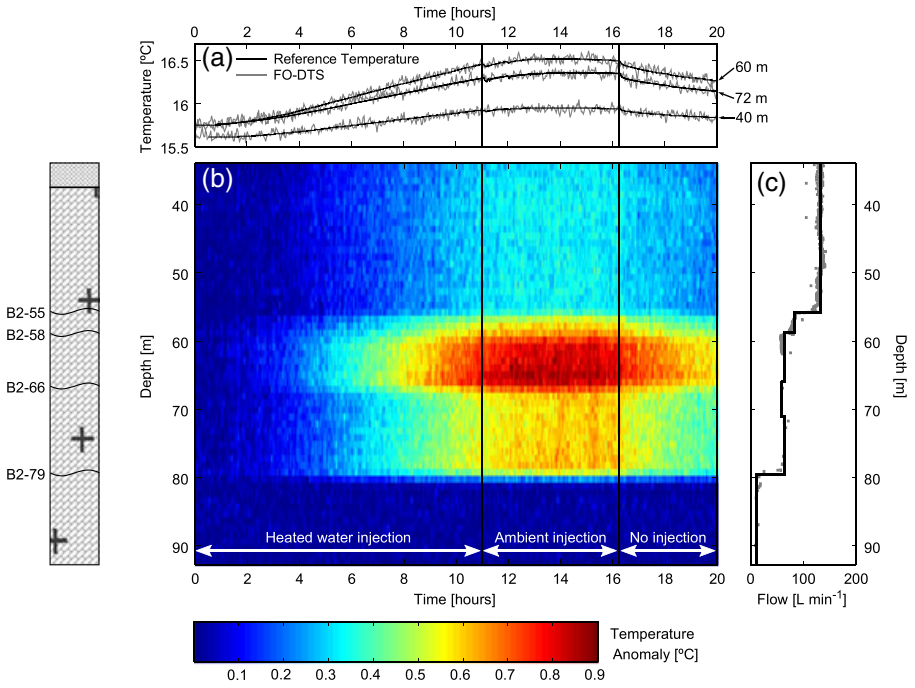

Figure 3. (a) Temperature logger and DTS measured temperature at the corresponding depths during the thermal tracer test from B1 to B2, (b) DTS measured temperature anomaly for all depths, and (c) measured flow in B2 for a pumping rate of 140 L min^{-1} with solid line to indicate the flow profile assumed for the application of equation (3).

[14] In the following, we estimate the contribution of each fracture to the transport of heat during the thermal tracer test and compare it to other tracer tests. Applying a simple conservative mixing equation, the temperature of groundwater entering the borehole from a fracture zone is given by:

$$T_f = \frac{Q_{above}T_{above} - Q_{below}T_{below}}{Q_{above} - Q_{below}} \quad (3)$$

For this calculation, the FO-DTS measured temperature in B2 was combined with flowmeter data (Figure 3c). The high frequency noise in the FO-DTS data, which would otherwise be amplified (approximately 0.1°C), was removed by fitting a second degree polynomial using a weighted linear least-squares regression to each of the thermal breakthrough curves along the borehole length. The flow log indicated that there was no detectable inflow at 66 m where the largest step change in temperature was observed, whereas two closely spaced fractures can be seen in an optical borehole log in this zone. For the purpose of the thermal breakthrough calculation, we assume that the fractures contribute 5 L min^{-1} as this is approximately the detection limit of the impeller flowmeter for the borehole diameter. The true temperature breakthrough from this fracture zone is likely to be higher than calculated in the following, as the flow from this fracture is potentially much less than this.

[15] Using equation (3), Figure 4 provides the calculated temperature of the inflow to B2 from each fracture zone. The largest temperature response (4.0°C) is from fracture B2-66. This breakthrough is very rapid and continues for approximately 1 h after the injection switched to a cold water push. In comparison, B2-79 responds more slowly and rises to a lower temperature (0.8°C). The calculated responses for fracture zones B2-58 and B2-55 confirm the initial observation that no heat was recovered from these fractures during the duration of the experiment.

[16] Compared to solute tracer tests, performed at the same location, the main differences observed are the time, amplitude, and spatial distribution of the breakthrough. For instance, with a slug injection of the fluorescent dye uranine, the peak arrives at B2 after around 20 min, but only very slight changes are observed at these times using heat as a tracer (Figure 4). Thus, the thermal breakthrough is significantly attenuated due to fracture-matrix heat exchange.

[17] *Dorn et al.* [2012] carried out a solute tracer test between B2 and B1 by injecting a saline tracer into the same

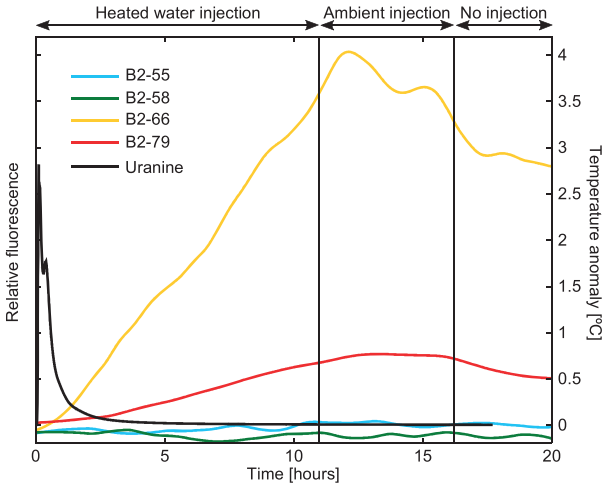

Figure 4. Uranine breakthrough and calculated temperature anomaly of the inflowing fractures B2-55, B2-58, B2-66, and B2-79 during the thermal tracer test.

fracture and pumping B2 at a rate of 30 L min^{-1}. During their test, the main contributing fracture in B2 was B2-79 [*Dorn et al.*, 2012, Figures 5 and 7]. Fracture B2-66 was detected in the ground-penetrating radar time-lapse images [*Dorn et al.*, 2012, Figure 10a], but did not contribute significantly to conductivity variations in the borehole. For the duration of our thermal test, the main contributive fracture was B2-66. These differences are significant as they confirm that thermal and solute tracer tests do not provide the same information on the transport pathways, even at the scale of a few meters. This could be explain by density effects that would drive the saline tracer downwards and heat upwards, while in addition, heat transfer is much more sensitive to fracture-matrix exchanges compared to solute transfer. Flow channeling may also be a factor since it may reduce the fracture-matrix exchange area [e.g., *Neuville et al.*, 2010]. In the present case, fracture B2-66 may be of a small aperture, with strongly channelized flow, that would explain a negligible flow contribution and only small solute tracer recovery but an important temperature breakthrough as we observe.

4. Conclusions

[18] We find that FO-DTS is significantly advance over the traditional point temperature sensors in the borehole environment that enables thermal dilution or thermal tracer tests to be monitored accurately and efficiently in both time and space. Such thermal experiments offer new insights in the characterization of fractured media, as they provide complementary information with respect to solute tracer experiments. In particular, the thermal dilution test was shown to be an efficient method to estimate cross flowing groundwater through a fracture zone.

[19] FO-DTS was also found very useful to provide a detailed characterization of heat transport through a fracture network. The thermal breakthrough curve is strongly attenuated due to fracture-matrix interactions, and the relative contribution of the different fractures is found to be strikingly different than for solute transport potentially due to channeling and density effects. For this application, the main advantages of FO-DTS are that it avoids the risk of disturbing the fluid column by raising and lowering a probe, and it generates a synchronous data set with measurements distributed over the entire borehole. Hence, we anticipate that FO-DTS combined with heating experiments will become a more commonplace geophysical method for aquifer characterization.

[20] **Acknowledgments.** Funding for this work was provided by the INTERREG IV project CLIMAWAT, Marie Curie ITN project IMVUL, the national network of hydrogeological sites H+, and a Natural Environment Research Council (NERC) studentship (NE/J500069/1) to Tom Read. The authors thank Alain Dassargues and S. Brouyère from the Université de Liegè for generously lending the portable water heater. We would also like to thank the two reviewers for their constructive comments.

[21] The Editor thanks Matthew Becker and Niklas Linde for their assistance in evaluating this paper.

References

Anderson, M. P. (2005), Heat as a ground water tracer, *Ground Water*, *43*(6), 951–68, doi:10.1111/j.1745-6584.2005.00052.X.

Becker, M. W., and A. M. Shapiro (2003), Interpreting tracer breakthrough tailing from different forced-gradient tracer experiment configurations in fractured bedrock, *Water Resour. Res.*, *39*(1), 1024, doi:10.1029/2001WR001190.

Brouyère, S., J. Batlle-Aguilar, P. Goderniaux, and A. Dassargues (2008), A new tracer technique for monitoring groundwater fluxes: The finite volume point dilution method, *J Contam. Hydrol.*, *95*(3-4), 121–40, doi:10.1016/j.jconhyd.2007.09.001.

Dorn, C., N. Linde, T. Le Borgne, O. Bour, and M. Klepikova (2012), Inferring transport characteristics in a fractured rock aquifer by combining single-hole ground-penetrating radar reflection monitoring and tracer test data, *Water Resour. Res.*, *48*, W11521, doi:10.1029/2011WR011739.

Freifeld, B. M., S. Finsterle, T. C. Onstott, P. Toole, and L. M. Pratt (2008), Ground surface temperature reconstructions: Using in situ estimates for thermal conductivity acquired with a fiber-optic distributed thermal perturbation sensor, *Geophys. Res. Lett.*, *35*, L14309, doi:10.1029/2008GL034762.

Geiger, S., and S. Emmanuel (2010), Non Fourier thermal transport in fractured geological media, *Water Resour. Res.*, *46*, W07504, 1–13, doi:10.1029/2009WR008671.

Hausner, M. B., F. Suárez, K. E. Glander, N. V. D. Giesen, J. S. Selker, and S. W. Tyler (2011), Calibrating single-ended fiber-optic Raman spectra distributed temperature sensing data, *Sensors*, *11*(11), 10,859–10,879, doi:10.3390/s111110859.

Hurtig, E., S. Großwig, M. Jobmann, K. Kuhn, and P. Marschall (1994), Fibre-optic temperature measurements in shallow boreholes: Experimental application for fluid logging, *Geothermics*, *23*(4), 355–364.

Illman, W. A., X. Liu, S. Takeuchi, T.-C. J. Yeh, K. Ando, and H. Saegusa, (2009), Hydraulic tomography in fractured granite : Mizunami underground research site, Japan, *Water Resour. Res.*, *45*, W01406, doi:10.1029/2007WR006715.

Le Borgne, T., O. Bour, J. R. de Dreuzy, P. Davy, and F. Touchard (2004), Equivalent mean flow models for fractured aquifers: Insights from a pumping tests scaling interpretation, *Water Resour. Res.*, *40*, W03512, doi:10.1029/2003WR002436.

Le Borgne, T., et al. (2007), Comparison of alternative methodologies for identifying and characterizing preferential flow paths in heterogeneous aquifers, *J. Hydrol.*, *345* (3-4), 134–148, doi:10.1016/j.jhydrol.2007.07.007.

Leaf, A. T., D. J. Hart, and J. M. Bahr (2012), Active thermal tracer tests for improved hydrostratigraphic characterization, *Ground Water*, *50*(5), 726–735, doi:10.1111/j.1745-6584.2012.00913.X.

Ma, R., C. Zheng, J. M. Zachara, and M. Tonkin (2012), Utility of bromide and heat tracers for aquifer characterization affected by highly transient flow conditions, *Water Resour. Res.*, *48*, W08523, doi:10.1029/2011WR011281.

Macfarlane, A., A. Förster, D. Merriam, J. Schrötter, and J. Healey (2002), Monitoring artificially stimulated fluid movement in the Cretaceous Dakota aquifer, western Kansas, *Hydrogeol. J.*, *10*(6), 662–673.

Neuman, S. P. (2005), Trends, prospects, and challenges in quantifying flow and transport through fractured rocks, *Hydrogeol. J.*, *13*, 124–147, doi:10.1007/s10040-004-0397-2.

Neuville, A., R. Toussaint, and J. Schmittbuhl (2010), Hydrothermal coupling in a self-affine rough fracture, *Phys. Rev. E*, *82*, 036317, doi:10.1103/PhysRevE.82.036317.

Novakowski, K., G. Bickerton, P. Lapcevic, J. Voralek, and N. Ross (2006), Measurements of groundwater velocity in discrete rock fractures, *J. Contam. Hydrol.*, *82*, 44–60, doi:10.1016/j.jconhyd.2005.09.001.

Paillet, F. L. (1998), Flow modeling and permeability estimation using borehole flow logs in heterogeneous fractured formations, *Water Resour. Res.*, *34*(5), 997–1010, doi:10.1029/98WR00268.

Pehme, P. E., J. P. Greenhouse, and B. L. Parker (2007), The active line source temperature logging technique and its application in fractured rock hydrogeology, *J. Environ. Eng. Geoph.*, *12*(4), 307–322, doi:10.2113/JEEG12.4.307.

Ruelleu, S., F. Moreau, O. Bour, D. Gapais, and G. Martelet (2010), Impact of gently dipping discontinuities on basement aquifer recharge: An example from Ploemeur (Brittany, France), *J. Appl. Geophys.*, *70*(2), 161–168, doi:10.1016/j.jappgeo.2009.12.007.

Selker, J. S., et al. (2006), Distributed fiber-optic temperature sensing for hydrologic systems, *Water Resour. Res.*, *42*, W12202, doi:10.1029/2006WR005326.

Tyler, S. W., J. S. Selker, M. B. Hausner, C. E. Hatch, T. Torgersen, C. E. Thodal, and S. G. Schladow (2009), Environmental temperature sensing using Raman spectra DTS fiber-optic methods, *Water Resour. Res.*, *45*, W00D23, doi:10.1029/2008WR007052.

Appendix B

Paper 2

Read, T., O. Bour, J. S. Selker, V. F. Bense, T. L. Borgne, R. Hochreutener, and N. Lavenant, Active-distributed temperature sensing to continuously quantify vertical flow in boreholes, *Water Resources Research*, *50*(5), 3706–3713, 2014

AGU PUBLICATIONS

Water Resources Research

RESEARCH ARTICLE
10.1002/2014WR015273

Active-Distributed Temperature Sensing to continuously quantify vertical flow in boreholes

T. Read[1], O. Bour[2], J. S. Selker[3], V. F. Bense[1], T. Le Borgne[2], R. Hochreutener[2,3], and N. Lavenant[2]

[1]School of Environmental Sciences, University of East Anglia, Norwich, UK, [2]Geosciences Rennes, CNRS, University of Rennes 1, Rennes, France, [3]Department of Biological and Ecological Engineering, Oregon State University, Corvallis, Oregon, USA

Key Points:
- A prototype system monitored with DTS was deployed in a fractured rock aquifer
- The temperature of a heated FO cable is sensitive to vertical fluid velocities
- Empirical or an analytical relationship presented gives the flow velocity

Supporting Information:
- ReadMe File
- Figure S1-S2
- Figure captions S1-S2

Correspondence to:
T. Read,
tom.read@uea.ac.uk

Citation:
Read, T., O. Bour, J. S. Selker, V. F. Bense, T. Borgne, R. Hochreutener, and N. Lavenant (2014), Active-Distributed Temperature Sensing to continuously quantify vertical flow in boreholes, *Water Resour. Res.*, *50*, doi:10.1002/2014WR015273.

Received 13 JAN 2014
Accepted 15 APR 2014
Accepted article online 19 APR 2014

Abstract We show how a distributed borehole flowmeter can be created from armored Fiber Optic cables with the Active-Distributed Temperature Sensing (A-DTS) method. The principle is that in a flowing fluid, the difference in temperature between a heated and unheated cable is a function of the fluid velocity. We outline the physical basis of the methodology and report on the deployment of a prototype A-DTS flowmeter in a fractured rock aquifer. With this design, an increase in flow velocity from 0.01 to 0.3 m s^{-1} elicited a 2.5°C cooling effect. It is envisaged that with further development this method will have applications where point measurements of borehole vertical flow do not fully capture combined spatiotemporal dynamics.

1. Introduction

1.1. Flow Logging

Fluid flow logs in boreholes provide direct insight into the hydrogeological conditions encountered with depth in the subsurface. Such information provides not only a qualitative addition to other geophysical logs, but can classically be used to derive hydraulic property variations with depth during pumping tests [*Molz et al.*, 1994; *Paillet*, 1998]. Various designs of flowmeter currently exist: impeller flowmeters [*Molz et al.*, 1989]; heat pulse flowmeters which rely on the time taken for a packet of heated water to reach a thermistor [*Hess*, 1982]; and electromagnetic flowmeters which output the voltage generated as water moves through a magnetic field [*Molz et al.*, 1994].

With the above mentioned methods, a flow log is obtained by continuously trolling a flowmeter down a borehole or by making stationary measurements at multiple depths. The use of traditional flowmeters can be time consuming where inversion methods used for aquifer characterization require many measurements in space, for example in multiple boreholes for flow tomography [*Klepikova et al.*, 2013], or space and time, for example for fracture zone storage coefficient estimation [*Paillet*, 1998]. Furthermore, the physical presence of a flowmeter causes a resistance to flow in the borehole, potentially disturbing the fluid flow [*Ruud et al.*, 1999]. We develop a new flow logging method based on Distributed Temperature Sensing (DTS) along Fiber Optic (FO) cables, a technology which gives spatially and temporally distributed measurements of temperature [*Selker et al.*, 2006; *Tyler et al.*, 2009]. With DTS, temperature measurements along a FO cable are derived from the return Stokes and anti-Stokes intensities; light at two predictable frequencies, backscattered from an initial laser pulse.

1.2. Fiber-Optic Distributed Temperature Sensing

DTS technology has found a wide range of applications in environmental monitoring [e.g., *Selker et al.*, 2006]. In boreholes, where temperature-depth profiles usually change only very slowly with time, the main applications of DTS have so far been where the subsurface is thermally altered to give a transient thermal response. Example thermal alterations may be the result of fluid injections [*Macfarlane et al.*, 2002; *Leaf et al.*, 2012; *Read et al.*, 2013], or heating cables [*Freifeld et al.*, 2008]. While these methods are thermally active, in that the temperatures at depth have been intentionally altered with a view to observing a transient thermal response, the FO cable is at the same temperature as its immediate surroundings and the DTS method is essentially passive.

Alternatively, DTS can be deployed in an active mode, which we call Active-DTS (A-DTS). Here we define A-DTS as the distributed measurement of temperature along a FO cable with a distributed heat source

incorporated into or in contact with the same cable, where the temperature data collected while actively heating are of primary interest. These temperature data reflect the combined efficiency of heat dissipation from the cable and the surrounding medium, so that spatially distributed estimates of the surrounding physical properties or fluid fluxes are possible. Temperature sensing FO cables are often ruggedized with steel armoring, allowing commonly available cables to be utilized for A-DTS by passing an electrical current through the metal cable materials. Example applications already exist in soil moisture studies. In an unsaturated porous medium, heat conduction from the heated cable depends on the moisture-dependent structure of soil water bridges between grains [*Sayde et al*., 2010; *Striegl and Loheide*, 2012], such that with A-DTS a distributed soil moisture sensor can be created.

A-DTS methods potentially can provide measurements of fluid fluxes in boreholes. *Liu et al*. [2013] showed that the temperature of a FO cable wrapped with a heating cable and deployed down hole is sensitive to horizontal groundwater flux through the surrounding porous medium. Here we propose a method based on A-DTS for the monitoring of vertical fluid velocity in boreholes. The general principle is that in steady state heat flow conditions, the temperature difference between a heated FO cable and adjacent unheated cable deployed down hole will be a function of the velocity of the fluid flowing parallel to the borehole axis. In this study, we first present an analytical relationship between fluid flow velocity and this quantity, ΔT. Here we make the assumption that using a differential temperature accounts for any warming of the fluid due to the electrical heating or background fluid temperature differences caused by inflows to the borehole. We then present temperature data from a prototype A-DTS flowmeter deployed in a fractured rock aquifer, which we invert for the fluid velocity using the analytical result, conditioned in part from field data.

2. Analytical Methods

Prediction of the temperature measured on a heated FO cable requires consideration of both the cable construction and environmental setting. For example, *Neilson et al*. [2010] quantified the undesirable temperature increase on the surface of FO cables submerged in flowing rivers and heated by solar radiation. This analytic approach accounted for the fluid velocity-dependent heat transfer coefficient at the cable-fluid interface. In the borehole setting considered here, we adopt a similar approach, except that the heat input occurs in the cable center. We therefore also need to consider heat conduction through the cable materials if we are to reasonably predict the DTS measured temperature.

In our A-DTS flowmeter, we use a BruSens cable (Brugg cables, Switzerland), which consists of a stainless steel capillary tube, surrounded by braided stainless steel, held in a polyamide (PA) cladding (Figure 1a). The optical fibers, along which the temperature is measured, are located centrally in the capillary tube. This general construction is typical of many armored FO cables manufactured for temperature sensing applications [*Tyler et al*., 2009]. Connecting the steel armoring to a power supply generates a constant amount of heat per unit length. In steady state heat flow conditions, this amount of heat is transferred from the steel to the cladding, and then across the interface between the cladding and fluid.

In the heat transfer model, we consider steady state heat conduction through the cylindrical shell prescribed by the electrically insulating cladding of thickness $r_2 - r_1$. We assume that the temperature gradient inside the steel is negligible, such that the temperature at the center of the cable is equivalent to the temperature at the steel-PA interface, r_1. If the heat transfer across the PA-fluid interface obeys Newton's Law of Cooling, then the diffusion equation in the cylinder can be solved to give:

$$T_1 - T_\infty = \Delta T = \frac{Q}{2\pi}\left(\frac{1}{hr_2} + \frac{1}{k_c}\ln\frac{r_2}{r_1}\right), \tag{1}$$

where T_1 is the temperature at r_1, T_∞ is the temperature of the fluid beyond the thermal boundary layer, Q (W m^{-1}) is the heat input to the cable, h (W m^{-2} K^{-1}) is the heat transfer coefficient, and k_c (W m^{-1} K^{-1}) is the thermal conductivity of the material between r_1 and r_2. From inspection of equation (1), it can be seen that the value of ΔT can be increased by increasing Q, decreasing k_c, and decreasing r_1. The effect of increasing r_2 has two opposing effects; a greater surface area for heat exchange decreases ΔT, while the resulting higher thermal resistance thus increases ΔT.

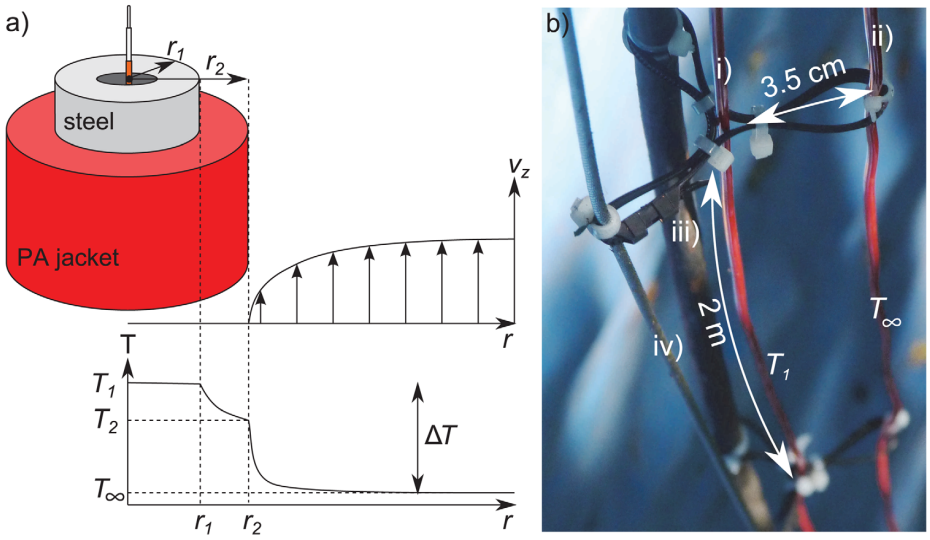

Figure 1. (a) Schematic of the heated FO-cable with idealized fluid velocity and temperature profiles radially from the center of the cable when the cable is electrically heated. (b) Section of the A-DTS tool with (i) centrally held heated FO-cable, (ii) reference FO-cable, (iii) power supply cable, and (iv) steel rope.

The heat transfer coefficient is a function of the thermal conductivity of the fluid, the Nusselt number, and the characteristic length:

$$h = \frac{k_f}{L} Nu, \tag{2}$$

where k_f is the thermal conductivity of the fluid, L [m] is the characteristic length (here we use 0.11 m, the diameter of the borehole). At low flow velocities, heat transfer by free convection, driven by buoyant forces, becomes significant. Therefore, in the present case Nu is the Nusselt number for combined forced (Nu_F) and free (natural) convection (Nu_N). This combined Nusselt number is given by [*Incropera et al.*, 2007]:

$$Nu = \left(Nu_F^n \pm Nu_N^n\right)^{\frac{1}{n}}, \tag{3}$$

where n typically ranges from 3 to 4. For a vertically orientated surface, n is usually taken as 3. The plus or minus sign in equation (3) depends on whether the buoyant fluid motion assists or opposes the fluid flow, thus either enhancing or reducing the efficiency of heat transfer. In the following interpretation of the field trial, we assume that all of the flow is upward (as would be expected to be the case while pumping from the top of the borehole), allowing the addition form of this equation to be used. The Nusselt number approximation for forced convection due to fluid flow is based on laminar flow over a flat isothermal plate, and is given by [*Incropera et al.*, 2007]:

$$Nu_F = 0.664 Re^{\frac{1}{2}} Pr^{\frac{1}{3}}, \tag{4}$$

where Pr is the Prandtl number, and Re, the Reynolds number, is calculated for the characteristic length L. Many relationships exist for free convection Nusselt number approximations over a range of geometries [e.g., *Churchill and Chu*, 1975]. Due to the sensitivity of ΔT to the value of Nu_N, in the following, Nu_N is treated as an unknown and used to fit the model to observed ΔT values.

3. Site Description

The field site at Stang-er-Brune, Brittany, France, was chosen to test the A-DTS method as a large amount of hydrogeophysical data for the site already exist [*De Dreuzy et al.*, 2006; *Bour et al.*, 2013]. Four boreholes up

to 100 m deep and shallower piezometers in close proximity are accessible in a fractured granite and micaschist. Previous field campaigns have identified the most transmissive fractures intersecting the boreholes and interborehole connectivity [*Le Borgne et al*., 2007], and flow routes through the fracture network [*Dorn et al*., 2012]. Hydraulic heads at the site generally increase with depth and drive a mainly upward vertical flow in the boreholes in ambient conditions. To test the prototype system, borehole B2 was used. This borehole is cased from the surface to 24.8 m and then open to a depth of 100 m. The cased section has a larger diameter (12.8 cm) than the open hole (10.4–10.9 cm). When pumped, flow to the borehole originates from fractures at depths of 27.9, 55.6, 58.9, 79.9, and 98.0 m [*Le Borgne et al*., 2007].

4. Field Methods

We constructed the prototype A-DTS flowmeter from a single 295 m length of BruSens FO cable. Of this, 78 m could be heated by connecting this electrically isolated section to a power supply. During the experiments, the heated cable was powered by 220 and 233 ACV, giving power intensities along the cable of 18.8 and 21.8 W m^{-1}, respectively. An equal length of unheated cable, obtained by bending the cable back on itself after the latter electrical connection, was held at a uniform distance away of 3.5 cm using cable ties every 2 m (Figure 1b). From DTS temperature measurements along these two parallel lengths of heated and unheated cable, the heating effect ΔT can be obtained. A power supply cable and a steel cable to support the weight of the system were also fixed relative to the central heated cable using cable ties. These cable tie centralizers also helped to ensure that the heated cable remained away from the borehole wall. The flowmeter was then installed in B2 to monitor the borehole vertical flow at all depths simultaneously.

For the DTS calibration, additional lengths of unheated cable at the surface were placed in ambient (water kept mixed with an air pump) and a cold calibration bath (water wetted ice in an insulated box). Because the tool was constructed from a single length of cable containing two fibers, spliced together at the far end, the resulting duplexed DTS data set contained four reference sections. In each bath a Tinytag logger (Gemini Data Loggers, UK), independently recorded the temperature. The Stokes and anti-Stokes backscatter intensities were obtained every 12.5 cm along the cable using a Silixa Ultima instrument with 5 km range. The instrument integrated the backscatter over times ranging from 1 to 10 s. The data were subsequently postprocessed to derive the temperature using the Stokes and anti-Stokes intensities from three of the reference sections and the single-ended algorithm outlined in *Hausner et al*. [2011].

To test the response of the A-DTS system to a range of flow velocities, we pumped the borehole from a depth of around 10 m at rates ranging from 5.2 to 181 L min^{-1}, generating upflow throughout the borehole. The ΔT response and relationship to flow, as reported in the following, corresponds to a 2 m spatially averaged value between depths of 25.4 and 27.4 m. This section is in the open borehole above all known inflow zones and is referred to as the test section.

5. Results and Discussion

To give an indication of the responsiveness of the A-DTS system, Figure 2 shows a spatially averaged time series of the heated cable and reference cable temperature over the test section. Upon heating, the A-DTS system responded very rapidly, with the heated cable increasing in temperature by almost 10°C. Within 15 s, 90% of this temperature plateau was achieved. Over the time frame shown, the reference cable does not experience any warming, suggesting that it is located far enough away to be out of the thermal boundary layer.

The relationship between ΔT and the fluid velocity in the test section is shown in Figure 3. The ΔT values shown here are after further spatial filtering for reasons outlined in the following. Over a velocity range from 0.01 to 0.33 m s^{-1}, a 2.5°C range in ΔT is obtained. The analytical solution, optimized to $Nu_N = 80$ and 86 for the heating rates of 18.8 and 21.8 W m^{-1}, respectively, suggests a diminishing sensitivity to fluid velocity toward low and high flow extremes. The lower limit to the sensitivity occurs as heat transfer to the fluid by free convection begins to dominate over forced convection. The upper limit to the flow sensitivity is the result of the thermal boundary layer reducing to a minimum. The A-DTS system as deployed here in this configuration, seems to be most suited to measuring midrange velocities that typically would be measured with an electromagnetic or impeller flowmeter.

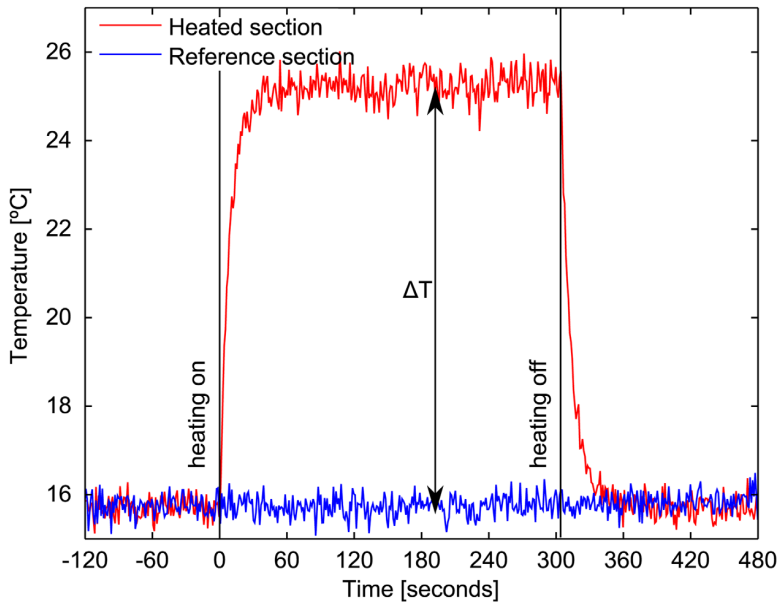

Figure 2. Spatially averaged temperature on the heated and reference cable over the test section (25.4–27.4 m), while pumping at 14.7 L min^{-1}.

A 5 min average of the entire heated section and reference section temperature while pumping at 180 L min^{-1} are shown in Figure 4a. The effect of the 2 m spaced centralizers is to locally reduce the heated cable temperature. We hypothesize that this is due to the development of more energetic turbulent flow as the water moves through the centralizer structure, enhancing the heat exchange between fluid and cable. For the borehole geometry and velocities we have here, the Reynolds number is up to 6×10^3, thus turbulence may be readily stimulated downstream of any obstructions. We do not account for this in the analytical model, and a full analysis of this would need a simulation of the applicable equations for turbulent flow within the flow geometry here. For the ΔT-flow calibration, the temperature data from the heated cable were first filtered to remove these artifacts introduced by the centralizers so that the analytical solution could be used with realistic parameters (bold line in Figure 4a). The cold spots in the heated cable profile were removed by applying a moving median filter to select the upper 25% of temperature data within a 2 m window. We assume that this results in heated cable temperatures that are unaffected by the centralizers, therefore, the ΔT-flow calibration can only be expected to provide reasonable velocity estimates either for the filtered data, or the unfiltered data away from the centralizers. It should however be noted that the removal of these artifacts is not essential as the flowmeter could be entirely empirically calibrated. The reference cable data were also processed but with a simple 2 m moving average.

The velocity profile for a pumping rate of 180 L min^{-1}, calculated from ΔT (Figure 4b), using equations (1)–(4) and the parameters in Table 1 is shown in Figure 4c. In addition, flow velocities measured with an impeller flowmeter (H+ Network, www.hplus.ore.fr), are also plotted. These data were obtained at a lower pumping rate of 42 L min^{-1} in July 2012. Despite this, the velocity profile should at least provide a qualitative comparison, since due to variations in the hydraulic conditions of each fracture, it cannot be expected to be entirely constant through time or scale exactly with the pumping rate [*Paillet*, 1998]. The profile of ΔT measured with the A-DTS flowmeter is clearly anticorrelated with the impeller measured fluid velocity, with the resulting flow log showing similar step changes in velocity arising from discrete fracture zone inflows.

Additionally, there are both some anomalously high and low values of ΔT that translate into anomalously low and high velocities, respectively, that cannot easily be explained just by considering vertical flow up the borehole. The high value of ΔT centered at around 60 m was present at all pumping rates and is thought to be due to the heated cable touching the borehole wall. This is likely to be an issue in most deployments of the system where there is any deviation in the borehole but is something we envisage can be minimized with alternative designs. The low value of ΔT at around 79 m appears to correspond to the fracture at this

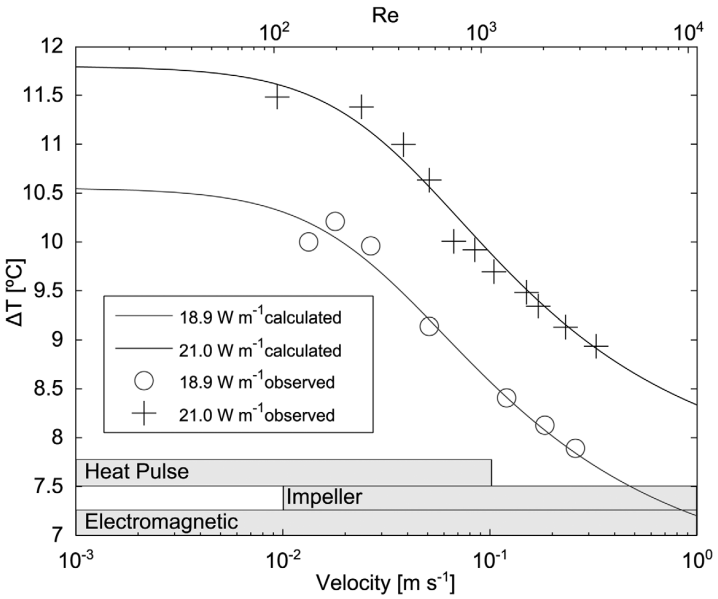

Figure 3. Observed ΔT based on the filtered data and computed ΔT relationship with fluid velocity for power inputs of 18.9 and 21.0 W m^{-1}, with typical sensitivity ranges of heat pulse, impeller, and electromagnetic flowmeters.

depth. Inflowing fractures generate nonaxial velocity components and even turbulence, that could locally increase heat dissipation from the heated cable. However, it may be difficult to quantitatively relate this ΔT value to fracture zone inflows due to the complexity of such regions and limited spatial resolution of

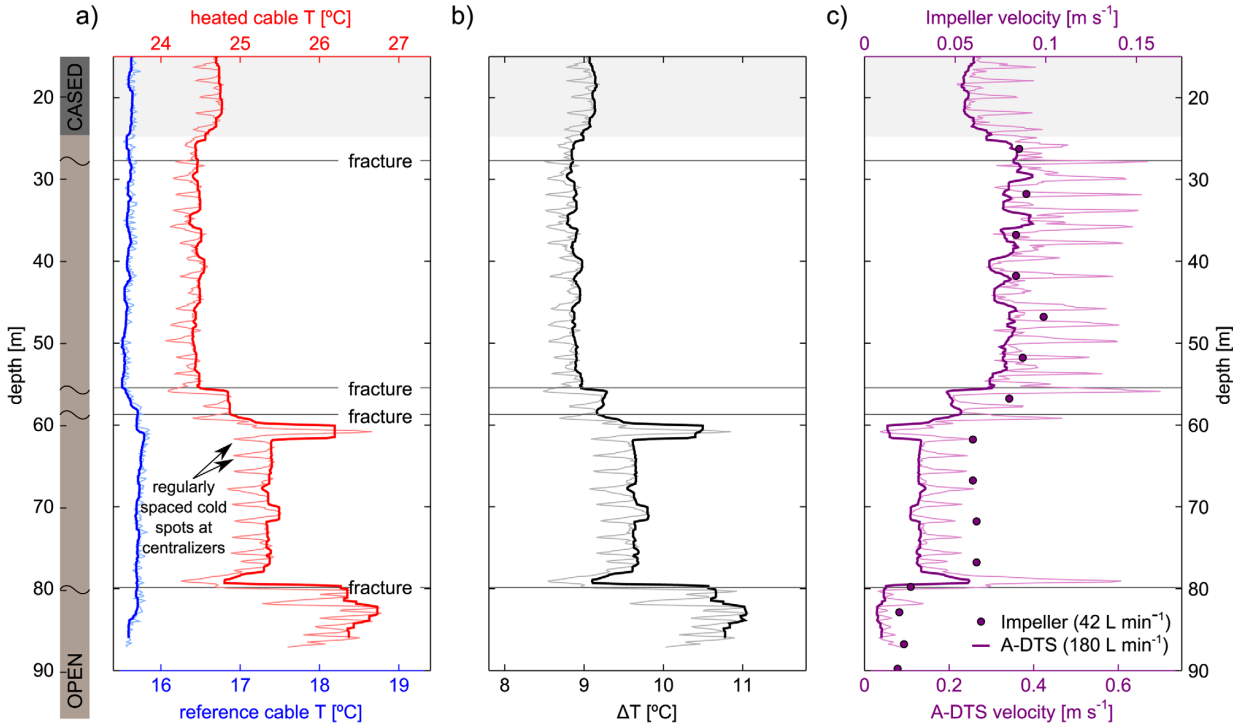

Figure 4. (a) Reference cable and heated cable temperatures while pumping from 7 m depth at 180 L min^{-1} (pale lines are temporally averaged, bold lines temporally averaged with additional spatial filtering). (b) Corresponding ΔT profile (the light line is the difference between the purely temporally averaged data, and the bold line is the difference between the combined time averaged and spatially filtered profiles). (c) Calculated velocity profile from ΔT and equations (1–4), with measurements of the flow velocity made using an impeller flowmeter while pumping at 42 L min^{-1} in July 2012 for comparison.

Table 1. BruSens FO Cable and Water Physical and Thermal Properties Used in the Analytical Solution

	BruSens Cable	Water	Units
Diameter of steel core	0.00226		m
Cable diameter	0.00385		m
Thermal conductivity	0.245	0.598	$W\,m^{-1}\,K^{-1}$
Density	2.41	1.00	$g\,cm^{-3}$
Dynamic viscosity		1.00E-03	$N\,s\,m^{-2}$
Kinematic viscosity		1.00E-06	$m^2\,s^{-1}$

standard DTS installations. Similar problems at discrete inflow zones are nevertheless also encountered with other flow logging methods.

A key issue in the future designs of A-DTS flowmeters is the centralizing mechanism. Where the cable touches the borehole wall, as would commonly happen in boreholes with any deviation, we have seen that this causes major temperature artifacts. The centralizers used in this study were designed to minimize this but they too give temperature artifacts of their own, which in this set up were readily identified due to their regular spacing. This effectively limited the spatial resolution of the flowmeter to detect changes in the fluid velocity to around 2 m, which is significantly poorer than the spatial resolution possible with the DTS deployed (0.29 m). A further unexpected outcome was that at the centralizer locations, ΔT had an enhanced sensitivity to flow at low velocities (see supporting information). This raises the possibility that future designs could include a denser centralizing system that uniformly disturbs the flow, and is optimized to provide maximum sensitivity over a given velocity range. This would give a spatial resolution for fluid flow logging similar to the spatial resolution of the DTS instrument. While it would be more difficult to forward model the temperature response of the A-DTS flowmeter, one could readily build up an empirical calibration between ΔT and flow velocity in the field as we also did here.

Additional work needs to be carried out to assess the significance of the flow direction on the ΔT response. Equation (3) suggests that at least at low flow velocities, two different ΔT responses may result depending on whether the fluid flow is acting in the same direction or opposing buoyancy driven flow. This need not be a prohibitive issue as the flow direction can be found from the gradient of the change in reference cable temperature relative to preheating. While Figure 2 shows that over a short time scale the warming of the fluid is negligible, after carrying out multiple simultaneous heating experiments, we observed that the reference cable temperature had increased. A similar effect can be seen in the recent work of *Banks et al*. [2014], where in the example from the Willunga field site the sign of the gradient of the fluid temperature profiles indicates that the flow direction is upward to the pump. This effect is apparent because the water just before it reaches the pump has a longer mean residence time and has therefore experienced more heating than water which has only just entered the borehole. So using the method proposed here, if in fact two ΔT-flow calibrations exist, then the appropriate calibration for flow can be chosen. This is something that we did not fully explore in this set of field experiments, but could be tested on a smaller scale with a laboratory setup.

6. Conclusions

We have shown that A-DTS is a feasible approach for monitoring spatially and temporally changing borehole vertical flows. The difference in temperature between an electrically heated fiber optic cable and a passive, nonheated reference cable can be related to vertical fluid velocities. With FO cables of small thermal inertia, as used here, the thermal time constant of the cable is likely to be much smaller than the time constant of the borehole when hydraulically stressed. Therefore, the A-DTS method is likely to find applications where it is necessary to monitor temporal changes in fluid flow. The general advantages of using DTS that have been found in other disciplines similarly apply here for fluid flow measurements with A-DTS. With an A-DTS flowmeter constructed from a single FO cable, full spatiotemporal coverage of flow measurements could be achieved simultaneously in multiple boreholes at a site. While we have shown here that in general the method shows great promise for fluid flow logging, future work is needed to address the issues related to field deployment, and to determine how to optimize the sensitivity for the desired application.

Acknowledgments
Funding for this work was provided by the INTERREG IV project CLIMAWAT, the national network of hydrogeological sites H+, the ANR project CRITEX ANR-11-EQPX-0011, and a Natural Environment Research Council (NERC) studentship (NE/J500069/1) to Tom Read. Part of the support for the participation of John Selker and provision of some of the fiber optic cables were provided by the Center for Transformative Environmental Monitoring Programs (CTEMPs) funded by the National Science Foundation. The data collected for this study will be available from the national network of hydrogeological sites H+, at http://hplus.ore.fr/en/. We thank the two anonymous reviewers and Editor for their constructive comments on the manuscript.

References

Banks, E. W., M. A. Shanafield, and P. G. Cook (2014), Induced temperature gradients to examine groundwater flowpaths in open boreholes, *Ground Water*. [Available at http://onlinelibrary.wiley.com/doi/10.1111/gwat.12157/full].

Bour, O., T. Le Borgne, N. Lavenant, T. Labasque, L. Longuevergne, L. Aquilana, R. Hochreutener, J. Jiminez-Martinez, and P. Davy (2013), The hydrogeological observatory of ploemeur (France): Long-term monitoring and experimentations, in *Abstracts With Programs*, *45*(7), 510, Geol. Soc. of Am.

Churchill, S. W., and H. Chu (1975), Correlating equations for laminar and turbulent free convection from a vertical plate, *Int. J. Heat Mass Transfer*, *18*, 1323–1329.

De Dreuzy, J.-R., J. Bodin, H. Le Grand, P. Davy, D. Boulanger, A. Battais, O. Bour, P. Gouze, and G. Porel (2006), General database for ground water site information, *Ground Water*, *44*(5), 743–748, doi:10.1111/j.1745-6584.2006.00220.x.

Dorn, C., N. Linde, T. L. Borgne, O. Bour, and M. Klepikova (2012), Inferring transport characteristics in a fractured rock aquifer by combining single-hole ground-penetrating radar reflection monitoring and tracer test data, *Water Resour. Res.*, *48*, W11521, doi:10.1029/2011WR011739.

Freifeld, B. M., S. Finsterle, T. C. Onstott, P. Toole, and L. M. Pratt (2008), Ground surface temperature reconstructions: Using in situ estimates for thermal conductivity acquired with a fiber-optic distributed thermal perturbation sensor, *Geophys. Res. Lett.*, *35*, L14309, doi:10.1029/2008GL034762.

Hausner, M. B., F. Suárez, K. E. Glander, N. V. D. Giesen, J. S. Selker, and S. W. Tyler (2011), Calibrating single-ended fiber-optic raman spectra distributed temperature sensing data, *Sensors*, *11*, 10,859–10,879, doi:10.3390/s111110859.

Hess, A. E. (1982), A heat-pulse flowmeter for measuring low velocities in boreholes, *Open File Rep*., 82–699, U.S. Geol. Surv., Denver.

Incropera, F. P., D. Dewitt, T. Bergman, and A. Lavine (2007), *Fundamentals of Heat and Mass Transfer*, John Wiley, New York.

Klepikova, M. V., T. Le Borgne., O. Bour, and J.-R. de Dreuzy (2013), Inverse modeling of flow tomography experiments in fractured media, *Water Resour. Res.*, *49*, 7255–7265, doi:10.1002/2013WR013722.

Le Borgne, T., et al. (2007), Comparison of alternative methodologies for identifying and characterizing preferential flow paths in heterogeneous aquifers, *J. Hydrol.*, *345*(3–4), 134–148, doi:10.1016/j.jhydrol.2007.07.007.

Leaf, A. T., D. J. Hart, and J. M. Bahr (2012), Active thermal tracer tests for improved hydrostratigraphic characterization, *Ground Water*, *50*(5), 726–735, doi:10.1111/j.1745-6584.2012.00913.x.

Liu, G., S. Knobbe, and J. Butler (2013), Resolving centimeter-scale flows in aquifers and their hydrostratigraphic controls, *Geophys. Res. Lett.*, *40*, 1098–1103, doi:10.1002/grl.50282.

Macfarlane, A., A. Förster, D. Merriam, J. Schrötter, and J. Healey (2002), Monitoring artificially stimulated fluid movement in the Cretaceous Dakota aquifer, western Kansas, *Hydrogeol. J.*, *10*(6), 662–673, doi:10.1007/s10040-002-0223-7.

Molz, F., R. Morin, A. Hess, J. Melville, and O. Given (1989), The impeller meter for measuring aquifer permeability variations: Evaluations and comparison with other tests, *Water Resour. Res.*, *25*, 1677–1683.

Molz, F., G. Boman, S. Young, and W. Waldrop (1994), Borehole flowmeters: Field application and data analysis, *J. Hydrol.*, *163*(3–4), 347–371, doi:10.1016/0022-1694(94)90148-1.

Neilson, B. T., C. E. Hatch, H. Ban, and S. W. Tyler (2010), Solar radiative heating of fiber-optic cables used to monitor temperatures in water, *Water Resour. Res.*, *46*, W08540, doi:10.1029/2009WR008354.

Paillet, F. L. (1998), Flow modeling and permeability estimation using borehole flow logs in heterogeneous fractured formations, *Water Resour. Res.*, *34*, 997–1010, doi:10.1029/98WR00268.

Read, T., O. Bour, V. Bense, T. Le Borgne, P. Goderniaux, M. Klepikova, R. Hochreutener, N. Lavenant, and V. Boschero (2013), Characterizing groundwater flow and heat transport in fractured rock using fiber-optic distributed temperature sensing, *Geophys. Res. Lett.*, *40*, 2055–2059, doi:10.1002/grl.50397.

Ruud, N., Z. Kabala, and F. Molz (1999), Evaluation of flowmeter-head loss effects in the flowmeter test, *J. Hydrol.*, *224*(1), 55–63.

Sayde, C., C. Gregory, M. Gil-Rodriguez, N. Tufillaro, S. Tyler, N. van de Giesen, M. English, R. Cuenca, and J. S. Selker (2010), Feasibility of soil moisture monitoring with heated fiber optics, *Water Resour. Res.*, *46*, W06201, doi:10.1029/2009WR007846.

Selker, J. S., et al. (2006), Distributed fiber-optic temperature sensing for hydrologic systems, *Water Resour. Res.*, *42*, W12202, doi:10.1029/2006WR005326.

Striegl, A. M., and S. P. I. Loheide (2012), Heated distributed temperature sensing for field scale soil moisture monitoring, *Ground Water*, *50*(3), 340–347, doi:10.1111/j.1745-6584.2012.00928.x.

Tyler, S. W., J. S. Selker, M. B. Hausner, C. E. Hatch, T. Torgersen, C. E. Thodal, and S. G. Schladow (2009), Environmental temperature sensing using Raman spectra DTS fiber-optic methods, *Water Resour. Res.*, *45*, W00D23, doi:10.1029/2008WR007052.

Appendix C

Paper 3

Read, T., V. Bense, O. Bour, T. Le Borgne, N. Lavenant, R. Hochreutener, and J.S. Selker, Thermal-Plume fiber Optic Tracking (T-POT) test for flow velocity measurement in groundwater boreholes, *Geoscientific Instrumentation, Methods and Data Systems Discussions*, *5*, 161–175, 2015

Geosci. Instrum. Method. Data Syst., 4, 197–202, 2015
www.geosci-instrum-method-data-syst.net/4/197/2015/
doi:10.5194/gi-4-197-2015

Geoscientific Instrumentation Methods and Data Systems
Open Access
EGU

Thermal-plume fibre optic tracking (T-POT) test for flow velocity measurement in groundwater boreholes

T. Read[1], V. F. Bense[2], R. Hochreutener[4], O. Bour[3], T. Le Borgne[3], N. Lavenant[3], and J. S. Selker[4]

[1]School of Environmental Sciences, University of East Anglia, Norwich Research Park, Norwich, NR4 7TJ, UK
[2]Hydrology and Quantitative Water Management Group, Department of Environmental Sciences, Wageningen University, 6700 AA Wageningen, the Netherlands
[3]Géosciences Rennes, UMR6118 – CNRS, University of Rennes 1, Rennes, France
[4]Biological and Ecological Engineering, Oregon State University, Corvallis, OR 97331, USA

Correspondence to: T. Read (tom.read@uea.ac.uk)

Received: 23 April 2015 – Published in Geosci. Instrum. Method. Data Syst. Discuss.: 11 June 2015
Revised: 24 September 2015 – Accepted: 7 October 2015 – Published: 28 October 2015

Abstract. We develop an approach for measuring in-well fluid velocities using point electrical heating combined with spatially and temporally continuous temperature monitoring using distributed temperature sensing (DTS). The method uses a point heater to warm a discrete volume of water. The rate of advection of this plume, once the heating is stopped, equates to the average flow velocity in the well. We conducted thermal-plume fibre optic tracking (T-POT) tests in a borehole in a fractured rock aquifer with the heater at the same depth and multiple pumping rates. Tracking of the thermal plume peak allowed the spatially varying velocity to be estimated up to 50 m downstream from the heating point, depending on the pumping rate. The T-POT technique can be used to estimate the velocity throughout long intervals provided that thermal dilution due to inflows, dispersion, or cooling by conduction does not render the thermal pulse unresolvable with DTS. A complete flow log may be obtained by deploying the heater at multiple depths, or with multiple point heaters.

1 Introduction

The measurement of the vertical flow in wells can improve our conceptual understanding of subsurface fluid movement, which can aid in, for example, groundwater resource management or geothermal resource assessments. In open or long-screened wells penetrating multiple permeable units or fractures, vertical flow typically occurs under hydraulically unstressed conditions due to the natural occurrence of a vertical head gradient. Flow logs obtained under unstressed conditions give a qualitative guide to fracture inflow and outflow zones (Hess, 1986). Alternatively, flow logs obtained in a pumping well at multiple different pumping rates allow the depth variability of transmissivity to be estimated (Paillet et al., 1987). Flow logs in observation wells affected by nearby pumping enable the connectivity of fractures to be determined (Paillet, 1998; Klepikova et al., 2013). In all cases, the in-well flow is not directly indicative of flow in the formation itself, since the presence of the well as a high permeability vertical conduit allows the short-circuiting of flow. In addition, flow logs have inherent value for geochemical sampling campaigns. Ambient vertical flow through the well may redistribute contaminants and mean that passive sampling approaches do not reproduce the same depth variability as present in the aquifer itself (Elci et al., 2003). Typical flow logging techniques involve lowering an impeller or electromagnetic flowmeter down a well and either measuring continuously (trolling) or at multiple points with the probe held stationary. At low flows a heat pulse flowmeter may be used at fixed depths (Paillet, 1998).

Alternatively, tracer-based approaches may be used. Most commonly, a tracer is emplaced over the entire length of the borehole and the change in concentration monitored over time. Typically, slightly saline (Maurice et al., 2011) or distilled water (Doughty et al., 2005) is added since fluid electrical conductivity (EC) can be easily logged with an EC meter. The EC is then monitored over depth and time by making re-

peated logs. The dilution of the saline profile at inflow locations or increase in EC if using distilled water can be used to estimate horizontal flow through the aquifer using simple analytical solutions (Pitrak et al., 2007). If there is vertical flow in the well, a salinity front then migrates up or down the well. In the case of multiple inflows with multiple salinity fronts, the response over depth and time may become complex and require numerical modelling (Maurice et al., 2011) or inversion methods to extract the vertical flow profile (Moir et al., 2014). A limitation of this method is that when the vertical velocity or losses from the borehole to the aquifer are high, the EC signal rapidly dissipates, and monitoring this process over a large depth interval with a single EC logger yields an incomplete data set. Additionally, density-induced flow effects in well bores are significant even for small gradients of fluid density (Berthold, 2010).

Instead of a hydrochemical signal that can be difficult to monitor over space and time, Leaf et al. (2012) introduced a slug of warm water to a target depth. By using temperature as the tracer, it is possible to monitor the response continuously over depth and time along a fibre optic cable installed in the well with the distributed temperature sensing (DTS) technique (see Selker et al. (2006) for a description of the DTS method). Leaf et al. (2012) heated water at the surface and injected it at multiple depths to identify the flow direction and velocity. However, the process of heating water is cumbersome, and its injection is likely to result in head changes in the well, resulting in an altered flow regime particularly if ambient or low pumping rate conditions are of interest. Sellwood et al. (2015) adapted this method by using an electrical heater to generate the thermal disturbance and carried out tests under non-hydraulically stressed conditions in a dual permeability sandstone aquifer. In this study we deploy a single electrical heater to warm a discrete interval of water at depth in a pumping well in a fractured rock aquifer, monitored with DTS. We apply post-collection averaging to the DTS temperature data and track the peak of the plume over time to estimate the mean vertical velocity. We call this method thermal-plume fibre optic tracking (T-POT).

2 T-POT field application

We employed T-POT at the H+ network research site (hplus.ore.fr/en), Ploemeur, France (Fig. 1a). The site has multiple boreholes up to 100 m deep, penetrating mica-schist and granitic rock. Open fractures, although sparse (fewer than five hydrogeologically significant fractures per borehole), are reasonably transmissive (up to $4 \times 10^{-3}\,\mathrm{m^2\,day^{-1}}$). We show T-POT results from borehole B3 (11.8 cm diameter), which is intersected by three previously identified transmissive fractures (Fig. 1b). Fractures B3-2 and B3-3 have similar transmissivities ($\sim 2 \times 10^{-3}\,\mathrm{m^2\,day^{-1}}$), while B3-1 is approximately an order of magnitude less transmissive (Klepikova, 2013).

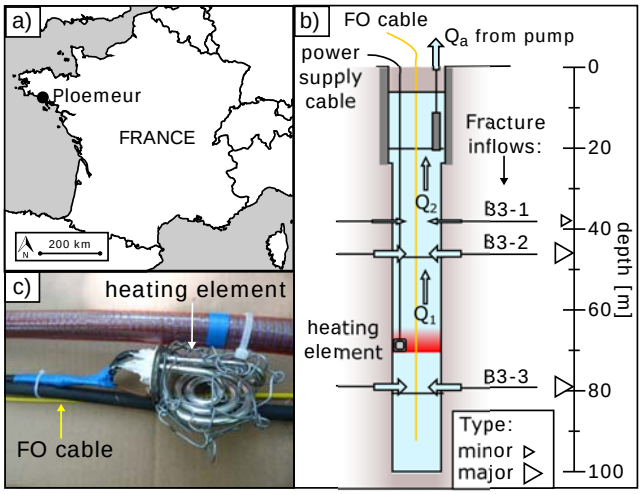

Figure 1. (a) Location of the Ploemeur research site; **(b)** heating element and fibre optic cable along which temperature is measured; **(c)** schematic of the set-up in borehole B3 at the site.

We used a 2 kW rated heating element as the heat source (Fig. 1c), lowered down to 68 m depth for the duration of the experiment. Additionally, an armoured fibre optic cable was installed in the well down to a depth of approximately 80 m. This allowed temperature measurements to be made over a time average of 5 s and a sampling interval of 0.12 m with DTS by connecting it to a Silixa ULTIMA base unit. The cable was configured for a duplexed single-ended measurement. The DTS data were calibrated using three reference sections from a cold and ambient bath, according to the method described by Hausner et al. (2011). The standard deviation of temperature in the cold and ambient baths for the 5 s integration time averaged 0.38 and 0.33 °C respectively over the duration of the T-POT tests.

We ran a series of tests at different pumping rates to determine the fracture inflow for each pumping rate, in order to evaluate the T-POT method. For each pumping rate, a similar procedure was followed: heat for $\sim$ 10 min, then switch off the heating and simultaneously turn on the pump at the selected rate. We repeated this procedure for pumping rates of 7.3, 40.0, 86.6, 104.0, and 136.2 L min^{-1}. During each experiment we measured the pumping rate manually and with an in-line flowmeter, drawdown, electrical power supplied to the heating element, and temperature along the length of the borehole with DTS.

3 T-POT results and interpretation

Figure 2 shows successive DTS temperature–depth profiles from the five T-POT experiments. A background temperature–depth profile, defined by a 1 min time average immediately prior to the start of heating, was subtracted from each data set. During the heating phase ($t < 0$ min), it

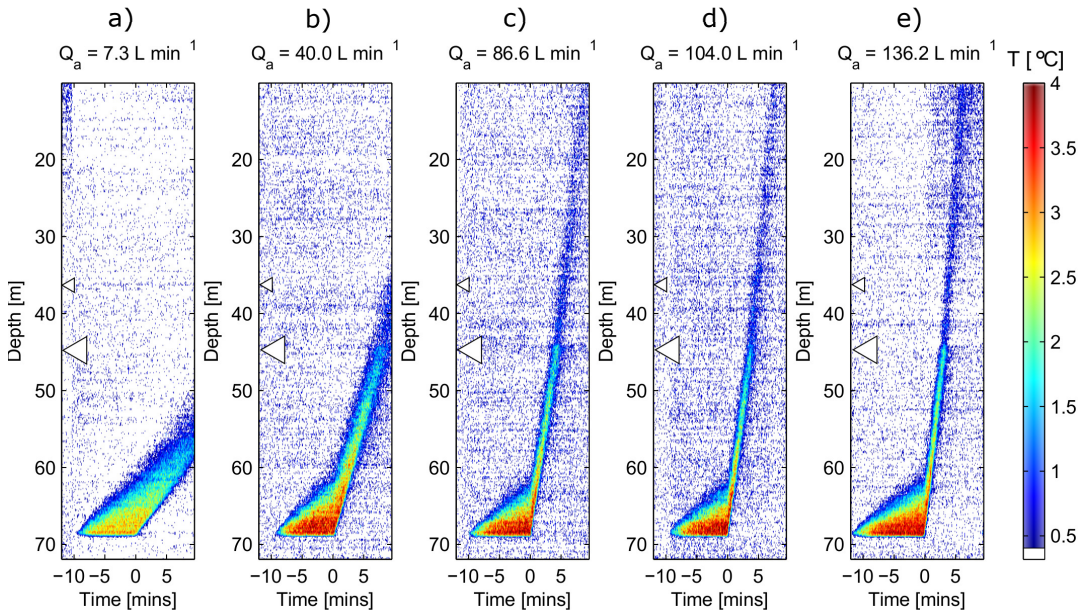

Figure 2. Temperature distribution with depth and time for T-POT tests at abstraction rates of **(a)** 7.3, **(b)** 40.0, **(c)** 86.6, **(d)** 104.0, and **(e)** 136.2 L min^{-1}. The temperature data have a background profile subtracted, with the lower limit to the colour scale starting 1 standard deviation (from reference bath temperature measurements) above the 0 °C change.

appears that the plume develops asymmetrically, with the base of the plume at 68 m at the approximate depth of the heater. The heater is switched off at $t = 0$ and at this moment pumping is initiated. The plume is then advected upwards at higher velocity. In all cases, the linear path of the plume in the temperature–depth–time plot suggests a uniform velocity from 68 m to around 45 m, as would be expected given the lack of transmissive fractures and uniform borehole diameter in this interval. At 45 m, the temperature signal is significantly reduced and the plume then continues to move upwards at higher velocity (steeper gradient in Fig. 2c–e). This coincides with a transmissive fracture identifiable in previous flowmeter tests and optical borehole logs (Le Borgne et al., 2007).

To aid the identification of the plume peak, the 5 s time averaged and 0.12 m spatially sampled DTS temperature data were then subsequently further averaged to give the equivalent of 15 s time-averaged DTS temperature data. Each point was then spatially smoothed with a nine-point moving average window. These are plotted as temperature–depth profiles in Fig. 3. Below 45 m, the plume is clearly defined. Above the inflow from B3-2 at 45 m, the plume becomes much less discernible (Fig. 3c–e).

The depth location of the maximum temperature was then extracted and plotted over time (Fig. 4). While the peak of the plume remains below fracture B3-2, the plume is readily resolvable in the temperature data. Linear least-squares regression yields an $r^2 \geq 0.98$ for all of the pumping rates. The average flow velocities v_1 and v_2 were calculated from the gradient of the best fit line through plume peak location data. The corresponding volumetric flow rates $Q_{\text{B3-3}}$ and $Q_{\text{B3-1,2,3}}$ were calculated from v_1 and v_2 respectively using the known borehole diameter over this interval.

Above 45 m, the peak of the plume was not detected for 1–2 min after the arrival of the plume peak at B3-2. This is because in this situation, the inflow from B3-2 greatly dilutes the thermal signal, such that until most of the plume has moved above the fracture, the highest temperature (and plume peak, as identified with this method) remains at the depth of the fracture. Once identified again, now at approximately the depth of B3-1, the peak location data show that the plume is now travelling at higher velocity. Here it is much less detectable, with an r^2 for the three cases where the plume passes this point of 0.76, 0.65, and 0.91. However, it is not possible to separately assess the flow contributions of B3-2 and B3-1, since two separate contributions are not apparent in Figs. 2–4. Therefore we are only able to estimate $Q_{\text{B3-3}}$ (the flow below 45 m) and $Q_{\text{B3-1,2,3}}$ representing the cumulative flow contribution from all transmissive fractures intersecting the well.

4 Discussion

The upwards expansion of the plume during the heating phase is driven by upward ambient fluid flow in the borehole. The rate of the ambient flow component between B3-3 and B3-2 has been measured at approximately 5 L min^{-1} in previous studies (Klepikova, 2013). When pumping at 7.3 L min^{-1}, the calculated flow between B3-3 and B3-2, $Q_{\text{B3-3}}$, is almost double the abstraction rate. At this low

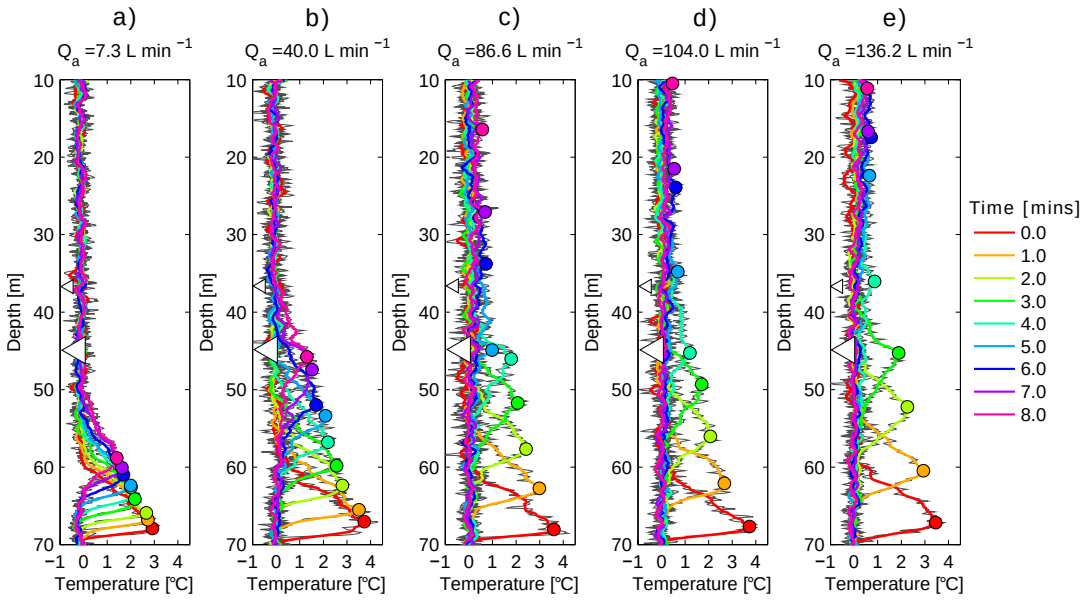

Figure 3. Temperature–depth profiles after pumping begins for the T-POT tests at abstraction rates of **(a)** 7.3, **(b)** 40.0, **(c)** 86.6, **(d)** 104.0, and **(e)** 136.2 L min^{-1}. The coloured profiles are 15 s time-averaged data that have then been spatially smoothed with a nine-point moving window. Filled circles identify the locations of the plume peaks.

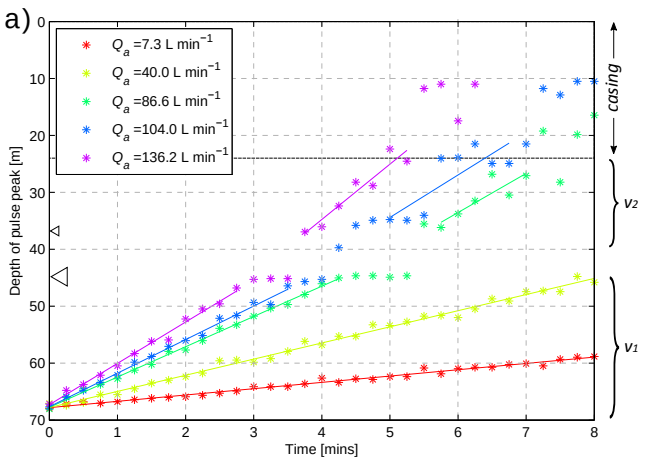

b)

v_1 [cm s^{-1}]	v_2 [cm s^{-1}]	$r^2(v_1)$	$r^2(v_2)$	$Q_{B3\text{-}3}$ [L min^{-1}]	$Q_{B3\text{-}1,2,3}$ [L min^{-1}]	Q_a [L min^{-1}]
1.85	-	0.99	-	12.12	-	7.3
4.73	-	0.99	-	31.01	-	40
8.86	11.45	1.00	0.76	58.12	75.10	86.6
9.82	12.44	0.99	0.65	64.40	81.61	104
12.09	16.20	0.99	0.91	79.34	106.32	136.2

Figure 4. Temperature peak depth over time for each of the pumping rates, with linear least-squares regression best fit lines used to estimate the in-well vertical flow velocity.

pumping rate, the hydraulic head in the borehole remains higher than the hydraulic head in B3-1, so that B3-1 remains an outflow. The flow from B3-3 is proportional to the pumping rate ($r^2 = 0.99$), as would be expected from linear scaling behaviour, giving us confidence in these flow estimates. The discrepancy between $Q_{\mathrm{B3\text{-}1,2,3}}$ and Q_{a} is at most 20 %. Much of this error may arise from the error determining the plume location above B3-1. Further additional sources of error that may contribute to the discrepancy in flow estimates are the high sensitivity of the volumetric flow estimate to the borehole diameter used for the calculation, and error in independently measuring the flow at the surface. The inability of the method to reliably track the velocity immediately downstream of fracture B3-2 in the present study is due to the strong dilution effect by inflow from the fracture of a similar magnitude to the vertical flow in the borehole. The relatively low r^2 for the peak depth–time data beyond this fracture and the discrepancy from Q_{a} is because the resulting plume is much more dispersed with a poorly defined peak. The T-POT method as used here would more likely perform better in cases where there are multiple outflows, rather than inflows. This is because inflows both affect the size and change the shape of the signal.

Free convection due to T-POT heating-induced buoyancy, as occurs naturally in groundwater wells even for small temperature gradients (Sammel, 1968), may disturb the in-well flow. The potential for heat transfer by natural convection in a fluid is expressed by the Rayleigh number, given by

$$Ra = \frac{\beta g \Delta T/\Delta z}{\kappa \nu} r^4, \quad (1)$$

where β is the thermal expansion coefficient, g is acceleration due to Earth's gravity, $\Delta T/\Delta z$ the temperature gradient, κ the thermal diffusivity, ν kinematic viscosity, and

r the characteristic length, which in this case is the borehole radius. For the T-POT experiments here in a borehole with radius 0.059 m, with $\Delta T/\Delta z$ at most $0.5\,^{\circ}\mathrm{C\,m^{-1}}$ during the heating phase, substituting values of $2 \times 10^{-4}\,^{\circ}\mathrm{C^{-1}}$, $9.81\,\mathrm{m\,s^{-2}}$, $0.14 \times 10^{-6}\,\mathrm{m^2\,s^{-1}}$, and $1 \times 10^{-6}\,\mathrm{m^2\,s^{-1}}$ for β, g, κ, and ν respectively gives a *Ra* of 85 000. Scaling the results of Berthold and Resagk (2012), who imaged flow velocities due to free convection in a vertical cylinder, using this Rayleigh number, suggests that in the absence of any forced convection, free convection due to T-POT heating would give rise to flow velocities of the order of $2\,\mathrm{cm\,s^{-1}}$. This is similar to the velocity that would be expected under ambient flow conditions. However, this velocity is the velocity magnitude in a diametrically anti-symmetric convection cell. Therefore, even though the velocity due to natural convection is of a similar magnitude to the ambient flow, if the convection cells are relatively small, then the warming front would not propagate up the well at this rate. A further in-depth analysis is beyond the scope of this paper, but we note that if present, the development of large convection cells would place a lower limit on the velocity estimate that can be obtained with the T-POT method.

The upper limit of velocity estimation is reached when the plume travels the length of the monitoring interval in less than the integration time of the DTS temperature measurement (i.e. $v_{\max} = Z/t_{\mathrm{i}}$, where Z is the length of the flow path away from the heater in the direction of flow, and t_{i} is the integration time of the DTS temperature measurement). The depth resolutions of the velocity estimate using the T-POT method are flow velocity dependent. At high velocities, the depth spacing between velocity estimates is $t_{\mathrm{i}}\,v$. At low flow velocities, the spatial sampling of the DTS instrument determines the number of velocity estimates with depth that the T-POT method can provide.

The basic method, using DTS with a fibre optic cable and point source electrical heating in the well, can easily be adapted to include the use of multiple heaters or more prolonged heating in a constant source type experiment. While the method at present assumes a constant velocity profile in time, time-varying velocities could be monitored by cycling through heating and non-heating phases. The method is completely complementary to and can easily be used alongside other fibre-optic down hole tests and to validate vertical velocity estimates made by other active DTS methods such as Read et al. (2014).

5 Conclusions

We employed the T-POT method in a groundwater well in fractured rock. By heating a discrete volume of the resident water in the borehole, estimates of vertical in-well velocity were obtained by tracking its subsequent migration with DTS. The plume was significantly reduced beyond a major inflowing fracture but was still detectable, albeit with much increased uncertainty. The advantage of this method is that it is quick and simple, especially if the well is already instrumented for fibre optic temperature monitoring.

Acknowledgements. Funding for this work was provided by INTERREG IV project CLIMAWAT, the national network of hydrogeological sites H+, ANR project CRITEX ANR-11-EQPX-0011, and a Natural Environment Research Council (NERC) studentship (NE/J500069/1) to Tom Read. Part of the support for the participation of John Selker and provision of some of the fibre optic cables were provided by the Center for Transformative Environmental Monitoring Programs (CTEMPs) funded by the National Science Foundation. The data collected for this study will be available from the national network of hydrogeological sites H+ at http://hplus.ore.fr/en/.

Edited by: A. Benedetto

References

Berthold, S.: Synthetic Convection Log —Characterization of vertical transport processes in fluid-filled boreholes, J. Appl. Geophys., 72, 20–27, doi:10.1016/j.jappgeo.2010.06.007, 2010.

Berthold, S. and Resagk, C.: Investigation of thermal convection in water columns using particle image velocimetry, Exp. Fluids, 52, 1465–1474, doi:10.1007/s00348-012-1267-7, 2012.

Doughty, C., Takeuchi, S., Amano, K., Shimo, M., and Tsang, C.-F.: Application of multirate flowing fluid electric conductivity logging method to well DH-2, Tono Site, Japan, Water Resour. Res., 41, W10401, doi:10.1029/2004WR003708, 2005.

Elci, A., Flach, G. P., and Molz, F. J.: Detrimental effects of natural vertical head gradients on chemical and water level measurements in observation wells: identification and control, J. Hydrol., 281, 70–81, doi:10.1016/S0022-1694(03)00201-4, 2003.

Hausner, M. B., Suárez, F., Glander, K. E., Giesen, N. V. D., Selker, J. S., and Tyler, S. W.: Calibrating Single-Ended Fiber-Optic Raman Spectra Distributed Temperature Sensing Data, Sensors, 11, 10859–10879, doi:10.3390/s111110859, 2011.

Hess, A. E.: Identifying hydraulically conductive fractures with a slow-velocity borehole flowmeter, Can. Geotech. J., 23, 69–78, 1986.

Klepikova, M. V.: Imaging of fractured rock properties from flow and heat transport: field experiments and inverse modelling, PhD thesis, Geosciences Rennes, Rennes, 2013.

Klepikova, M. V., Le Borgne., T., Bour, O., and de Dreuzy, J.-R.: Inverse modeling of flow tomography experiments in fractured media, Water Resour. Res., 49, 7255–7265, doi:10.1002/2013WR013722, 2013.

Leaf, A. T., Hart, D. J., and Bahr, J. M.: Active Thermal Tracer Tests for Improved Hydrostratigraphic Characterization, Ground Water, 50, 726–735, doi:10.1111/j.1745-6584.2012.00913.x, 2012.

Le Borgne, T., Bour, O., Riley, M., Gouze, P., Pezard, P., Belghoul, A., Lods, G., Le Provost, R., Greswell, R., Ellis, P., Isakov, E., and Last, B.: Comparison of alternative methodologies for identifying and characterizing preferential flow paths in heterogeneous aquifers, J. Hydrol., 345, 134–148, doi:10.1016/j.jhydrol.2007.07.007, 2007.

Maurice, L., Barker, J., Atkinson, T., Williams, A., and Smart, P.: A Tracer Methodology for Identifying Ambient Flows in Boreholes, Ground Water, 49, 227–238, doi:10.1111/j.1745-6584.2010.00708.x, 2011.

Moir, R. S., Parker, A. H., and Bown, R. T.: A simple inverse method for the interpretation of pumped flowing fluid electrical conductivity logs, Water Resour. Res., 50, 6466–6478, doi:10.1002/2013WR013871, 2014.

Paillet, F. L.: Flow modeling and permeability estimation using borehole flow logs in heterogeneous fractured formations, Water Resour. Res., 34, 997–1010, doi:10.1029/98WR00268, 1998.

Paillet, F. L., Hess, A. E., Cheng, C. H., and Hardin, E.: Characterization of Fracture Permeability with High-Resolution Vertical Flow Measurements During Borehole Pumping, Ground Water, 25, 28–40, doi:10.1111/j.1745-6584.1987.tb02113.x, 1987.

Pitrak, M., Mares, S., and Kobr, M.: A Simple Borehole Dilution Technique in Measuring Horizontal Ground Water Flow, Ground Water, 45, 89–92, doi:10.1111/j.1745-6584.2006.00258.x, 2007.

Read, T., Bour, O., Selker, J. S., Bense, V. F., Borgne, T. L., Hochreutener, R., and Lavenant, N.: Active-distributed temperature sensing to continuously quantify vertical flow in boreholes, Water Resour. Res., 50, 3706–3713, doi:10.1002/2014WR015273, 2014.

Sammel, E. A.: Convective flow and its effect on temperature logging in small diameter wells, Geophysics, 33, 1004–1012, doi:10.1190/1.1439977, 1968.

Selker, J. S., Thévenaz, L., Huwald, H., Mallet, A., Luxemburg, W., Van De Giesen, N., Stejskal, M., Zeman, J., Westhoff, M., and Parlange, M. B.: Distributed fiber-optic temperature sensing for hydrologic systems, Water Resour. Res., 42, W12202, doi:10.1029/2006WR005326, 2006.

Sellwood, S., Hart, D., and Bahr, J.: An in-well heat-tracer-test method for evaluating borehole flow conditions, Hydrogeol. J., doi:10.1007/s10040-015-1304-8, in press, 2015.

Appendix D

Paper 4

Bense, V.F, T. Read, and A. Verhoef, Using distributed temperature sensing to monitor field scale dynamics of ground surface temperature and related substrate heat flux, *Agricultural and Forest Meteorology*, *220*, 207-215, 2016

Agricultural and Forest Meteorology 220 (2016) 207–215

Contents lists available at ScienceDirect

Agricultural and Forest Meteorology

journal homepage: www.elsevier.com/locate/agrformet

Short communication

Using distributed temperature sensing to monitor field scale dynamics of ground surface temperature and related substrate heat flux

V.F. Bense [a,*], T. Read [b], A. Verhoef [c]

[a] Department of Environmental Sciences, Wageningen University, Wageningen, Netherlands
[b] School of Environmental Sciences, University of East Anglia, Norwich, UK
[c] Department of Geography and Environmental Science, The University of Reading, UK

ARTICLE INFO

Article history:
Received 13 April 2015
Received in revised form 8 September 2015
Accepted 20 January 2016

Keywords:
Fibre-optic distributed temperature sensing
Temperature
Wet meadows
Thermal patterns
Vegetation structure
Energy balance closure

ABSTRACT

We present one of the first studies of the use of distributed temperature sensing (DTS) along fibre-optic cables to purposely monitor spatial and temporal variations in ground surface temperature (GST) and soil temperature, and provide an estimate of the heat flux at the base of the canopy layer and in the soil. Our field site was at a groundwater-fed wet meadow in the Netherlands covered by a canopy layer (between 0 and 0.5 m thickness) consisting of grass and sedges. At this site, we ran a single cable across the surface in parallel 40 m sections spaced by 2 m, to create a 40 m × 40 m monitoring field for GST. We also buried a short length (≈10 m) of cable to depth of 0.1 ± 0.02 m to measure soil temperature. We monitored the temperature along the entire cable continuously over a two-day period and captured the diurnal course of GST, and how it was affected by rainfall and canopy structure. The diurnal GST range, as observed by the DTS system, varied between 20.94 and 35.08 °C; precipitation events acted to suppress the range of GST. The spatial distribution of GST correlated with canopy vegetation height during both day and night. Using estimates of thermal inertia, combined with a harmonic analysis of GST and soil temperature, substrate- and soil-heat fluxes were determined. Our observations demonstrate how the use of DTS shows great promise in better characterizing area-average substrate/soil heat flux, their spatiotemporal variability, and how this variability is affected by canopy structure. The DTS system is able to provide a much richer data set than could be obtained from point temperature sensors. Furthermore, substrate heat fluxes derived from GST measurements may be able to provide improved closure of the land surface energy balance in micrometeorological field studies. This will enhance our understanding of how hydrometeorological processes interact with near-surface heat fluxes.

1. Introduction

1.1. Importance of the land surface thermal regime

The thermal regime at the land surface is the result of the interactions between vegetation, soil and atmosphere (e.g. transpiration, evaporation, soil water- and heat transfer). These processes are affected by micro-topography, local hydraulic and thermal properties, and radiative and structure parameters, such as canopy height and leaf area index (e.g. Moene and van Dam, 2014; Rodriguez-Iturbe et al., 1999). These complex interactions can be formalized via the energy balance, which is closely related to the water balance via the evapotranspiration term. The energy balance describes how the net radiation received at the land surface, R_n, is distributed between evapotranspiration (latent heat flux, LE), sensible heat flux, H, and substrate heat flux, G_{sub}. The latter flux concerns heat that gets stored in (during the day) or released from (night-time) a substrate layer, consisting of topsoil and leaf-litter.

However, some researchers consider a skin layer heat flux (e.g. Holtslag and de Bruin, 1988; Steeneveld et al., 2006), where the skin layer consists of vegetation, within-canopy air space, leaf litter and top soil, with related effective temperature: the skin temperature. Following a Fourier-type heat transfer law, the skin layer heat flux depends on 'skin conductivity' and the topsoil-skin temperature gradient. Skin conductivity is a complex parameter, that is affected by soil/vegetation thermal properties, within-canopy temperature profiles (affecting canopy heat storage) as well as by within-canopy aerodynamic transfer.

The substrate heat flux, G_{sub}, more generally referred to as surface soil heat flux, as both litter layer and canopy layer are often ignored (in particular for short canopies), is a particularly

* Corresponding author.
E-mail address: victor.bense@wur.nl (V.F. Bense).

http://dx.doi.org/10.1016/j.agrformet.2016.01.138
0168-1923/

important component of the land-surface energy balance under sparse or heterogeneous canopies. Whereas area-average estimates of the atmospheric fluxes (sensible and latent heat fluxes) can be reliably obtained from eddy covariance measurements, G_{sub} is commonly derived from a small number of point estimates, generally by using soil heat flux plates buried beneath the soil, combined with an estimate of heat storage above the plate, to yield an estimate of heat flux at the soil/substrate surface. Alternatively, G_{sub} can be determined from temperature measurements at or below the soil surface (e.g. Verhoef, 2004; Verhoef et al., 2012; van der Tol, 2012), as long as estimates of near-surface soil thermal properties are available. These temperatures are generally obtained using in-situ temperature probes installed (just) below the surface (e.g. Mayocchi and Bristow, 1995; Sauer and Horton, 2005). If leaf area index (LAI) varies considerably spatially, surface soil heat (substrate) flux estimates obtained at one or a few locations only may lead to poor energy balance closure ($R_n - G_{sub} \neq H + LE$), which is a widely observed phenomenon (Foken, 2008) that is not only caused by non-representative G_{sub} estimates, but can also be the result of atmospheric phenomena (e.g. advection).

The skin-, or land surface temperature (LST), plays a key role in all four energy balance fluxes. It is generally assumed to be a skin temperature to which the soil/litter layer (i.e. via the ground surface temperature, GST) and all canopy elements contribute, although with most of the signal coming from the top canopy layer. Quantifying the magnitude and spatial distribution of LST is important in micrometeorological and remote sensing studies, with the aim to further our understanding of the intricate functioning of natural or managed ecosystems. For example, through complex feedbacks the land surface thermal regime affects the spatial distribution of fauna and flora, and is a factor in controlling rates of primary production and biogeochemical processes. The spatial patterning of LST within a given habitat may provide thermal refugia for temperature sensitive species, enhancing the resilience of the ecosystem to short-term temperature maxima or minima (e.g. Ashcroft and Gollan, 2013).

LST can be monitored at the large scale using airborne thermal infrared techniques (e.g. Schmugge et al., 2002; Bertoldi et al., 2010). At an intermediate scale, ground based thermal infrared (IR) thermometers and cameras can be set up to monitor temperature variability over a scale of a few metres (Verhoef, 2004; Pfister et al., 2010), to hundreds of metres (Heinl et al., 2012). However, in the presence of a canopy layer, thermal IR imaging will only provide an effective skin temperature, with the uppermost canopy elements (e.g. sunlit top leaves) contributing most, so no explicit information on GST (i.e. at the base of the vegetation layer) will be available. Furthermore, LST, as well as GST, will be highly variable, in space as well as in time. To address this issue we need sensors that can measure temperatures in a spatially distributed and temporally near-continuous fashion.

Distributed temperature sensing (DTS) along fibre-optic cables, installed on the substrate surface or within the soil, provide a convenient means to obtain information on (the variability of) substrate and soil temperatures, e.g. for the verification of (below- and above-ground) multi-component soil-vegetation-atmosphere-transfer (SVAT) model outputs (e.g. Verhoef and Allen, 2000) for which separate measurements of vegetation and soil surface/substrate temperatures are required. Furthermore, line-averaged G_{sub} estimates, if the DTS temperature measurements are combined with measurements or estimates of thermal properties as mentioned above, would allow improved calculations of flux-partitioning when sensible heat flux is derived from scintillometry (Evans et al., 2012), whereas area-averaged estimates of G_{sub} (by using a horizontal multi-loop configuration) are more representative of flux tower footprint areas, and hence these are expected to lead to better energy balance closure than point-scale measurements with standard soil heat flux equipment. Hence, this paper aims to demonstrate the use of DTS technology in the determination of the spatio-temporal dynamics of soil- and near surface heat fluxes, and our purpose is not to advance the technology of DTS itself. As far as we are aware DTS has not been used for calculations of soil heat flux nor used to illustrate the implications of using a single measurement point as is practised widely in energy balance studies using a single heat flux plate (e.g. Wilson et al., 2002), to obtain soil heat flux for the determination of energy balance closure in heterogeneous canopies.

1.2. Distributed temperature sensing for monitoring ecosystem temperatures

Distributed temperature sensing (DTS) is being increasingly used for environmental temperature monitoring between the point and regional scale (e.g. Selker et al., 2006). DTS provides temperature measurements along an optical fibre at spatial intervals typically of around 1 m or less and temporal intervals of less than 1 min. The optical fibre can be configured into almost any spatial pattern such that a two- or three-dimensional space can be monitored for temperature from a single device. This approach, therefore has the potential to bridge the gap between point measurements which provide good temporal but poor spatial information, and remotely captured data which provide detailed spatial measurements but often poor temporal information. Furthermore, one continuous length of DTS cable can be partly placed on the soil and in the substrate, and within the canopy (at different heights, including near the canopy top to emulate IR-derived surface temperatures), thereby providing detailed information on GST and within-canopy temperature profiles, respectively.

The principle behind DTS is that a laser pulse is directed into a fibre optic cable and the intensity of backscattered photons arising from temperature dependent Raman scattering detected subsequently. Some photons return at higher frequencies, while others return at a lower frequencies. These are known as the anti-Stokes and Stokes intensities, respectively. The temperature, which more strongly affects the anti-Stokes signal, is computed from the ratio of these two intensities. For a more detailed explanation of the fundamental physical principles of the DTS method the reader is referred to Tyler et al. (2009).

A few examples exist of studies deploying DTS for monitoring temperature in natural or managed ecosystem applications. Krause et al. (2012) deployed DTS to investigate the extent to which invasive Rhododendron in a UK woodland modifies canopy temperatures. Similarly, Lutz et al. (2012) measured ground surface temperatures using DTS in both thinned and unthinned forests. In both cases the presence of a canopy was found to significantly moderate the ground surface temperature. These studies look at temperature along transects of cables; however, a two-dimensional configuration in the vertical was utilized by Thomas et al. (2011) to monitor atmospheric-surface layer flows by attaching the optical cable to a frame and system of pulleys. This type of approach (in the horizontal) is to our knowledge yet to be attempted for the monitoring of GST and the derivation of heat fluxes. To demonstrate how DTS can be used to map GST in relatively low canopies, how these temperatures are affected by canopy structure, and how such data can be used to obtain estimates of the spatiotemporal variation of substrate- and soil heat fluxes, we deployed a DTS system in a groundwater-fed meadow in the Netherlands.

2. Materials and methods

2.1. Field site and measurements of ground surface temperatures with DTS

The field site of De Maashorst Nature Reserve is located approximately 2 km southwest of the town of Uden in the southeast of the Netherlands (Fig. 1a). The site has a high ecological value and is an example of a groundwater-fed wet meadow. A shallow (<1 m) water table is maintained by the Peel Boundary Fault to the southwest of the site (Fig. 1b), which acts as a barrier to lateral groundwater flow (in this case, from northeast to southwest). The resultant strong vertical hydraulic gradient, and highly heterogeneous Quaternary cover sands, combine to give localized seepage, visible in aerial photographs of nearby cultivated fields and readily detectable in the agricultural drainage network of the area using temperature-based and hydrochemical methods (Bense and Kooi, 2004; Bonte et al., 2013).

At the study site, these localized seepage phenomena have resulted in a highly variable spatial distribution of plant species. Some regions are dominated by plants adapted for very moist conditions and are densely vegetated by for instance Reed Mannagrass (*Glyceria maxima*), Tufted Sedge (*Carex acuta*), Lesser Pond Sedge (*Carex acutiformis*), Marsh Horsetail (*Equisetum palustre*) and Marsh Marigold (*Caltha palustris*). Neighbouring areas can have much shorter and more sparse vegetation, including Churchyard Moss (*Rhytidiadelphus squarrosus*), Pointed Spear Moss (*Calliergonella cuspidate*), Calliergon Moss (*Calliergon cordifolium*), Thread Rush (*Juncus filiformis*), and Soft Rush (*Juncus effusus*), reflecting a greater depth to groundwater. In these systems the GST can be expected to be highly spatially organized, and be controlled by the structure (density, height and LAI) of the vegetation cover through variation in light extinction, as well as by its radiative, thermal and aerodynamic properties that affect the overall energy balance.

To measure the ground surface temperature, approximately 900 m length of steel armoured multimode fibre-optic cable (manufactured by Brugg Cables, http://www.bruggcables.com) was used. The fibre-optic cable we used had an outer blue polyamide jacket. This cable was laid out in a field directly adjacent to the Peel boundary fault zone (Fig. 1b). Here, fire-optic cable was installed in 21 parallel sections of 40 m length, with a 2 m spacing between each line. We refer to this area as the *monitoring field*. The cable was loosely secured to the ground, approximately every 2 m. This resulted in the cable sitting at slightly variable heights above the soil surface (Fig. 1c), estimated to be ranging between 0 and 10 cm. A ≈10 m long section (Fig. 1b; *buried cable section*) was buried to a depth of 10 ± 2 cm, and at the surface a parallel section of cable was installed of roughly equal length (Fig. 1d).

Temperature data were collected along the DTS cable continuously over a 48 h period (25-August and 26-August, 2009) using an Oryx DTS (Sensornet, Herts, UK), powered by a battery pack and charged by a solar panel. Data along the buried cable section were only collected on 26-August. Measurements were obtained over 1.01 m intervals along the cable with an integration time of 2.5 min, using a double-ended configuration (see van de Giesen et al. (2012) for a full explanation and description of the principle of double-ended DTS measurements). Using the double-ended DTS configuration a correction was made to the raw data for the differential attenuation of light along the fibre. To account for temperature offset and instrument drift, a 20 m section of coiled cable

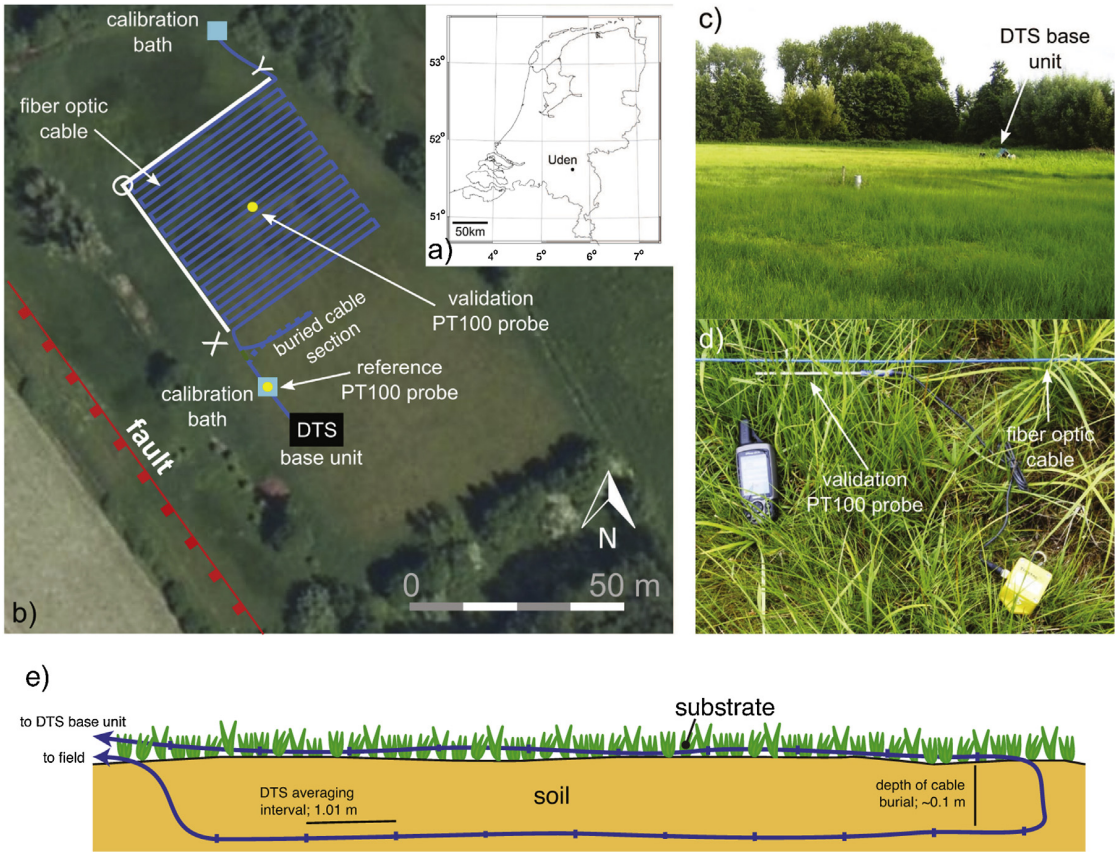

Fig. 1. (a) Location of the field site near the village of Uden, Netherlands, (b) the configuration of the DTS monitoring set-up, (c) wet meadow area where the fibre optic cable was deployed, and (d) validation PT100 probe adjacent to the fibre optic cable, (e) configuration of the buried cable section.

and a reference PT100 probe were placed in an insulating box filled with water. The DTS data were subsequently post-processed by comparing the average DTS coil temperature with the PT100 probe, and applying a time-varying offset. A second PT100 probe was placed in the centre of the field adjacent to the cable to validate the calibration procedure. Although the DTS derived temperatures were calibrated, following the procedure outlined above, it is likely that some discrepancies will still exist between ambient temperatures and those sensed along the fibres in the cable. This is due to heat absorption of the cable as a result of solar heating. Consequently, DTS temperatures can be higher than ambient during sunny periods of the day, whilst the magnitude of this effect is dependent on cable colour and thickness (de Jong et al., 2015). For the blue cable (diameter: 4 mm) we use in this study this bias might amount to up to 1–2 °C.

The variation in vegetation height was measured manually using a yardstick, to the nearest 5 cm, at 2 m intervals within the monitoring field. We consider that the vegetation height, albeit being a simple variable, should reflect well the LAI.

Meteorological data including air temperature and precipitation were obtained at hourly intervals from a weather station at Volkel, located at a distance of 6 km from the field site. At the field site, no meteorological data were collected.

2.2. Calculation of substrate- and soil heat flux from DTS measurements

We consider the *substrate* as that zone directly surrounding the above-ground DTS cable in the monitoring field where heat is stored in/released from and transferred to/from a substrate consisting of soil, above ground litter and fresh leaf matter and air (Fig. 1e). We employ the term *soil* in the conventional way and used the soil temperatures as measured in the buried cable section to calculate a soil heat flux at the depth of cable burial and the GST measurements to derive substrate heat flux.

The original 2.5 min averaged DTS temperature were averaged to give 30-minute average temperature values for each 1.01 m along the DTS cable. The temperature measurements were subjected to a harmonic analysis, which allowed calculation of substrate- and soil heat flux (G_{sub} and G_{soil}), using one estimate of average substrate thermal properties across the entire monitoring field, and that of the soil along the length of buried cable, respectively. We recognize that the thermal properties of the substrate and soil will be spatially variable, but we did not quantify this variability at our field site. For the soil, the texture and moisture content over a site will vary to a certain degree but at soil moisture contents above 50% of saturation (see Murray and Verhoef, 2007) this sensitivity is very strongly reduced. At our site with very shallow groundwater tables it is likely that soils are near saturation. Nevertheless, soil thermal properties could have been determined by using a heat-pulse needle probe, but substrate properties would have been impossible to obtain in this way due to lack of contact between probe and the bulk of the substrate, and there is currently no way of routinely obtaining such data in the field. We accept that for some locations we will overestimate or underestimate soil/substrate heat fluxes by assuming spatially constant thermal properties. However, we expect that the overall variability in heat fluxes would not change significantly if the detailed variability in thermal properties would have been known. This is because the biggest determinant of variability in diurnal peak value in heat fluxes is the amplitude of temperature which will be most strongly influenced by parameters like canopy properties, such as height and density, causing variations in shading, and within-canopy and near soil-surface aerodynamic resistances. Finally, high moisture contents in the capillary fringe and moisture fluxes due to root water uptake may affect the ground surface temperatures, but these effects are implicit in the temperature fluctuations and spatial distributions of temperature, hence they are already implicitly included in the soil heat flux as it is calculated following the methodology outlined below.

Substrate- and soil heat fluxes were calculated using the method described in Verhoef (2004) and Murray and Verhoef (2007). This involved a harmonic analysis of DTS temperatures, which was followed by calculation of the heat flux G [W m^{-2}] using an analytical method. This approach requires the estimation of thermal inertia (Γ [J m^{-2} K^{-1} s$^{-0.5}$]) for both the soil and the substrate. Γ is defined as $\sqrt{\lambda C_h}$ where λ [W m^{-1} K^{-1}] is thermal conductivity, and C_h [J m^{-3} K^{-1}] is volumetric heat capacity.

The soil type at the field site was peat and typical values of peat thermal properties were selected from the literature. For C_h, a value of 3×10^6 J m^{-3} K^{-1} was selected and thermal diffusivity, D_h, equalled 1.1×10^{-7} m^2 s^{-1} (near-saturation values derived from Table 1.2.4 in Grossnickle (2000)) which led to a thermal conductivity ($\lambda = D_h C_h$) of 0.33 W m^{-1} K^{-1}. In turn, this resulted in an estimate for soil thermal inertia, Γ_{soil}, of 995 J m^{-2} K^{-1} s$^{-0.5}$, which was used for the calculation of soil heat flux (G_{soil}), based on below ground DTS measurements.

However, the substrate also consisted of grass and air as it was impossible at the field site to have the fibre-optic cable touching the ground or leaf/litter surfaces throughout the entirety of its length. Nevertheless, this set-up provides a good approximation of the skin layer heat flux, as introduced in Section 1.1. With C_h for grass equal to 2.8×10^6 J m^{-3} K^{-1} (which is similar to peat) and $\lambda = 1.1$ W m^{-1} K^{-1} (Yaghoobian et al., 2010), we found $\Gamma = 1755$ J m^{-2} K^{-1} s$^{-0.5}$, whereas thermal inertia for air is 5.5 J m^{-2} K^{-1} s$^{-0.5}$. From visual estimates in the field we assume a substrate composition of about 35% air, 40% grass and 25% soil over each metre length of cable, hence $\Gamma_{substrate} = 955$ J m^{-2} K^{-1} s$^{-0.5}$.

With an estimate of thermal inertia we obtain a value for G using:

$$G = \Gamma \sum_{n=1}^{M} A_n \sqrt{n\omega} \left[\sin \left[n\omega t + \phi_n + \frac{\pi}{4} \right] \right] \quad (1)$$

where M is the total number of harmonics (n) used (20), A_n [°C] the amplitude of the nth harmonic, ϕ_n the phase shift of the nth harmonic, t [s] the time and ω is the angular frequency ($24 \times 60 \times 60$s). A_n and ϕ_n are derived from the harmonic analysis of DTS temperatures.

3. Results

3.1. Temporal ground surface temperature dynamics

The two full days (25-August and 26-August) covered by DTS measurements had contrasting meteorological conditions. On 25-August, rainfall overnight was followed by further rainfall approximately between 10:00 and 12:00 h (Fig. 2a). This totalled only 0.2 mm at the Volkel meteorological station. From 12:00 h, there was no further precipitation recorded at Volkel. The following day (26-August) was relatively warm and had been preceded by a cold night.

Fig. 2b plots the mean and range in GST across the monitoring field, as observed by DTS. Comparing these time series to those of air–temperature (Fig. 2a) shows that GST varies in a way similar to air temperature. Note that prior to the rainfall event on the 25-August, the GST is consistently below the air temperature at Volkel, and has a relatively small range (Fig. 2b). From approximately 20:00 on 25-August, the range in GST is in general much larger, except around 08:00 and 20:00 h when it reaches a minimum. Furthermore, the absolute value of GST is almost always higher than the air temperature during the day and lower at night.

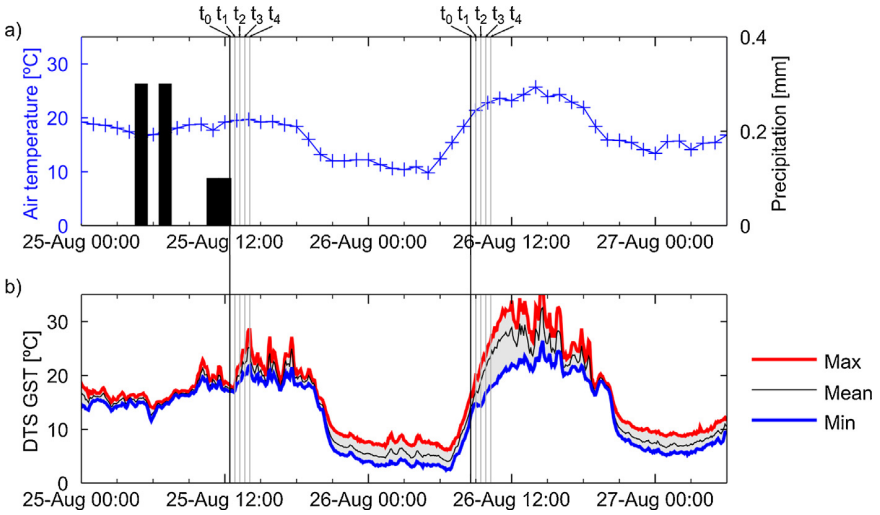

Fig. 2. (a) Air temperature and precipitation measured at Volkel and (b) time series of maximum, mean, and minimum GST recorded with the DTS along the fibre optic cable.

3.2. Spatial and temporal dynamics during warming

In order to investigate the spatiotemporal dynamics of GST across the monitoring field we selected two sequences from the entire data set. We consider the daytime temperature dynamics following the rainfall event on 25-August (between 10:00 h and 12:00 h), and compare this with the warming recorded during the morning of the following day with antecedent dry conditions. For every location along the cable, the difference in temperature (ΔGST), was calculated relative to the spatially averaged GST at reference times (t_0; Fig. 2a) of 12:25 h and 08:35 h on the 25th and 26th August, respectively. Values of ΔGST were calculated at four times (t_{1-4} after t_0, separated by 25 min, on both days. The ΔGST values were then spatially mapped onto a grid with 2 m spacing in the O-X direction, and 1 m spacing in the O-Y direction to replicate the spatial sampling interval in the field.

Fig. 3 shows the spatially mapped ΔGST values at the four times after t_0 on 25-August (a–d), and 26-August (e–h). On 25-August, there is little change in GST after the first 25 min. After this, both the range and mean ΔGST have increased - a trend which continues until 14:05 h. By now there is a spatial organization to the ΔGST which correlates with the vegetation height; the vegetation height is shown on each plot using contour lines. This correlation is further illustrated in Fig. 4. Those areas with the shortest vegetation, and hence with the lowest LAI, experience the greatest warming. On 26-August the initial warming is more rapid, and by 10:15 h there exists a pattern of ΔGST similar to that in vegetation height.

3.3. Impact of vegetation on GST dynamics

To investigate the effect of variable vegetation cover on the temperature dynamics, each DTS temperature measurement location was assigned to one of six groups according to vegetation height at that point. The group ranges were chosen such that the number of samples (n) in each group was as equal as possible, whilst still maintaining a distinct group which had the tallest vegetation only. The time series of average GST for each group was calculated, and the mean field temperature then subtracted to give the difference from the mean GST for each group (Fig. 4).

A clear diurnal signal emerges; areas with the lowest canopy height (<5 cm) are colder at night and warmer during the day, than those areas with tall (50–90 cm) vegetation (Fig. 4a). A transition, where the total range of GST is low, and the tallest vegetation regions switch from being the coldest to being the warmest regions, occur at 20:00 h on both days. The reverse happens at around 08:00 h on 26-August and to a lesser extent at around the same time on the previous day. The magnitude of the daytime vegetation shading effect is much reduced on 25-August, due to increased cloud cover which means there is less direct radiation reaching the canopy. A prevalence of diffuse radiation will lead to much less pronounced differences in GSTs between low and high crop height/LAI areas. In contrast, on a sunny day there would be distinct sunlit and shaded areas, due to considerable differences in radiation extinction, which is highly affected by LAI.

The presence of taller plant species has a clear moderating effect on the variation in GSTs. During August 26, at any point in the monitoring field the maximum of the range of diurnal GST variations was 35.08 °C while the minimum was 20.94 °C (Fig. 4b). The temperature range visually strongly correlates with the vegetation height ($r^2 = 0.48$), and is greatest where there is little or no vegetation cover.

Fig. 5 shows the observed temperatures in the buried cable section for 26-August. The temperatures along the cable show clearly where the cable enters the soil (Fig. 5a) at which point a transition zone occurs in which the temperatures recorded are in between those recorded at the surface (substrate) and in the soil (soil) (Fig. 5b). The data show that the spatial variation of temperature within each section (substrate and soil) is fairly low and varies slightly over time.

3.4. Substrate- and soil heat flux dynamics

The calculated spatiotemporal trends in substrate- and soil heat flux (G_{sub} and G_{soil}, respectively) are discussed for 26-August only, a day with a more clearly defined diurnal temperature signal than 25-August. Moreover, data for the buried cable section are only available for 26-August.

Fig. 6 shows the evolution of the calculated G_{sub} for 26-August (a predominantly sunny day, but with broken cloud occurrences in the afternoon) spatially averaged across the monitoring field, together with the G_{soil} in the buried section. Following standard behaviour of substrate and soil heat fluxes G_{sub} and G_{soil} vary diurnally, with negative values during the night and positive values between sunrise and sunset. For G_{sub} this denotes ground surface heat loss to and heat gain from the in-canopy air space, respectively; for G_{soil} these negative and positive fluxes are representative of heat loss

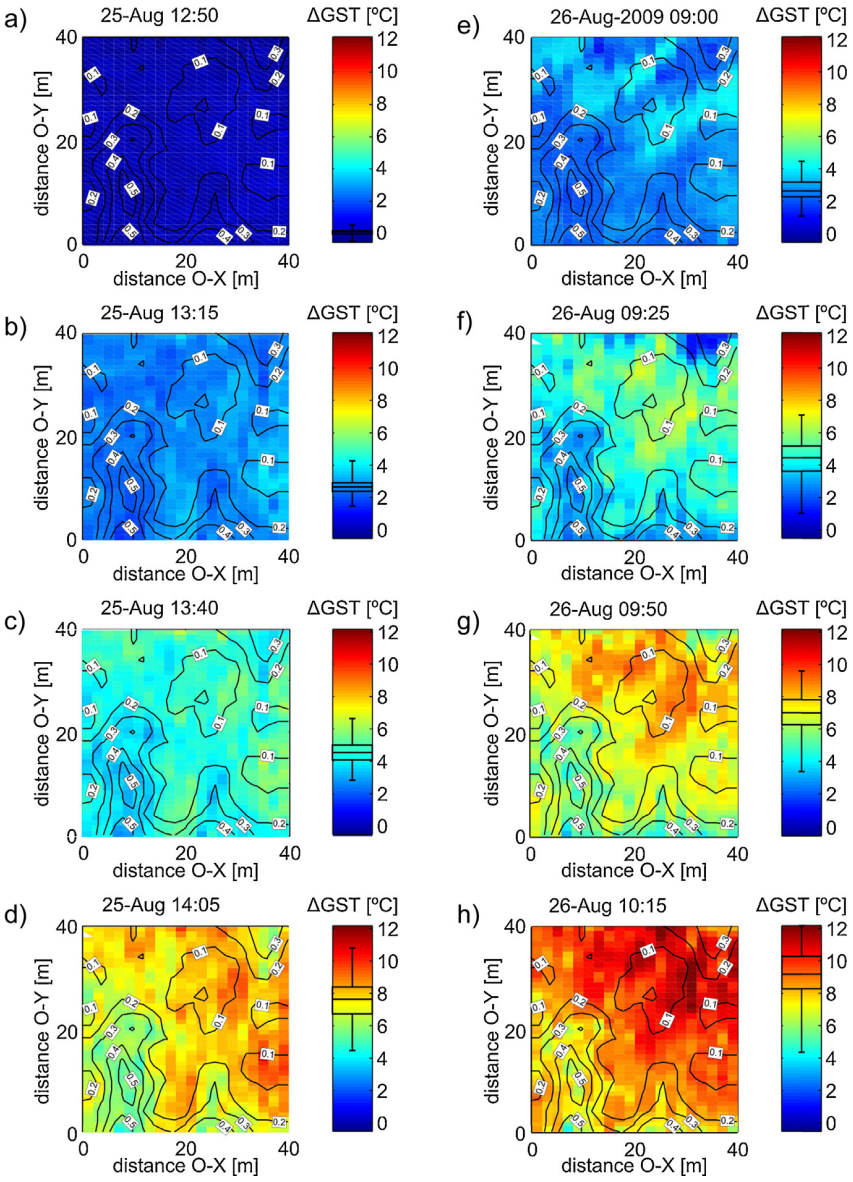

Fig. 3. (a–d) ΔGST distribution at 12:50 h (t_1; Fig. 2b), 13:15 h (t_2), 13:40 h (t_3), and 14:05 h (t_4) on 25-August, and (e–h) 09:00 h (t_1), 09:25 h, (t_2), 09:50 h (t_3), and 10:15 h (t_4) on 26-August. Each plot is overlaid with contour plots of the vegetation height [m]. The box plot in each colour bar gives the minimum, lower quartile, median, upper quartile, and maximum ΔGST.

to and heat gain from the soil layer above the below-ground DTS installation depth.

The magnitude of the substrate soil heat flux (peak value of around 190 W m^{-2}) fits with 26-August being a warm, predominantly sunny day and the substrate being relatively exposed (crop height <0.5 m and low LAI from visual inspection). Values of G_{sub} at their maximum (around 11:00 h) ranged between 76 W m^{-2} and 190 W m^{-2} with an average of 150 W m^{-2}, whereas for G_{soil} values between 17 and 36 W m^{-2} were found (average of 24 W m^{-2}). The soil heat flux values in the buried cable section peak around 12:00 h whilst the mean substrate heat fluxes across the field peaks earlier at 10:30–11:00 h. This reflects standard behaviour where the amplitude of diurnal variability is dampened in the soil, and a delay of peak values occurs.

Fig. 6b–d shows values of G_{sub} for 26-August, overlain by contours of vegetation height, to illustrate how G_{sub} varies considerably over the monitoring field over the duration of a day. Early in the day, at 05:00 h (Fig. 6b), all calculated G_{sub} values are negative indicating that the substrate is cooling. The more exposed areas are cooling more rapidly, indicated by a more negative G_{sub} in those parts of the field. At 11:00 h when values peak (Fig. 6c), the latter pattern is inverted to a degree where at this time of day the more exposed areas display the higher G_{sub} values. This is to be expected as the places where the canopy is sheltering the soil to a lesser degree, will have received more radiation and hence will exhibit larger substrate heat fluxes. Later in the day at 17:00 h (Fig. 6d) a similar pattern of G_{sub} arises as was present in the morning arises indicating that more exposed areas are cooling more rapidly than secluded areas. It is noticeable that in the afternoon of 26-August the mean and range in G_{sub} are strongly fluctuating at a time-scale of hours alternating between mean average and positive values. These cannot be directly attributed to fluctuations in air-temperature, which do not display such variability (Fig. 2), and most likely coincide with variations in incoming radiation.

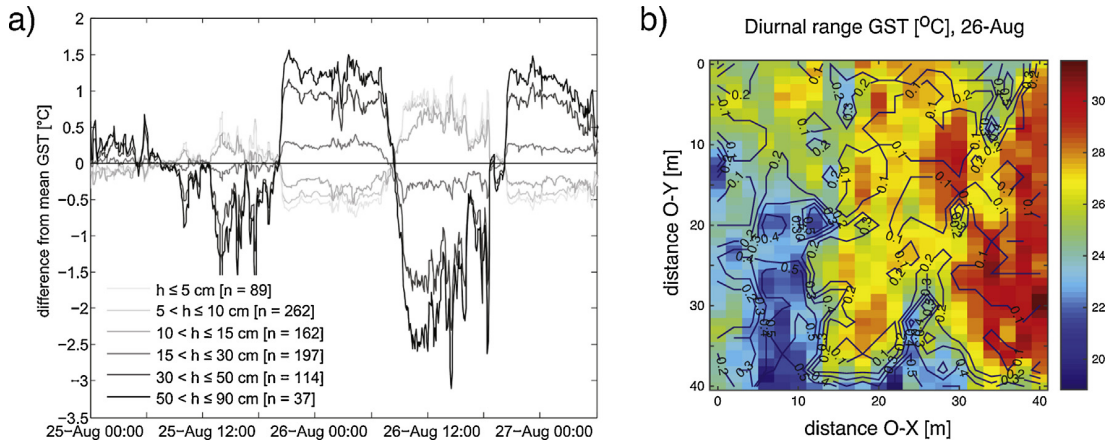

Fig. 4. (a) Difference between the mean GST relative to the temporal mean of the monitored area, for different vegetation height groupings. (b) The spatial variability of the diurnal range in GST on 26-August. The plot is overlaid with contours of the vegetation height [m].

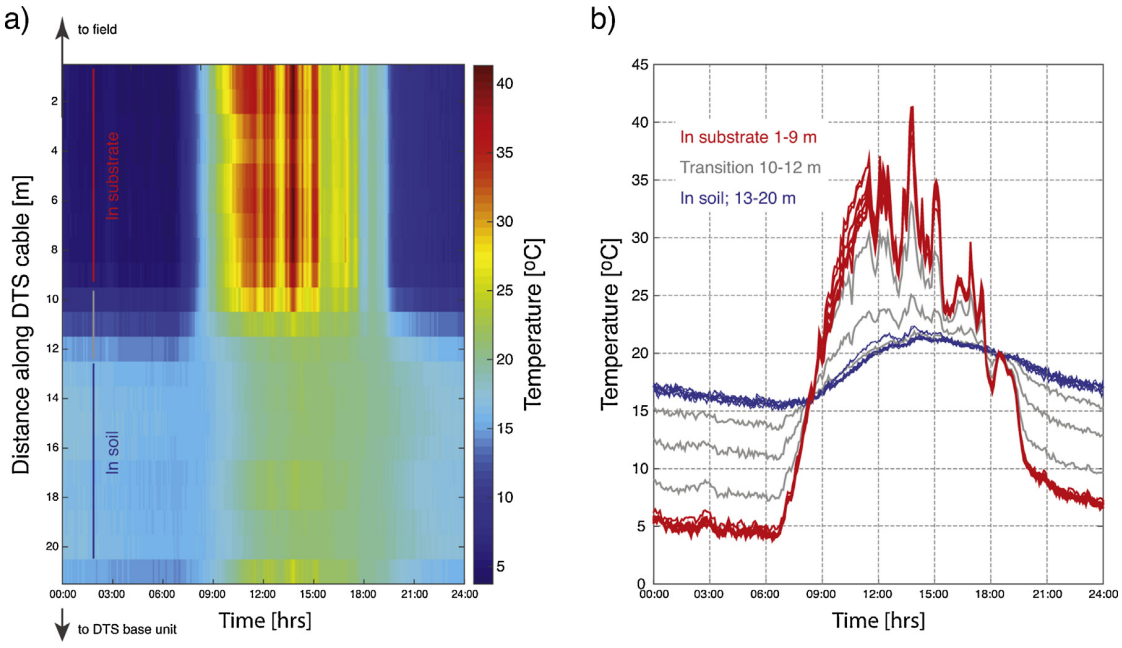

Fig. 5. (a) DTS temperature data for the buried cable section on 26-August. Location and set-up used to obtain these data are shown in Fig. 1a and d respectively. (b) DTS temperature in time for each part of the cable in the buried cable section. Data have a time resolution of 2.5 min.

4. Discussion and conclusions

We deployed distributed temperature sensing to monitor near surface temperatures in a wet meadow site in the Netherlands, in the late summer season. Using a relatively simple cable configuration, we were able to map considerable temperature patterns in great spatio-temporal detail. Temperature data like these, as we collected using DTS, would be practically impossible to collect with any other field methodology. In the discussion of our results we aim to separate spatial patterns and temporal dynamics present in our data.

The emerging spatial trends in the temperature data correlate with vegetation height, in particular, when the diurnal range of temperatures is considered (Fig. 4b), as well as for the calculated substrate heat fluxes (Fig. 6b–d). For taller vegetation, diurnal GST and G_{sub} variations are significantly smaller indicating that the thicker canopy more effectively dampens air temperature fluctuations. This results in temperatures that are higher underneath thicker vegetation during the night but relatively cool during daytime (Fig. 4a). These spatiotemporal differences in the diurnal range of GST and G_{sub} are a combination of radiative, aerodynamic and thermodynamic effects. Examples are a reduction in direct solar radiation (via canopy radiative extinction) received during the day and prevention of radiative cooling via long-wave outgoing radiation, and substrate heat loss driven by a temperature gradient between soil and substrate temperature, at night. When precipitation events occur these are observed to have an immediate temperature homogenizing effect which is largely independent of vegetation height (Figs. 2 and 3). This likely is the result of evaporation of intercepted water and the fact that radiation will be predominantly diffuse during and just after rainfall. Our data set allowed us to illustrate how the substrate surface temperature distribution evolves from such thermally homogeneous conditions which can either be caused by a rainfall event (Fig. 3a–d) or from the presence of dew in combination with the impact of diurnal incoming radiation temperature dynamics (Fig. 3e–h).

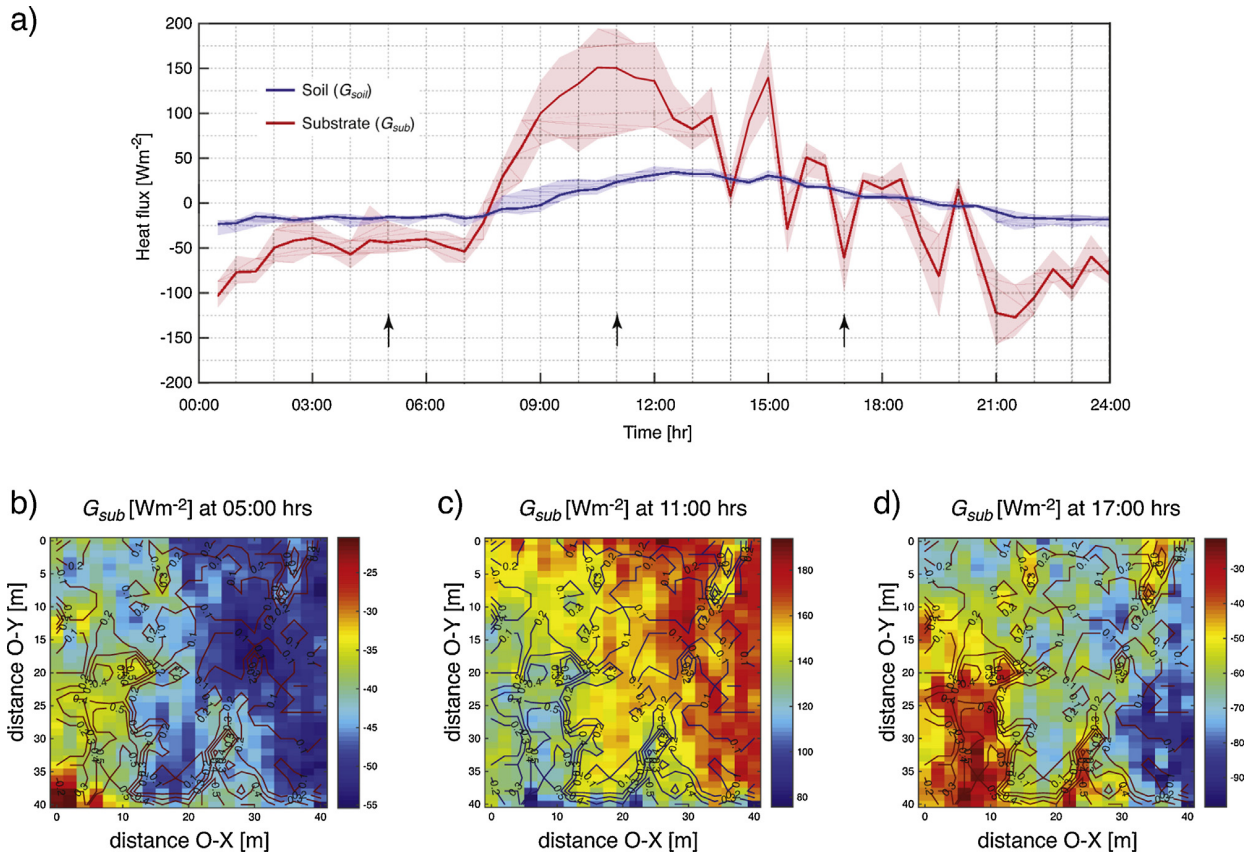

Fig. 6. (a) Substrate- and soil heat flux calculated for the field, and the buried cable section respectively, on 26-August. The mean heat flux values are indicated by the solid lines, while the range of the observed values is indicated by the shaded area. A total of 860 DTS observations were used to calculate the substrate heat flux at each 30 min time step, whilst for the soil heat flux in the BG section only 8 DTS observations were available (see Fig. 5). The arrows indicate the time steps for which the spatial distribution of the substrate heat fluxes are shown in (b–d). The spatial variability of G_{sub} is shown for (b) 05:00 h, (c) 11:00 h, and (d) 17:00 h. Each plot is overlaid with contours of the vegetation height [m].

In future studies, the collection of on-site auxillary data such as meteorological and independent heat flux observations will aid to understand correlations between observed temperature distributions and meteorological and soil conditions. However, we emphasize that even if such measurements at selected locations are obtained their use would be hampered by a series of issues. Temperature measurements with thermocouples or IR thermometers have their own particular problems such as radiation effects/contact issues with thermocouples, or lack of surface emissivity data for IR measurements. Furthermore, independent measurements of soil heat flux using soil heat flux plates should not be viewed as a 'standard' or reference method. They suffer as well from a range of shortcomings, such as interference with soil moisture flow, contact problems, and inaccuracies in the calculation of above-plate heat storage. These limitations reduce the usability of such data for the interpretation, or validation, of DTS derived temperatures and associated heat fluxes.

The DTS technique illustrated here also shows great promise in getting a better handle on area-average substrate and below-ground soil heat flux estimates, and their spatio-temporal variability, when the temperature measurements are combined with a harmonic analysis and subsequent calculation of soil heat flux with an analytical method (Verhoef, 2004). It seems that the heat flux directly at or below the soil surface can be obtained from DTS cables placed at the soil surface or buried in the soil, but the installation needs to be conducted very carefully. That is, the cable is either secured right against the soil/litter layer surface or the below-ground installation depth is known with as high a precision as possible. Verhoef (2004) and van der Tol (2012) have shown that the *surface* soil heat flux derived from soil temperatures, which requires a more complex analytical equation than Eq. (1) (see Verhoef, 2004: Eq. (6) and Verhoef et al., 2012: Eq. (9)) that uses C_h and D_h explicitly (rather than the composite thermal property, Γ), as well as the distance between the measurement location and the soil surface, is very sensitive to errors in the assumed installation depth. Furthermore, it would be preferable to install further parts of the cable at different heights throughout the canopy so that estimates of canopy heat storage can be obtained in the context of skin layer conductivity/skin layer heat transfer (see Section 1.1). Knowledge of the heat exchanged with or stored within the canopy would lead to significantly reduced errors in energy balance closure (Moderow et al., 2009).

We conclude that our DTS measurements have captured the temperature dynamics resultant from soil–vegetation–atmosphere energy exchanges in great spatial and temporal detail. However, in the absence of further experimental data such as field-average net radiation and sensible and latent heat fluxes, or within-field variation in leaf temperatures, it is not possible to evaluate the relative importance of different heat fluxes in this ecosystem, and interpret the DTS data in more detail, for example using SVAT modelling. In addition to the monitoring of these variables and fluxes in future studies, the DTS component can be expanded to include sections where the cable is buried into the soil, in order to potentially capture soil moisture dynamics as pioneered by Steele-Dunne et al. (2010). Shading effects could be further evaluated by using white and black jacketed fibre-optic cables in a similar way as described

by Petrides et al. (2011) who studied shading over stream channels using DTS.

Also, in the present study, we only look at two-dimensional spatial variation in temperature. However, it is possible to configure the cable such that any geometry in space may be monitored. This could be made to include the soil, canopy, and above canopy at a number of different heights. It is also possible, by coilling the fibre optic cable around a vertical cylinder, for example, to increase the effective spatial resolution (e.g. Vogt et al. (2010) for a stream bed and van Emmerik et al. (2013) for a lake application). When considering the energy balance at the land surface, and in particular the role of within-canopy storage, several of these high resolution vertical profiles could be included, as part of the same fibre optic cable.

Moreover, ground based- (e.g. Cardenas et al., 2008; Pfister et al., 2010) or airborne thermal imaging (e.g. Richter et al., 2009), mostly capturing the temperature of surface elements at or near the top of the canopy, can be combined with DTS which in our set-up monitors temperatures inside the canopy. This may lead to more accurate estimates of sensible heat flux when this flux is determined from bulk transfer equations, that rely on a surface-air temperature gradient. Although our field campaign was limited to only a few days at the end of the summer season (late August); longer term monitoring would yield further information on the temperature effects of vegetation dynamics in terms of the energy balance, but also in the context of soil respiration, for example, as this is strongly affected by seasonal changes in soil temperature and presence of vegetation (vigorous root growth/respiration during summer, versus winter vegetation dormancy with microbial respiration only). All of these efforts would further our understanding of the interactions between near-surface heat flow dynamics and ecohydrological processes.

Acknowledgement

Nico Ettema of the Institute for Nature Education and Sustainability, Uden, Netherlands is thanked for valuable advice during field work. The research reported in this paper was supported by a Natural Environment Research Council (NERC) studentship (NE/J500069/1) to Tom Read. Data underlying this research can be provided upon request by contacting the corresponding author.

References

Ashcroft, M.B., Gollan, J.R., 2013. Moisture, thermal inertia, and the spatial distributions of near-surface soil and air temperatures: understanding factors that promote microrefugia. Agric. Forest Meteorol. 176, 77–89.
Bense, V.F., Kooi, H., 2004. Temporal and spatial variations of shallow subsurface temperature as a record of lateral variations in groundwater flow. J. Geophys. Res. B: Solid Earth 109 (4).
Bertoldi, G., Notarnicola, C., Leitinger, G., Endrizzi, S., Zebisch, M., Della Chiesa, S., Tappeiner, U., 2010. Topographical and ecohydrological controls on land surface temperature in an alpine catchment. Ecohydrology 3 (2), 189–204.
Bonte, M., Geris, J., Post, V., Bense, V., van Dijk, H., Kooi, H., 2013. Mapping surface water–groundwater interactions and associated geological faults using temperature profiling. In: Groundwater and Ecosystems of IAH Series on Hydrogeology, chapter 8, pp. 81–94.
Cardenas, B., Harvey, J., Packman, A., Scott, D., 2008. Ground-based thermography of fluvial systems at low and high discharge reveals potential complex thermal heterogeneity driven by flow variation and bioroughness. Hydrol. Process., 22.
de Jong, S.A.P., Slingerland, J.D., van de Giesen, N.C., 2015. Fiber optic distributed temperature sensing for the determination of air temperature. Atmos. Measur. Techn. 8, 335–339.
Evans, J.G., McNeil, D., Finch, J.W., Murray, T., Harding, R.J., Ward, H., Verhoef, A., 2012. Determination of turbulent heat fluxes using a large aperture scintillometer over undulating mixed agricultural terrain. Agric. Forest Meteorol. 166–167, 221–233.
Foken, T., 2008. The energy balance closure problem: an overview. Ecol. Appl. 18, 1351–1367.
Grossnickle, S., 2000. Ecophysiology of Northern Spruce Species: The Performance of Planted Seedlings. NRC Research Press.
Heinl, M., Leitinger, G., Tappeiner, U., 2012. Diurnal surface temperature regimes in mountain environments. Phys. Geogr. 33 (4), 344–359.
Holtslag, A.A.M., de Bruin, H., 1988. Applied modelling of the night-time surface energy balance over land. Boundary-Layer Meteorol. 27, 689–704.
Krause, S., Taylor, S.L., Weatherill, J., Haffenden, A., Levy, A., Cassidy, N.J., Thomas, P., 2012. Fibre-optic distributed temperature sensing for characterizing the impacts of vegetation coverage on thermal patterns in woodlands. Ecohydrology.
Lutz, J.A., Martin, K.A., Lundquist, J.D., 2012. Using fiber-optic distributed temperature sensing to measure ground surface temperature in thinned and unthinned forests. Northwest Sci. 86 (2), 108–121.
Mayocchi, C., Bristow, K., 1995. Soil surface heat flux: some general questions and comments on measurements. Agric. Forest Meteorol. 75, 43–50.
Moderow, U., Aubinet, M., Feigenwinter, C., Kolle, O., Lindroth, A., Molder, M., Montagnani, L., Rebmann, C., Bernhofer, C., 2009. Available energy and energy balance closure at four coniferous forest sites across Europe. Theor. Appl. Climatol. 98 (3-4), 397–412.
Moene, A., van Dam, J., 2014. Transport in the Atmosphere-Vegetation-Soil Continuum. Cambridge University Press.
Murray, T., Verhoef, A., 2007. Moving towards a more mechanistic approach in the determination of soil heat flux from remote measurements: i. A universal approach to calculate thermal inertia. Agric. Forest Meteorol. 147, 80–87.
Murray, T., Verhoef, A., 2007. Moving towards a more mechanistic approach in the determination of soil heat flux from remote measurements: ii. Diurnal shape of soil heat flux. Agric. Forest Meteorol. 147, 88–97.
Petrides, A., Huff, J., Arik, A., van de Giesen, N., Kennedy, A.M., Thomas, C.K., Selker, J.S., 2011. Shade estimation over streams using distributed temperature sensing. Water Resour. Res. 47, W07601.
Pfister, L., McDonnell, J.J., Hissler, C., Hoffmann, L., 2010. Ground-based thermal imagery as a simple, practical tool for mapping saturated area connectivity and dynamics. Hydrol. Pro 21, 3123–3132.
Richter, K., Palladino, M., Vuolo, F., Dini, L., D'Urso, G., 2009. Spatial distribution of soil water content from airborne thermal and optical remote sensing data. In: Proceedings of SPIE – The International Society for Optical Engineering, p. 7472.
Rodriguez-Iturbe, I., D'Odorico, P., Porporato, a., Ridolfi, L., 1999. On the spatial and temporal links between vegetation, climate, and soil moisture. Water Resour. Res. 35 (12), 3709.
Sauer, T.J., Horton, R., 2005. Soil heat flux. In: Micrometeorology in Agricultural Systems, vol. 47 of Agronomy Monograph, pp. 131–154, chapter 7.
Schmugge, T., Kustas, W., Ritchie, J., Jackson, T., Rango, A., 2002. Remote sensing in hydrology. Advances in Water Resources 25 (8–12), 1367–1385.
Selker, J., Thévenaz, L., Huwald, H., Mallet, A., Luxemburg, W., Van De Giesen, N., Stejskal, M., Zeman, J., Westhoff, M., Parlange, M., 2006. Distributed fiber-optic temperature sensing for hydrologic systems. Water Resour. Res. 42 (12).
Steele-Dunne, S., Rutten, M., Krzeminska, D., Hausner, M., Tyler, S., Selker, J., Bogaard, T., Van De Giesen, N., 2010. Feasibility of soil moisture estimation using passive distributed temperature sensing. Water Resour. Res. 46, W03534.
Steeneveld, G., van de Wiel, B., Holtslag, A., 2006. Modeling the evolution of the atmospheric boundary layer coupled to the land surface for three contrasting nights in cases-99. J. Atmos. Sci. 63, 920–935.
Thomas, C.K., Kennedy, A.M., Selker, J.S., Moretti, A., Schroth, M.H., Smoot, A.R., Tufillaro, N.B., Zeeman, M.J., 2011, November. High-resolution fibre-optic temperature sensing: a new tool to study the two-dimensional structure of atmospheric surface-layer flow. Boundary-Layer Meteorol., 177–192.
Tyler, S.W., Selker, J.S., Hausner, M.B., Hatch, C.E., Torgersen, T., Thodal, C.E., Schladow, S.G., 2009, January. Environmental temperature sensing using Raman spectra DTS fiber-optic methods. Water Resour. Res. 45, 1–11.
van de Giesen, N., Steele-Dunne, S.C., Jansen, J., Hoes, O., Hausner, M.B., Tyler, S., Selker, J., 2012. Double-ended calibration of fiber-optic Raman spectra distributed temperature sensing data. Sensors, 5471–5485.
van der Tol, C., 2012. Validation of remote sensing of bare soil ground heat flux. Remote Sens. Environ. 121, 275–286.
van Emmerik, T., Rimmer, a., Lechinsky, Y., Wenker, K., Nussboim, S., van de Giesen, N., 2013. Measuring heat balance residual at lake surface using distributed temperature sensing. Limnol. Oceanogr. Methods 11 (1991), 79–90.
Verhoef, A., 2004. Remote estimation of thermal inertia and soil heat flux for bare soil. Agric. Forest Meteorol. 123, 221–236.
Verhoef, A., Allen, S., 2000. A SVAT scheme describing energy and CO_2 fluxes for multi-component vegetation: calibration and test for a Sahelian Savannah. Ecol. Model. 127, 245–267.
Verhoef, A., Ottle, C., Cappelaere, B., Murray, T., Saux-Picart, S., Zribi, M., Maignan, F., Boulain, N., Demarty, J., Ramier, D., 2012. Spatio-temporal surface soil heat flux estimates from satellite data; results for the AMMA experiment at the Fakara (Niger) supersite. Agric. Forest Meteorol. 154–155, 55–66.
Vogt, T., Schneider, P., Hahn-Woernle, L., Cirpka, O.A., 2010. Estimation of seepage rates in a losing stream by means of fiber-optic high-resolution vertical temperature profiling. J. Hydrol. 380 (1–2), 154–164.
Wilson, K.B., Goldstein, A.H., Falge, E., Aubinet, M., Baldocchi, D., Berbigier, P., Bernhofer, C., Ceulemans, R., Dolman, H., Field, C., Grelle, A., Law, B., Meyers, T., Moncrieff, J., Mon-son, R., Oechel, W., Tenhunen, J., Valentini, R., Verma, S., 2002. Energy balance closure at FLUXNET sites. Agric. Forest Meteorol. 113, 223–243.
Yaghoobian, N., Kleissl, J., Krayenhoff, E., 2010. Modeling the thermal effects of artificial turf on the urban environment. J. Appl. Meteor. Climatol. 49, 332–345.

References

Acuña, V., and K. Tockner, Surface-subsurface water exchange rates along alluvial river reaches control the thermal patterns in an Alpine river network, *Freshwater Biology*, *54*(2), 306–320, doi:10.1111/j.1365-2427.2008.02109.x, 2009.

Anderson, M. P., Heat as a ground water tracer., *Ground water*, *43*(6), 951–68, doi:10.1111/j.1745-6584.2005.00052.x, 2005.

Arnon, A., N. G. Lensky, and J. S. Selker, High-resolution temperature sensing in the dead sea using fiber optics, *Water Resources Research*, *50*(2), 1756–1772, doi:10.1002/2013WR014935, 2014a.

Arnon, A., J. Selker, and N. Lensky, Correcting artifacts in transition to a wound optic fiber: Example from high-resolution temperature profiling in the dead sea, *Water Resources Research*, *50*(6), 5329–5333, doi:10.1002/2013WR014910, 2014b.

Asmundsson, R., et al., High temperature instruments and methods developed for supercritical geothermal reservoir characterisation and exploitationthe hiti project, *Geothermics*, *49*, 90 – 98, doi:http://dx.doi.org/10.1016/j.geothermics.2013.07.008, iceland Deep Drilling Project:The first well, IDDP-1, drilled into Magma, 2014.

Aufleger, M., M. Conrad, M. Goltz, S. Perzlmaier, and P. Porras, Innovative dam monitoring tools based on distributed temperature measurement, *Jordan Journal of Civil Engineering*, *1*(1), 29–37, 2007.

Bakker, M., R. Caljé, F. Schaars, K.-J. van der Made, and S. de Haas, An active heat tracer experiment to determine groundwater velocities using fiber optic cables installed with direct push equipment, *Water Resources Research*, *51*(4), 2760–2772, 2015.

Banks, E., C. Simmons, a.J. Love, and P. Shand, Assessing spatial and temporal connectivity between surface water and groundwater in a regional catchment: Implications for regional scale water quantity and quality, *Journal of Hydrology*, *404*(1-2), 30–49, doi:10.1016/j.jhydrol.2011.04.017, 2011.

Banks, E. W., M. A. Shanafield, and P. G. Cook, Induced temperature gradients to examine groundwater flowpaths in open boreholes, *Groundwater*, pp. n/a–n/a, doi:10.1111/gwat.12157, 2014.

Beck, A. E., F. M. Anglin, and J. H. Sass, Analysis of heat flow datain situ thermal conductivity measurements, *Canadian Journal of Earth Sciences*, *8*(1), 1–19, doi:10.1139/e71-001, 1971.

Becker, M. W., B. Bauer, and A. Hutchinson, Measuring Artificial Recharge with Fiber Optic Distributed Temperature Sensing, *Ground Water*, pp. 1–9, doi:10.1111/j.1745-6584.2012.01006.x, 2012.

Belghoul, A., Caracterisation petrophysique et hydrodynamique du socle cristallin, Ph.D. thesis, Geophysics, Universite Montpellier II-Sciences et Techniques du Languedoc, 2007.

Benoit, D., and S. Thompson, Development and testing of a single ended distributed temperature sensing system at the beowawe, nevada geothermal reservoir, *Geothermal Resources Council Transactions*, *22*, 1998.

Bense, V., T. Read, and A. Verhoef, Using distributed temperature sensing to monitor field scale dynamics of ground surface temperature and related substrate heat flux, *Agricultural and Forest Meteorology*, *220*, 207 – 215, doi:http://dx.doi.org/10.1016/j.agrformet.2016.01.138, 2016.

Bense, V. F., and H. Kooi, Temporal and spatial variations of shallow subsurface temperature as a record of lateral variations in groundwater flow, *Journal of Geophysical Research: Solid Earth*, *109*(B4), n/a–n/a, doi:10.1029/2003JB002782, 2004.

Bense, V. F., M. A. Person, K. Chaudhary, Y. You, N. Cremer, and S. Simon, Thermal anomalies indicate preferential flow along faults in unconsolidated sedimentary aquifers, *Geophysical Research Letters*, *35*(24), n/a–n/a, doi:10.1029/2008GL036017, l24406, 2008.

Berthold, S., Synthetic convection log - characterization of vertical transport processes in fluid-filled boreholes, *Journal of Applied Geophysics*, *72*(1), 20–27, doi:10.1016/j.jappgeo.2010.06.007, 2010.

Berthold, S., and C. Resagk, Investigation of thermal convection in water columns using particle image velocimetry, *Experiments in Fluids*, *52*(6), 1465–1474, doi:10.1007/s00348-012-1267-7, 2012.

Bour, O., T. Le Borgne, N. Lavenant, T. Labasque, L. Longuevergne, L. Aquilana, R. Hochreutener, J. Jiminez-Martinez, and P. Davy, The hydrogeological observatory of ploemeur (France): Long-term monitoring and experimentations, in *Abstracts with Programs*, vol. 45, p. 510, Geological Society of America, 2013.

Bredehoeft, J. D., and I. S. Papaopulos, Rates of vertical groundwater movement estimated from the earth's thermal profile, *Water Resources Research*, *1*(2), 325–328, doi:10.1029/WR001i002p00325, 1965.

Briggs, M. A., L. K. Lautz, and J. M. McKenzie, A comparison of fibre-optic distributed temperature sensing to traditional methods of evaluating groundwater inflow to streams, *Hydrological Processes*, *26*(9), 1277–1290, doi:10.1002/hyp.8200, 2012a.

Briggs, M. A., L. K. Lautz, J. M. McKenzie, R. P. Gordon, and D. K. Hare, Using high-resolution distributed temperature sensing to quantify spatial and temporal variability in vertical hyporheic flux, *Water Resources Research*, *48*(2), n/a–n/a, doi:10.1029/2011WR011227, 2012b.

Brouyère, S., J. Batlle-Aguilar, P. Goderniaux, and A. Dassargues, A new tracer technique for monitoring groundwater fluxes: the Finite Volume Point Dilution Method., *Journal of Contaminant Hydrology*, *95*(3-4), 121–40, doi:10.1016/j.jconhyd.2007.09.001, 2008.

Cao, D., B. Shi, H. Zhu, K. Zhu, G. Wei, and K. Gu, Performance evaluation of two types of heated cables for distributed temperature sensing-based measurement of soil

moisture content, *Journal of Rock Mechanics and Geotechnical Engineering*, pp. –, doi:http://dx.doi.org/10.1016/j.jrmge.2015.09.005, 2015.

Carslaw, H., and J. Jaeger, *Conduction of heat in solids*, Oxford science publications, Clarendon Press, 1959.

Churchill, S. W., and H. Chu, Correlating equations for laminar and turbulent free convection from a vertical plate, *International Journal of Heat and Mass Transfer*, *18*, 1323–1329, 1975.

Coleman, T. I., B. L. Parker, C. H. Maldaner, and M. J. Mondanos, Groundwater flow characterization in a fractured bedrock aquifer using active {DTS} tests in sealed boreholes, *Journal of Hydrology*, *528*, 449–462, doi:10.1016/j.jhydrol.2015.06.061, 2015.

COMSOL, *COMSOL Multiphysics Reference Manual (version 4.4)*, 2013.

Conant, B., Delineating and quantifying ground water discharge zones using streambed temperatures, *Groundwater*, *42*(2), 243–257, 2004.

Daley, T. M., et al., Field testing of fiber-optic distributed acoustic sensing (das) for subsurface seismic monitoring, *The Leading Edge*, *32*(6), 699–706, doi:10.1190/tle32060699.1, 2013.

De Dreuzy, J.-R., J. Bodin, H. Le Grand, P. Davy, D. Boulanger, A. Battais, O. Bour, P. Gouze, and G. Porel, General database for ground water site information, *Ground Water*, *44*(5), 743–748, doi:10.1111/j.1745-6584.2006.00220.x, 2006.

Dorn, C., N. Linde, T. L. Borgne, O. Bour, and L. Baron, Single hole GPR reflection imaging of solute transport in a granitic aquifer, *38*(March), 1–5, doi:10.1029/2011GL047152, 2011.

Dorn, C., N. Linde, T. L. Borgne, O. Bour, and M. Klepikova, Inferring transport characteristics in a fractured rock aquifer by combining single-hole ground-penetrating radar reflection monitoring and tracer test data, *Water Resources Research*, *48*(11), W11521, doi:10.1029/2011WR011739, 2012.

Doughty, C., S. Takeuchi, K. Amano, M. Shimo, and C.-F. Tsang, Application of multirate flowing fluid electric conductivity logging method to well dh-2, tono site, Japan, *Water Resources Research*, *41*(10), n/a–n/a, doi:10.1029/2004WR003708, 2005.

Druillennec, T. L., G. Ielsch, O. Bour, C. Tarits, G. Tymen, G. Alcalde, and L. Aquilina, Hydrogeological and geochemical control of the variations of 222rn concentrations in a hard rock aquifer: Insights into the possible role of fracture-matrix exchanges, *Applied Geochemistry*, *25*(3), 345 – 356, doi:http://dx.doi.org/10.1016/j.apgeochem.2009.12.002, 2010.

Drury, M., A. Jessop, and T. Lewis, The detection of groundwater flow by precise temperature measurements in boreholes, *Geothermics*, *13*(3), 163–174, doi:10.1016/0375-6505(84)90013-0, 1984.

Elci, A., F. J. Molz, and W. R. Waldrop, Implications of observed and simulated ambient flow in monitoring wells, *Ground Water*, *39*(6), 853–862, doi:10.1111/j.1745-6584.2001.tb02473.x, 2001.

Elci, A., G. P. Flach, and F. J. Molz, Detrimental effects of natural vertical head gradients on chemical and water level measurements in observation wells: identification and control, *Journal of Hydrology*, *281*(12), 70–81, doi:10.1016/S0022-1694(03)00201-4, recent Advances in Aquifer Hydraulics and Their Applications to Aquifer and Vadose Zone Characterization, Remediation, and Dewatering, 2003.

Farahani, M., and T. Gogolla, Spontaneous Raman scattering in optical fibers with modulated probe light for distributed temperature Raman remote sensing, *Journal of Lightwave Technology*, *17*(8), 1379–1391, doi:10.1109/50.779159, 1999.

Foerster, A., J. Schroetter, D. F. Merriam, and D. D. Blackwell, Application of optical-fiber temperature logging; an example in a sedimentary environment, *Geophysics*, *62*(4), 1107–1113, doi:10.1190/1.1444211, 1997.

Freeze, R., and J. Cherry, *Groundwater*, Prentice Hall, 1979.

Freifeld, B., T. Daley, P. Cook, R. Trautz, and K. Dodds, The modular borehole monitoring program: a research program to optimize well-based monitoring for geologic carbon sequestration, *Energy Procedia*, *63*, 3500–3515, 2014.

Freifeld, B. M., S. Finsterle, T. C. Onstott, P. Toole, and L. M. Pratt, Ground surface temperature reconstructions: Using in situ estimates for thermal conductivity acquired with a fiber-optic distributed thermal perturbation sensor, *Geophysical Research Letters*, *35*(14), L14309, doi:10.1029/2008GL034762, 2008.

Freifeld, B. M., T. M. Daley, S. D. Hovorka, J. Henninges, J. Underschultz, and S. Sharma, Recent advances in well-based monitoring of {CO2} sequestration, *Energy Procedia*, *1*(1), 2277–2284, doi:10.1016/j.egypro.2009.01.296, greenhouse Gas Control Technologies 9Proceedings of the 9th International Conference on Greenhouse Gas Control Technologies (GHGT-9), 1620 November 2008, Washington DC, {USA}, 2009.

Ge, S., Estimation of groundwater velocity in localized fracture zones from well temperature profiles, *Journal of Volcanology and Geothermal Research*, *84*, 93–101, 1998.

Giese, R., et al., Monitoring at the co 2 sink site: a concept integrating geophysics, geochemistry and microbiology, *Energy Procedia*, *1*(1), 2251–2259, 2009.

Grosswig, S., E. Hurtig, and K. Kuehn, Fibre optic temperature sensing; a new tool for temperature measurements in boreholes, *Geophysics*, *61*(4), 1065–1067, doi:10.1190/1.1444027, 1996.

Hare, D. K., M. A. Briggs, D. O. Rosenberry, D. F. Boutt, and J. W. Lane, A comparison of thermal infrared to fiber-optic distributed temperature sensing for evaluation of groundwater discharge to surface water, *Journal of Hydrology*, *530*, 153 – 166, doi:http://dx.doi.org/10.1016/j.jhydrol.2015.09.059, 2015.

Hausner, M. B., F. Suárez, K. E. Glander, N. V. D. Giesen, J. S. Selker, and S. W. Tyler, Calibrating Single-Ended Fiber-Optic Raman Spectra Distributed Temperature Sensing Data, *Sensors*, *11*, 10,859–10,879, doi:10.3390/s111110859, 2011.

Hausner, M. B., L. Kryder, J. Klenke, R. Reinke, and S. W. Tyler, Interpreting variations in groundwater flows from repeated distributed thermal perturbation tests, *Groundwater*, pp. n/a–n/a, doi:10.1111/gwat.12393, 2015.

Hawkins, A. J., and M. W. Becker, MEASUREMENT OF THE SPATIAL DISTRIBUTION OF HEAT EXCHANGE IN A GEOTHERMAL ANALOG BEDROCK SITE USING FIBER OPTIC DISTRIBUTED TEMPERATURE SENSING, *October*, 2012.

Henninges, J., J. Schrötter, K. Erbas, S. Böde, and E. Huenges, Permanent installation of fibre-optic DTS cables in boreholes for temperature monitoring, in *EGS - AGU - EUG Joint Assembly*, p. 11394, 2003.

Henninges, J., E. Huenges, and H. Burkhardt, In situ thermal conductivity of gas-hydrate-bearing sediments of the mallik 5l-38 well, *Journal of Geophysical Research: Solid Earth*, *110*(B11), n/a–n/a, doi:10.1029/2005JB003734, 2005.

Hermans, T., S. Wildemeersch, P. Jamin, P. Orban, S. Brouyère, A. Dassargues, and F. Nguyen, Quantitative temperature monitoring of a heat tracing experiment using cross-borehole {ERT}, *Geothermics*, *53*(0), 14–26, doi:10.1016/j.geothermics.2014.03.013, 2015.

Hess, A., A heat-pulse flowmeter for measuring low velocities in boreholes, *Open file report*, U.S Geological Survey, 1982.

Hess, A. E., Identifying hydraulically conductive fractures with a slow-velocity borehole flowmeter, *Canadian Geotechnical Journal*, *23*(1), 69–78, 1986.

Hiscock, K. M., and V. F. Bense, *Hydogeology Principles and Practice*, Wiley-Blackwell, 2014.

Hurtig, E., S. Grosswig, and K. Kuhn, Fibre optic temperature sensing: application for subsurface and ground temperature measurements, *Tectonophysics*, *257*, 101–109, 1996.

Ikeda, N., K. Uogata, K. Seiki, and K. Haruguchi, Delineation of fractured reservoir by transient temperature analysis using fiber optic sensor, *Proceedings World Geothermal Congress*, 2000.

Incropera, F. P., D. Dewitt, T. Bergman, and A. Lavine, *Fundamentals of Heat and Mass Transfer*, John Wiley, 2007.

Klepikova, M. V., Imaging of fractured rock properties from flow and heat transport: field experiments and inverse modelling, Ph.D. thesis, Geosciences Rennes, 2013.

Klepikova, M. V., T. L. Borgne, O. Bour, and P. Davy, A methodology for using borehole temperature-depth profiles under ambient, single and cross-borehole pumping conditions to estimate fracture hydraulic properties, *Journal of Hydrology*, *407*(14), 145–152, doi:10.1016/j.jhydrol.2011.07.018, 2011.

Klepikova, M. V., T. Le Borgne., O. Bour, and J.-R. de Dreuzy, Inverse modeling of flow tomography experiments in fractured media, *Water Resources Research*, *49*, doi:10.1002/2013WR013722, 2013.

Kurth, A.-M., N. Dawes, J. Selker, and M. Schirmer, Autonomous distributed temperature sensing for long-term heated applications in remote areas, *Geoscientific Instrumentation, Methods and Data Systems*, *2*(1), 71–77, doi:10.5194/gi-2-71-2013, 2013.

Lauer, F., H.-G. Frede, and L. Breuer, Uncertainty assessment of quantifying spatially concentrated groundwater discharge to small streams by distributed temperature sensing, *Water Resources Research*, *49*(1), 400–407, doi:10.1029/2012WR012537, 2013.

Le Borgne, T., Equivalent mean flow models for fractured aquifers: Insights from a pumping tests scaling interpretation, *Water Resources Research*, *40*(3), 1–12, doi: 10.1029/2003WR002436, 2004.

Le Borgne, T., et al., Comparison of alternative methodologies for identifying and characterizing preferential flow paths in heterogeneous aquifers, *Journal of Hydrology*, *345*(3-4), 134–148, doi:10.1016/j.jhydrol.2007.07.007, 2007.

Leaf, A. T., D. J. Hart, and J. M. Bahr, Active Thermal Tracer Tests for Improved Hydrostratigraphic Characterization, *Ground Water*, *50*(5), 726–735, doi:10.1111/j. 1745-6584.2012.00913.x, 2012.

Lewis, D. C., G. J. Kriz, and R. H. Burgy, Tracer dilution sampling technique to determine hydraulic conductivity of fractured rock, *Water Resources Research*, *2*(3), 533–542, doi:10.1029/WR002i003p00533, 1966.

Liebel, H. T., K. Huber, and B. r. S. Frengstad, Thermal response testing of a fractured hard rock aquifer with and without induced groundwater flow, *Engineering Geology*, pp. 435–445, doi:10.1007/s10064-012-0422-y, 2012.

Liu, G., S. Knobbe, and J. Butler, Resolvingcentimeter-scale flows in aquifers and their hydrostratigraphic controls, *Geophysical Research Letters*, pp. n/a–n/a, doi:10.1002/ grl.50282, 2013.

Macfarlane, A., A. Förster, D. Merriam, J. Schrötter, and J. Healey, Monitoring artificially stimulated fluid movement in the Cretaceous Dakota aquifer, western Kansas, *Hydrogeology Journal*, *10*(6), 662–673, doi:10.1007/s10040-002-0223-7, 2002.

Maurice, L., J. A. Barker, T. C. Atkinson, A. T. Williams, and P. L. Smart, A Tracer Methodology for Identifying Ambient Flows in Boreholes, *Ground Water*, *49*(2), 227–238, doi:10.1111/j.1745-6584.2010.00708.x, 2011.

Moir, R. S., A. H. Parker, and R. T. Bown, A simple inverse method for the interpretation of pumped flowing fluid electrical conductivity logs, *Water Resources Research*, *50*(8), 6466–6478, doi:10.1002/2013WR013871, 2014.

Molz, F., R. Morin, A. Hess, J. Melville, and O. Given, The impeller meter for measuring aquifer permeability variations: evaluations and comparison with other tests, *Water Resources Research*, *25*, 1677–1683, 1989.

Molz, F., G. Boman, S. Young, and W. Waldrop, Borehole flowmeters: field application and data analysis, *Journal of Hydrology*, *163*(3-4), 347–371, doi:10.1016/ 0022-1694(94)90148-1, 1994.

Neilson, B. T., C. E. Hatch, H. Ban, and S. W. Tyler, Solar radiative heating of fiber-optic cables used to monitor temperatures in water, *Water Resources Research*, *46*(8), W08540, doi:10.1029/2009WR008354, 2010.

Neuman, S. P., Trends, prospects and challenges in quantifying flow and transport through fractured rocks, *Hydrogeology Journal*, *13*(1), 124–147, doi:10.1007/ s10040-004-0397-2, 2005.

Noni, M. M. MacLaughlin, and H. F. Wang, Validation of fiber-optic strain sensing cable for deep underground installation, in *45th U.S Rock Mechanics*, p. 8, San Francisco, CA, 2011.

Novakowski, K., G. Bickerton, P. Lapcevic, J. Voralek, and N. Ross, Measurements of groundwater velocity in discrete rock fractures., *Journal of contaminant hydrology*, *82*(1-2), 44–60, doi:10.1016/j.jconhyd.2005.09.001, 2006.

Paillet, F. L., Flow modeling and permeability estimation using borehole flow logs in heterogeneous fractured formations, *Water Resources Research*, *34*(5), 997–1010, doi:10.1029/98WR00268, 1998.

Paillet, F. L., A. E. Hess, C. H. Cheng, and E. Hardin, Characterization of fracture permeability with high-resolution vertical flow measurements during borehole pumping, *Ground Water*, *25*(1), 28–40, doi:10.1111/j.1745-6584.1987.tb02113.x, 1987.

Paillet, F. L., J. H. Williams, J. Urik, J. Lukes, M. Kobr, and S. Mares, Cross-borehole flow analysis to characterize fracture connections in the melechov granite, bohemian-moravian highland, czech republic, *Hydrogeology Journal*, *20*(1), 143–154, doi:10.1007/s10040-011-0787-1, 2011.

Parker, T., S. Shatalin, and M. Farhadiroushan, Distributed acoustic sensing–a new tool for seismic applications, *first break*, *32*(2), 61–69, 2014.

Pehme, P., J. Greenhouse, and B. Parker, The active line source temperature logging technique and its application in fractured rock hydrogeology, *Journal of Environmental and Engineering Geophysics*, *12*(4), 307–322, 2007.

Pehme, P., B. Parker, J. Cherry, J. Molson, and J. Greenhouse, Enhanced detection of hydraulically active fractures by temperature profiling in lined heated bedrock boreholes, *Journal of Hydrology*, *484*(0), 1–15, doi:10.1016/j.jhydrol.2012.12.048, 2013.

Petty, S., Y. Nordin, W. Glassley, T. Cladouhos, and M. Swyer, Improving geothermal project economics with multi-zone stimulation results from the newberry volcano egs demonstration, in *Thirty-Eighth Workshop on Geothermal Reservoir Engineering*, Stanford University, Stanford, California, 2013.

Pitrak, M., S. Mares, and M. Kobr, A simple borehole dilution technique in measuring horizontal ground water flow, *Ground Water*, *45*(1), 89–92, doi:10.1111/j.1745-6584.2006.00258.x, 2007.

Read, T., O. Bour, V. Bense, T. Le Borgne, P. Goderniaux, M. Klepikova, R. Hochreutener, N. Lavenant, and V. Boschero, Characterizing groundwater flow and heat transport in fractured rock using fiber-optic distributed temperature sensing, *Geophysical Research Letters*, *40*(10), 2055–2059, doi:10.1002/grl.50397, 2013.

Read, T., O. Bour, J. S. Selker, V. F. Bense, T. L. Borgne, R. Hochreutener, and N. Lavenant, Active-distributed temperature sensing to continuously quantify vertical flow in boreholes, *Water Resources Research*, *50*(5), 3706–3713, doi:10.1002/2014WR015273, 2014.

Read, T., V. F. Bense, O. Bour, T. Le Borgne, N. Lavenant, R. Hochreutener, and J. S. Selker, Thermal-plume fibre optic tracking (t-pot) test for flow velocity measurement in groundwater boreholes, *Geoscientific Instrumentation, Methods and Data Systems Discussions*, *5*(1), 161–175, doi:10.5194/gid-5-161-2015, 2015.

Reinsch, T., J. Henninges, and R. smundsson, Thermal, mechanical and chemical influences on the performance of optical fibres for distributed temperature sensing in a hot geothermal well, *Environmental Earth Sciences*, *70*(8), 3465–3480, doi:10.1007/s12665-013-2248-8, 2013.

Rogers, A., Distributed optical-fibre sensing, *Measurement Science and Technology*, *10*(8), R75–R99, 1999.

Ruelleu, S., F. Moreau, O. Bour, D. Gapais, and G. Martelet, Impact of gently dipping discontinuities on basement aquifer recharge: An example from ploemeur (brittany, france), *Journal of Applied Geophysics*, *70*(2), 161 – 168, doi:http://dx.doi.org/10.1016/j.jappgeo.2009.12.007, 2010.

Ruud, N., Z. Kabala, and F. Molz, Evaluation of flowmeter-head loss effects in the flowmeter test, *Journal of Hydrology*, *224*(1), 55–63, 1999.

Saar, M. O., Review: Geothermal heat as a tracer of large-scale groundwater flow and as a means to determine permeability fields, *Hydrogeology Journal*, *19*(1), 31–52, 2011.

Sakaguchi, K., and N. Matsushima, Temperature logging by the distributed temperature sensing technique during injection tests, *Proceedings World Geothermal Congress*, 2000.

Sammel, E. A., Convective flow AND its effect on temperature logging in small diameter wells, *GEOPHYSICS*, *33*(6), 1004–1012, doi:10.1190/1.1439977, 1968.

Sayde, C., C. Gregory, M. Gil-Rodriguez, N. Tufillaro, S. Tyler, N. van de Giesen, M. English, R. Cuenca, and J. S. Selker, Feasibility of soil moisture monitoring with heated fiber optics, *Water Resources Research*, *46*(6), n/a–n/a, doi:10.1029/2009WR007846, 2010.

Sayde, C., C. Thomas, J. Wagner, and J. Selker, High resolution mapping of wind speed using active distributed temperature sensing, A54B-03, AGU Fall Meeting, San Francisco, 2013.

Sayde, C., J. B. Buelga, L. Rodriguez-Sinobas, L. El Khoury, M. English, N. van de Giesen, and J. S. Selker, Mapping variability of soil water content and flux across 11000 m scales using the actively heated fiber optic method, *Water Resources Research*, *50*(9), 7302–7317, doi:10.1002/2013WR014983, 2014.

Sayde, C., C. K. Thomas, J. Wagner, and J. Selker, High-resolution wind speed measurements using actively heated fiber optics, *Geophysical Research Letters*, pp. n/a–n/a, doi:10.1002/2015GL066729, 2015GL066729, 2015.

Schuetz, T., and M. Weiler, Quantification of localized groundwater inflow into streams using ground-based infrared thermography, *Geophysical Research Letters*, *38*(3), 1–5, doi:10.1029/2010GL046198, 2011.

Sebok, E., C. Duque, J. Kazmierczak, P. Engesgaard, B. Nilsson, S. Karan, and M. Frandsen, High-resolution distributed temperature sensing to detect seasonal groundwater discharge into lake vng, denmark, *Water Resources Research*, *49*(9), 5355–5368, doi:10.1002/wrcr.20436, 2013.

Selker, J. S., S. Tyler, and N. van de Giesen, Comment on "capabilities and limitations of tracing spatial temperature patterns by fiber-optic distributed temperature sensing" by liliana rose et al., *Water Resources Research*, *50*(6), 5372–5374, doi:10.1002/2013WR014979, 2014.

Selker, J. S., et al., Distributed fiber-optic temperature sensing for hydrologic systems, *Water Resources Research*, *42*(12), W12202, doi:10.1029/2006WR005326, 2006.

Sellwood, S., D. Hart, and J. Bahr, An in-well heat-tracer-test method for evaluating borehole flow conditions, *Hydrogeology Journal*, *23*(8), 1817–1830, doi:10.1007/s10040-015-1304-8, 2015a.

Sellwood, S. M., D. J. Hart, and J. M. Bahr, Evaluating the use of in-well heat tracer tests to measure borehole flow rates, *Groundwater Monitoring & Remediation*, pp. n/a–n/a, doi:10.1111/gwmr.12134, 2015b.

Shen, P. Y., and a. E. Beck, Stabilization of Bottom Hole Temperature With Finite Circulation Time and Fluid Flow, *Geophysical Journal International*, *86*(1), 63–90, doi:10.1111/j.1365-246X.1986.tb01073.x, 1986.

Silliman, S. E., and C. E. Neuzil, Borehole determination of formation thermal conductivity using a thermal pulse from injected fluid, *Journal of Geophysical Research: Solid Earth*, *95*(B6), 8697–8704, doi:10.1029/JB095iB06p08697, 1990.

Siska, P., J. Latal, P. Bujok, A. Vanderka, M. Klempa, P. Koudelka, V. Vasinek, and P. Pospisil, Optical fiber based distributed temperature systems deployment for measurement of boreholes temperature profiles in the rock massif, *Optical and Quantum Electronics*, *48*(2), 1–21, doi:10.1007/s11082-016-0379-3, 2016.

Stotler, R. L., S. K. Frape, B. M. Freifeld, B. Holden, T. C. Onstott, T. Ruskeeniemi, and E. Chan, Hydrogeology, chemical and microbial activity measurement through deep permafrost, *Ground Water*, *49*(3), 348–364, doi:10.1111/j.1745-6584.2010.00724.x, 2011.

Striegl, A. M., and S. P. i. Loheide, Heated Distributed Temperature Sensing for Field Scale Soil Moisture Monitoring, *Ground Water*, *50*(3), 340–347, doi:10.1111/j.1745-6584.2012.00928.x, 2012.

Suárez, F., J. E. Aravena, M. B. Hausner, a. E. Childress, and S. W. Tyler, Assessment of a vertical high-resolution distributed-temperature-sensing system in a shallow thermohaline environment, *Hydrology and Earth System Sciences*, *15*(3), 1081–1093, doi:10.5194/hess-15-1081-2011, 2011.

Taniguchi, M., Evaluation of vertical groundwater fluxes and thermal properties of aquifers based on transient temperature-depth profiles, *Water Resources Research*, *29*(7), 2021–2026, doi:10.1029/93WR00541, 1993.

Touchard, F., Caracterisation hydrogeologique d'un aquifere en socle fracture, Ph.D. thesis, Geosciences Rennes, 1999.

Tyler, S. W., J. S. Selker, M. B. Hausner, C. E. Hatch, T. Torgersen, C. E. Thodal, and S. G. Schladow, Environmental temperature sensing using Raman spectra DTS fiber-optic methods, *Water Resources Research*, *45*, 1–11, doi:10.1029/2008WR007052, 2009.

USGS, http://water.usgs.gov/ogw/bgas/flowmeter/, last accessed 16/12/2015, 2013.

van de Giesen, N., S. C. Steele-Dunne, J. Jansen, O. Hoes, M. B. Hausner, S. Tyler, and J. Selker, Double-Ended Calibration of Fiber-Optic Raman Spectra Distributed Temperature Sensing Data, *Sensors*, pp. 5471–5485, doi:10.3390/s120505471, 2012.

Vigneresse, J. L., J. Jolivet, M. Cuney, and G. Bienfait, Heat flow, heat production and granite depth in western france, *Geophysical Research Letters*, *14*(3), 275–278, doi:10.1029/GL014i003p00275, 1987.

Vogt, T., P. Schneider, L. Hahn-Woernle, and O. A. Cirpka, Estimation of seepage rates in a losing stream by means of fiber-optic high-resolution vertical temperature profiling, *Journal of Hydrology*, *380*(12), 154–164, doi:10.1016/j.jhydrol.2009.10.033, 2010.

Wagner, V., T. Li, P. Bayer, C. Leven, P. Dietrich, and P. Blum, Thermal tracer testing in a sedimentary aquifer: field experiment (lauswiesen, Germany) and numerical simulation, *Hydrogeology Journal*, *22*(1), 175–187, doi:10.1007/s10040-013-1059-z, 2014.

Wisian, K. W., D. D. Blackwell, S. Bellani, J. A. Henfling, R. A. Normann, P. C. Lysne, A. Förster, and J. Schrötter, Field comparison of conventional and new technology temperature logging systems, *Geothermics*, *27*(2), 131–141, doi:10.1016/S0375-6505(97)10013-X, 1998.

Yamano, M., and S. Goto, Long-term temperature monitoring in a borehole drilled into the nojima fault, southwest Japan, *Island Arc*, *10*(3-4), 326–335, doi:10.1111/j.1440-1738.2001.00331.x, 2001.

Yamano, M., and S. Goto, Long-term monitoring of the temperature profile in a deep borehole: Temperature variations associated with water injection experiments and natural groundwater discharge, *Physics of the Earth and Planetary Interiors*, *152*(4), 326–334, doi:10.1016/j.pepi.2005.04.010, thermally controlled processes and preserved thermal signatures within the Earth, 2005.